

Reconstruction of rift basins in the Eastern Cordillera
and Middle Magdalena Valley, Colombia: Analysis of
the extensional phase and structural styles of tectonic
inversion

Dissertation

zur Erlangung des mathematisch-naturwissenschaftlichen
Doktorgrades

"Doctor rerum naturalium"

der Georg-August-Universität Göttingen

im Promotionsprogramm Geowissenschaften / Geographie
der Georg-August University School of Science (GAUSS)

vorgelegt von

Martin Javier Reyes Correa

Aus: Bucaramanga, Kolumbien.

Göttingen 2021

Betreuungsausschuss:

- **Prof. Dr. Jonas Kley**
Geowissenschaftliches Zentrum der Universität Göttingen
- **Dr. Andrés Roberto Mora Bohorquez**
Ecopetrol-Brazil
- **Dr. David Hindle**
Geowissenschaftliches Zentrum der Universität Göttingen

Mitglieder der Prüfungskommission

- Referent: **Prof. Dr. Jonas Kley**
Geowissenschaftliches Zentrum der Universität Göttingen
- Korreferent: **Prof. Dr. Hilmar von Eynatten**
Geowissenschaftliches Zentrum der Universität Göttingen

weitere Mitglieder der Prüfungskommission:

- **Dr. Andrés Roberto Mora Bohorquez**
Ecopetrol-Brazil
- **Dr. István Dunkl**
Geowissenschaftliches Zentrum der Universität Göttingen
- **Dr. David Hindle**
Geowissenschaftliches Zentrum der Universität Göttingen
- **Dr. Bernd Leiss**
Geowissenschaftliches Zentrum der Universität Göttingen

Tag der mündlichen Prüfung: 30 November 2021

“No estás deprimido, estás distraído,

Distraído de la vida que te puebla.

Distraído de la vida que te rodea:

Delfines, bosques, mares, montañas, ríos.”

Facundo Cabral (1937-2011)

"You're not depressed, you're distracted,

Distracted from the life that populates you.

Distracted from the life that surrounds you:

Dolphins, forests, seas, mountains, rivers."

Facundo Cabral (1937-2011)

Co-Authors Contribution

This dissertation contains six chapters that were structured and organized with the support and help of the co-authors. Here I describe the contributions made by the different co-authors and myself for the different chapters.

1. The Introduction and Motivation chapter was written by myself, but with the guidance and support of Prof. Dr. Jonas Kley and Dr. Andrés Mora in the structure and general ideas to complement the research.
2. The Chapter “Onset and style of Mesozoic extension in the Eastern Cordillera and Middle Magdalena Valley constrained by the first volcanic events” is co-authored with Prof. Dr. Jonas Kley, Dr. Andrés Mora, Dr. Istvan Dunkl, and Juan Carvajal Torres. The field work and sample collection were performed by Martin Reyes. Sample preparation and analysis was conducted by Martin Reyes under the supervision of Dr. Istvan Dunkl and Prof. Jonas Kley. The Data analysis and synthesis was made under supervision of Prof. Jonas Kley and Dr. Andrés Mora. Text edition and initial draft preparation was made by all the authors. The final draft preparation was elaborated by Prof. Jonas Kley, Dr. Andres Mora and Martin Reyes.
3. The Chapter " Mesozoic Geometry and Structural styles in the Middle Magdalena Valley and the Western Foothills of the Eastern Cordillera” are joint-work with Prof. Dr. Jonas Kley, Dr. Andrés Mora, Dr. David Hindle and Juan Carvajal Torres. The idea generation was made by Prof. Jonas Kley and Martin Reyes. The data management and seismic interpretation was performed by Martin Reyes. The data analysis and draft preparation was done by Martin Reyes under the supervision mainly of Prof. Jonas Kley. The other co-authors also contributed to the final draft with meetings and result analysis.
4. The Chapter “La Cira Basement-high, Middle Magdalena Valley Basin Colombia” is co-authored with Prof. Dr. Jonas Kley, Dr. Andrés Mora, Daniel Bello-Palacios, Andres Felipe Vargas, Juan Carvajal and Jose Osorno. The idea was developed by Martin Reyes and Prof. Dr. Jonas Kley. The seismic interpretation was performed by Martin Reyes under the supervision of Prof. Jonas Kley, Dr. Andrés Mora, Daniel Bello and Andres Vargas. The data analysis was conducted in a joint group to discuss the evolution and analysis of this basement-high. The final draft preparation was made by Martin Reyes, Prof. Jonas Kley and Dr. Andrés Mora.

5. The Chapter “Kinematic Restoration of the Mesozoic Extensional Basins in the Middle Magdalena Valley and Eastern Cordillera” is co-authored with Prof. Dr. Jonas Kley, Dr. Andrés Mora. The initial idea was developed by Martin Reyes but the chapter still in preparation. The fission track analysis and cross-section restoration were conducted by Martin Reyes under the supervision of Prof. Jonas Kley and Dr. Andrés Mora.
6. The Chapter “Basin Modeling of the Mesozoic Extensional Basins in the Middle Magdalena Valley and Eastern Cordillera” is co-authored with Prof. Dr. Jonas Kley, Juan Carlos Hidalgo, Dr. Andres Mora. The development of the idea was by Martin Reyes and Juan Carlos Hidalgo. The basin modeling was conducted by Martin Reyes under the supervision of Juan Carlos Hidalgo. The outcome analysis was made by Martin Reyes with the support of all the co-authors.

This project was possible from the funding and scholarship provided by the Ministry of Science, Technology and Innovation of Colombia (former Colciencias).

Acknowledgments

First, I want to express my gratitude to everybody who directly or indirectly supported me during this formation time.

I want to mention that this project was supported by the Colciencias funding *Doctorados en el exterior 756*, a stipend that could increase to sponsor more students and solve the social differences present in our country.

During my career as a geologist, I have been involved in many research groups. I was guided by different leaders and researchers where I had the privilege of learning and obtaining the best ideas, concepts, and workflows to polish me as the young professional who I am. So thanks to all my mentors and Professors.

The first time I saw the Jurassic and Cretaceous contact in the Los Santos, Santander around the Chicamocha Canyon was when I was ten years old, and I was trying to shepherd the goats of my family farm. So indirectly, this landscape view and the hard topography exposed there impacted me to work in outdoor areas, and it was one of the reasons to identify what happened there to have this mountains with some different colors. The grandma's brothers were also a considerable influence, They were field assistants when Ward, Cediél, and other geologists did their field work during the 60s. They never attended to the university, but they were constantly astonished by the kind of rocks, minerals, and chemical reactions. I want to mention specially Alfredo Mantilla (R.I.P) and Daniel Mantilla many thanks.

Moving from my background to the recent years, I am totally in debt with my advisor Jonas Kley; the first mail that I sent to him to arrive here got me an unexpected response and was the beginning of this beautiful steep Ph.D. path. I want to thank Professor Jonas first for allowing me to be his student and work in this research group, which was a entire scientific pleasure. I had the privilege to have several talks about geology with Professor Jonas and again totally glad for his patience even when I was quite lost with the challenge to be in front of this research. Besides all my admiration to him for the way to transfer knowledge and the excellent way to be a top scientist and human, I'm speechless to say thanks for everything, Professor.

Thanks to Dr. Andres Mora for his advice and always the kind and fun way to explain geology to me; thanks for his confidence in supporting this project even when he was busy but always finding a spot to discuss the ideas or analysis, many thanks.

Here is important to mention the number of professionals involved in this project. My friend Daniel Bello for his geological modeling tips and tricks and his patience. Thanks to Juan Carlos Hidalgo from Schlumberger for his patience and for teaching me how to approach the basin modeling in PetroMod and acquire the licenses with Dr. Bjorn Wygrala and Raul Hernandez. Thanks to Dr. Klaus Wemmer for the support and help in teaching me how to prepare the samples for dating. Also, thanks to Dr. Istvan Dunkl for the geochronological dating, patience, and support. It is important to mention Jose Fernando Osorno for his kindness and confidence in supporting this project with the data transfer from the ANH. It is, without doubt, one of the ways to increase the Geoscience knowledge in our country.

Thanks to Leidy Castro "Negri" for her support as a friend and as a geologist, for being in tough times during this road even when the darkness was more, and the arm was broken ;). Juan Carvajal

Torres, another friend, thanks for all your comments and our exciting talks about geology. Ani, thanks for the fieldwork assistance and support during this time.

I would also like to thank all my structural geology department co-workers, and friends Renas Koshnaw, Hernan Silva, Ali “Baba”, Kathie Ford, Mattias Hueck, and all the members of our department that in somehow contributed to the development of this project. Thanks to Maria Hesse for all the administrative support; and our talks about weather, food and gardening. I want to mention some of my close friends that I met during this time in Gottingen Crí, Ani Vergel, Daniel Cantor, Diego Tapias, Janosch, Ana Ebriedades, Pedri, Dario, Arturito; and all the members of our initial team Chingones FC, people that helped me during my stay and were my family during this stage.

My friends worldwide were always concerned about my progress and life specially in difficult times as in 2020, Gordito, Pulli, Camilin, Dani Carrera, Ruso, Ardo, Coli, Aleja Diaz, Negro, thanks for your time and friendship.

The last is for my family. I can not imagine this process without them, I want to express all my admiration and gratitude to my parents and my grandparents. Thanks to my Ma for all her support, for always listened to me when I was confused or tired, and transferred me energy just with her voice and courage. Thanks to my Pa for being so relaxed in terms of the future and shared me some ideas to adapt in my life, thanks to my loved sister Nenita, for all her support and her talks when I needed it, I can not imagine this life without my sister. The last words are for my Nonita, we have been blessed with your presence, and I love all the talks, especially when we had to talk about traditions of habits just to distract my mind and recharged myself; thanks to you all and also to the other members of my family that sent me good vibes during this short time. Thanks to the life that allowed me to put this last phrase as the end of this project.

ABSTRACT

The Middle Magdalena Valley (MMV) and the Eastern Cordillera (EC) are regional tectonic units of the northern Andes in Colombia that comprise a total area of about 100.000 km². The MMV is an intermontane basin located between the Central Cordillera in the west and the EC in the east, bounded by the San Lucas range to the west and the La Salina fault system to the east. Its sedimentary infill records the uplift of the two adjacent cordilleras in Late Cretaceous to Recent time. The eastern margin of the MMV is affected by thick- and thin-skinned thrusts associated with the La Salina system. The EC today is a large pop-up structure uplifted between the La Salina system and the Guaicaramo system which forms its border to the undeformed Llanos foreland in the east. Both the MMV and EC are underlain by a Mesozoic rift basin that was inverted during the Andean Cenozoic orogeny to obtain its present-day thrust belt architecture. This project integrates geological and geophysical information from the MMV as well as surface and geochronological information from the EC with the primary aim to reconstruct the extensional (rift) setting during the Mesozoic.

As a basis for a regional overview of the tectonic evolution in the MMV and EC, we integrated pre-existing data including stratigraphy, geochemistry, age dates and structural information to compile a new Mesozoic chronostratigraphic chart. Two field campaigns were conducted to study the Mesozoic volcanism in the area. We constrained the possible onset of extension in the MMV and EC through new field observations and new geochronological data.

Based on that information, we conclude that extension in the MMV and EC began in the Late Triassic. Geochemical data suggest a close link of volcanism to a magmatic arc and thus an intra-arc setting for the early rift basins. The regional Santa Marta-Bucaramanga strike-slip fault has played an essential role in the Mesozoic basin development and the distribution of volcanics since the Late Triassic. According to the NW, transpressive trending in relation to the NE trending Boyacá and Soapaga normal faults are interpreted as splay structures of the Santa Marta-Bucaramanga fault and defined as a horsetail that started its extension since the Late Triassic.

Our geochronological analyses from the Mesozoic tuff layers along the strike of the EC basin reveal different asynchronous volcanic pulses whose spatial distribution and timing may be linked to northwestward slab migration and retreat of the magmatic arc. We therefore interpret that most of the Mesozoic basin infill was deposited in a back-arc tectonic setting in accordance with previous

studies and the new data as a basis for a regional overview of the tectonic evolution in the MMV and EC, we integrated pre-existing data including stratigraphy, geochemistry, age dates and structural information to compile a new Mesozoic chronostratigraphic chart. Two field campaigns were conducted to study the Mesozoic volcanism in the area. We constrained the possible onset of extension in the MMV and EC through new field observations and new geochronological data. from this project.

3100 km of 2D seismic reflection data from the MMV and EC were analyzed and interpreted in the time domain. The analysis and interpretation were constrained using data such as well logs, additional geophysical data (gravity measurements), and geological surface data (dips and thicknesses). Using the velocity logs and the seismic attributes, pseudo-3D velocity models were generated to perform the time-depth domain conversion. The final interpretation in the depth domain and surface information allowed us to construct serial cross-sections along the basin. We tested all structural interpretations through geometric forward modeling. In this way we constrained structural geometries in the MMV and EC and validated the previous ideas about thick-skinned and thin-skinned thrusting domains. One principal conclusion is related to forebulge migration and the influence of inherited Mesozoic structures in the present configuration. From north to south the cross-sections exhibit variations in structural domains and styles. Our analysis suggests these are linked to variations in the magnitude and timing of the evolving orogenic load. The proportions of thick- vs. thin-skinned thrusting and fault displacements also vary. The displacement on the La Salina fault decreases southward. The thin-skinned domain appears probably linked to a weakness of the sedimentary cover that detached from the basement associated with a weak basement fault.

Triassic-middle Cretaceous sediments were deposited in an intra-arc/back arc setting, which was intruded by granitoid linked to the back-arc configuration. At the end of this extensional event, the basins experienced the maximum depth probably linked to the sag and the post-rift starting.

Fission track data obtained during the last two decades was compiled and organized according to the proximity of the cross-sections. This information was employed to reconstruct the exhumation magnitude and style over time. According to other authors' thermochronological data and stratigraphic sequence analysis, the basins experienced uplift since the Late Cretaceous-early Paleocene; different uplifting events have been identified during the Andean Cenozoic Orogeny, where the major shortening is linked since the late Miocene.

Basin modeling was employed to test and further constrain the validity of the geometries and the events previously identified. Stepwise kinematic restoration of two cross-sections spanning both the rifting and the inversion phase was used to construct transformation ratio, vitrinite reflectance models employing the stratigraphic, geochemical data i.e., TOC (Total organic content), kerogen, hydrogen index; and heat flow scenarios divided in different tectonic settings, the initial extension phase started from a basal a heat flow of 60~45 mWm⁻²q with a highest peak to 80 mWm⁻²q. Followed by a gradual thermal subsidence with a basal heat flow of 75 ~60 mWm⁻²q. Episodes of compression, uplift, erosion and cooling started since the Paleocene to the present-day with a basal heat flow of 70~25 mWm⁻²q.

The best-fitting models suggests an initial pulse of hydrocarbon generation in the Paleocene, when the inversion phase started in the northern area.

The main generation phase occurred during the Oligocene, but the absence of accumulations at this time was associated to the trapping and seal formation, the structures presented in the basins had not significant cut-offs to preserve hydrocarbons in most of the areas. Moreover the sedimentary environment was fluvial mainly and the seal generation is associated with intra lagoon environments.

In addition and based on these restrictions, is important to highlight the relevance of Mesozoic inverted structures that play a role in the migration path and trapping; these structures allowed to generated the potential traps, as is the case of the La Salina Fault, where its compression domain with an ideal juxtaposition between layers to preserve hydrocarbons.

The unconformities generated during the inversion phase served as migration paths and were in charge to transport the hydrocarbons from the source to the intermontane MMV basin. Furthermore, the absence of Cenozoic reservoirs in the Eastern Cordillera is attributed to the inversion and uplift at that time.

The improved understanding of the inversion in fold and thrust belts requires integrating different data and methodologies to reduce uncertainty in such complex areas. This work was carried out to provide new insights in order to contribute to the basin development comprehension.

The new perspectives obtained in this work are the initial extension and its configuration started from the Late Triassic, and the extension continues during the Mesozoic with different peaks linked to the magmatic activity. Moreover, the basin development began with an intra- arc to a back-arc

configuration, and during the Late Cretaceous the basin experienced the compression and inversion attributed to the Cenozoic Orogeny by different authors. We identified the relevance of the Mesozoic inherited structures in the present-day configuration, and the fundamental role of the Inversion fold and thrust belts in the sedimentary development. The depozones in the MMV are controlled by the orogenic load migration to the south and its variations in size and weight. The double vergence structures in the MMV reflects the Central and Eastern Cordilleras uplifting. The basement high in the MMV could be generated by an east verging deep crustal blind thrust, that propagates during the Central Cordillera uplift, nevertheless another hypotheses is associated with the forebulge migration due the coeval orogenic load. According to the kinematic restorations we considered that the extensional phase ended during the middle Cretaceous, but the increase of thickness data will support it. During the Late Cretaceous the basin experienced a cooling event and it is associated to the thermal subsidence, then at the end of that time and early Paleocene the basin experienced the compression and inversion attributed to the Central Cordillera and Eastern Cordillera uplift. The major deformation occurred during the late Miocene, attributed to the Eastern Cordillera uplifting event. Our basin modeling indicates that the principal organic matter transformation occurred during the Oligocene and this generation is due the lithostatic chart and the basal heat flow variation. The vitrinite reflectance models suggest that the maturity of the hydrocarbon source rocks is affected by the deformation stage since the Miocene and the basal heat flow variations, moreover the source rocks located in the intermontane basin are in oil window generation in relation to the the hinterland source rocks that are mature or overmature for the present-day configuration. In summary the inversion of the Mesozoic extensional configuration played a fundamental role in the development of the structures such as folds, faults that preserved the hydrocarbon in the MMV.

CONTENTS

1. Introduction and Motivation	1
Thesis structure	4
Dataset and Methods	5
Geological setting and previous studies	9
2. Onset and style of Mesozoic extension in the Eastern Cordillera and Middle Magdalena Valley constrained by the first volcanic events	18
Chapter Overview	18
Abstract	19
Introduction	20
Outline of the Mesozoic Evolution	23
Geological description	25
Methods	29
Results	30
Mesozoic stratigraphic synthesis	30
Thin section petrography	34
Zircon texture	35
U-Pb Geochronology	37
Structural cross-sections	43
Discussion	51
Geochronological dating significance	51
Conclusions	63
3. Mesozoic Geometry and Structural styles in the Middle Magdalena Valley and the Western Foothills of the Eastern Cordillera	64
Chapter Overview	64
Abstract	65
Introduction	66
Data and Methodology	69
Data	69

Methodology.....	71
Results.....	75
Seismic Interpretation.....	75
Discussion.....	86
Conclusion.....	92
4. La Cira Basement-high, Middle Magdalena Valley Basin Colombia	94
Chapter Overview.....	94
Abstract.....	95
Introduction	97
Seismic Interpretation.....	104
Kinematic Restoration.....	109
Alternative models for the La Cira Basement-high.....	115
Conclusions	117
5. Kinematic Restoration of the Mesozoic Extensional Basins in the Middle Magdalena Valley and the Eastern Cordillera	118
Chapter Overview.....	118
Abstract.....	119
Introduction	120
Data and Methodology.....	123
Data	123
Methodology.....	123
Stratigraphy summary.....	127
Results.....	128
Kinematic Restoration.....	129
Conclusions	145
6. Basin Modeling of the Mesozoic Extensional Basins in the Middle Magdalena Valley and the Eastern Cordillera	146
Chapter Overview.....	146
Abstract.....	147

Introduction	148
Methodology.....	151
Results.....	153
Burial History.....	153
Heat flow analysis.....	159
Possible Accumulations.....	174
Conclusions	177
General Conclusions.....	179
Recommendations.....	182
References	184
Appendix	202
1. U/Pb LA-ICP-MS geochronology on zircons from the Mesozoic formations in the Eastern Cordillera and Middle Magdalena.....	202
2. Borehole Data of the Middle Magdalena Valley basin and the Eastern Cordillera. ...	225
3. Seismic Data of the Middle Magdalena Valley basin and the Eastern Cordillera.....	226
CV MARTIN JAVIER REYES CORREA.....	232

TABLE OF FIGURES

Figure 1-1 Digital elevation map of the northernmost Andes of South America. This map is showing the main basins and tectonic structures. Purple box denotes the study area location see in Figure 1-3. This area comprises the eastern and central part of the MMV (Middle Magdalena Valley), and the western and central side of the EC (Eastern Cordillera). CP (Caribbean Plate), SAP (South American Plate), NP (Nazca Plate). Main structural elements are SNSM (Sierra Nevada de Santa Marta), LMV (Lower Magdalena Valley), MMV (Middle Magdalena Valley), MA (Merida Andes), EC (Eastern Cordillera), UMV (Upper Magdalena Valley), CC (Central Cordillera), WC (Western Cordillera) and CR (Cordillera Real). 3

Figure 1-2 Database composed of seismic reflection lines, boreholes provided by the ANH, and thickness data compiled in this project. SL: San Lucas range, MMV: Middle Magdalena Valley and EC: Eastern Cordillera, the purple and green lines represent their boundaries. See location in Figure 1-1..... 7

Figure 1-3 Digital elevation map of the study area with the main localities and major mountain expressions. See the Location in Figure 1-1..... 9

Figure 1-4 a) Paleotectonic reconstruction of continental northwestern South America and surrounding Pacific and Caribbean regions for the Late Triassic-Jurassic adapted and modified from Cediél et al., 2003. b) Unscaled cross section illustrating the Late Triassic-Early Jurassic extensional model proposed by Cediél et al., 2003. LAB (Lithosphere–asthenosphere boundary).10

Figure 1-5 a) Tectonic reconstruction of the subduction zones along western Pangaea during the Late Triassic- Early Jurassic determined using an arc-trench distance of 300 km, and constant slab-dip adapted and modified from Spikings et al., 2015. b) Unscaled cross section of the northwestern of South America within the western Pangea during the Late Triassic – Early Jurassic, showing the location of the back arc basin and the Triassic extensional axis adapted and modified from Spikings et al., 2015..... 11

Figure 1-6 a) Early Jurassic reconstruction of the northwestern South American and Caribbean adapted and modified from Pindell and Kenan 2009. b) Unscaled cross section of the northwestern South America, showing the accretion of para–autochthonous terranes model adapted and modified from Bayona et al., 2020.12

Figure 1-7. a. Regional geologic map modified from Gomez et al. 2015. CC: Central Cordillera, SL: San Lucas range, MMV: Middle Magdalena Valley, WF: Western Foothills, MTB: Magdalena-Tablazo sub-basin, TSB: Tunja-Sogamoso sub-basin, CYB: Cocuy sub-basin, FH: Floresta high, FM: Floresta massif, SH: Santander high, SM: Santander massif, CNB: Cundinamarca sub-basin. b. Structural cross section of the Middle Magdalena Valley and Eastern Cordillera, modified from Caballero et al., 2013 and Tesón et al., 2013.13

Figure 2-1. a. Present tectonic configuration of the northern Andes, showing the main tectonic features in the study area (orange box), MMV (Middle Magdalena Valley), WC (Western Cordillera), CC (Central Cordillera), EC (Eastern Cordillera) b. General geological map of the Eastern Cordillera (green outline) and Middle Magdalena Valley (purple outline), after Gomez et al. (2015). Principal folds shown are LC (Los Cobardes anticline), AA (Arcabuco anticline), PA

(Portones Anticline) and NM (Nuevo Mundo syncline). Sub-basins in the Eastern Cordillera (after Sarmiento, 2001) are MTSB (Magdalena Tablazo Sub-basin), FM (Floresta Massif), FH (Floresta High), SM (Santander Massif), TSSB (Tunja Sogamoso Sub-basin), CYSB (Cocuy Sub-basin), SB (Sabana de Bogota), CSB (Cundinamarca Sub-basin). Main faults shown are LCF (La Campana fault), LMF (La Morena fault), SMBF (Santa Marta Bucaramanga fault), LSF (La Salina Fault), SF (Suarez fault), AF (Aratoca paleofault), BF (Boyaca fault), SOF (Soapaga fault). 22

Figure 2-2. Mesozoic stratigraphic chart of the Eastern Cordillera and Middle Magdalena Valley, showing the depositional environments, lithologies, and magmatic activity. Data compiled from Renzoni (1962);(1967), Cediél (1968), Cooper et al. (1995), Clavijo (1996), Mojica et al. (1996), Sarmiento (2001), Sarmiento-Rojas et al. (2006), Kammer and Sanchez (2006), Mora et al. (2006, 2009, 2013), Clavijo et al. (2008), Caballero et al. (2010, 2013), Horton et al. (2010, 2015), Sanchez et al. (2012), Moreno et al. (2013), Reyes-Harker et al. (2015), Nova et al. (2019), Bayona et al.(2020), Rodriguez-Garcia et al. (2020) and integrated with the new measurements and data obtained in this work. See Figure 2.1 for locations of sub-basins in the Eastern Cordillera following the subdivision by Sarmiento (2001)..... 25

Figure 2-3. Stratigraphic columns for sections analyzed in this work. Sources: Noreán and Bocas Fms. from Clavijo (1996); Girón and Jordán formations from Cediél (1968), the Palermo, Montebel, La Rusia and Arcabuco Fms. are compiled from Renzoni (1967). See Fig 1. for locations. 26

Figure 2-4. Outcrop photographs: a) Photographs of the extrusive member of the Noreán formation. b) Evidence of an intrusive body at the top in contact with a red volcanic tuff. Noreán formation. c) Basal member of the Girón formation. evidence intercalation between red layers and conglomerates with presence of small volcanic flows (less than 3m). d) welded tuffs defined by Cediél (1968), Jordán formation. e) Contact between the Early Cretaceous and Jurassic along the Chicamocha Canyon. f) Intercalation of sandstones and mudstones, associated with fluvial channels. Tambor formation. g) Contact between Tambor formation and the red shales Jordán Formation. h) Volcanic flows associated to the Montebel formation. i) Hinge of the Arcabuco anticline. Color lines description: orange line: tuffs and volcanoclastic material. Purple line: dikes and intrusive bodies. Green line: fluvial channels. Red line: geological contact between the Cretaceous and Jurassic. 28

Figure 2-5. Characteristic microphotographs: a) Resorbed quartz as evidence of volcanic origin. Noreán formation. b) Porphyritic texture, major population of quartz grains, angular clasts. Noreán formation c) Porphyritic texture, principal component of plagioclase, evidence of mafic minerals. Bocas formation. d) Porphyritic texture, presence of pumice in major percentage. Jordán formation. 35

Figure 2-6. a) Zircon morphology classification after Pupin (1980) with the main crystal families from the sample analysis. Cathodoluminescence images of the studied samples. b) grains from the Noreán formation c) Jordán formation grains d) Arcabuco formation grains. (Blue spots are the ablated regions)..... 36

Figure 2-7. Wetherill concordia plots of zircon U-Pb results drawn by ISOPLOT.(Ludwig 2012) a) General concordia plot of the Noreán formation. b) Detail of the square concordia plot of Figure 2.7a for the Mesozoic ages of Noreán formation. c) Complete concordia plot with evidences of heritage. Noreán formation. d) Detailed concordia plot for the Mesozoic box in Figure 2.7c Noreán formation. e) Average age plot of the Noreán formation. f) Concordia plot of the Noreán formation. g) General concordia plot of the Girón formation. h) Detailed of the Mesozoic square box in Figure 2.7g Girón formation 39

Figure 2-8. Wetherill concordia plots of zircon U-Pb results drawn by ISOPLOT (Ludwig 2012). a) General concordia plot of the Girón formation. b) Detailed of the square concordia plot of Figure

2.8a. for the Mesozoic ages of Girón formation. c) Average age plot of the Jordán formation. d) Concordia plot of the Jordán formation. e) General Concordia plot of the Jordán formation. f) Detailed Mesozoic box of the Mesozoic box of Figure 2.8e Jordán formation. g) General concordia plot of the Rusia formation note the absence of Mesozoic grains. h) Detailed of the younger ages of Figure 2.8g Rusia formation.....41

Figure 2-9. Wetherill concordia plots of zircon U-Pb results drawn by ISOPLOT (Ludwig 2012). a) General concordia plot of the Montebel formation. b) Detailed Concordia plot of the younger ages in the Figure 2.9a. Montebel formation. c) Concordia plot of the Arcabuco formation. d) Detailed concordia plot of the younger ages in Figure 2.9c. Arcabuco formation..... 42

Figure 2-10. Balanced cross sections along the north study area in the Noreán Region from the La Morena fault to the Middle Magdalena Valley. Notice also the sample location illustrated through the pentagons. a) Structural cross section in the Northernmost part of the study area at present-configuration. b) Restored structural cross section (Figure 2.10a.) for the Late Cretaceous. Note the absence of sediments linked to the main unconformities (Miocene - Oligocene, Early Eocene – Late Paleocene, and Early Cretaceous)..... 45

Figure 2-11. Balanced cross sections along the central part of the study area in the Los Cobardes Region from the footwall of the Suarez fault in the Eastern Cordillera to the Middle Magdalena Valley. From east to west Crossing the Los Cobardes anticline to the Nuevo Mundo Syncline. Note the sample location drawn through the blue polygon. a) Structural cross section in the central part of the study area at present-configuration. Notice the two main faults of La Salina and Suarez that control the fold geometry. b) Restored structural cross section (Figure 2.11a.) for the Late Cretaceous. Note the Mesozoic thinning to the west (Middle Magdalena Valley).....46

Figure 2-12. Balanced cross sections along the central part of the study area in the Jordán Region along the Chicamocha canyon. From east the Aratocha paleo-fault to the hanging-wall of the Suarez fault in the Eastern Cordillera. Note sample location drawn through the blue pentagon. a) Structural cross section in the Jordán Region at present-day configuration. Notice the blind normal fault and the Aratocha paleo-fault as boundaries of the Jordán Fm. b) Restored structural cross section (Figure 2.12a.) for the Late Cretaceous. Note the Mesozoic thinning to the east.....48

Figure 2-13. Balanced cross sections along the southern part of the study area in the Arcabuco Region. From west the Boyacá fault to the east the Soapaga fault. Notice sample location is illustrated through the blue polygon. a) Structural cross section at present-day configuration. Notice the blind normal fault to the hangingwall of the Soapaga fault, and the Mesozoic absence to the western area. b) Restored structural cross section (Figure 2.13a.) for the Late Cretaceous..... 50

Figure 2-14. Mesozoic magmatic bodies of the Eastern Cordillera and Middle Magdalena valley (after Bayona et al. 2020; Rodriguez-Garcia et al. 2020). Note the alignment of intrusions parallel to the strike of the Bucaramanga-Santa Marta strike slip fault (SMBF). See Figure 2.1. for abbreviations of sub-basins in the Eastern Cordillera as well as folds and faults..... 54

Figure 2-15. Tectonic evolution model for the Late Triassic to Late Cretaceous in the Northern Andes of Colombia. Illustrates the migration of the magmatic arc and the depositional environment in the Eastern Cordillera. see Figure 2.2. to the conventions of the sedimentary environments. Inspired in the tectonic evolution image style of Horton et al. 2010. The sample and cross sections are located in a regional scale. 57

Figure 2-16. Mesozoic paleo structural maps of the Eastern Cordillera and Middle Magdalena Valley. Illustrates the development of the extensional structures as La Salina (LSF), Suarez (SF), Boyacá (BF), Paya-Pajarito (PPF) through the Mesozoic, the relation with the plutonism and the strike slip

fault of Santa Marta Bucaramanga Fault (SMBF). The light blue hexagon reflects the geochronology samples dated in this work. Line faults without symbology show the inactivity for each time.61

Figure 3-1. a) Present tectonic configuration of the northern Andes, showing the main tectonic features in the study area (orange box), MMV (Middle Magdalena Valley), WC (Western Cordillera), CC (Central Cordillera), EC (Eastern Cordillera). Orange box shows the study area location in Figure 3.1b. b) Digital elevation model of the study area showing the principal folds and faults. MTB (Magdalena Tablazo sub-basin), FM (Floresta Massif). IF (Infantas Fault), LSF (La Salina Fault), CF (Carmen Fault), SF (Suarez Fault), BF (Boyaca Fault), SPF (Soapaga Fault) SMBF (Santa Marta Bucaramanga Fault), LDF (Landazuri Fault), EF (Ermitaño Fault), LCF (La Corcovada Fault), SSF (San Fernando Fault), AF (Arrugas Fault)..... 68

Figure 3-2. Digital elevation model of the study area showing the principal folds and faults, also the data employed to generate the seismic composite lines in blue. The boreholes that are projected in the composited seismic lines are labeled with their names. 70

Figure 3-3. Generalized stratigraphic column of the Middle Magdalena Valley and western foothills of the Eastern Cordillera, showing the seismic response for the principal units. 72

Figure 3-4. Diagram adapted from Veerke, 2007, showing the Vint (interval velocity) and Vavg (average velocity) relations and concepts. 74

Figure 3-5. a) Schematic cross-section depicting a revised concept of a foreland basin system, with the wedge-top, foredeep, forebulge depozones shown at approximately true scale. (modified from DeCelles and Giles) This illustration shows the possible location of each depozone and its relation with the study area. . b) Foreland basin progradation through the time in response of a orogenic load migration (modified from DeCelles and Giles, 1996) c) Flexural response of a visco-elastic lithosphere that relaxes stress (modified from Catuneanu, 2004). In this diagram shows static loading in the fold-thrust belt, which leads to foredeep subsidence and forebulge uplift. The foredeep becomes deeper and narrower through the time..... 77

Figure 3-6. a) Uninterpreted composite seismic section S₁ in depth domain (the scale is in kilometers) and the colors scale bar refers the seismic amplitude. b) Interpreted seismic reflection line in depth domain. Showing the structural and stratigraphic relationship. The buried east-verging structure is discussed in the chapter 4. See Location in Figure 3.1 and boreholes location in Figure 3-2.80

Figure 3-7. a) Uninterpreted composite seismic section S₂ in depth domain (the scale is in kilometers) and the colors scale bar refers the seismic amplitude. b) Interpreted seismic reflection line in depth domain. Showing the structural and stratigraphic relationship. See Location in Figure 3.1 and boreholes location in Figure 3-2.81

Figure 3-8 a) Uninterpreted composite seismic section S₃ in depth domain (the scale is in kilometers) and the colors scale bar refers the seismic amplitude. b) Interpreted seismic reflection line in depth domain. Showing the structural and stratigraphic relationship. See Location in Figure 3.1 and boreholes location in Figure 3-2. 82

Figure 3-9 a) Uninterpreted composite seismic section S₄ in depth domain (the scale is in kilometers) and the colors scale bar refers the seismic amplitude. b) Interpreted seismic reflection line in depth domain. Showing the structural and stratigraphic relationship. See Location in Figure 3.1 and boreholes location in Figure 3-2. 83

Figure 3-10 a) Uninterpreted composite seismic section S₅ in depth domain (the scale is in kilometers) and the colors scale bar refers the seismic amplitude. b) Interpreted seismic reflection line in depth domain. Showing the structural and stratigraphic relationship. See Location in Figure 3.1 and boreholes location in Figure 3-2.84

Figure 3-11. a) Uninterpreted composite seismic section S6 in depth domain (the scale is in kilometers) and the colors scale bar refers the seismic amplitude. b) Interpreted seismic reflection line in depth domain. Showing the structural and stratigraphic relationship. See Location in Figure 3.1 and boreholes location in Figure 3-2. 85

Figure 3-12. Shortening values along the strike from the different seismic cross sections. See in Figure 3-1 the location of the different cross sections. 90

Figure 3-13. Percentage of shortening of the La Salina Fault vs. Total Shortening for each seismic composite line. See in Figure 3-1 the location of the different cross sections. 91

Figure 4-1. a) Regional tectonic map of the northern Andes. CP (Caribbean Plate), SAP (South American Plate), NP (Nazca Plate). Main structural elements are SNSM (Sierra Nevada de Santa Marta), LMV (Lower Magdalena Valley), MMV (Middle Magdalena Valley), MA (Merida Andes), EC (Eastern Cordillera), UMV (Upper Magdalena Valley), CC (Central Cordillera), WC (Western Cordillera) and CR (Cordillera Real). The red box shows the location of Figure 4.1b. b) Geological map of the central segment of the Eastern Cordillera and Middle Magdalena Valley, modified from Gomez et al. (2015). The purple box indicates location of the study area. 96

Figure 4-2. a) Geological map showing the main structural elements of the western foothills of the Eastern Cordillera. TF (La Tigra fault), LSF (La Salina fault), NMS (Nuevo Mundo syncline), AF (Arrugas fault), IF (Infantas fault), SF (Suarez fault), LCA (Los Cobardes anticline), CF (Carmen fault), MF (Mugrosa fault), The seismic lines are in red, and the purple polygon is the 3D model illustrated in Figure 4.5. 98

Figure 4-3. Uninterpreted seismic reflection profile A-A” in depth domain. Location of seismic profile in Figure 4.2. The color scale is in seismic amplitude units. 100

Figure 4-4. Interpreted seismic reflection profile A-A” in depth domain. Location of seismic profile in Figure 4.2. 101

Figure 4-5. 3D Model of La Cira Basement-high. Contoured Early Jurassic horizon (top of Girón Fm.) bounded by the east vergent reverse fault system to the west and truncated by the inverted Infantas fault system to the east. No vertical exaggeration..... 102

Figure 4-6. Regional stratigraphic chart of the Middle Magdalena Valley Basin and Eastern Cordillera (Modified from Caballero et al. 2013; location of transect in Figure 4.1)..... 103

Figure 4-7. Uninterpreted seismic reflection profiles in depth domain. Showing the seismic features from north to south. Location in Figure 4.2..... 105

Figure 4-8. Three seismic reflection profiles from north to south in depth domain (km). Varying seismic quality as well as changing stratigraphic and structural relationships are evident. Location in Figure 4.2. IF (Infantas fault) WTa(West thrust system a) and WTb (West thrust system b)... 106

Figure 4-9. Interpreted seismic reflection profiles in depth domain. Showing the structural and stratigraphic relationship from north to south. Location in Figure 4.2..... 108

Figure 4-10. evolution of the La Cira Basement-high from middle Cretaceous to present-day configuration. The individual stages were created by stepwise kinematic restoration of Figure 4.10.i 111

Figure 4-11 Forward model of La Cira Basement-high. a) Pre-thrusting configuration (middle Cretaceous). b) Initial compression with anticlinal folding and further uplift of pre-configured composite horst over the basement thrust fault. Material above the black dashed line is eroded in (b). The dashed dotted lines are a grid of markers drawn approximately parallel to top basement. These illustrate that the deformation of the basement but do not coincide with actual geologic contacts..... 112

Figure 4-12. a) Regional geological map showing the location of the cross-section in (b) Regional cross-section of the MMVB between the Cantagallo fault in the west and the La Salina fault system in the east. The dashed fault between the La Cira Basement-high and La Salina fault is the upper detachment of the hypothetical blind basement thrust (see Figure 4.11). It is tentatively shown here to have undergone west-directed reactivation as a splay of the La Salina fault. This splay links up with the Infantas fault, inducing reverse reactivation of only its uppermost part in this scenario and creation of a new emergent branch across the Cenozoic cover. 114

Figure 4-13. Alternative interpretations of the La Cira Basement-high. a) Geological map showing the main structural elements of the western foothills of the eastern cordillera. TF(La Tigra fault), LSF (La Salina fault), NMS (Nuevo Mundo syncline), AF (Arrugas fault), IF (Infantas fault), SF (Suarez fault), LCA (Los Cobardes anticline), CF (Carmen fault), MF (Mugrosa fault). b) Morales 1958; Dickey 1992: Basement anticline with west-verging thrust. c) Gomez et al., 2005: Basement high without emergent faults and probably linked to buried basement thrust (dashed line). Notice different vertical exaggeration. d) ANH 2006: Basement high associated with a thick-skin triangle zone. e) Kammer et al., 2020: Basement high linked to normal faulting (tilted block) with superimposed Infantas thrust fault. 116

Figure 5-1. a) Present tectonic configuration of the northern Andes, showing the main tectonic features in the study area (orange box), MMV (Middle Magdalena Valley), WC (Western Cordillera), CC (Central Cordillera), EC (Eastern Cordillera). Orange box shows the study area location in Figure 5.1b. b) Digital elevation model of the study area showing the principal folds and faults, distribution of the thermochronologic information and structural cross-sections. The main structural features are named in the map. NMS (Nuevo Mundo Syncline), LSF (La Salina Fault), CF (Carmen Fault), LC (Los Cobardes Anticline), SF (Suarez Fault), AA (Arcabuco Anticline), BF (Boyaca Fault), SPF (Soapaga Fault), PA (Portones Anticline), OA (Opon Anticline), DS (De Armas Syncline), CA (La Corcovada Anticline)..... 122

Figure 5-2. a) Digital elevation model of the study area showing the principal folds and faults, and the distribution of the stratigraphic chart described further in Figure 5.2b b) Regional stratigraphic chart modified from Moreno et al. 2013 comparing the stratigraphy of the Middle Magdalena Valley and the Eastern Cordillera, (WF) Western Foothills, (FM) Floresta Massif and (CCY) Cocuy sub-basin..... 126

Figure 5-3. Geological map of the northern region, showing the AFT and ZFT samples and the northern cross-sections. Main structural features are showed in the map LSF (La Salina Fault), LC (Los Cobardes Anticline), SF (Suarez Fault), AA (Arcabuco Anticline), SMBF (Santa Marta Bucaramanga strike slip fault), BF (Boyaca Fault), SPF (Soapaga Fault). See location in Figure 5.1. 130

Figure 5-4. Structural cross-section Cs1 located in the northern region. Showing the major structural features and the projection of the AFT and ZFT samples in the northern region. See location in Figure 5.3. Vertical exaggeration 2x..... 131

Figure 5-5. Geological map of the southern region, showing the AFT and ZFT samples and the northern cross-sections. Main structural features are showed in the map LSF (La Salina Fault), PA (Portones Anticline), SF (Suarez Fault), AA (Arcabuco Anticline), BF (Boyaca Fault), SPF (Soapaga Fault), DS (De Armas Syncline), CA (La Corcovada Anticline). See location in Figure 5.1..... 132

Figure 5-6. Structural cross-section Cs4 located in the southern region. Showing the major structural features and the projection of the AFT and ZFT samples in the northern region. See location in Figure 5.5. Vertical exaggeration 2x..... 133

Figure 5-7. a) Digital elevation map of the study area showing the northern and southern regions vs the pollen samples location and AFT sections modeled and compiled from different authors. b) Paleo elevation estimation based on pollen data collected by Hooghiemstra et al. (2006). 135

Figure 5-8. Samples from the northern section projected to cross-section Cs₁ (Figure 5.4 and see location in Figure 5-7a) a) Plot of the AFT vs depositional ages from the Cantagallo Fault. b) Plot of the AFT vs depositional ages from the La Salina Fault. c) Plot of the AFT vs depositional ages from the Carmen Fault. HF (hanging wall), FW (footwall)..... 137

Figure 5-9. Samples from the southern section projected to cross-section Cs₄(Figure 5.6 and see location in Figure 5-7a) a) Plot of the AFT vs depositional ages from the La Salina Fault. b) Plot of the AFT vs depositional ages from the Boyacá Fault. HF (hanging wall), FW (footwall)..... 138

Figure 5-10. Geologic evolution of the northern region cross-section Cs₁ from middle Cretaceous to present-day configuration. The individual stages were created by stepwise kinematic restoration of Figure 5.10h. See Location in Figure 5.3..... 139

Figure 5-11 Geologic evolution of the northern region cross-section Cs₂ from middle Cretaceous to present-day configuration. The individual stages were created by stepwise kinematic restoration of Figure 5.11h. See Location in Figure 5.3. 140

Figure 5-12. Geologic evolution of the northern region cross-section Cs₃ from middle Cretaceous to present-day configuration. The individual stages were created by stepwise kinematic restoration of Figure 5.12h. See Location in Figure 5.3..... 141

Figure 5-13. Geologic evolution of the southern region cross-section Cs₄ from middle Cretaceous to present-day configuration. The individual stages were created by stepwise kinematic restoration of Figure 5.13h. See Location in Figure 5.5..... 142

Figure 5-14. Geologic evolution of the southern region cross-section Cs₅ from middle Cretaceous to present-day configuration. The individual stages were created by stepwise kinematic restoration of Figure 5.14h. See Location in Figure 5.5 143

Figure 5-15. Geologic evolution of the southern region cross-section Cs₆ from middle Cretaceous to present-day configuration. The individual stages were created by stepwise kinematic restoration of Figure 5.15i. See Location in Figure 5.5..... 144

Figure 6-1. a) Present tectonic configuration of the northern Andes, showing the main tectonic features in the study area (orange box), MMV (Middle Magdalena Valley), WC (Western Cordillera), CC (Central Cordillera), EC (Eastern Cordillera). Orange box shows the study area location in Figure 6.1b. b) Digital elevation model of the study area showing the principal oil and gas fields, distribution of the vitrinite reflectance and boreholes employed in this chapter. S₁ cross-section northern region. S₆ cross-section southern region. Also the main structural features are labeled. NMS (Nuevo Mundo Syncline), LSF (La Salina Fault), SMBF (Santa Marta Bucaramanga Fault), LC (Los Cobardes Anticline), SF (Suarez Fault), DS (De Armas Syncline), CA (La Corcovada Anticline), PA (Portones Anticline), AA (Arcabuco Anticline), BF (Boyaca Fault), SPF (Soapaga Fault)..... 150

Figure 6-2. a) Cross-section S₁ from the northern region (see location in Figure 6.1) showing the location of the 1D burial models (A, B, C, D, E) extracted from the 2D basin model, from west to east respectively. b) Subsidence curves from the different pseudo boreholes extracted from the cross-section S₁..... 155

Figure 6-3. a) Cross-section S₆ from the southern region (see location in Figure 6.1) showing the location of the 1D burial models (A, B, C, D) extracted from the 2D basin model, from west to east respectively. b) Subsidence curves from the different pseudo boreholes extracted from the cross-section S₁..... 158

Figure 6-4. a) Heat flow curve for the scenario A modified from (Gonzalez et al., 2020) b) Transformation ratio reconstruction for the Paleocene and the Present-day configuration (TR<=50% are considered optimal to generate hydrocarbon during this time). c) Vitrinite reflectance reconstruction for the Paleocene, early Miocene and Present-day configuration. All those models are from the cross-section S₁ (see location Figure 6.1) testing the scenario A. Vertical exaggeration 3x..... 161

Figure 6-5. a) Heat flow curve for the scenario A modified from (Gonzalez et al., 2020) b) Transformation ratio reconstruction for the Paleocene and the Present-day configuration (TR<=50% are considered optimal to generate hydrocarbon during this time). c) Vitrinite reflectance reconstruction for the Paleocene, early Miocene and Present-day configuration. All those models are from the cross-section S₆ (see location Figure 6.1) testing the scenario A. Vertical exaggeration 3x.....162

Figure 6-6. a) Heat flow curve for the scenario B b) Transformation ratio reconstruction for the Paleocene and the Present-day configuration (TR<=50% are considered optimal to generate hydrocarbon during this time). c) Vitrinite reflectance reconstruction for the Paleocene, early Miocene and Present-day configuration. All those models are from the cross-section S₁ (see location Figure 6.1) testing the scenario B. Vertical exaggeration 3x.....165

Figure 6-7. a) Heat flow curve for the scenario B b) Transformation ratio reconstruction for the Paleocene and the Present-day configuration (TR<=50% are considered optimal to generate hydrocarbon during this time). c) Vitrinite reflectance reconstruction for the Paleocene, early Miocene and Present-day configuration. All those models are from the cross-section S₆ (see location Figure 6.1) testing the scenario B. Vertical exaggeration 3x.....166

Figure 6-8. a) Heat flow curve for the scenario C b) Transformation ratio reconstruction for the Eocene and the Present-day configuration (TR<=50% are considered optimal to generate hydrocarbon during this time). c) Vitrinite reflectance reconstruction for the Eocene, early Miocene and Present-day configuration. All those models are from the cross-section S₁ (see location Figure 6.1) testing the scenario C. Vertical exaggeration 3x.169

Figure 6-9. a) Heat flow curve for the scenario C b) Transformation ratio reconstruction for the Eocene and the Present-day configuration (TR<=50% are considered optimal to generate hydrocarbon during this time). c) Vitrinite reflectance reconstruction for the Eocene, early Miocene and Present-day configuration. All those models are from the cross-section S₆ (see location Figure 6.1) testing the scenario C. Vertical exaggeration 3x.170

Figure 6-10. a) Heat flow curve for the scenario D b) Transformation ratio reconstruction for the Eocene and the Present-day configuration (TR<=50% are considered optimal to generate hydrocarbon during this time). c) Vitrinite reflectance reconstruction for the Eocene, early Miocene and Present-day configuration. All those models are from the cross-section S₁ (see location Figure 6.1) testing the scenario D. Vertical exaggeration 3x.172

Figure 6-11. a) Heat flow curve for the scenario D b) Transformation ratio reconstruction for the Eocene and the Present-day configuration (TR<=50% are considered optimal to generate hydrocarbon during this time). c) Vitrinite reflectance reconstruction for the Eocene, early Miocene and Present-day configuration. All those models are from the cross-section S₆ (see location Figure 6.1) testing the scenario D. Vertical exaggeration 3x. 173

Figure 6-12. a) Western side of the cross-section S1 with the projected boreholes with vitrinite reflectance (Ro%) (See location in Figure 6.1). b) Vitrinite reflectance (Ro%) vs depth, showing the expected vitrinite reflectance (green line from Sweeney and Burnham, 1990) vs measured vitrinite reflectance.175

Figure 6-13. Petroleum saturation model in cross-section S1. Dashed purple circles highlight the possible hydrocarbon accumulations.....176

1. INTRODUCTION AND MOTIVATION

The northernmost Andes were created by a complex interaction between the South America continental plate and Nazca and Caribbean oceanic plates. This complexity is recorded in the development of sedimentary basins that originated in an extensional intra-arc to back arc setting, evolved further through several foreland basin stages and finally were partly incorporated into the growing mountain belt. This work's main objective is to better understand the early phase of basin evolution and its tectonic setting in the western part of the Eastern Cordillera (EC) and the adjacent Middle Magdalena Valley (MMV) in Mesozoic time. To achieve this we have to restore the effects of mostly Cenozoic basin inversion and orogeny that dominate the architecture today. Apart from presenting a scientific challenge, the MMV is one of Colombia's most prolific hydrocarbon basins with several billions of barrels of reserves discovered in oil and gas fields, beginning one century ago with the first giant find, the La Cira-Infantas field for which we present a new interpretation. The improved understanding of the tectonic evolution and basin-forming mechanisms will reduce the uncertainty and risk for future exploration.

Since the last decade of exploration, energy resources are decreasing. Different analysts argue that with the reduced hydrocarbon resources and scarce important discoveries, Colombia is probably approaching the limit of reserves and will soon have to import oil and gas (IHS, 2020). Despite some success, it is evident that exploration has become more challenging, in part due to the structural and stratigraphic complexities arising from Mesozoic extensional features pre-conditioned the Cenozoic geometry. However, this influence is difficult to detect through the standard range of oil industry seismic programs.

Different authors (e.g., Cooper et al., 1995; Sarmiento, 2001; Kammer and Sanchez, 2006; Mora et al., 2006; 2009; 2010) presented evidence that the EC is a Mesozoic basin inverted during the Cenozoic. Several studies were carried out in the EC to understand its tectonic evolution and relation with the surrounding foreland basins including the intermontane MMV. The area studied here (Figure 1.1) comprises many major structures such as the La Salina, Suarez, Boyacá, and Bucaramanga faults, which have been interpreted to be inherited from the extensional phase and to have experienced strong reactivation during the inversion phase.

This project aimed to re-evaluate the kinematics of the principal Mesozoic structures in the EC and MMV, including the timing and spatial distribution of the extensional events that created the rift

Chapter 1. Introduction

basins. Stratigraphic thicknesses and correlations should be re-assessed, and volcanoclastic units dated to constrain the rifting events. One aim was the compilation and integration of essentially all available surface and subsurface information to obtain a more complete picture of basin and structure evolution.

To better understand the Mesozoic evolution of the EC and MMV, the following questions were to be answered:

1. How were the rift basins distributed in space, and what is their relation with the volcanism?
2. When did the main rifting phase(s) occur that conditioned the EC and mainly the MMV?
3. Which was the plate tectonic configuration that controlled the basin development during the Mesozoic?
4. How does the Mesozoic inheritance control the relationship between thick- and thin-skinned structural domains?
5. Does Mesozoic extension play a role in the evolution of the La Cira-Basement high, a debated structure in the MMV?
6. Which were the periods when elevated heat flow typical of rifting occurred?

To solve these questions, during this project, we used the geological maps published in the last years by the SGC (Colombian Geological Survey) and the geophysical and borehole data provided by the ANH (National Hydrocarbon Agency), in addition to the information obtained during the two field campaigns and a variety of information such as thermochronological, stratigraphic, structural, geochronological and geochemical data published during recent years by different authors.

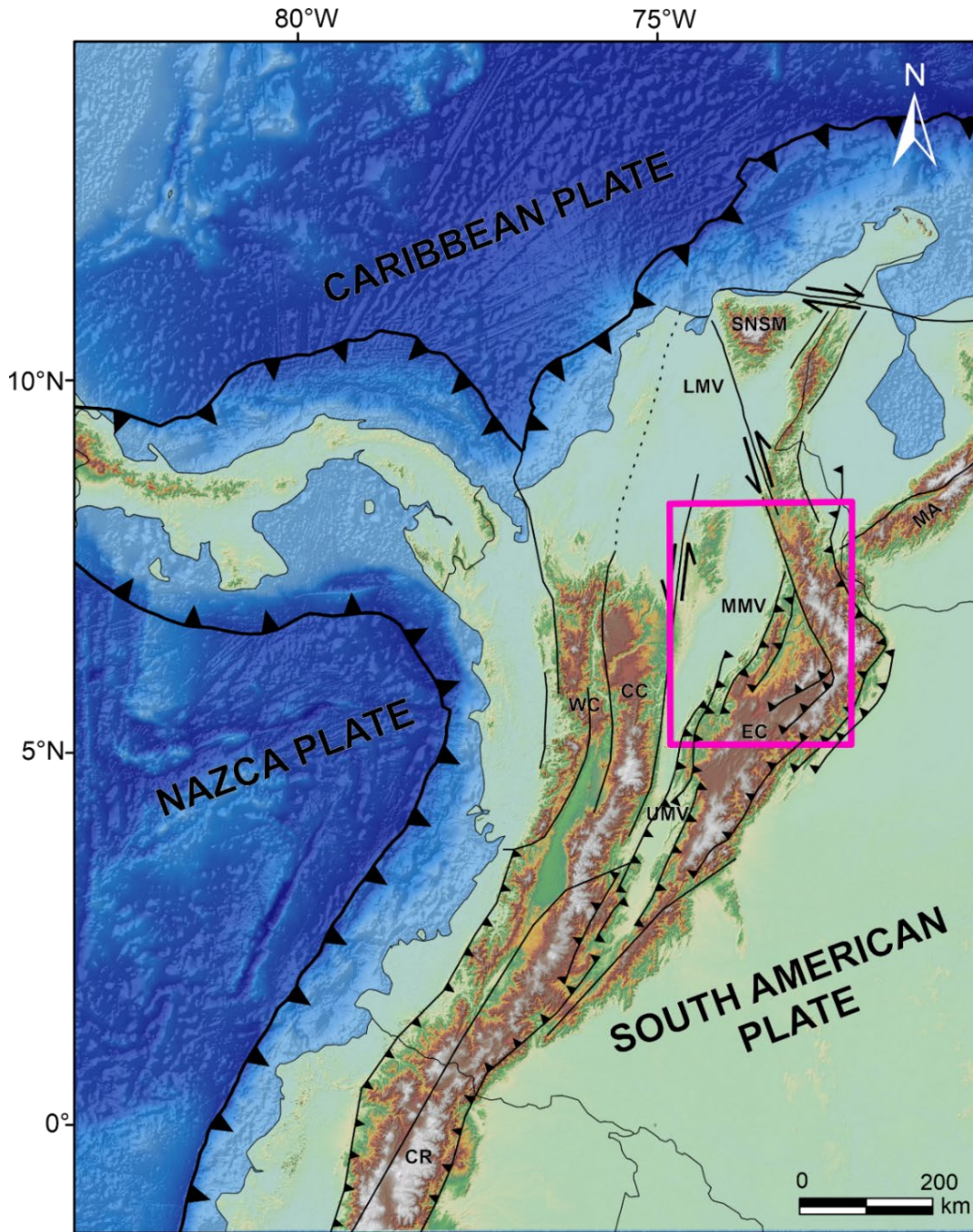


Figure 1-1 Digital elevation map of the northernmost Andes of South America. This map is showing the main basins and tectonic structures. Purple box denotes the study area location see in [Figure 1-3](#). This area comprises the eastern and central part of the MMV (Middle Magdalena Valley), and the western and central side of the EC (Eastern Cordillera). CP (Caribbean Plate), SAP (South American Plate), NP (Nazca Plate). Main structural elements are SNSM (Sierra Nevada de Santa Marta), LMV (Lower Magdalena Valley), MMV (Middle Magdalena Valley), MA (Merida Andes), EC (Eastern Cordillera), UMV (Upper Magdalena Valley), CC (Central Cordillera), WC (Western Cordillera) and CR (Cordillera Real).

Thesis structure

This thesis is structured following the main research questions previously exposed. It is an attempt at holistic basin modeling by integrating information from the surface to field production data. The MMV is considered a mature hydrocarbon basin with declining oil production in the last decades. Nevertheless, some aspects of its evolution remain poorly understood. The Mesozoic sequences buried below the MMV are exposed in the EC, and present a key to reconstruct the early stages of basin evolution in the Mesozoic. This project seeks to identify and constrain the events and processes that controlled the basin development and hydrocarbon prospectivity by combining several tools.

The first chapter of the thesis introduces the reader to the general problem and the main questions proposed for this research. The general geological context is summarized in this part to provide the reader with a geological and tectonic synthesis of the study area.

The second chapter analyzes the timing and style of extension in the EC and MMV. In this part, we employed data collected during the two field campaigns such as petrography, U-Pb zircon geochronology, thickness values and correlated it with seismic reflection, geochemical and surface data previously published. Based on these relationships, we characterize the timing, distribution, origin, and mechanism of the Mesozoic extension. This part aimed to solve the first three questions about the distribution and genesis of the extensional events in the EC and MMV.

The third chapter focuses on the geometrical evolution and basin development; this part seeks to define the principal structural domains in the EC and MMV, using seismic reflection, boreholes, and fieldwork information to produce well-constrained serial cross-sections across the strike of the EC and MMV. In addition, this part analyzes the basin infill and its relation to different structural domains (thick and thin-skinned) and the fault displacement variations.

The fourth chapter comprises a detailed analysis of the La Cira-Basement high. Employing seismic reflection and borehole information, we produce a stepwise kinematic model for this high to understand the evolution and the role of this high during the Mesozoic. We analyze and test different geometries through forward and backward modeling, considering the main uplifting events defined by other authors through thermochronology.

The fifth thesis chapter focuses on stepwise kinematic restoration of six key cross-sections; the main aim of this chapter is to illustrate the evolution in detail from the extensional phase over early

inversion to maximum shortening and the present-day configuration. We compiled all fission-track data available for the study area; this information was projected onto the cross-sections to calibrate the kinematic evolution.

The sixth chapter integrates all the previous results with field production, organic geochemistry, heat flow scenarios to produce a basin model for the studied sector of the MMV and EC. This part analyzed possible oil and gas migration scenarios and the influence of the geometry, heat flow, and burial record in resource accumulation using Petromod (Schlumberger © Software). It presents a test case for this kind of analysis in complex areas such as the EC and MMV.

The final chapter of the thesis summarizes the main findings and gives recommendations for future analysis based on lessons learned during this work.

Dataset and Methods

This study integrates surface and subsurface information intending to generate or validate tectonic interpretations for the Mesozoic. It is essential to highlight that our principal Mesozoic exposures are located in the axial region of the EC, linked to folds and faults (re)-activated during the Cenozoic Andean orogeny. Due to this situation, a close tie between the subsurface and surface data is essential to produce accurate results. In order to illustrate the processes and analysis performed on each dataset, we will split the data into different groups based on the type of data.

1. Field data.

Two field campaigns were conducted during 2018 and 2019 to sample the different volcanoclastic units from the Mesozoic deposits. During this period, we visited different outcrops on different structures in the EC and MMV, such as the Los Cobardes and Arcabuco anticlines. This massive fieldwork allowed us to obtain samples from different geological formations including the Noreán Fm., Jordán Fm., Girón Fm., and others. In the field we also validated different thicknesses proposed by other authors. All samples were macroscopically checked to select the potential datable samples. From these samples thin sections were prepared and analyzed to identify the samples suitable for U-Pb geochronology (see in [Appendix 1](#) the sample data). Other data collected during fieldwork were structural measurements (mainly dips); this information was added to the GIS (Geographical Information System) database in ArcGIS (ESRI © Software) see [Figure 1.2](#).

Chapter 1. Introduction

2. Seismic data

Thanks to the ANH, we obtained 144 2D seismic reflection lines in SGY format (Figure 1.2) (see in [Appendix 3](#) the seismic program details) and with different levels of processing. This information was acquired from the 1950s to 2004 and with different arrays based on the exploration targets. This data was analyzed and qualified according to the quality and the seismic response. All the information was uploaded in Petrel (Schlumberger © Software) in the time domain and shifted to one base datum; this value was selected according to the principal population of seismic lines and calibrated with a DEM (Digital Elevation Model) in the time domain. The interpretation of the seismic lines was conducted by tying the boreholes and the surface dips in areas without boreholes. Time-depth conversion was performed using the velocity logs from different boreholes. These formed the basis for creating a pseudo-3D Velocity Model in Petrel (Schlumberger © Software); this model follows the present geometry interpreted in the time domain of continuous horizons in the area and populates the values with the velocity logs to generate a pseudo-3D velocity model. Once this model is generated, the time-depth conversion is calibrated and constrained using the thickness values from the boreholes. Afterwards, we applied different seismic attributes to increase the seismic response and reduce the noise, such as TecVa. We interpreted in the depth domain in Petrel (Schlumberger © Software), and finally, all interpreted seismic lines were transferred to Move (Petroleum Experts © Software).

3. Borehole data

We obtained information from 28 boreholes (see location in Figure 1.2) (see in [Appendix 2](#) the borehole details); the majority has a basic well log combo composed of gamma-ray, spontaneous potential, resistivity, neutron porosity, bulk density, and velocity logs as VSP or check shots. Furthermore, some boreholes contained data on TOC, kerogen, chromatography, and other detailed information recently acquired. The ANH provided this information under the agreement to promote science in Colombia. These boreholes were analyzed one by one, filtered, and organized according to data quality. This information was uploaded in Petrel (Schlumberger © Software) and interpreted employing the petrophysical tools.

We defined or validated the geological formation tops and identified lateral facies variations and thicknesses changes. Besides this, we compiled all the information published until the present day on thickness values from surface and subsurface data. This information composed of more than

480 values was integrated into the database of this project and transferred to ArcGIS (Esri © Software).

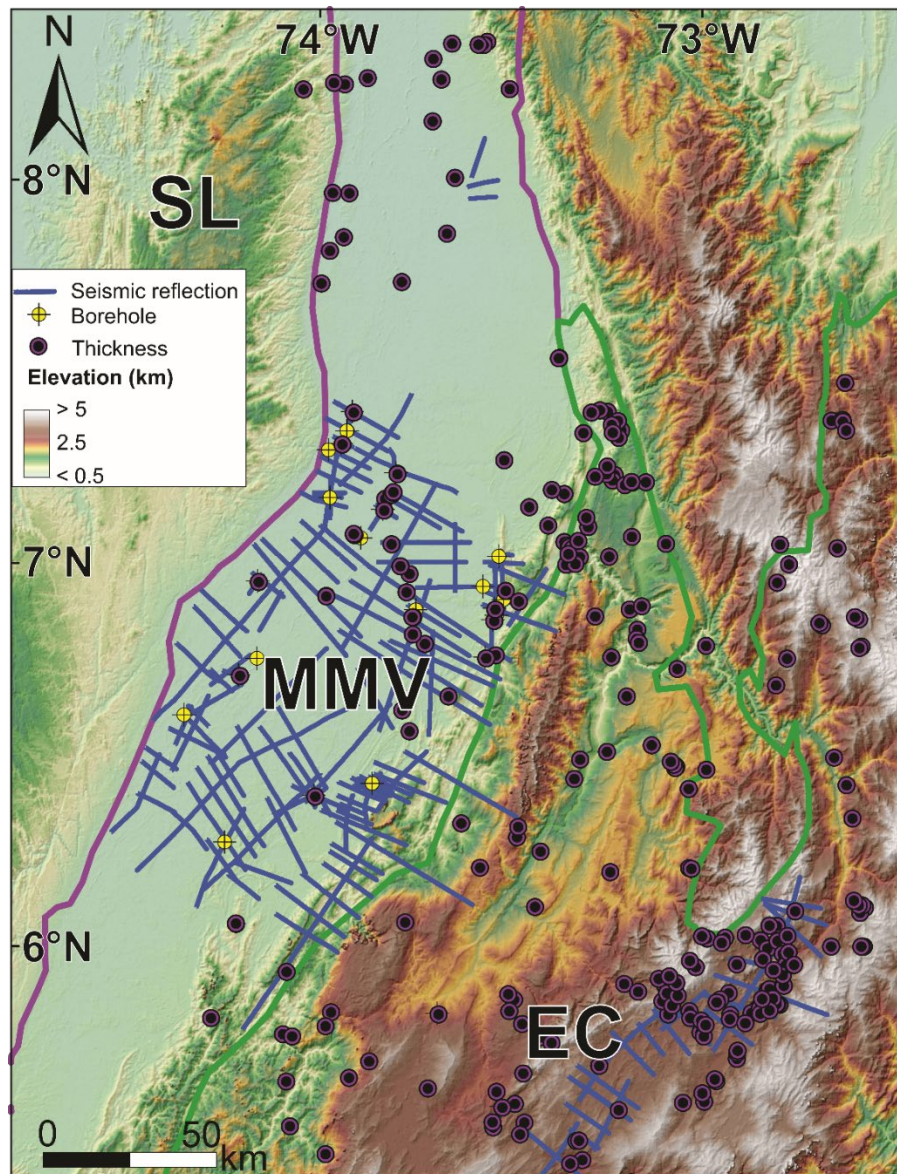


Figure 1-2 Database composed of seismic reflection lines, boreholes provided by the ANH, and thickness data compiled in this project. SL: San Lucas range, MMV: Middle Magdalena Valley and EC: Eastern Cordillera, the purple and green lines represent their boundaries. See location in **Figure 1-1**.

We ran several processes to integrate and unify all the datasets. First, all the results obtained in this project were uploaded and transferred to a GIS database. In addition, we included the relevant results from external projects that could support our study. This database was the principal input to calibrate the other procedures. We extracted from it the thicknesses, dips, and other geological

Chapter 1. Introduction

information available in our area and transferred it to Move (Petroleum Experts © Software), together with the interpreted seismic lines and boreholes in the depth domain from Petrel (Schlumberger © Software). We merged all the information in Move (Petroleum Experts © Software) and validated the interpretation, analyzing the fault displacements and bed-length balancing the cross-sections. The Move software was also employed to complement and build the cross-sections. Cross-section restoration was conducted employing the “Fault parallel flow” and “Flexural slip unfolding” algorithms. Once the sections were restituted in 8 steps mainly focused on the extensional phase, we selected the two best constrained sections with their stepwise kinematic restoration. These two sections were then transferred to Petromod (Schlumberger© Software), for the basin modeling.

Geological setting and previous studies

The study area comprises the northwestern side of the Eastern Cordillera across the Santander, Boyaca, and Cesar states and the central-eastern part of the Middle Magdalena Valley. In this location, we have several geographical features that limit our study area. These include the San Lucas range to the northwest, (average (avg.) elevation of 1200 m), and to the northeast, the Cerro Colorado, a range of the Eastern Cordillera (avg. elevation of 1600 m). To the southwest, the area extends to the El Peñon range (avg. elevation of 2600 m), and to the southeast, the principal highlands belong to the Arcabuco high (avg. elevation of 2800 m and La Rusia paramo (avg. elevation of 3700m), the highest peak in the study area see [Figure 1.3](#). The axial part of the study area is located in the Los Cobardes highland (avg. 2500 m).

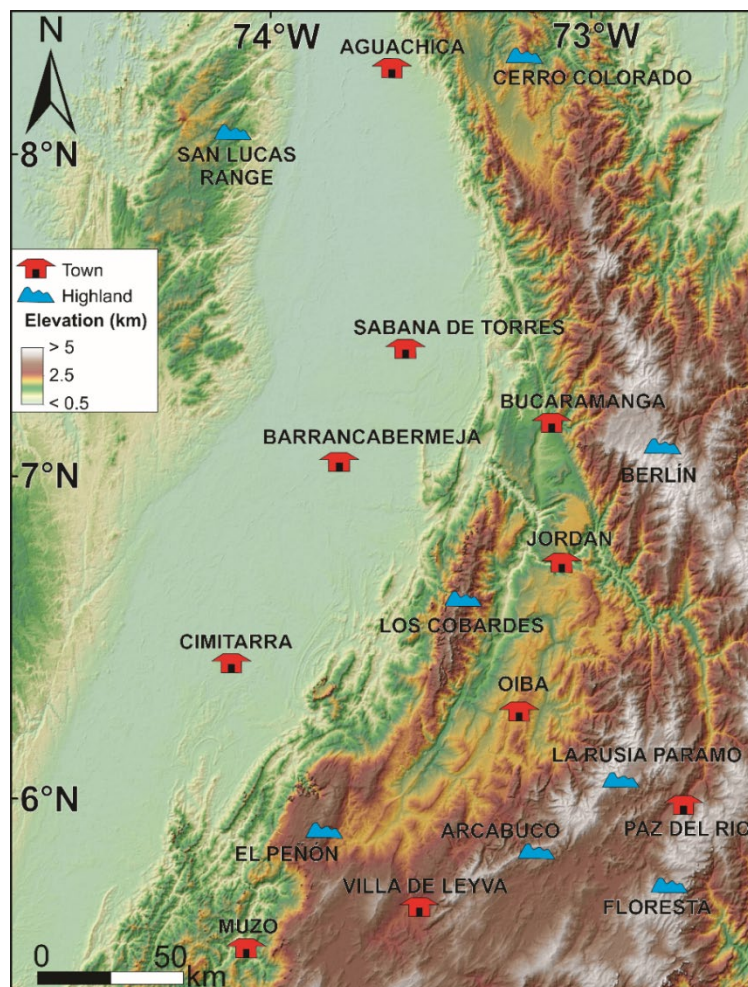


Figure 1-3 Digital elevation map of the study area with the main localities and major mountain expressions. See the Location in [Figure 1-1](#).

Chapter 1. Introduction

Different studies have been conducted in the EC (Eastern Cordillera) and MMV (Middle Magdalena Valley) for centuries since the first generation of geologists who started the exploration in the northern Andes in the 19th century as Grosse, Gansser, T. Ospina, Renz, Hubach, G. Botero, Bürgl and others (Cediel and Shaw, 2018).

The MMV and the EC are part of the Colombian Northern Andes. The configuration of the Northern Andes is the product of the interaction between the Nazca and Caribbean oceanic plates with the continental plate of South America (Taboada et al., 2000; Sarmiento et al., 2011). The Colombian Andes are composed of three principal mountain ranges the Western, Central, and Eastern Cordilleras. The Western and Central Cordilleras are divided by the Cauca River, and the Magdalena River separates the Central and Eastern Cordilleras (Cooper et al., 1995; Sarmiento, 2001).

The sedimentary basins of the MMV and EC were created in an extensional regime during the Mesozoic rifting stage along the northwest of South America (Caceres et al., 2003; Cooper et al., 1995; Sarmiento, 2001, Toro et al., 2004). Several models have been proposed to explain the Triassic – Jurassic extension in the tectonic context:

- (Extensional Model) Intracontinental rift in the northwest of Gondwana (Cediel et al., 2003; Mojica and Kammer 1995) The plutonic bodies are linked to the intracontinental extension see in Figure 1-4.

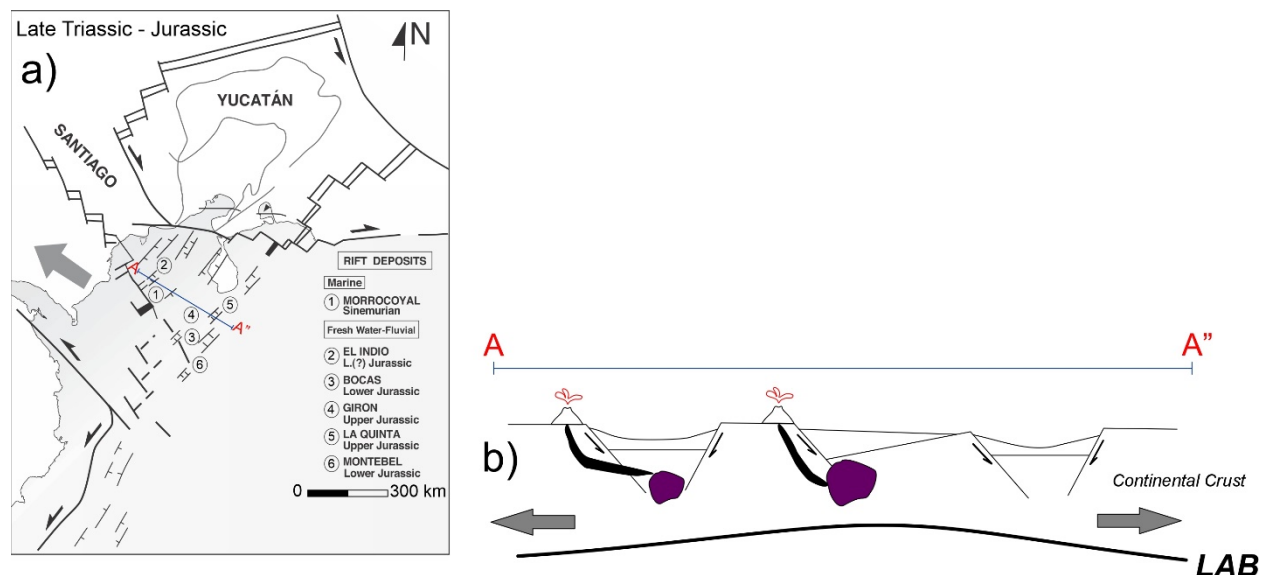


Figure 1-4 a) Paleotectonic reconstruction of continental northwestern South America and surrounding Pacific and Caribbean regions for the Late Triassic-Jurassic adapted and modified from Cediel et al., 2003. **b)** Unscaled cross section illustrating the Late Triassic-Early Jurassic extensional model proposed by Cediel et al., 2003. LAB (Lithosphere-asthenosphere boundary).

Chapter 1. Introduction

- (Subduction Model) Back-arc extension and subduction migration, in this model, the continental block is static, and the northward margin of America does not affect the intraplate settings of Gondwana (Maze, 1984; Cochrane et al., 2014; Spikings et al., 2015) see in Figure 1-5.

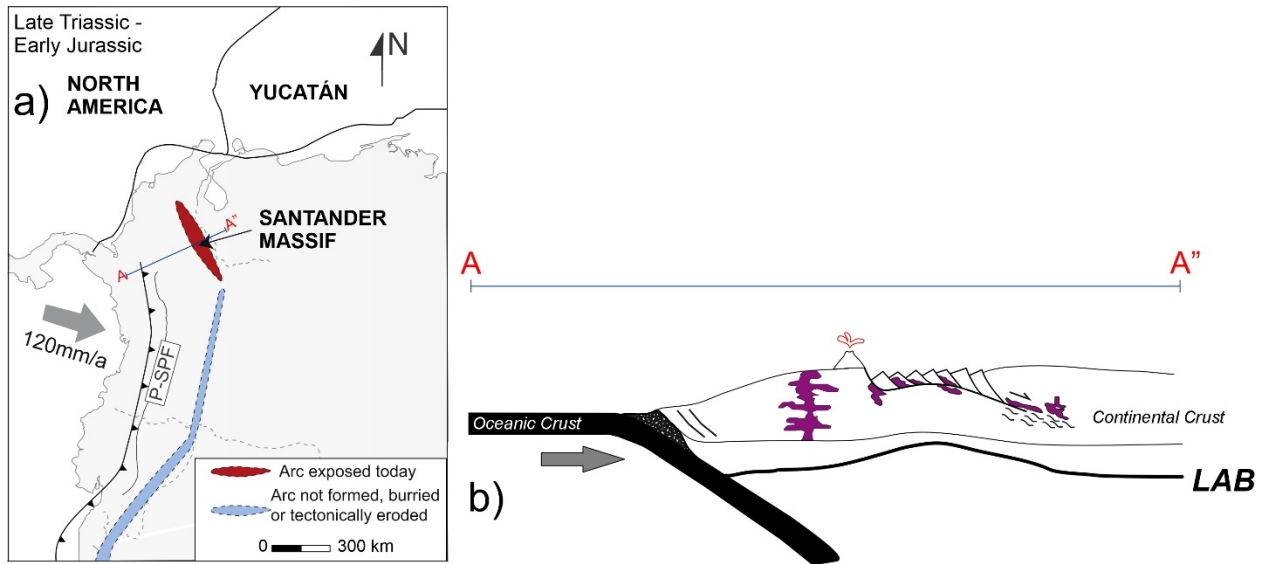


Figure 1-5 a) Tectonic reconstruction of the subduction zones along western Pangaea during the Late Triassic- Early Jurassic determined using an arc-trench distance of 300 km, and constant slab-dip adapted and modified from Spikings et al., 2015. b) Unscaled cross section of the northwestern of South America within the western Pangaea during the Late Triassic – Early Jurassic, showing the location of the back arc basin and the Triassic extensional axis adapted and modified from Spikings et al., 2015.

- (Accretion of para-autochthonous terranes) Variations in the convergence angle as the primary factor controlling the subduction, magmatism, and displacement of terranes. (Toussaint, 1995; Bayona et al., 2006; Pindell and Kenan) see in Figure 1-6.

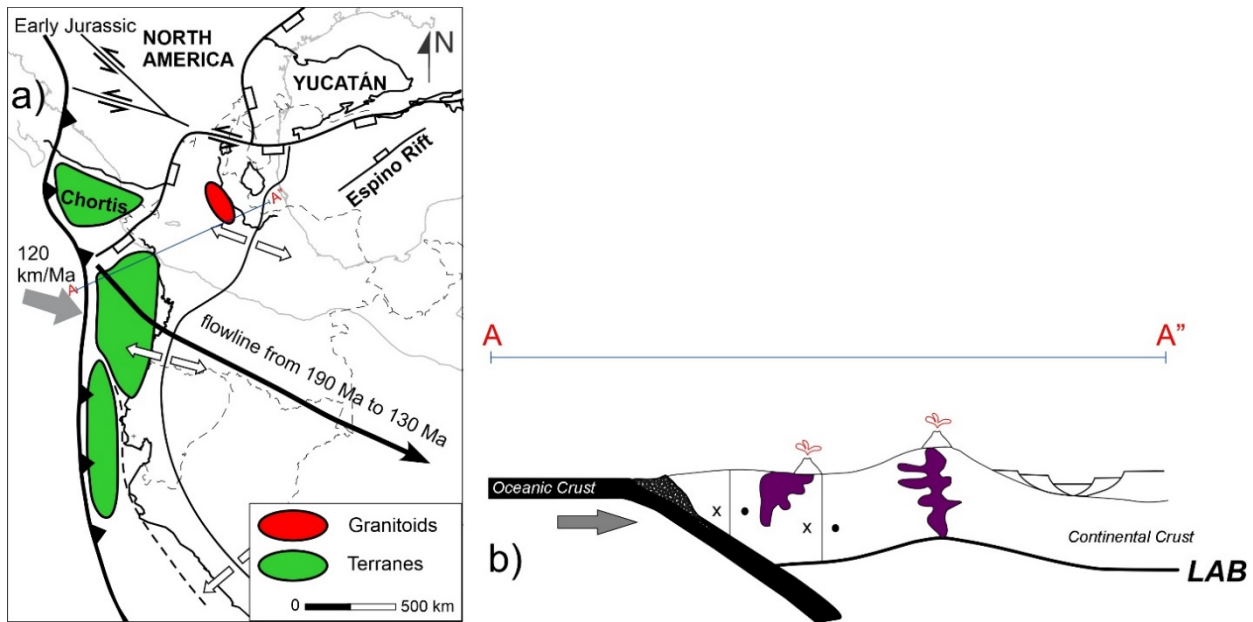


Figure 1-6 a) Early Jurassic reconstruction of the northwestern South American and Caribbean adapted and modified from Pindell and Kenan 2009. b) Unscaled cross section of the northwestern South America, showing the accretion of para–autochthonous terranes model adapted and modified from Bayona et al., 2020.

The MMV and EC basement is mainly composed of Precambrian – early Paleozoic metamorphic rocks (Cochrane et al., 2014; Restrepo–Pace et al., 1997; van der Lelij et al., 2016; Ward et al., 1973). This basement consists of medium to high grade metamorphic rock, e.g., the Silgara schists and the Bucaramanga gneiss (Ward et al., 1973) located in the eastern side along the Santander Massif see [Figure 1-7a](#).

The initial basin development started in the Triassic probably related to the break-up of Pangea, and later to back-arc extension (Cooper, 1995; Maze, 1984; Sarmiento 2001; 2011). According to Maze (1984) the basins were affected by transtensional strain probably linked to the Santa Marta-Bucaramanga strike-slip fault (Kammer and Sanchez, 2006). The major extensional depocenters during the Mesozoic were the Magdalena-Tablazo sub-basin located in the western central part of the EC and the Cocuy sub-basin in the eastern central segment of the EC. (Cooper et al., 1995; Fabre, 1983; Sarmiento, 2001). These two sub-basins are divided by the Santander Massif. According to Sarmiento (2001) based on lithosphere stretching analysis, the initial extension (Triassic-Jurassic) developed a narrow (<150km) asymmetrical rift. The principal sedimentary infill was deposited in a fluvial environment with a volcanic influence (Cediel, 1968; Mojica, 1995; Clavijo, 1996). Nevertheless, some geological formations recorded a shallow marine environment as a consequence of local transgressions. (Clavijo, 1996; Kammer and Sanchez, 2006; Renzoni, 1967).

Those deposits are primarily bounded by inverted normal faults such as the La Salina, Boyacá, Soapaga, Suarez and Guaicaramo faults.

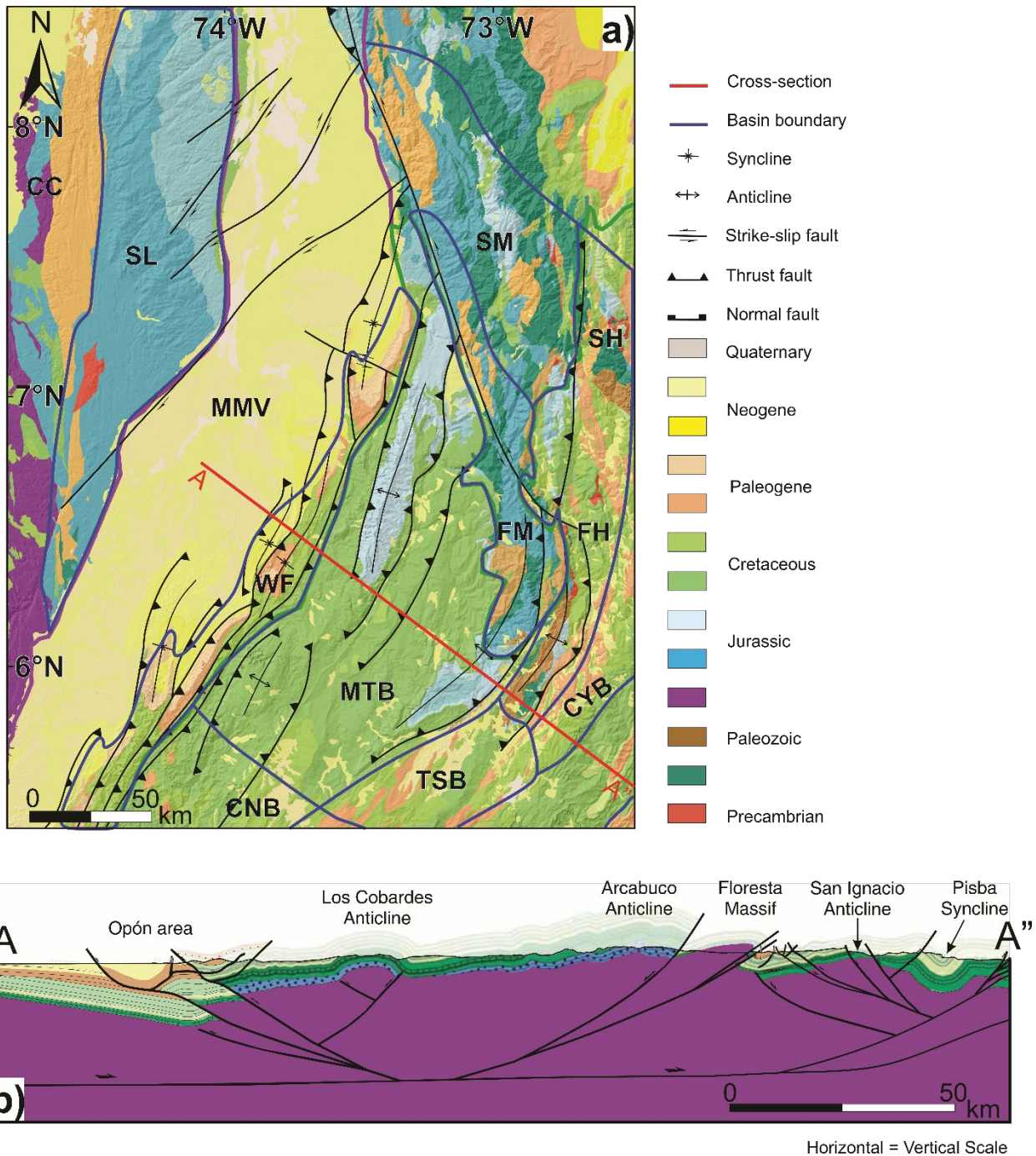


Figure 1-7. a. Regional geologic map modified from Gomez et al. 2015. CC: Central Cordillera, SL: San Lucas range, MMV: Middle Magdalena Valley, WF: Western Foothills, MTB: Magdalena-Tablazo sub-basin, TSB: Tunja-Sogamoso sub-basin, CYB: Cocuy sub-basin, FH: Floresta high, FM: Floresta massif, SH: Santander high, SM: Santander massif, CNB: Cundinamarca sub-basin. **b.** Structural cross section of the Middle Magdalena Valley and Eastern Cordillera, modified from Caballero et al., 2013 and Tesón et al., 2013.

During the Early Cretaceous, the extensional phase was presumably controlled by lithosphere stretching in an extensional back-arc domain; the basin developed as a wide (>180 km) asymmetrical rift (Sarmiento, 2001; Toro et al., 2004). As a result, the thickest marine strata were deposited during the Early to middle-Cretaceous in the EC and MMV (Cooper et al., 1995; Sarmiento 2001). Based on the subsidence vs. extension analysis conducted by Sarmiento (2001), the Early Cretaceous deposits are less preserved in the MMV, while significant accumulations occur in the footwall of the Western EC frontal thrust; this relationship allows to deduce higher subsidence in the EC than the MMV.

The Early Cretaceous subsidence events are associated with lithosphere thinning (Toro et al., 2004). Subsidence analysis based on surface and subsurface information indicates stretching factors up to 1.4 for the crustal and up to 3.4 for the subcrustal lithosphere (Fabre, 1983; Cooper et al., 1995; Sarmiento, 2001). In some areas where the crust reached the maximum stretching around 1.4, some mafic intrusions occurred (Sarmiento, 2001). However, Fabre (1983) explained the origin of these intrusions as the result of the major subsidence phase during the middle Cretaceous. The pre-existing Mesozoic faults play an essential role in the magmas rising; those faults served as channels to reach the upper crust level (Vasquez et al., 2006). As a result of variable stretching and magmatism, the basins present different heat flow, lithosphere structure, and stretching factors (Vasquez et al., 2006). Lithosphere thinning and the mafic intrusions suggest that the basin experienced high heat flow during the Early Cretaceous (Fabre 1983; Toro et al., 2004; Vasquez et al., 2006).

The MMV and EC experienced selective reactivation indicated by thickness variations and subsidence analysis. The lateral variations in thicknesses show that many reverse and thrust faults were normal faults before the Andean Cenozoic Orogeny (Sarmiento, 2001; Toro et al., 2004; Mora et al., 2006; 2009).

Nevertheless, the presence of minor subsidence in the MMV is decreasing to the west and is associated with the location of non-reactivated Mesozoic structures, rather than major subsidence that occurred in the footwall of the Western frontal thrust of the EC and the Mesozoic inverted structures. Mora et al. (2006) argue that the selective reactivation in the eastern flank of the EC is due to the tectonic stress orientation with respect to previous anisotropies.

Topography presumably started to evolve since the Late Cretaceous-Paleogene in the MMV and EC (Gomez et al., 2005; Parra et al., 2009, 2012; Mora et al., 2020); as a consequence of the Central Cordillera uplift and eastward thrust migration, this hypothesis is substantiated by thermochronology, vitrinite reflectance, and provenance analysis (Caballero et al., 2013) that allow elucidating the age of the main unconformity. This event was a compression phase and also it was a consequence of the Mesozoic basin inversion in the EC and MMV; the age was initially thought to be middle Eocene (Villamil, 1999) or late Paleocene- late Eocene (Restrepo-Pace et al., 2004). Nevertheless, by combining vitrinite reflectance and thermochronology, Parra et al., 2012 proposed a Late Cretaceous–Paleocene age for this uplifting event. During the Late Cretaceous, the MMV and EC basins experienced transgressive cycles until the Turonian, when the basins reached their maximum depth (Villamil, 1999). Following this marine succession fluvial continental deposits were deposited, evidencing a sea-level fall until the Late Cretaceous. These Maastrichtian deposits are thought to reveal the end of thermal subsidence in the basins and the onset of contraction and inversion of the Central Cordillera (Villamil, 1999; Toro et al., 2004).

According to Cortes et al. (2006) south of the western foothills of the EC during the Paleocene, the Northern Andes experienced a compressional phase with a W-E to WSW-ENE directed σ_1 . This stress was oblique to the N-E-SW trending faults, which became wrench faults during inversion. Nevertheless, in the MMV and EC study area, these structures were reactivated into reverse faults (Cooper et al., 1995; Gomez et al., 2005; Restrepo-Pace et al., 2004; Parra et al., 2012; Sarmiento, 2001). The compressional deformation and uplift of the Central Cordillera generated a regional foreland basin in the MMV and EC during the Paleocene (Cooper et al., 1995; Gomez et al., 2005). This orogenic front migration from west to east generated the inversion of the Mesozoic basins in the MMV and EC (Sarmiento, 2001) this migration started since the Late Cretaceous-early Paleocene in the northern area (Parra et al., 2012). Flexural analysis reveals that the MMV basin required loading by both thrust systems to produce the Paleogene subsidence that is not explained only for the Central Cordillera Paleogene topography, but also a partial inversion of the extensional basin during the Paleogene (Sarmiento, 2001). Thin Mesozoic deposits experienced major subsidence during the Cenozoic due to a decrease in lithosphere effective elastic thickness (Toro et al., 2004) this decline values could be attributed to the Cenozoic compression and thermal activity. Compressional tectonics continued during the Miocene, and according to Gomez et al. (2005) during this period there was a significant erosion of the Paleocene deposits. The basin configuration

was characterized by the thrust front of the Central Cordillera advancing eastward (Cooper et al., 1995; Mora et al., 2006, 2009; Parra et al., 2012; Restrepo-Pace et al., 2004; Sarmiento, 2001). Uplift of the western foothills of the EC is first recorded by middle -Late Eocene alluvial to fluvial deposits (Caballero et al., 2010; Gomez et al., 2005). The major deformation occurred there during the middle – Late Miocene, creating new thrusts and reactivating Mesozoic extensional faults that had not been reactivated during the previous contractional events (Cooper et al., 1995).

The present-day configuration of the Eastern Cordillera documents a total shortening ranging from 60-230 km ([Figure 1-7b](#)) according to different studies that analyzed the total shortening of the Eastern Cordillera and its geometry development. Some shortening values proposed are 105 km (Coletta et al., 1990), 150 km (Dengo and Covey, 1993), 68 km (Cooper et al., 1995), 230km (Roeder and Chamberlain, 1995). The latter model exceeds the total amount of the most accepted values in the study area. Moreover, it proposes a lithosphere-scale ramp-flat thrust that is challenging to validate. Shortening values proposed more recently are 120 km (Taboada et al., 2000) and 60 km (partial section) (Toro et al., 2004). Restrepo et al. (2004) analyzed the shortening in the western foothills from north to south, where the shortening accumulated ranges from 12-8 km decreasing to the south. Sanchez et al. (2012) evaluated the shortening rates in the Opon section decreasing from the northern to the southern section 27-24 km. Values of total shortening obtained by Tesón et al.(2013) ([Figure 1-7b](#)) vary from 62-80 km. These authors defined the total shortening of the EC as modest, around 25% of the original length, and with the major deformation localized in the marginal thin-skinned domains, whereas the internal structure of the mountain chain is dominated by basement-involved structures produced by inversion. Teixell et al. (2015) in the Sabana de Bogota south of the study area obtained shortening values of 89 km, and integrated the salt diapirism in the evolution of the EC. These authors proposed that the salt layers were deposited in a marine environment during Cretaceous extension and later acted as decollement levels for developing thin-skinned structures in the EC.

According to these restorations and following the geographical distribution of the cross-sections, the values most plausible of shortening are ~25-30% of the original length. Those shortening values were obtained in the cross-sections of Cooper et al. (1995) and Tesón et al. (2013), based on the serial cross-sections made by Tesón et al. (2013) the shortening does not reflect important variations along the strike from north to south. Nevertheless, the southern section presented by Teixell et al. (2015) reflects a slight southward shortening increase, this cross section illustrates the influence of

salt bodies in the structural development of the internal part of La Sabana de Bogota, where the deformation is controlled by thin-skinned detached from weak layers, concerning to the Magdalena Tablazo and Cocuy sub-basins where the shortening is highly controlled by the reactivation of the Mesozoic normal faults. This shortening represents the 27% of the original length (Teixell et al., 2015) and according to Kammer et al. (2020) the shortening variations from different authors depends on the dips employed for the main faults, and shortening generation (thrusting, folding). The shortening analysis conducted in the Western Foothills of the Eastern Cordillera from north to south, showed a southward shortening decrease (Restrepo-Pace et al., 2004; Sanchez et al., 2012). Based on the Tesón et al. (2013) analysis the shortening could increase southward along the Eastern Foothills and decrease to the south in the Western Foothills. The deformation is distributed along the strike from Mesozoic inverted structures, buckling deformation in the axial areas, and thin-skinned structures in the Western and Eastern Foothills. The shortening values are dependent on thin- and thick-skinned geometries, the style of individual structures present in each section such as back thrusting, triangle zones, passive roof duplexes, salt diapirism, internal folding, and reactivation of inherited faults (Mora et al., 2006; Restrepo-Pace et al., 2004, Sanchez et al., 2012, Teixell et al., 2015; Tesón et al., 2013, Toro et al., 2004).

2. ONSET AND STYLE OF MESOZOIC EXTENSION IN THE EASTERN CORDILLERA AND MIDDLE MAGDALENA VALLEY CONSTRAINED BY THE FIRST VOLCANIC EVENTS

This chapter is a reorganized version of the manuscript submitted to International Journal of Earth Sciences in June 2021.

Authors: Martin Reyes, Jonas Kley, Andrés Mora, Istvan Dunkl, Juan Carvajal-Torres.

Chapter Overview

This chapter addresses the geological evolution and initial basin configuration during the Mesozoic. The chronostratigraphic chart showed in this chapter is integrated through different methods and previous works.

This chapter includes petrography, geochronology, structural and stratigraphic data obtained during the last decades in the Middle Magdalena Valley and Eastern Cordillera. Furthermore, new data collected during the field campaigns allow us to date the volcanism and merge it with the previously mentioned information.

In this chapter, the primary goal is to establish the onset of the rifting in the Eastern Cordillera and Middle Magdalena Valley, and this analysis will contribute to understanding the style of extension and its genesis.

Abstract

The Mesozoic magmatism that occurred along the Eastern Cordillera (EC) and Middle Magdalena Valley (MMV) is primarily attributed to the interaction between the Farallon plate that subducted beneath the South American plate. Nevertheless, the differences in the geochemical signatures between the Late Triassic-Jurassic and Cretaceous magmatism impede a definition of a unique evolutionary model. Yet, it incentivizes the development of a tectonic model integrating the structural setting and their relationship with the Mesozoic volcanism. The correct understanding of the Mesozoic magmatism allows us to combine it with stratigraphic and structural data and reconstruct the basin evolution and contributes to a better understanding of the influence of Mesozoic structural inheritance in the basin configuration.

Previous studies carried out in the Eastern Cordillera and Middle Magdalena Valley focused on stratigraphy as well as petrography and geochronology (K/Ar), in plutonic bodies mainly. In this study, we employ geochronology (U/Pb) dating in zircons. Besides the ages from volcanic and volcanoclastic deposits, some detrital zircon ages were also analyzed. We correlate our new ages with published plutonic ages (K/Ar), (Ar/Ar), (U/Pb) and with structural, stratigraphic, and petrographic data to integrate a tectonic model with an updated stratigraphic chart for the Mesozoic.

From the Girón Fm. we obtained Late Triassic – Early Jurassic ages, which date the initial syn-rift infill of the Eastern Cordillera and are synchronous with calc-alkaline magmatism. The ages obtained from the Jordán Fm. are Early Jurassic and are associated with major plutonic activity. Middle Jurassic ages collected from the Noreán Fm. are not synchronous with plutonism due to a significant lull in intrusive activity. Lower Cretaceous mafic bodies in the Eastern Cordillera are scarce and related to the last extension events. We interpret the Mesozoic extension as the result of lithospheric stretching in the back-arc domain due to interaction of the Farallon and South American plates. Subsequently, the magmatic arc of the subducting plate migrated westwards while the locus of extension and lithospheric thinning ceased by the Late Cretaceous.

Keywords

Mesozoic, Extension, Eastern Cordillera, Geochronology, Middle Magdalena Valley

Introduction

Unravelling the relationship between the magmatism and the tectonism that controlled the basin development during the Mesozoic is fundamental to complement the tectonic evolutionary models, especially during the less-documented initial stage (Triassic-Jurassic) and also to understand the influence in its present configuration.

Several studies have been conducted in the northwestern Andes of Colombia aimed to understand its Mesozoic tectono-magmatic evolution (e.g., McCourt et al. 1984; Aspden et al. 1987; Bayona et al., 2006; Bustamante et al. 2016; Cochrane et al., 2014; Rodríguez-García et al., 2020; Vasquez and Altenberger 2005; Vasquez et al. 2010) and show the existence of a subduction related magma. Our study integrates geochronology, petrography, stratigraphy and structural cross sections to illustrate the Mesozoic basin development in the northern Andes and the influence of this initial magmatism within the tectonic setting of the northwestern Andes.

The Eastern Cordillera of the northwestern Andes in Colombia originated as a Mesozoic extensional basin on a continental margin during the Late Jurassic to Early Cretaceous (Sarmiento 2001).

According to Jaillard et al. (1990; 2000), Toussaint (1995), Ramos and Aleman (2000), Sarmiento-Rojas et al. (2006), Ramos and Folguera (2009) and Pindell and Kennan (2009), the evolution of the Northwestern Andes Mesozoic magmatic arc along the margin is a consequence of the subduction of the Farallon plate beneath northwestern South America.

The Colombian Geological Survey has conducted several studies and different authors have evaluated the magmatic development during the Mesozoic to describe the plutonism along the margin, developing petrographical, geochemical, and geochronological studies. The Triassic – Jurassic plutonism principally comprises calc-alkaline magmas that originated in the magmatic arc (McCourt et al. 1984; Aspden et al. 1987; Rodríguez- García et al. 2020).

At the end of the Jurassic period, plutonism ceased in the Eastern Cordillera and Middle Magdalena Valley (McCourt et al. 1984; Aspden et al. 1987; Bayona et al. 2020). Proposed explanations for the termination of magmatism include shallowing of the slab dip or changes in convergence velocity (Cross and Pilger 1982; Jarrard 1986; Metcalf and Smith 1995). According to Bustamante et al. (2016), the steepening of the subduction angle associated with a rollback behavior or changes in convergence obliquity were the mechanisms controlling the spatial distribution of magmatism.

Small intrusive bodies (~60 km²) of Early – Middle Cretaceous age have been identified along the Eastern Cordillera, with a transition in geochemical composition from mafic alkaline to tholeiitic magmas interpreted as a shift from a low to a high degree of melting (Vasquez and Altenberger 2005; Vasquez et al. 2010). According to the geochemical results along the Eastern Cordillera during the Mesozoic obtained from the calc-alkaline to tholeiitic magmatism, and based on Jarrard (1986), the basin experienced shallow dipping subduction during the initial stages that migrated until the onset of regional extension.

The basin located in the area of the modern Eastern Cordillera, passed from a Jurassic to Early Cretaceous back-arc to a Late Cretaceous to Paleogene retroarc foreland and later, to Neogene independent basins. (Villagomez and Spikings 2013; Horton et al. 2015; Silva et al., 2013) The resulting thick-skinned fold-and-thrust belt of the Eastern Cordillera is almost 600 km long from north to south, and has a maximum east-west width of about 220 km. It has an unusual triangular shape widening to the northeast with a main NNE structural trend ([Figure 2.1a](#)). The eastern and western foothills expose thrust structures in Cenozoic units, while the axial zone exposes Mesozoic units. To the west, the Eastern Cordillera is bordered by the Middle and Upper Magdalena Valley, an intermountain foreland basin separating the Central and Eastern Cordilleras. To the east it is bounded by the Llanos foreland. Both the eastern and western borders of the Eastern Cordillera were thrust over the adjacent basins during inversion, inducing foreland basin deposition and configuring a complex combination of thick-skinned and thin-skinned structures (Mora et al. 2006; Sánchez et al. 2012; Moreno et al. 2013; Nemcok et al. 2013; Teixell et al. 2015). The interior of the Eastern Cordillera exhibits diverse structural styles resulting from the extensional and contractional tectonic regimes ([Figure 2.1b](#)).

During the last decades, campaigns to collect geochronological and geochemical information have been carried out in some plutonic bodies. However, as Bayona et al. (2020) noted, unconstrained stratigraphic positions of the samples, and their scarcity, hinder the elaboration of a chronostratigraphic model that integrates plutonism, volcanism, and sedimentary rocks of specific time slices and tectonic settings.

In this paper, we present new U/Pb ages from the sedimentary units in the axial zone of the Eastern Cordillera such as the Girón, Jordán, Palermo, Montebel and Arcabuco formations, and also include U/Pb ages from the Noreán formation in the northern part of the Middle Magdalena Valley. We combine all of these new results regarding petrography, geochronology and sedimentary thickness

analyses. Likewise, we incorporated recent information regarding structural cross sections, plutonism, volcanism, sedimentation, and structural data to constrain the initial stretching events and their relationship with the magmatism during the Mesozoic in the Eastern Cordillera and Middle Magdalena Valley.

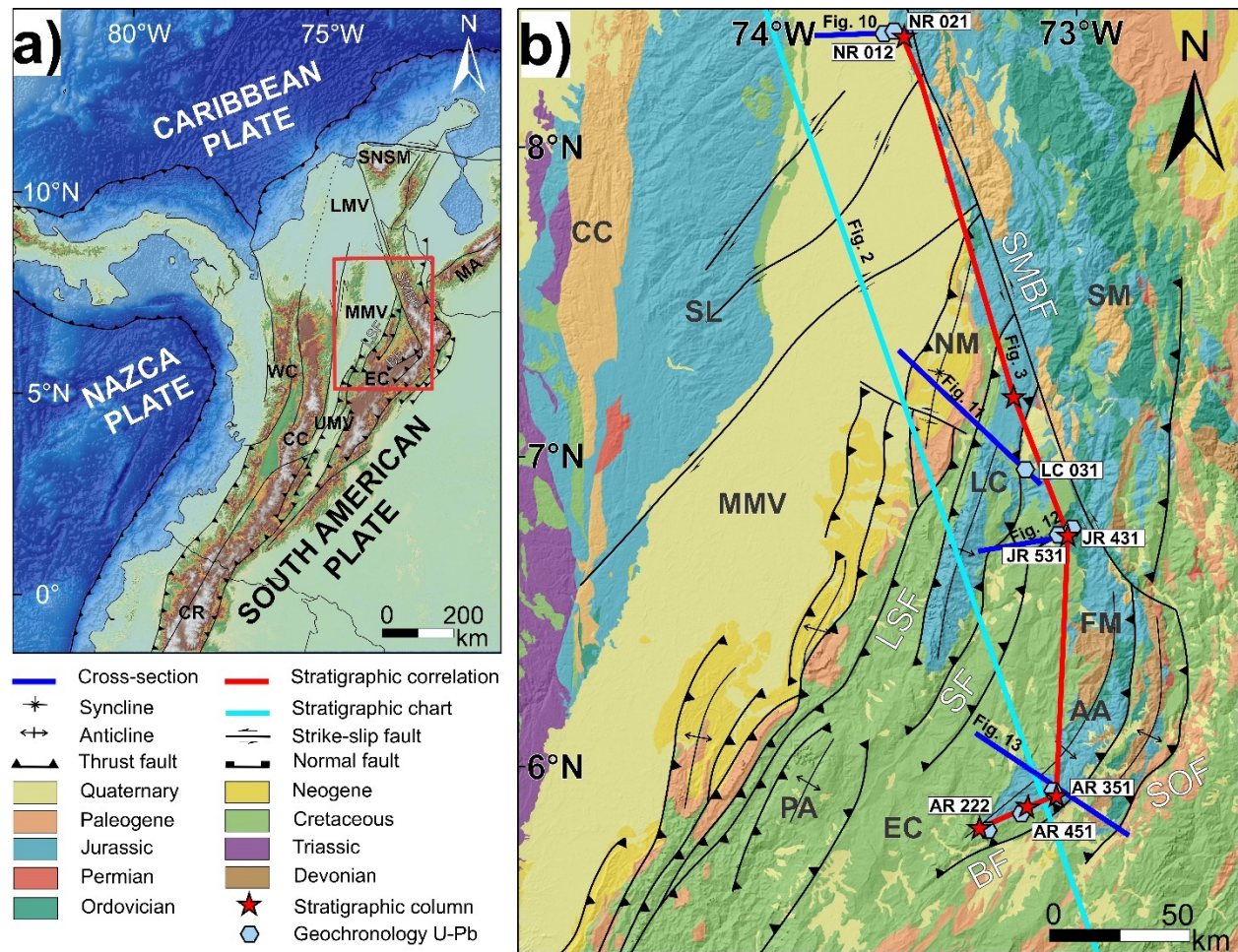


Figure 2-1. a. Present tectonic configuration of the northern Andes, showing the main tectonic features in the study area (orange box), MMV (Middle Magdalena Valley), WC (Western Cordillera), CC (Central Cordillera), EC (Eastern Cordillera) b. General geological map of the Eastern Cordillera (green outline) and Middle Magdalena Valley (purple outline), after Gomez et al. (2015). Principal folds shown are LC (Los Cobardes anticline), AA (Arcabuco anticline), PA (Portones Anticline) and NM (Nuevo Mundo syncline). Sub-basins in the Eastern Cordillera (after Sarmiento, 2001) are MTSB (Magdalena Tablazo Sub-basin), FM (Floresta Massif), FH (Floresta High), SM (Santander Massif), TSSB (Tunja Sogamoso Sub-basin), CYSB (Cocuy Sub-basin), SB (Sabana de Bogota), CSB (Cundinamarca Sub-basin). Main faults shown are LCF (La Campana fault), LMF (La Morena fault), SMBF (Santa Marta Bucaramanga fault), LSF (La Salina Fault), SF (Suarez fault), AF (Aratoca paleofault), BF (Boyaca fault), SOF (Soapaga fault).

Outline of the Mesozoic Evolution

Our project area comprises the north-central part of the Eastern Cordillera and the northeastern side of the Middle Magdalena Valley ([Figure 2.1](#)). The evolution of the Eastern Cordillera and Middle Magdalena Valley basins reflects the interaction between the South American, Caribbean, and Pacific Plates (Colleta et al. 1990; Cooper et al. 1995; Taboada et al. 2000). The Mesozoic covers a time of rifting from the Late Triassic to the Early Cretaceous (Kammer and Sánchez 2006; Sarmiento-Rojas et al. 2006) following the documented presence of Mesozoic normal faults (Casero et al. 1997; Sarmiento 2001; Branquet et al. 2002; Kammer and Sánchez 2006; Mora et al., 2006).

Documented magmatic events occurred during pre-Andean and Andean evolutionary stages, starting at the early Paleozoic in a range between 485-482 Ma, and are distributed along the Colombian Andean margin (Cediel et al., 2003; Leal-Mejia et al., 2011; Mantilla et al., 2012; Van der Lelij et al., 2016). The initial magmatism is extensively distributed in the northern Andes from the Cordillera Real in Ecuador to the Sierra Nevada de Santa Marta. According to Leal-Mejia et al., 2019 there are three initial magmatism pulses within the Colombian Andes; 1) early Paleozoic-mid-Ordovician, 2) Carboniferous and 3) Permian to middle Triassic.

During the Early Triassic the Colombian Andes experienced the beginning of the Pangea breakup (Vinasco et al., 2006; Restrepo et al., 2011). The Late Triassic-Early Jurassic comprised the major magmatic activity presented in the Colombian Andes. (Maze 1984; Aspden et al., 1987; Cediel et al., 2003). This magmatism is associated with the northern extensional system-oriented SW to NE, and this arc segment extends into the Ecuador and Peru (Cediel et al., 2003; Spikings et al., 2015)

Recently Rodriguez-Garcia et al. (2020) suggested that the Late Triassic-Jurassic magmatism occurred along different subduction zones that were active at different times by analyzing the geochemical composition.

The last stage of magmatism during the Mesozoic is associated with Early – Middle Cretaceous mafic intrusions, recorded in the Cocuy and the Cundinamarca sub-basins. This magmatism is due to crustal thinning and the differences in the magmas are linked to the depth and inhomogeneity of the mantle. (Vasquez and Altenberger 2005; Vasquez et al. 2010) ([Figure 2.1b](#)). The Middle Magdalena Valley and Eastern Cordillera basement is mainly composed of high-grade Mesoproterozoic metamorphic rocks, such as the Bucaramanga gneiss in the Santander Massif ([Fig. 1b](#)) (Nova et al. 2019) associated with the Caparonensis Orogeny during the Early Ordovician

(Restrepo-Pace and Cediél 2010; Van der Lelij et al. 2016). The Triassic – Jurassic stratigraphic sequence has been described by Julivert (1963), Renzoni (1967), Cediél (1968), Clavijo (1996), Mojica and Kammer (1995); Mojica et al. (1996) and Kammer and Sánchez (2006); as having been deposited in continental environments. The rock units are dominant successions conglomerates and sandstones with sporadic volcanic effusive and pyroclastic deposits as well as local presence of marine facies to the south, for instance the Montebel Fm. described by Renzoni (1967) and Sarmiento (2001). The volcanoclastic and pyroclastic deposits of the Latest Triassic to Early Middle Jurassic (Mojica et al. 1996) accumulated in sub-basins along the continental margin that were created by asynchronous extension (Mojica and Kammer 1995). The Cretaceous in the Eastern Cordillera is represented by fluvial deposits at the early stages, followed by a succession of shallow marine deposits laid down in progressively deepening environments until maximum water depth was reached during the Middle Cretaceous time (Mora et al. 2009). This maximum flooding was followed by multiple transgressive-regressive events due to the accretion of the Western Cordillera terrane. Nonetheless, this also caused an increase in the sedimentation resulting in continental deposition during the Paleocene and part of the Eocene. (Sarmiento 2001; Sarmiento-Rojas et al. 2006; Caballero et al. 2013; Carvajal-Torres; 2021, personal communication) ([Figure 2.2](#)).

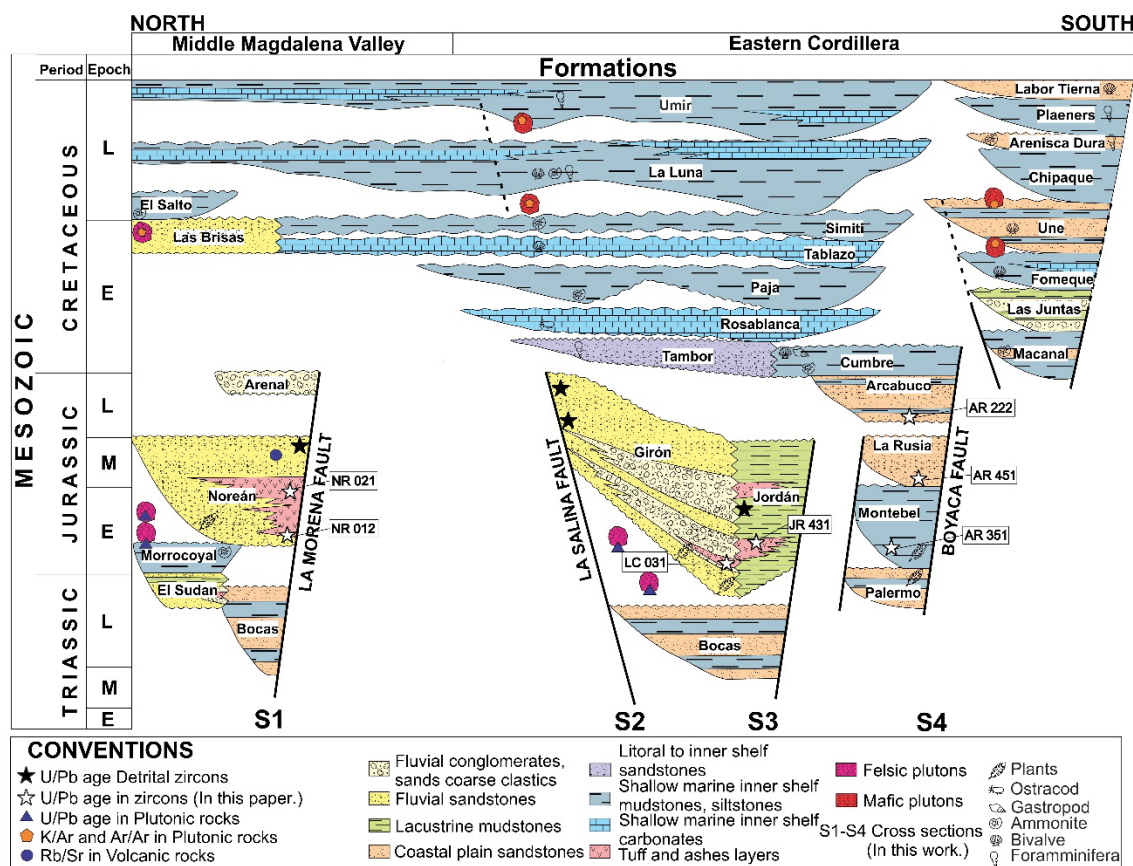


Figure 2-2. Mesozoic stratigraphic chart of the Eastern Cordillera and Middle Magdalena Valley, showing the depositional environments, lithologies, and magmatic activity. Data compiled from Renzoni (1962);(1967), Cediell (1968), Cooper et al. (1995), Clavijo (1996), Mojica et al. (1996), Sarmiento (2001), Sarmiento-Rojas et al. (2006), Kammer and Sanchez (2006), Mora et al. (2006, 2009, 2013), Clavijo et al. (2008), Caballero et al. (2010, 2013), Horton et al. (2010, 2015), Sanchez et al. (2012), Moreno et al. (2013), Reyes-Harker et al. (2015), Nova et al. (2019), Bayona et al.(2020), Rodriguez-Garcia et al. (2020) and integrated with the new measurements and data obtained in this work. See [Figure 2.1](#) for locations of sub-basins in the Eastern Cordillera following the subdivision by Sarmiento (2001).

Geological description

Mesozoic strata are exposed along the Eastern Cordillera's axis, with significant variations in thickness from hundreds to thousands of meters for some of the deposits. In this work, samples from the Noreán, Bocas, Girón, Jordán, La Rusia, Montebel, and Arcabuco Fms were analyzed ([Figure 2.2](#) and [Figure 2.3](#)). In its type locality, the Noreán Fm. has been described as a continental rock unit that also records a spike of volcanic activity. In some areas, the total thickness of this formation has been reported to exceed 4500 m. For example, on the road from Buturama to Bombeadero in the Noreán region. ([Figure 2.4a, b](#)) (Clavijo, 1996). The samples analyzed in this work come from the Epiclastic unit as defined by Clavijo (1996), mostly comprising pink-colored

lithic andesite to dacite tuffs with intercalated conglomeratic mudstones. The sequence is well stratified and has a thickness of 1500 m (Figure 2.3). Tuffs were macroscopically identified along the entire section and samples were selected for analysis and microscopic description.

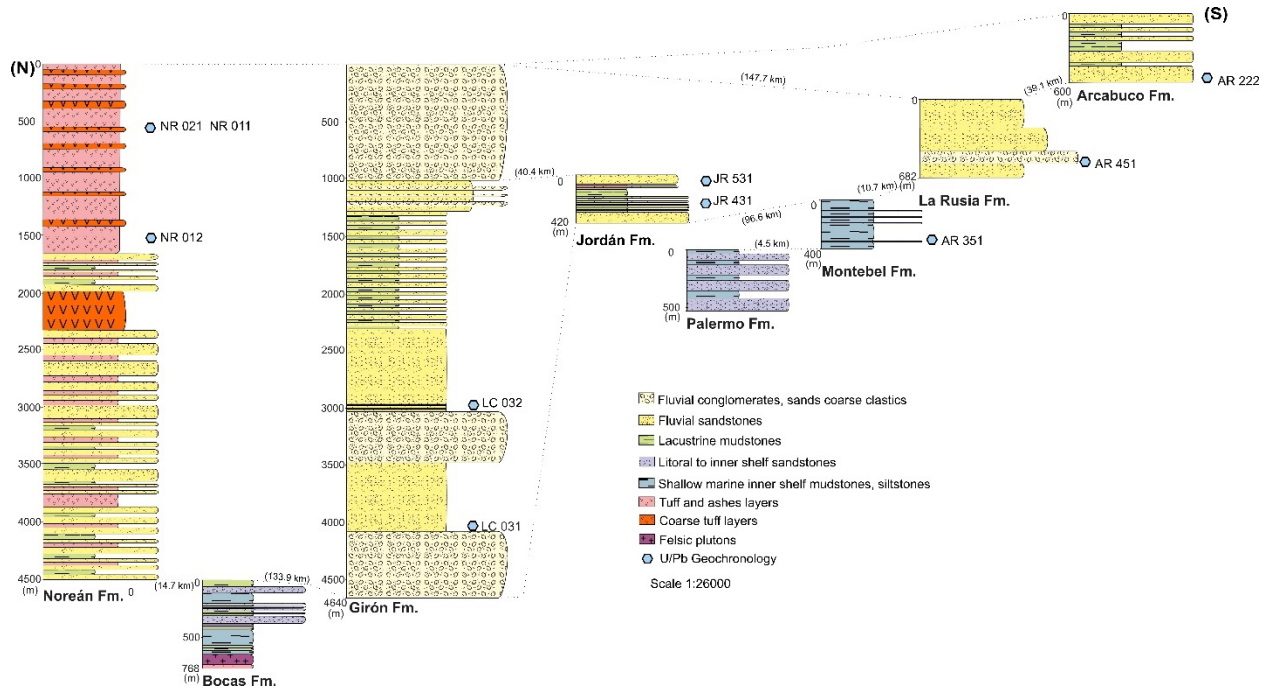


Figure 2-3. Stratigraphic columns for sections analyzed in this work. Sources: Noreán and Bocas Fms. from Clavijo (1996); Girón and Jordán formations from Cediél (1968), the Palermo, Montebel, La Rusia and Arcabuco Fms. are compiled from Renzoni (1967). See Fig 1. for locations.

The type locality of the Bocas Fm. is near the town of Aguachica. The studied outcrops of the Bocas Fm. are located along the Rio de Oro in the northern part of the total study area (Figure 2.1). The section was previously described by Clavijo (1996). It preserves a thick succession of gray sands and mudstones with intercalated tuffs and volcanic flows of intermediate composition, with a total thickness of 781 m (Figure 2.3).

The Girón Formation has been described and defined by Cediél (1968) in the Lebrija river, where he measured a thickness of 4640 m. It is considered to be a continental deposit composed of intercalated mudstones and sandy conglomerates with volcanoclastic rocks at the base (Figure 2.4c). Higher up, the sequence presents variation between mudstones and sandstones with coarse-grained red sandstones, and near the top the predominant mudstones give way to conglomerates. (Figure 2.3). Sampling was conducted around the valley of the Sogamoso river (Figure 2.1b); while macroscopic analysis was applied to the sandstones and the volcanoclastic layers at the bottom.

The Jordán Fm. was defined and described by Cediél (1968) near the town of Jordán, along the horse path from the Los Santos municipality. It essentially consists of coarse-grained sandstones and sparse conglomerates with sporadic intercalations of mudstones, followed by an alternation of red beds. This section presents intercalated red tuffs known as the welded tuffs of Jordán ([Figure 2.4d](#)). The section has a total thickness of 420 m ([Figure 2.3](#)).

On the horse path from Jordán to Los Santos, and close to the town a complete continental sequence of the Early Cretaceous is exposed in the La Peña region, and the contact with the Jordán Fm. is evident. ([Figure 2.4e, f, g](#))

In the area of the Las Varas creek along the eastern flank of the Arcabuco Anticline, the Montebel Fm. was described by Shell Geologists (in Renzoni, 1967) as interbedded black shales and mudstones with the presence of several lenses of red sands, and with an accumulated thickness of 400 m ([Figure 2.3](#)) including some levels of volcanoclastic deposits ([Figure 2.4h](#)). Overlying this formation along the eastern flank of the Arcabuco Anticline, an intercalation of sandstones and conglomerates with a total thickness of 682 m ([Figure 2.3](#)) was defined by Renzoni (1967) as La Rusia Fm. To the south, along the anticline plunge ([Figure 2.4i](#)), a section composed of interbedded sandstones with thin layers of shale and a thickness of 600 m ([Figure 2.3](#)) was defined as the Arcabuco Fm. by Renzoni (1967).

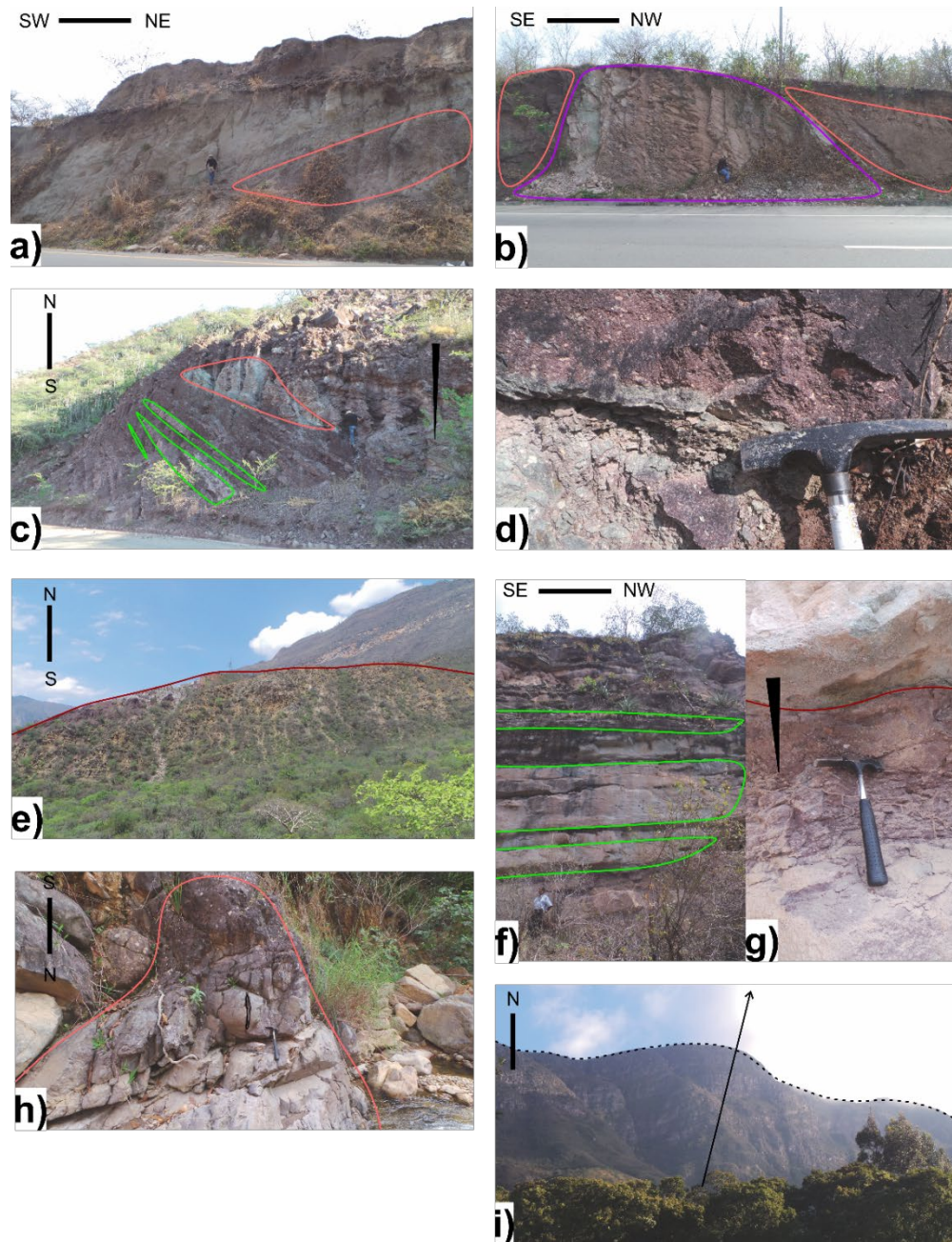


Figure 2-4. Outcrop photographs: a) Photographs of the extrusive member of the Noreán formation. b) Evidence of an intrusive body at the top in contact with a red volcanic tuff. Noreán formation. c) Basal member of the Girón formation. evidence intercalation between red layers and conglomerates with presence of small volcanic flows (less than 3m). d) welded tuffs defined by Cediél (1968), Jordán formation. e) Contact between the Early Cretaceous and Jurassic along the Chicamocha Canyon. f) Intercalation of sandstones and mudstones, associated with fluvial channels. Tambor formation. g) Contact between Tambor formation and the red shales Jordán Formation. h) Volcanic flows associated to the Montebel formation. i) Hinge of the Arcabuco anticline. Color lines description: orange line: tuffs and volcanoclastic material. Purple line: dikes and intrusive bodies. Green line: fluvial channels. Red line: geological contact between the Cretaceous and Jurassic.

Methods

We visited the Mesozoic outcrops in the Eastern Cordillera and Middle Magdalena Valley, where the sampling in the field focused on the volcanic rocks that erupted during the Mesozoic. Our main objective was to date the syn-rift rock units to define the possible onset of the extension in the northeastern Andes and complement the Mesozoic tectonic evolution model. We collected samples from four areas 1) the Noreán region which is located in the north part of the Middle Magdalena Valley and where we collected information from the Noreán and Bocas Fms. In this part we obtained samples from the hanging wall blocks of the La Campana and La Morena faults ([Figure 2.10](#)). 2) The Los Cobardes region ([Figure 2.11](#)) which is located in the central part of the Eastern Cordillera along the Los Cobardes anticline. In this section we obtained samples from the Girón Fm. and basal Cretaceous rock unit. The dated samples were collected from the Footwall block of the Suarez fault. 3) The Jordán region ([Figure 2.12](#)) which is located in the Chicamocha canyon to the east of the Los Cobardes region. In this area we obtained samples from the Jordán Fm. in the hanging wall block of the Aratoca fault. 4) The Arcabuco region ([Figure 2.13](#)) which is located in the southeast part of the Eastern Cordillera and exposes the older rock units of the Mesozoic in the Eastern Cordillera. Here, we collected the samples from the Arcabuco, Montebel, La Rusia, Palermo Fms. from the Arcabuco anticline in the hangingwall of the Boyacá fault.

Description and classification of different lithologies was performed through microscopical analysis, including the selection of samples for dating. The microscopical mineral relation was developed by employing the classifications suggested by Streckeisen (1978) and Schmid (1978) to volcanic rocks and volcanoclastic material respectively.

The in-situ geochronological U-Pb measurements were performed by laser-ablation single-collector sector-field inductively coupled plasma mass spectrometry (LA-SF-ICP-MS) on zircon, conducted in the GÖochron Laboratories, University of Göttingen, following the analysis procedures and protocols of Frei and Gerdes (2009). The data was collected using single spot analysis with a laser beam diameter of 33 μm and a crater depth of approximately 10 μm . The laser was fired at a repetition rate of 5 Hz with a nominal laser energy output of 25 %. Two laser pulses were used for pre-ablation. The carrier gas was He and Ar. The ICP-MS measured analytes of ^{238}U , ^{235}U , ^{232}Th , ^{208}Pb , ^{207}Pb , ^{206}Pb , mass 204 , and ^{202}Hg . The data reduction was based on the processing of ca. 50 selected time slices (corresponding to ca. 14 seconds) starting ca. 3 seconds after the beginning of the signal. If the ablation hit zones or inclusions with highly variable actinide concentrations or

isotope ratios, the integration interval was slightly resized, or the analysis was discarded (~1% of the spots). The individual time slices were tested for possible outliers by an iterative Grubbs test (applied at P=5% level). This test filtered out only the extremely biased time slices, and in this way, less than 2% of the time slices were usually rejected. The age calculation and quality control are based on the drift- and fractionation correction by standard-sample bracketing using GJ-1 zircon reference material (Jackson et al. 2004). For further control, the Plešovice zircon (Sláma et al. 2008) and the 91500 zircons (Wiedenbeck et al.1995) were analyzed as "secondary standards." The age results of the standards were consistently within 2σ of the published ID-TIMS values. Drift- and fractionation corrections and data reductions were performed by our in-house software UranOS (Dunkl et al. 2008). The level of the Hg-corrected ^{204}Pb signal was deficient; thus, no typical lead correction was required. The Concordia plots and age spectra were constructed with the help of Isoplot/Ex 3.75 (Ludwig 2012) age measurements, and analytical results are attached in the supplementary material.

Based on previous geological mapping, and stratigraphic and structural measurements, we constructed new balanced cross-sections to show the present-day configuration in the Eastern Cordillera and the Middle Magdalena Valley and the restored sections in order to illustrate the rifting styles throughout the study area. A Mesozoic stratigraphic chart was constructed by employing data from boreholes and previous studies from the northeast of the Middle Magdalena Valley to the southwest of the Eastern Cordillera. The chronostratigraphic markers we employed are based on geochronological data from the last decades and biostratigraphic information to calibrate the regional-scale correlations.

Results

Mesozoic stratigraphic synthesis

This paper integrates the pre-existent Mesozoic information published about facies, thicknesses, sedimentology, and ages. (See Table 2.1). [Figure 2.2](#) illustrates the changes in the depositional environments throughout time and space during the Mesozoic. The basin configuration and the role of tectonic events were evaluated by structural and stratigraphic analyses. We present an integrated chart from the northern to southern of the study area.

- **Triassic**

The basin development of the northeastern part of the Andes range started during the Triassic-Early Cretaceous (Cediel 1968; 2019; Maze 1984; Jaillard et al., 1990; Cooper et al., 1995; Sarmiento 2001; 2011). The Triassic rocks rest unconformably over Paleozoic rock units and metamorphic basement. The continental clastic sequence is characterized by a Regressive cycle (Cooper et al., 1995; Cediel 2019). Nevertheless, the sedimentary record was deposited in a marginal environment that transgressed southward of the Sierra Nevada de Santa Marta (Irving 1975). The lithostratigraphic formation consists of coastal sandstones interbedded with mudstones and siltstones at the base, while at the top of the sequence a red sandstones and conglomerates are interbedded with tuffaceous sandstones and mudstones (Cediel 1968; Geyer 1969; 1982; Mojica et al. 1996; Clavijo et al., 2008). The Bocas Fm. Triassic sandstones were deposited in a marginal environment that transgressed southward of the Sierra Nevada de Santa Marta (Irving 1975). According to Ward (1973), the Santa Marta Bucaramanga (SMB) strike-slip fault played a fundamental role during the early stage of the Mesozoic rifting. The SMB fault activity has been defined as Late Triassic – Early Jurassic according to the radiometric ages from the Santander Massif ages and its distribution along the strike-slip fault (Cediel et al. 2003; Kammer and Sanchez 2006).

- **Jurassic**

According to Sarmiento et al. (2006), the sedimentation infill during the Triassic – Jurassic occurred in two basin compartments, defined as Payande, San Lucas, and Sierra Nevada (Etayo-Serna, 1986) along the NE strike of the Central Cordillera, while the second compartment comprises the Eastern Cordillera with its foreland basins and the western sectors of the Guyana Shield (Cediel et al., 2003; Sarmiento et al., 2006).

The initial Jurassic deposition along the study area from north to south is characterized by transitional mudstones interbedded with clastic rock units principally deposited in continental environments (Cediel, 1968; Mojica et al., 1996; Sarmiento, 2001). The presence of bivalves and ammonites register the local marine ingression predominantly during the Early Jurassic (Renzoni, 1967; Geyer, 1969). Volcaniclastic and pyroclastic deposits are distributed from north to south and were mainly deposited during the Middle Jurassic (Clavijo, 1996; Mojica et al., 1996; Sarmiento, 2001). However, in the Los Cobardes region on the central side of the study area, those deposits have occurred since the Early Jurassic. (Cediel, 1968). The coarse-grained deposits are linked to the

Chapter 2. Onset and Style of Mesozoic extension in the EC and MMV

Jurassic activity of the Mesozoic normal faults, and the red beds are an indicator of the reduction of the continental environment (Mojica et al., 1996; Sarmiento, 2001; Kammer and Sanchez, 2006).

Table 2-1. Geological information summary employed to construct the stratigraphic chart in [Figure 2.2](#).

Unit	Description	Environment	Thickness meters (min-max)	Description Author	Age	Age Method	Age Reference	Cross Section (in this work)
El Sudan Fm.	red sandstones and conglomerates interbedded with tuffaceous sandstones and mudstones	Fluvial – alluvial	200-300	INGEOMINAS – UIS 2006	Late Triassic	Ammonites ?	Geyer 1982	North of S1
Morrocoyal Fm.	mudstones and siltstones with bivalves and ammonites	Shallow marine	60-100	Geyer 1969	Early Jurassic	Ammonites	Geyer 1969	North of S1
Bocas Fm.	Interbedded mudstones and sandstones to the top thin limestone	Shallow marine	550-800	Clavijo 1996	Early Jurassic	Plant Fossils	Remy 1975	S1
Noreán	Effusive volcanoclastic and coarse grained sandstones	Fluvial	600-4500	Clavijo 1996- Clavijo 2008	Early Jurassic - Middle Jurassic	Plant Fossils - U/Pb Geochronology	Clavijo 1996 - This Work	S1
Arenal Fm.	Conglomerates	Fluvial	120-220	Clavijo 1996	Late Jurassic	Field relationship	Clavijo 1996	S1
Las Brisas Fm.	Volcano-sedimentary succession	Fluvial	Unknown	INGEOMINAS – UIS 2006	Albian ?	Field relationship - intrusive K-Ar dating	INGEOMINAS – UIS 2006	West of S1
El Salto Fm.	Interbedded limestones and mudstones	Shallow marine	50-140	INGEOMINAS – UIS 2006	Early Cenomanian	Ammonites	INGEOMINAS – UIS 2006	West of S1
Tablazo Fm.	Highly fossiliferous limestones with intercalations of mudstones	Shallow marine	90-260	Etayo-Serna 1968	late Aptian-early Albian	Bivalves	Etayo-Serna 1968	S1, S2, S3, S4
Simiti Fm.	Black laminated mudstones with local carbonate concretions	Middle Platform	120-650	Etayo-Serna 1968 - Villamil 1998	middle Albian - late Albian	Ammonites	Etayo-Serna 1968	S1, S2, S3, S4
Luna Fm.	Fossiliferous black mudstone	Deep Platform	90-950	Morales 1958- Villamil 1998	Early Turonian to Coniacian	Ammonites, bivalves, and foraminifera	Morales 1958	S1, S2, S3, S4
Umir Fm.	Shales with interbedded carbonates, presents iron concretions	Shallow marine	170-1500	Morales 1958- Villamil 1998- Sarmiento 2001	Campanian to Maastrichtian	Foraminifera	Petters 1955- Tchegliakova 1995	S1, S2, S3, S4
Giron Fm.	Conglomerates with interbedded volcanoclastic deposits	Fluvial	170-4650	Cediel 1968	Early Jurassic- Late Jurassic	U/Pb Geochronology	Horton et al. 2015 - This Work	S2, S3, S4
Jordán Fm.	Red beds and welded tuffs	Fluvial	180-650	Cediel 1968	Sinemurian- Toarcian	U/Pb Geochronology	This Work	S3
Palermo Fm.	Conglomerates with red pebbles	Fluvial	400-550	Renzoni 1967	Rhaetian	Plant debris	Lagenheim 1961	S4
Montebel Fm.	Black shales with interbedded mudstone packs	Shallow marine	420-960	Renzoni 1967	Late Triassic (Rhaetian) - Early Jurassic	Plant fossils	Lagenheim 1961	S4
La Rusia Fm.	Coarse-grained succession composed of sandstones and sandy conglomerates	Fluvial	320-800	Renzoni 1967	Middle Jurassic	Field relationship	Renzoni 1967	S4
Arcabuco Fm.	White sandstones with interbedded red shales	Fluvial	220-1600	Renzoni 1967	Late Jurassic	Field relationship	Renzoni 1967	S4
Tambor Fm.	Red sandstones with conglomerates and shales	Transitional	150-650	Morales 1958	Valanginian-Berriasian	Foraminifera-well analysis	Morales 1958- Guerrero 2018	S2, S3, S4
Cumbre Fm.	Sandstones with interbedded claystone and siltstones	Shallow marine	50-150	Moreno 1990	Berriasian-early Valanginian	Ammonites-gastropods, bivalves	Ballesteros 1989- Renzoni 1967	S2, S4
Rosablanca Fm.	Limestones with some interbedded mudstones	Shallow marine	170-620	Etayo-Serna 1968, Ward 1973, Moreno 1990	Late Valanginian-early Hauterivian	Field relationship, Ostracods from Bürgl 1954	Etayo-Serna 1968	S2, S3, S4
Paja Fm.	Mudstones with interbedded thin sandstones	Shallow marine	70-320	Etayo-Serna 1968	Early Barremian	Ammonites	Patarroyo 1997	S2, S3, S4
Macánal Fm.	Black mudstones with interbedded siltstones and sandstones, at the top some plat fossils	Proximal	1000-3000	Fabre 1983	Berriasian-early Hauterivian	Ammonites, bivalves	Petters 1954, Haas 1960	S4
Las Juntas Fm.	Coarse-grained sandstone deposits interbedded with mudstones and conglomerates	Transitional	380-2200	Ulloa and Rodriguez 1976	Hauterivian-Berriamian	Field relationship	Ulloa and Rodriguez 1976, Fabre 1983	S4
Fomeque Fm.	Black mudstones interbedded with sandstones and limestones	Shallow marine	500-950	Ulloa and Rodriguez 1976	Middle Barremian-early Albian	Field relationship, bivalves	Burgi 1961	S4
Une Fm.	Interbedded sandstones with siltstones and mudstones	Deltaic	?	Hubach 1957	Albian-Cenomanian	Bivalves	Ulloa and Rodriguez 1976	S4
Chipaqué Fm.	Interbedded black siltstones with limestones and plant remains	Shallow marine	150-720	Renzoni 1962	Late Cenomanian-Coniacian	Field relationship	Ulloa and Rodriguez 1976	S4
Arenisca dura Fm.	Fine-grained sandstone with interbedded siltstones	Shallow marine	410-580	Perez and Salazar 1971	Santonian	Ammonites, foraminifera	Etayo-Serna 1964	S4
Plaeners Fm.	Mudstones with variable organic content	Shallow marine	50-150	Perez and Salazar 1971	Campanian to Maastrichtian	Foraminifera	Perez and Salazar 1971	S4
Labor y Tierna Fm.	Medium-grained sandstones interbedded with siltstones and mudstones	Shallow marine	50-170	Renzoni 1962	Maastrichtian	Bivalves	Perez and Salazar 1971	S4

- **Cretaceous**

The Cretaceous units crop out mainly in the Eastern Cordillera while they remain buried in the adjacent basins (Hinterland Upper-Middle Magdalena and Llanos basins). The Cretaceous infill is characterized by a transgressive – regressive cycle (Cooper et al., 1995; Villamil, 1998; Sarmiento, 2001). The sedimentation occurred along a wide NW-SW oriented rift basin divided by the Santander and Floresta Massifs into the Magdalena Tablazo to the west and the Cocuy sub-basin to the east (Sarmiento, 2001). The beginning of the sedimentation occurred in a transitional environment along the Magdalena Tablazo sub-basin, with local variations in grain size that are smaller at the top of the sequence, and with an abundant presence of fossils, i.e., foraminifera, bivalves, ammonites, and gastropods (Renzoni, 1967; Cediél, 1968; Etayo-Serna, 1986; Cooper et al., 1995; Villamil, 1998; Sarmiento, 2001). According to Villamil (1998) and Sarmiento (2001), the basin reached its maximum tectonoeustatic base level during the Cenomanian to Coniacian; and the basin deepening started during the Late Cenomanian when detrital supply decreased (Villamil, 1998). During the Late Cretaceous, the basin recorded a general regression from transitional to the coastal plain environment (Cooper et al., 1995; Villamil, 1998). According to the provenance analysis from Parra et al. (2012) and Caballero et al. (2013), the Upper Cretaceous and Paleocene rock units preserve pebbles from the Central Cordillera. The western supply and absence of the Upper Cretaceous rock units in the Central Cordillera are indicators of a gradual uplift (Cooper et al., 1995; Parra et al., 2012; Caballero et al., 2013).

Thin section petrography

Microscopic analyses were performed on samples from volcanoclastic lithologies identified as potential targets for age dating.

Sample NR-021 from the Noreán formation presents a porphyritic texture, composed of mainly by crystals of plagioclase (80%), quartz (15%) and accessories (5%). A compound of muscovite, lithics, zircon, and devitrified glass constitutes the matrix, considered to be lithic andesite ash (Figure 2.5a). For the samples NR-011 and NR-012, the mineralogical composition is quartz (90-95%) and plagioclase or accessories (5%), the matrix is composed of quartz, devitrified glass, and feldspar. According to the mineral relation this was classified as a lithic rhyolite ash (Figure 2.5b). In the Bocas section, the samples NR-333 and NR-322, display a high percentage of plagioclase (85-90%). Accessory minerals are quartz (2-5%), lithics (5-10%), and mafic minerals (2-8%). The matrix is composed of quartz, feldspar, pumice, and chlorite, permitting a classification as lithic andesite ashes (Figure 2.5c).

Samples JR-412 and JR-432 from the Jordán Fm. are composed of pumice (60-40%), quartz (30-10%) plagioclase (10-5%) lithics (5-15%), and muscovite (2-5%). The matrix is composed of pumice, quartz, devitrified glass, feldspar and it is classified as lithic rhyolite ash (Figure 2.5d).

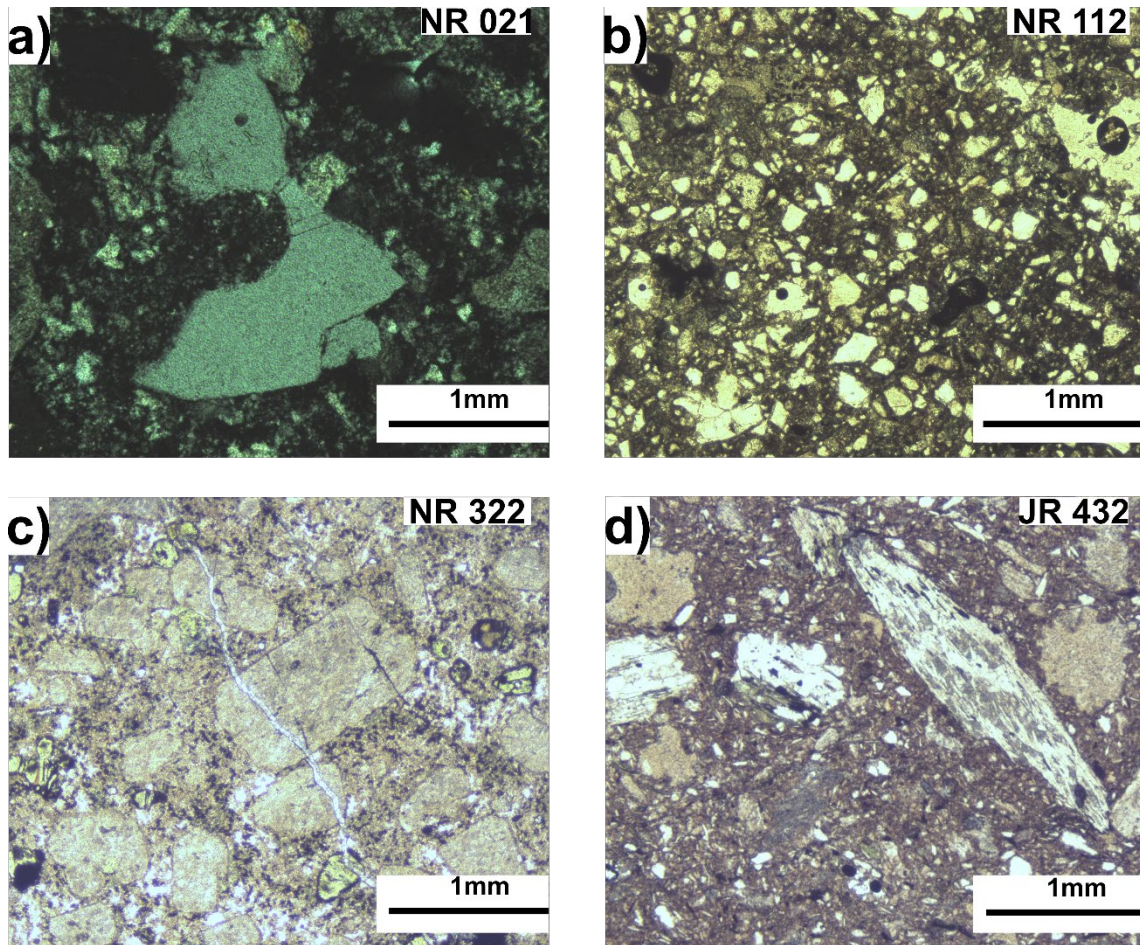


Figure 2-5. Characteristic microphotographs: a) Resorbed quartz as evidence of volcanic origin. Noreán formation. b) Porphyritic texture, major population of quartz grains, angular clasts. Noreán formation c) Porphyritic texture, principal component of plagioclase, evidence of mafic minerals. Bocas formation. d) Porphyritic texture, presence of pumice in major percentage. Jordán formation.

Zircon texture

A total of 305 zircon crystals in 10 samples from the different sections were analyzed using a binocular lens and cathodoluminescence images to distinguish the different populations and correlate them with petrogenetic indicators. Three formations are described to show the crystal variations from north to south.

To characterize the crystal morphology, we employed the Pupin (1980) classification for shape variations (Figure 2.6a). This classification uses a combination of prisms and pyramids to describe crystal shapes. Specific shapes are represented by different letters i.e., S, P, R and others. In our samples the largest population of crystals is P₂.

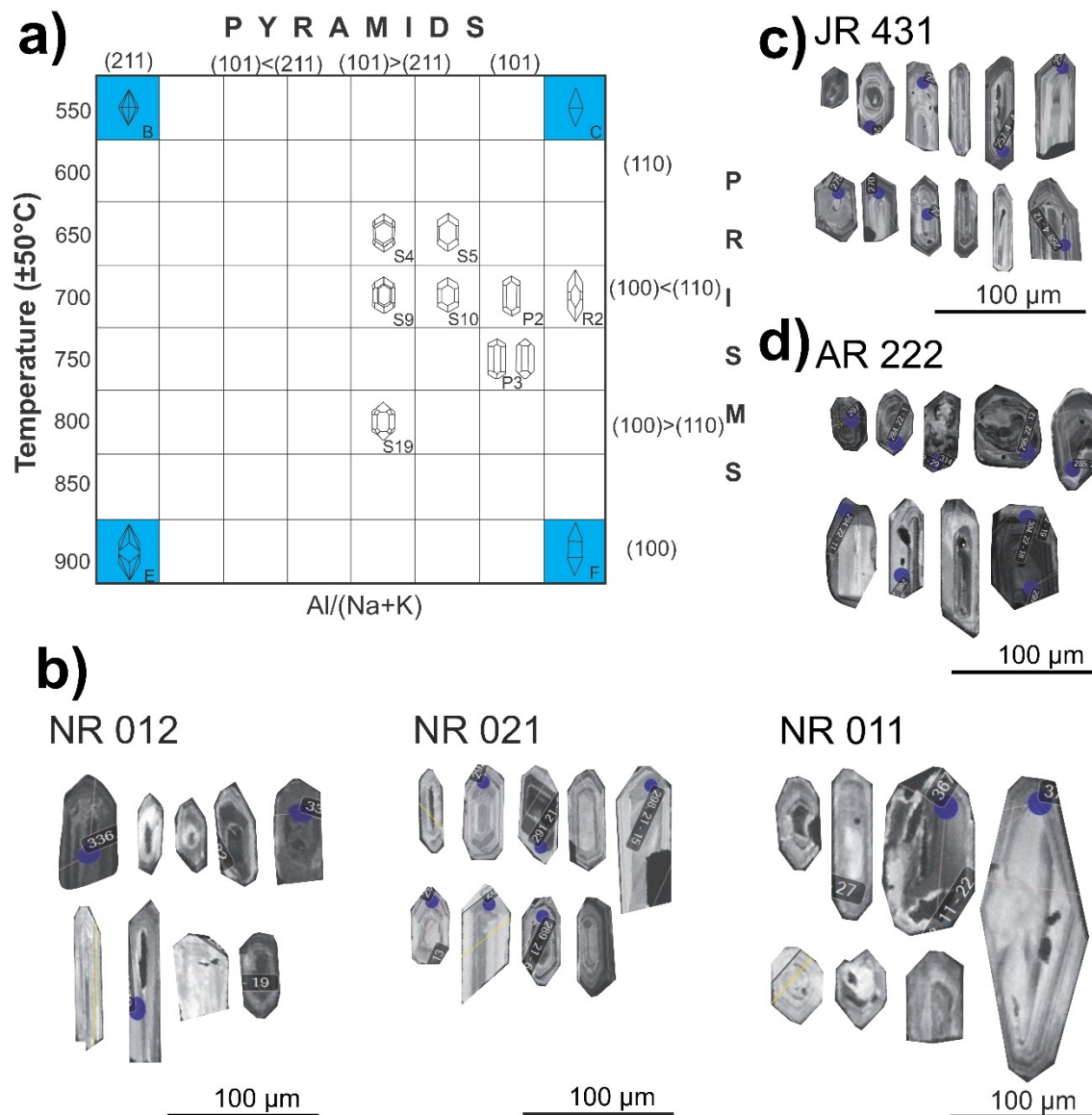


Figure 2-6. a) Zircon morphology classification after Pupin (1980) with the main crystal families from the sample analysis. Cathodoluminescence images of the studied samples. b) grains from the Noreán formation c) Jordán formation grains d) Arcabuco formation grains. (Blue spots are the ablated regions).

- **Noreán Formation**

The three samples analyzed from this formation allowed us to identify the significant crystal populations within the Formation. The predominant color is light brown; nevertheless, gray, colorless, and yellowish crystals are also present. Magmatic zoning is common in the samples NR-012 and NR-021, where the zircons show a better selection and where the major population of zircons is P₂ crystals (Figure 2.6b), whereas Sample NR-011 contains a poor selection of crystals with

S₄, S₉, S₁₀, S₁₉, P₁, P₂, and R₂ according to the typological classification of Pupin (1980). Inclusions are present mainly in crystals with rounded edges (Figure 2.6b).

- **Jordán Formation**

The primary crystal population in this area is colorless to light brown. Sample JR-431 (Figure 2.6c) reflects an excellent selection of crystals with the majority consisting of P₁ and P₂. The crystals have well-preserved edges, and show clear evidence of magmatic zoning.

- **Arcabuco Formation**

The detrital sample AR-222 presents different shapes from oval to rounded crystals. Most of the zircons are not well preserved and with significant changes in size between 50 to 200 microns (Figure 2.6d). The sample section is badly evidenced in the different crystal types i.e., P₂, P₃, S₅, S₁₀ and S₁₉. A significant amount of the total crystals (80%) analyzed in this sample present inclusions and magmatic zoning is scarce.

U-Pb Geochronology

We dated 10 samples using the U-Pb technique. In the following section we describe the results and new ages obtained (See Figure 2.1 for sampling locations, Figure 2.2 for the chronostratigraphic chart and Figure 2.3 for the stratigraphic levels analyzed, the sample details are enlisted below in Table 2-2).

Table 2-2. Sample list for U-Pb geochronology samples in the Eastern Cordillera and Middle Magdalena Valley basins.

Sample	Latitude	Longitude	Formation	Lithology	Stratigraphic age	Concordant age	Number of grains
NR-011	8°23'0.8329" N	73°36'1.4127" W	Noreán	Andesite ash	Early - middle Jurassic	177.6±1.6	27
NR-012	8°22'0.8120" N	73°36'0.165" W	Noreán	Andesite ash	Early - middle Jurassic	178.8±1.2	25
NR-021	8°23'14.8148" N	73°34'36.8688" W	Noreán	Tuffs	Early - middle Jurassic	176.85±0.85	26
LC-031	6°53'57.551" N	73°11'35.5" W	Girón	Volcaniclastic	Early - Late Jurassic	200.8±1	26
LC-032	6°54'10.702" N	73°10'59.219" W	Girón	Sandstone	Early - Late Jurassic	199.5±1.8	14
JR-431	6°44'30.3732" N	73°05'26.2361" W	Jordán	Red tuffs	Sinemurian - Toarcian	195.7±1.3	23
JR-531	6°44'00.0" N	73°05'59.1" W	Jordán	Red tuffs	Sinemurian - Toarcian	187.3±2.5	33
AR-451	5°54'14.2" N	73°04'27.0" W	La Rusia	Sandstone	Middle Jurassic	466.2±4	30
AR-351	5°52'44.8" N	73°09'42.2" W	Montebel	Sandstone	Rhaetian	471.4±2	50
AR-222	5°43'39.321" N	73°23'13.53" W	Arcabuco	Sandstone	Late Jurassic	466±4	50

- **Noreán formation: Samples NR-011, NR-012 and NR-021**

In Sample NR-011, 27 ages were obtained with values between 175 to 1550 Ma ([Figure 2.7a](#)), displaying a multimodal distribution with a principal population of Early Jurassic ages, and a Concordia age of 177.6 ± 1.6 Ma (Toarcian) with a MSWD (Mean Squared Weighted Deviation) of 2.1 ([Figure 2.7b](#)). For the sample NR-012, a total of 25 ages were analyzed with values between 176 to 1620 Ma ([Figure 2.7c](#)). The distribution for this range is multimodal with a significant peak at the Early Jurassic, and with a Concordia age of 178.8 ± 1.2 Ma (Toarcian) and a MSWD of 1.03 ([Figure 2.7d](#)). Both samples contain Precambrian and Paleozoic inherited zircons that are associated with metamorphism and magmatic events. For the sample NR-021, which contains no inherited zircons ([Figure 2.7e](#)), a precise unimodal distribution was obtained from 26 concordant ages where the dominant peak has a Toarcian Concordia age of 176.85 ± 0.63 and with an MSWD of 0.075 ([Figure 2.7f](#)).

- **Girón Formation: Samples LC-031 and LC-032**

Sample LC-031 yielded a total of 26 ages that vary from $200 \pm$ to 1600 Ma ([Figure 2.7g](#)). The distribution of the ages is multimodal, with two maximum peaks at 200 Ma and 460 Ma. The most representative group contains Late Triassic ages, with a Concordia age of 200.8 ± 1.9 Ma (Hettangian) and an MSWD=1.05 ([Figure 2.7h](#)). For the sample LC-032, a total amount of 14 grains were analyzed, with ages that range between 190 to 1500 Ma ([Figure 2.8a](#)). This yielded a multimodal distribution with a significant population of Early Jurassic ages, and with a Concordia age of 199.5 ± 1.8 Ma (Hettangian) ([Figure 2.8b](#)). Nevertheless, both samples have inherited ages from Precambrian and Paleozoic ages associated with metamorphism and magmatic events, respectively.

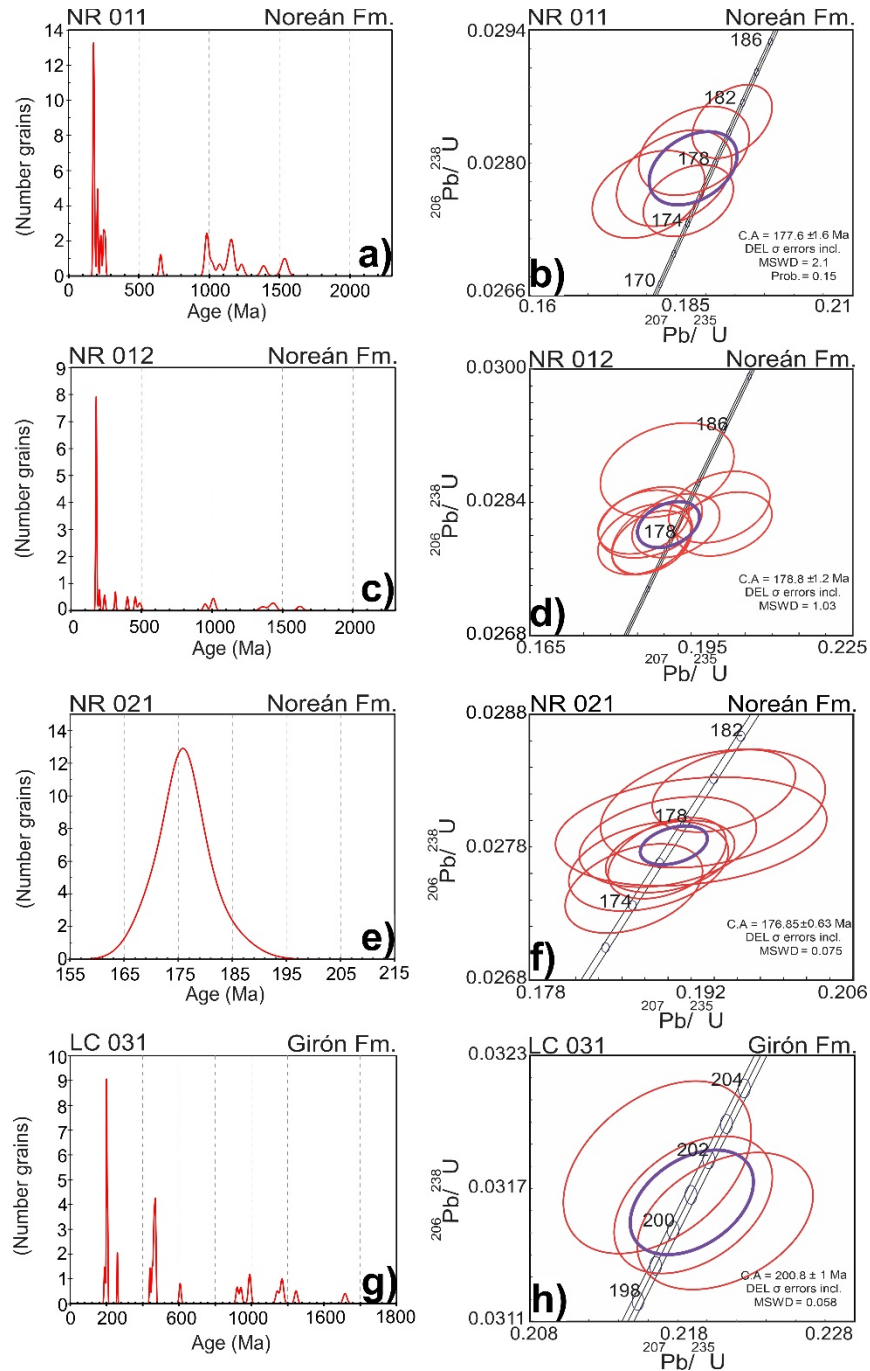


Figure 2-7. Wetherill concordia plots of zircon U-Pb results drawn by ISOPLOT. (Ludwig 2012) a) General concordia plot of the Noreán formation. b) Detail of the square concordia plot of [Figure 2.7a](#) for the Mesozoic ages of Noreán formation. c) Complete concordia plot with evidences of heritage. Noreán formation. d) Detailed concordia plot for the Mesozoic box in [Figure 2.7c](#) Noreán formation. e) Average age plot of the Noreán formation. f) Concordia plot of the Noreán formation. g) General concordia plot of the Girón formation. h) Detailed of the Mesozoic square box in [Figure 2.7g](#) Girón formation

- **Jordán formation: Samples JR-431 and JR-531**

The sample JR-431 contains a long prismatic zircon that was analyzed, and 23 ages were obtained with values between 190 and 205 Ma ([Figure 2.8c](#)), generating a unimodal distribution with a Concordia age of 195 ± 1.3 Ma (Sinemurian) ([Figure 2.8d](#)). Sample JR-531 includes an amount of 33 ages in a range between 185 to ± 1400 Ma ([Figure 2.8e](#)). The distribution is multimodal with a major population of Precambrian ages. Nevertheless, the presence of Mesozoic grains is also evident in which a Concordia age of 187.3 ± 2.5 Ma (Pliensbachian) and an MSWD of 1.0 was obtained ([Figure 2.8f](#)). This sample presents both Precambrian and Paleozoic grains.

- **La Rusia formation: Sample AR-451**

From sample AR-451, 30 ages were obtained in a range of $450 \pm$ to 1500 Ma ([Figure 2.8g](#)), with a multimodal distribution. With a significant population of Ordovician values, the Concordia age is recorded at 465.4 ± 3.3 Ma (Darriwilian) ([Figure 2.8h](#)). The older zircons with Precambrian and Paleozoic ages are related to metamorphism and magmatic events.

- **Montebel formation Sample AR-351**

For sample AR-351, a total of 50 ages were analyzed, with one age range between 440 and 1750 Ma ([Figure 2.9a](#)), which yielded a multimodal distribution with a significant peak of Ordovician ages. The Concordia age is 471.4 ± 2.0 Ma (Florian) ([Figure 2.9b](#)), with the oldest and youngest ages are associated with metamorphic and magmatic events, respectively

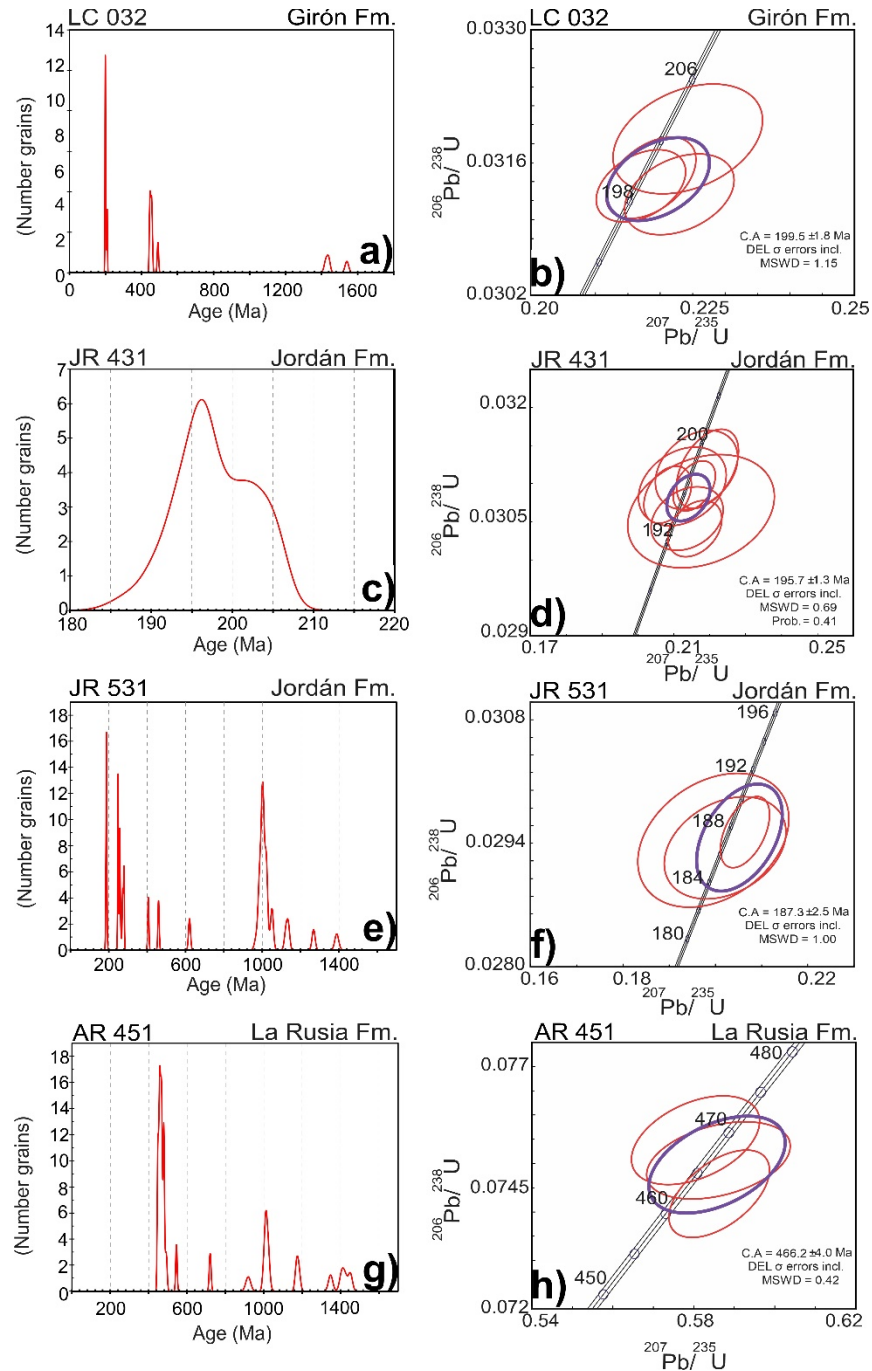


Figure 2-8. Wetherill concordia plots of zircon U-Pb results drawn by ISOPLOT (Ludwig 2012). a) General concordia plot of the Girón formation. b) Detailed of the square concordia plot of [Figure 2.8a](#), for the Mesozoic ages of Girón formation. c) Average age plot of the Jordán formation. d) Concordia plot of the Jordán formation. e) General Concordia plot of the Jordán formation. f) Detailed Mesozoic box of the Mesozoic box of [Figure 2.8e](#) Jordán formation. g) General concordia plot of the Rusia formation note the absence of Mesozoic grains. h) Detailed of the younger ages of [Figure 2.8g](#) Rusia formation.

• **Arcabuco formation Sample AR-222**

In the sample AR-222, 50 ages were obtained ranging from 370 to 1500 Ma (Figure 2.9c), with a multimodal distribution showing a significant peak of Ordovician ages. The Concordia age for this range is 466.0 ± 4.0 Ma (Darriwilian) (Figure 2.9d). The Precambrian and Paleozoic grains are related to metamorphic and magmatic events. According to Leal-Mejia et al. (2019) the basin experienced different pulses of Magmatism since the Early Paleozoic, moreover the shape and the evidence of fluids allow us to interpret the older grains as inherited material generated from metamorphic and magmatic events during the pre-Andean configuration.

The ages obtained were employed to define and constrain the magmatism and volcanism associated with the rifting stages. The integration of the geological information allows us to obtain a chronostratigraphic chart for the Mesozoic that includes the magmatic events in the study area (Figure 2.2).

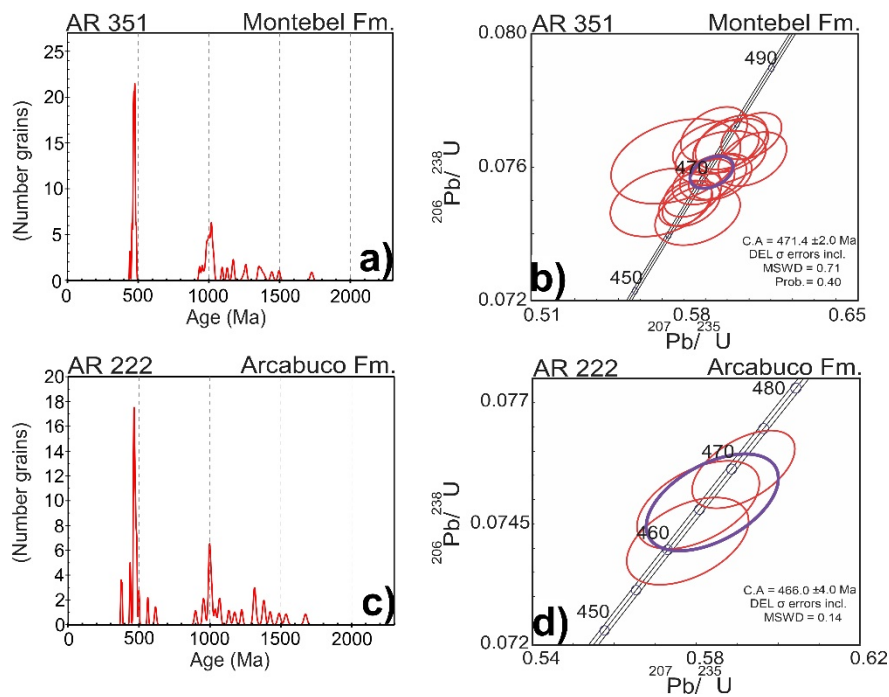


Figure 2-9. Wetherill concordia plots of zircon U-Pb results drawn by ISOPLOT (Ludwig 2012). a) General concordia plot of the Montebel formation. b) Detailed Concordia plot of the younger ages in the Figure 2.9a. Montebel formation. c) Concordia plot of the Arcabuco formation. d) Detailed concordia plot of the younger ages in Figure 2.9c. Arcabuco formation.

Structural cross-sections

We illustrate the main Mesozoic structural domains in four cross-sections constrained by outcrop and subsurface data. The cross-sections were constructed using the software MOVE (Petroleum Experts ©). The o

method employed for horizon construction was kink band extrapolation (Suppe, 1985) based on the simplicity of restoring the geometry. For restoration we employed the fault parallel flow and flexural slip unfolding algorithms. The kinematic restoration was calibrated using the thermochronological data published by Gomez et al. (2003, 2005), Mora et al. (2010), Parra et al. (2012), Caballero et al. (2013), and Moreno et al. (2013). However, in this chapter, only two stages will be shown; the present-day and the Cretaceous post-rift configuration. The cross-sections are described in the following paragraphs from north to south.

- **Noreán Region**

In the northeastern sector of the Middle Magdalena Valley basin, near the northern limit with the Eastern Cordillera, the boundary of the most important topographic expression is controlled by the La Morena and La Campana faults (Fig. 1b). In this region, the La Campana thrust forms the Andean front and divides the western foothills from the Middle Magdalena Valley basin. The La Campana is considered to be a basement-involved or thick-skinned structure, striking NW-SE. Moreover, we also interpret this fault as an ancestral normal fault that is inverted in contraction ([Figure 2.10](#)). In contrast, the La Morena fault is interpreted to be a bypass structure (e.g., Moreno et al., 2013) in the hanging-wall of the La Campana fault (i.e., we interpret the La Morena fault as sharing the same root at depth with the La Campana fault, but at shallower levels the La Morena fault evolves into an independent fault plane). The folds linked to the La Campana and La Morena fault are defined as long wavelength folds. At the present-day ([Figure 2-10a](#)), the eastern part of the cross-section is formed by structures with a decollement level along the Devonian sequence. The western part of the cross-section is characterized by a thin Cenozoic sedimentary sequence (less than 1100 m preserved in the Middle Magdalena basin). According to our kinematic restoration and interpretation, we consider La Campana fault reactivation as the structure that controlled the significant erosion in the eastern area. We infer that the eroded Cenozoic thickness was similar or greater than the total thickness preserved in the foreland. The Mesozoic sedimentary sequence is thickening to the east from ≈ 3500 to ≈ 7500 m. Nevertheless, the absence of Cretaceous sediments along the foothills prevents us from estimating the top of the rift-phase units. The La Campana and

La Morena faults are the thrusts that uplift and exhume the Jurassic and older deposits. The detachment level for these structures is assumed to be located at ≈ 20 km based on previous studies carried out in the northern segment of the Eastern Cordillera (Cooper et al., 1995; Tesón et al., 2013) and the kinematic restoration carried by Siravo et al. (2018), we also compared with previous works that constrained the depth to detachment in different areas of the entire orogen through seismic reflection and structural analysis (Cortes et al., 2006; Mora et al., 2008; 2015). The high levels of erosion in the northern region are linked to the orogenic pulses of the Central and Eastern Cordilleras along the northern Andes and the orogenic front migration (Sarmiento 2001; Gomez 2003; Mora et al., 2015; Mora et al., 2020). Based on our structural restoration ([Figure 2.10b](#)), the Noreán region started the extensional pulse coeval with the deposition of the Bocas Fm. (Early Jurassic) Moreover, according to the thicknesses and lithologic analyses, the basin experienced extension during deposition of the Arenal Fm. (Late Jurassic). We interpret the La Campana fault as the principal structure that controlled the basin development in this area. Significant subsidence occurred in the hanging-wall, and the footwall uplift is evident until the Late Jurassic. Nevertheless, we consider that new and more detailed mapping is needed to define the end of the rift phase in this region.

S1 Noreán Region

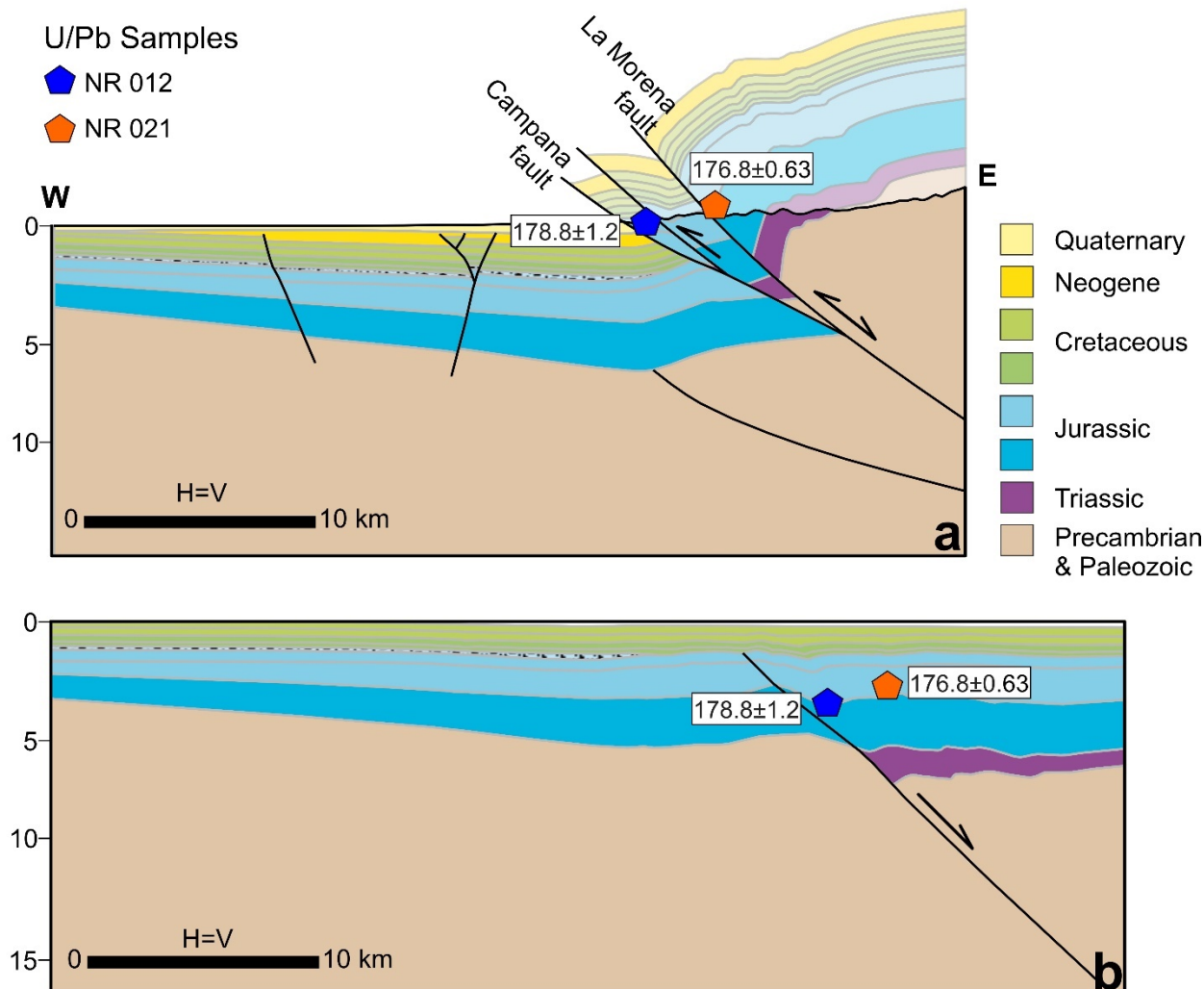


Figure 2-10. Balanced cross sections along the north study area in the Noreán Region from the La Morena fault to the Middle Magdalena Valley. Notice also the sample location illustrated through the pentagons. a) Structural cross section in the Northernmost part of the study area at present-configuration. b) Restored structural cross section (Figure 2.10a.) for the Late Cretaceous. Note the absence of sediments linked to the main unconformities (Miocene - Oligocene, Early Eocene - Late Paleocene, and Early Cretaceous)

- **Los Cobardes Region**

Located in the central part of the study area (Figure 2.1b), the cross-section traverses from northwest to southeast the Lisama buried anticline, the Nuevo Mundo syncline, and the Los Cobardes anticline (See location in Figure 2.1). The La Salina thrust forms the western front of the Eastern Cordillera. Thick-skinned and thin-skinned structures characterize the cross-section. The present-day structure (Figure 2.11a) shows that the basement of the Eastern Cordillera has been

uplifted on the top of La Salina and Suarez basement faults, with both interpreted as reactivated normal faults. This region is characterized by fault propagation folds and basement involved faults.

The shallower thick-skinned structures detach at Paleozoic levels and the thin-skinned roots are at Paleogene levels (Caballero et al., 2013; Moreno et al., 2013). Deeper basement involved faults can also be interpreted and they are rooted in intra-crustal levels that may eventually reactivate intra-crustal detachments at depths greater than 20 km (Figure 2.11).

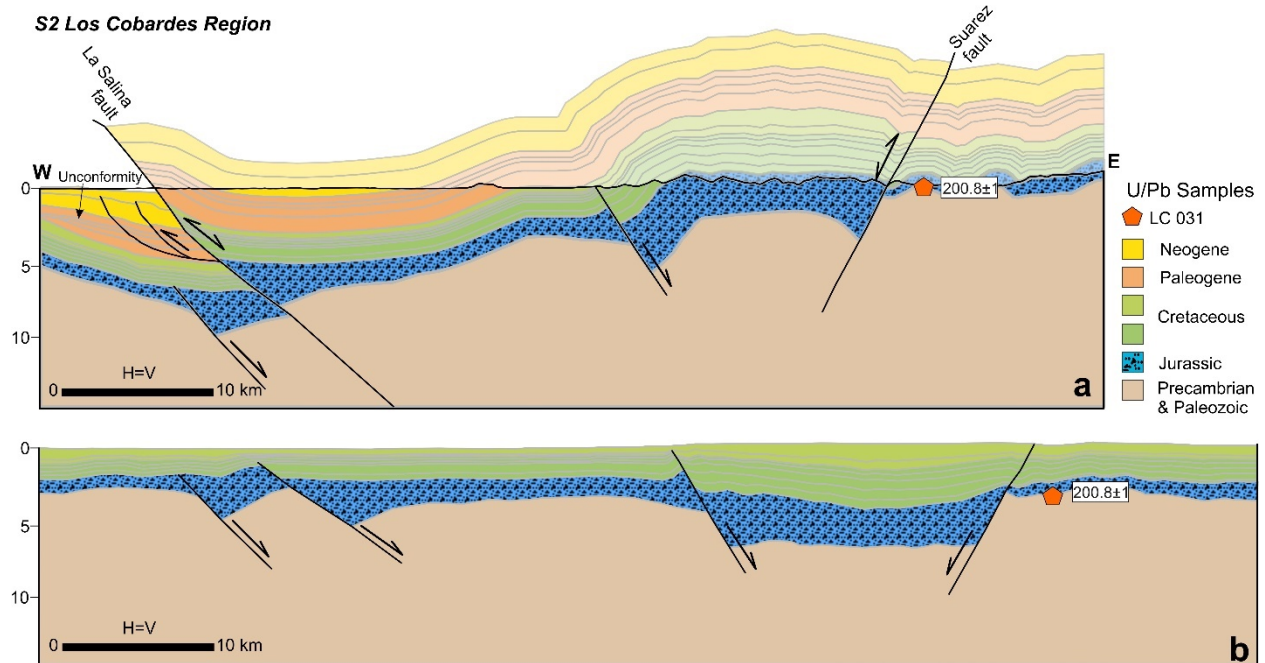


Figure 2-11. Balanced cross sections along the central part of the study area in the Los Cobardes Region from the footwall of the Suarez fault in the Eastern Cordillera to the Middle Magdalena Valley. From east to west Crossing the Los Cobardes anticline to the Nuevo Mundo Syncline. Note the sample location drawn through the blue polygon. a) Structural cross section in the central part of the study area at present-configuration. Notice the two main faults of La Salina and Suarez that control the fold geometry. b) Restored structural cross section (Figure 2.11a.) for the Late Cretaceous. Note the Mesozoic thinning to the west (Middle Magdalena Valley).

In this sector, the preserved strata increase compared to the Noreán region. The thick Cenozoic deposits preserved in the Middle Magdalena basin measure ≈ 5500 m. We assume a similar or greater amount of thickness in the eroded areas. Nevertheless, the Mesozoic values change considerably from the western to eastern areas from ≈ 2000 m to ≈ 9000 m respectively, and it is important to mention that the major depocenter occurred where the Los Cobardes anticline that is defined by Tesón et al. (2013) as a basement fold is currently located.

The principal structures that control the deformation are thick-skinned structures of the west-verging La Salina and the east-verging Suarez faults, interpreted as Mesozoic faults inverted during the Andean Cenozoic orogeny (Cooper et al. 1995; Samiento 2001, 2011; Kammer and Sanchez 2006; Sarmiento et al. 2006).

These thrust structures detached deeper than ≈ 20 km; they are responsible for initial Mesozoic basin development and the late stages of deformation and rock uplift in the Eastern Cordillera (Parra et al., 2012; Caballero et al., 2013; Moreno et al., 2013). Subsurface evidence and thickness variations identified by Gomez et al. (2003; 2005), Parra et al. (2012) and Caballero et al. (2013) show a Paleogene angular unconformity along the Middle Magdalena Valley with diachronous units above and below its surface, and the thinning to reach the total absence of rock units to the west of the Middle Magdalena Valley ([Figure 2.11a](#)). This unconformity is linked to the Late Paleocene to Early Eocene exhumation recorded by different thermochronometers (e.g., Parra et al., 2012; Caballero et al., 2013). However, previous positive relief (Late Cretaceous) could also be linked to the Central Cordillera front migration.

Based on our kinematic restoration ([Figure 2.11b](#)), we interpreted the La Salina and Suarez as Mesozoic normal faults. However, we interpret the presence of some non-reactivated Mesozoic structures, documenting a selective reactivation similar to what was suggested in the southern sectors of the Eastern Cordillera (Mora et al., 2006; Mora et al., 2009). According to the thickness distribution and the fault kinematics, we propose that the onset of rifting in this area occurred during the initial deposition of the Girón Fm. The evidence of significant subsidence in the Suarez and La Salina fault hanging-wall blocks was coeval to the pronounced footwall uplift of the adjacent fault blocks. Based on the Cretaceous sequence variations, we suggest the end of the rift to have happened by the Early Cretaceous.

- **Jordán Region**

The Jordán region is located at the core of the Eastern Cordillera ([Figure 2.11b](#)), ≈ 20 km away from the previously-analyzed Los Cobardes region. The cross-section crosses the eastern side of the Los Cobardes anticline and extends to the boundary of the Santander Massif.

The main structure along this cross section is the inverted Mesozoic Suarez fault. The main documented structural style is basement-involved deformation. The present-day configuration ([Figure 2.12a](#)) exposes the thick-skinned domain and the extensional non-reactivated faults to the

east, for example, the Aratoca fault (Julivert 1963). In this region, the Cenozoic strata are eroded, and according to Tesón et al. (2013), in the northern segment of the Eastern Cordillera, the exhumation is less than 7 km based on estimates of potentially removed amounts of overburden. The Mesozoic sediments are thickening to the west from ≈ 2500 to ≈ 9000 m in the major depocenter area (Figure 2.12b). Two main fault systems are implied in the basin development during the Mesozoic. Based on the cross-section restoration (Figure 2.12b), we proposed two different rifting events. The early rifting is linked to the Jordán Fm. deposition and is controlled by the non-reactivated normal faults. The next rifting stage is related to the Suarez fault development and started coeval with the deposition of the Girón Fm. The end of the rifting for the first event is probably associated with the Tambor Fm. based on the Aratoca fault activity discussed by Julivert (1963) and the geological map relationships. According to the thickness variations, we inferred that extension along the Suarez fault plane and accommodated by hanging-wall subsidence ended during the Early Cretaceous.

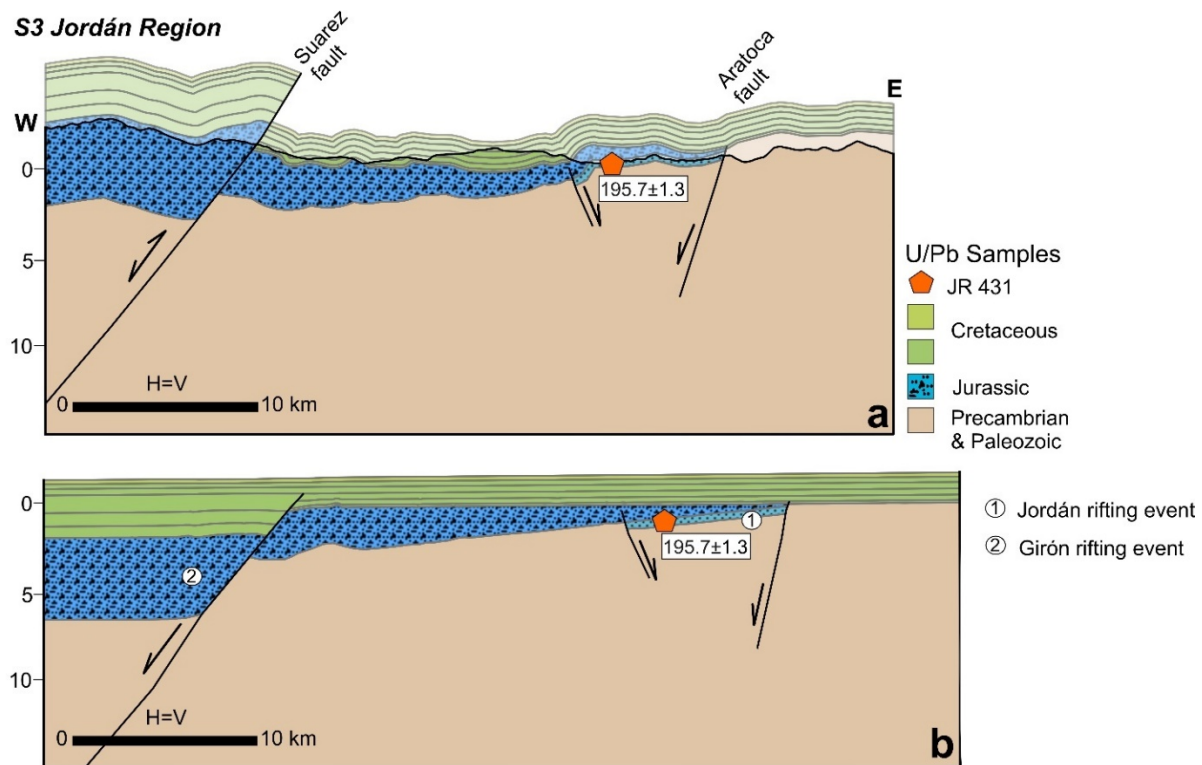


Figure 2-12. Balanced cross sections along the central part of the study area in the Jordán Region along the Chicamocha canyon. From east the Aratoca paleo-fault to the hanging-wall of the Suarez fault in the Eastern Cordillera. Note sample location drawn through the blue pentagon. a) Structural cross section in the Jordán Region at present-day configuration. Notice the blind normal fault and the Aratoca paleo-fault as boundaries of the Jordán Fm. b) Restored structural cross section (Figure 2.12a.) for the Late Cretaceous. Note the Mesozoic thinning to the east.

- **Arcabuco Region**

The southernmost cross-section analyzed in this work is located in the eastern region of the Magdalena Tablazo and the Tunja Sogamoso sub-basins (Figure 2.1b). The structural cross-section crosses the Arcabuco and Floresta anticlines from east to west, while the section is located in the Eastern Cordillera axial zone. The main structures that controlled the folding are linked to the Boyacá and Suarez faults (Kammer and Sanchez 2006). The cross-section is characterized by its thick-skinned deformation (Figure 2.13a). The Boyacá and Soapaga east-verging faults strike NE-SW, and are interpreted as Mesozoic inverted faults with a strike-slip influence linked to the Santa Marta Bucaramanga fault (Cooper et al. 1995; Kammer 1999; Kammer and Sanchez 2006; Sarmiento et al. 2006). The Arcabuco anticline (Figure 2.13 see location in Figure 2.1) is a first order fold controlled by the Boyacá fault, these folds are basement involved structures highly controlled by the Mesozoic extensional faults in their present configuration. (Kammer and Sanchez 2006; Tesón et al., 2013). Basement involved folding west of the Soapaga fault (Fig. 13, Floresta Antiform) has been interpreted as related with a buttressing effect associated with the Soapaga footwall block prior to the movement along the Soapaga fault (Kammer, 1996. Figure 2.13). The preserved Cenozoic strata in the Floresta region could reach ≈ 2200 m including the Middle Eocene. According to thickness estimations, ≈ 4000 m is the difference between the hanging wall and footwall blocks along the Boyacá fault (Tesón et al., 2013). We interpreted the Boyacá and Soapaga faults as thick-skinned structures detached at a deeper level than ≈ 25 km. Based on our kinematic restoration and Mesozoic rock units present in this region (Figure 2.13b), we defined two rifting events. The initial phase is related to the Boyacá fault, and probably started during the deposition of the Palermo Fm. The younger rifting is linked to the Soapaga fault and is limited locally by one structure to the west. The last phase began coeval with the Girón Fm. deposition.

The tentative end of rifting in the Arcabuco region is determined according to the thickness variations of the Early Cretaceous rock units e.g., Cumbre Fm. where near to the Arcabuco anticline the thickness varies from 129 m to 150 m (Renzoni 1967; Pulido 1985), moreover the lithological variations from the Arcabuco Fm. a deltaic rock unit to shallow marine rock unit Cumbre Fm. allow us to infer and consider the end of rifting to have happened by the end of the Early Cretaceous. So far, we have no conclusive evidence for the end of the Mesozoic rifting. For all of these we recommend to conduct new stratigraphic measurements and lithological analysis of the Cretaceous rock units to support or restate this hypothesis.

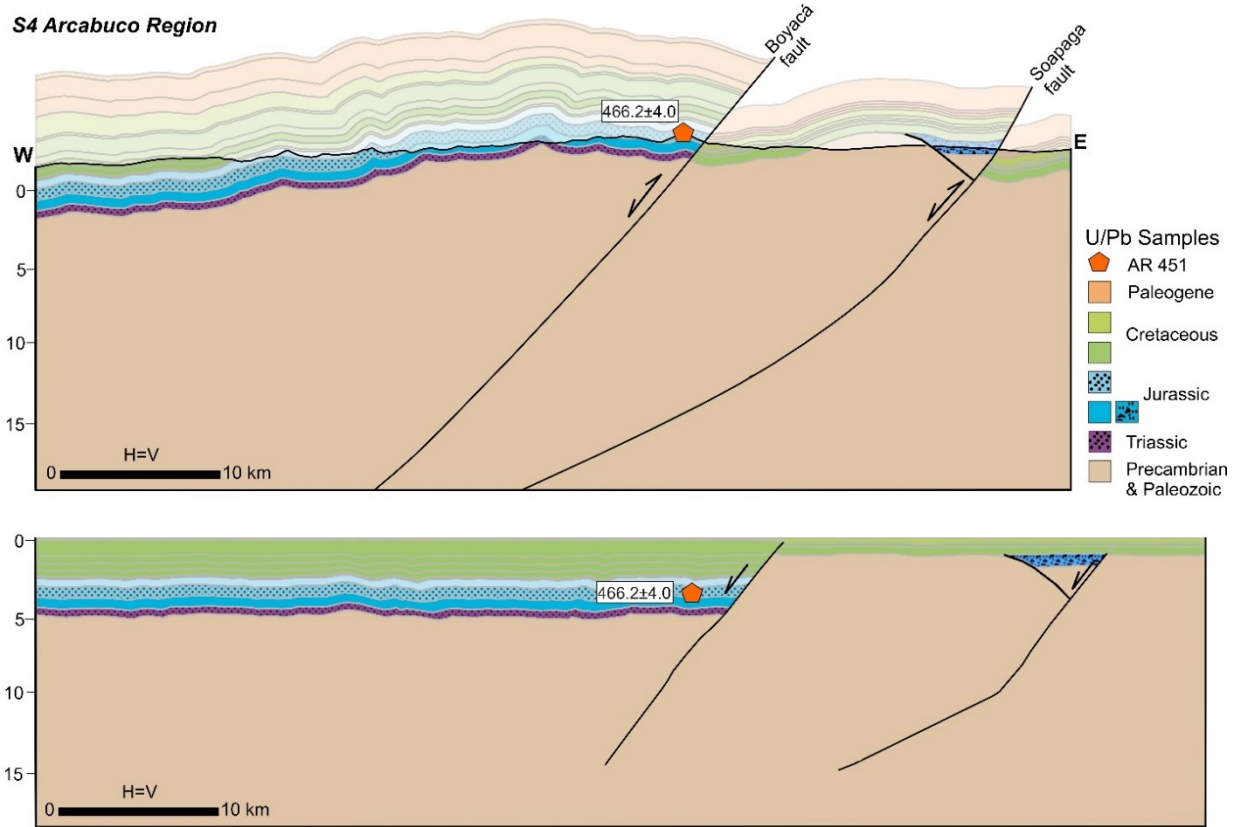


Figure 2-13. Balanced cross sections along the southern part of the study area in the Arcabuco Region. From west the Boyacá fault to the east the Soapaga fault. Notice sample location is illustrated through the blue polygon. a) Structural cross section at present-day configuration. Notice the blind normal fault to the hangingwall of the Soapaga fault, and the Mesozoic absence to the western area. b) Restored structural cross section (Figure 2.13a.) for the Late Cretaceous.

Discussion

The new data collected in this work and the integration with the previous results regarding the surrounding Eastern Cordillera and Middle Magdalena basins allow us to generate a Mesozoic conceptual evolutionary model for the study area. The model includes the magmatic events and the relation between the initial extension and magmatism in the Eastern Cordillera and Middle Magdalena Valley.

Geochronological dating significance

The age of 200.8 Ma obtained from the volcanoclastic sample LC-031 in the Girón Fm. represents a crystallization age for this unit. However, this sample contains Late Triassic crystals assumed in this paper to be the older ages related to the extensional event along the Eastern Cordillera. These ages are linked to the oldest population found in the Eastern Cordillera, and are attributed to the initial magmatic event.

As shown in the cross-section from the Los Cobardes region ([Figure 2.11a](#) and [Figure 2.11b](#)), the sample LC-031 was collected from the footwall of the Suarez fault. The age interval between 190-205 Ma obtained in the Los Cobardes region correlates with the age of crystallization of the quartz monzonites of La Corcova (202.7 ± 1.2 Ma) (Rodríguez et al. 2017a), Agua Blanca (201 ± 3.6 Ma) (González et al. 2015), and Mogotes (202.5 ± 1.3 Ma) (Correa-Martínez et al. 2016). It also correlates with the rhyolite of Los Cacaos (205.2 ± 2.6) (Correa-Martínez et al. 2018). The Late Triassic-Early Jurassic ages from the Girón Fm. that match with the age of crystallization and geochemical signature of the plutonic bodies, illustrate the relationship of the deposition of the Girón Fm. with the tectonic domain.

In the Jordán Fm. the crystallization ages from the volcanic rocks range from 187 to 200 Ma, contemporaneous with the age of crystallization of the quartz monzonites of Pescadero (Zapata et al. 2016) and Rionegro (Arango et al. 2016), the granodiorites of Rionegro (Arango et al. 2016), Guamoco and Norosí (González et al. 2015), the La Malena dacite (González et al. 2015), and the tonalite of San Martín (Rodríguez et al. 2017b). The samples from the Jordán Fm. were collected in the Chicamocha canyon and the sample JR-431 is located in the hanging wall of the fossilized Aratocha normal fault as shown in the cross-section ([Figure 2.12a](#) and [Figure 2.12b](#)).

The ages for the Noreán Fm. in the northernmost study area range from 178 to 176 Ma. No plutonic rocks are exposed in the Eastern Cordillera and Middle Magdalena Valley.

Chapter 2. Onset and Style of Mesozoic extension in the EC and MMV

For the Arcabuco, La Rusia and Montebel Fms. the ages obtained are Lower and Middle Ordovician from the Arcabuco anticline. The samples were collected from the Arcabuco anticline in the hanging-wall of the Boyacá fault, evidenced in the cross-section ([Figure 2.13a](#) and [Figure 2.13b](#)). In these samples, no Mesozoic grains were found.

Two tectonic models have been proposed for the evolution of the Jurassic and Early Cretaceous along the northwestern Andes in Colombia. The first model suggests the development of an intracontinental rift, supported by paleogeographic reconstructions based on structural and stratigraphic data (Cediel et al. 2003; Pindell and Kenan 2009), while the second model, based on geochemical and petrographic analysis, suggests that extension is subduction related and therefore defined as a back arc extension (Maze 1984; Aspden et al. 1987; Toussaint 1995; Bayona et al. 2006; Villagómez et al. 2011; Cochrane et al. 2014; Bustamante et al. 2016; Zapata et al. 2016).

The sedimentary Mesozoic infill along the Eastern Cordillera and Middle Magdalena Valley basins is associated with the geometrical distribution controlled by the main Mesozoic rift structures (Mora et al. 2009).

Regarding the Upper Triassic age (200.8 ± 1 ; sample LC-031) obtained within the Girón Fm. ([Figure 2.7h](#)), we hypothesize that the syn-kinematic character of the Girón Fm. and the stratigraphic location of the sample (within the middle to lower segments of this unit, Figs. 2 and 11) suggest that this age post-dates the onset of rifting, all of these based on the fluvial and alluvial environment that is attributed to the development of the Mesozoic normal faults.

The Lower Jurassic ages (195.7 ± 1.3 Ma) obtained from samples within the Jordán Fm. ([Figure 2.7d](#), see sample JR-431 in Fig. 2 and Fig 12) are interpreted as corresponding with the continuation into the Jurassic of this initial rifting event within the Eastern Cordillera, because of the following evidence, the pyroclastic deposits of red tuffs deposited in the Jordán region with the same geochemical signature of the main magmatism for the Lower Jurassic, moreover, the continental environment, the coarse grain variations between the conglomeratic deposits from the Girón Fm and the red tuffs and mudstones from the Jordán Fm.

The value obtained in the Noreán Fm. refers to the top of the Lower Jurassic ([Figure 2.7b](#)).

The samples NR-011 (177.6 ± 1.6 Ma), NR-012 (178 ± 1.2 Ma) and NR-021 (176.8 ± 0.63 Ma), are located to the northeast of the Middle Magdalena Valley ([Figure 2.1b](#)). The samples are considered to be related with units associated with the northeastern continuation of the rifting in the Eastern

Cordillera and Middle Magdalena Valley basins during the deposition of the uppermost Lower Jurassic units. We can infer the possible tectonic setting throughout the basin as related with the distribution of the plutonism through time and changes in composition ([Figure 2.14](#))

1. Rhaetian – Hettangian (208.5-199.3 Ma)

The presence of volcanic rocks synchronic with plutonism characterizes the Late Triassic and Early Jurassic in the study area. This is considered to be the product of the Farallon plate subducting beneath the South American plate. (Pindell and Kennan 2009)

The distribution of this plutonism along the basin is primarily associated with the Santa Marta – Bucaramanga fault strike to the south where the main Rhaetian plutonic bodies are located, such as the Corcova, Mogotes and Aguablanca. The crystallization ages vary from 201 to 205 U/Pb and have been principally described as quartz monzonites, with S- and I-type granites. (González et al. 2015; Correa-Martinez et al. 2016; Correa-Martinez et al. 2018; Rodriguez et al. 2017a) ([Figure 2.14](#)).

According to Whalen et al. (1987) and Frost et al. (2001), when the majority of plutonism is dominated by granite type I, this is a main characteristic of a magmatic arc. Furthermore, the presence of type S granite allows us to interpret this as the product of the fusion of continental crust. The content of SiO₂ in all the bodies oscillates between 55 to 77%. These features are typical of a magmatic arc, although the different ages obtained in the dikes and intrusions suggest that they were generated by multiple pulses (Rodriguez et al. 2017a).

The sample LC-031 was collected from the basal strata of the Girón Fm. (Fig. 11) and thus the crystallization age for the volcanoclastic sample suggests that sedimentation and volcanic activity related to the extension was ongoing at 200 Ma in the northern axial zone of the Eastern Cordillera. We consider that this was the initial stage of rifting in the study area ([Figure 2.15a](#)).

Nevertheless, the relatively small thickness of tuff layers in the thick conglomeratic fluvial deposits suggests that most of this volcanism originated from activity far from the site of deposition, that prevented a unimodal distribution in the magmatic zircons. Conversely, this formation is characterized by high energy deposition with conglomerates deposited in a fluvial environment and due to this we can infer that most of the magmatic zircons were eroded and lost.

In the structural cross section ([Figure 2.11](#)) we can observe the major differences between the syn-rift deposits specially in the hanging-wall of the Suarez Fault, where the thickness of the Girón Fm.

was measured in the field and it was estimated to range from 3350 m to 4500 m (Osorio-Afanador and Velandia 2021; Cediell 1968) compared to the footwall thickness that decreases to the 20% of the total amount preserved in the hanging wall block. Westward, in the hanging-wall of the La Salina Fault the thickness variation is constrained from the axial zone of the Los Cobardes anticline (Fig. 1b) where the syn-rift Girón Fm. has a thickness that range between 2250 m to 1400 m (Navas 1963 and Julivert 1958). To the west in the Middle Magdalena Valley based on seismic reflection and structural cross sections we inferred a total thickness of syn-rift units for the footwall of the La Salina Fault which range between 1500 m to 500 m.

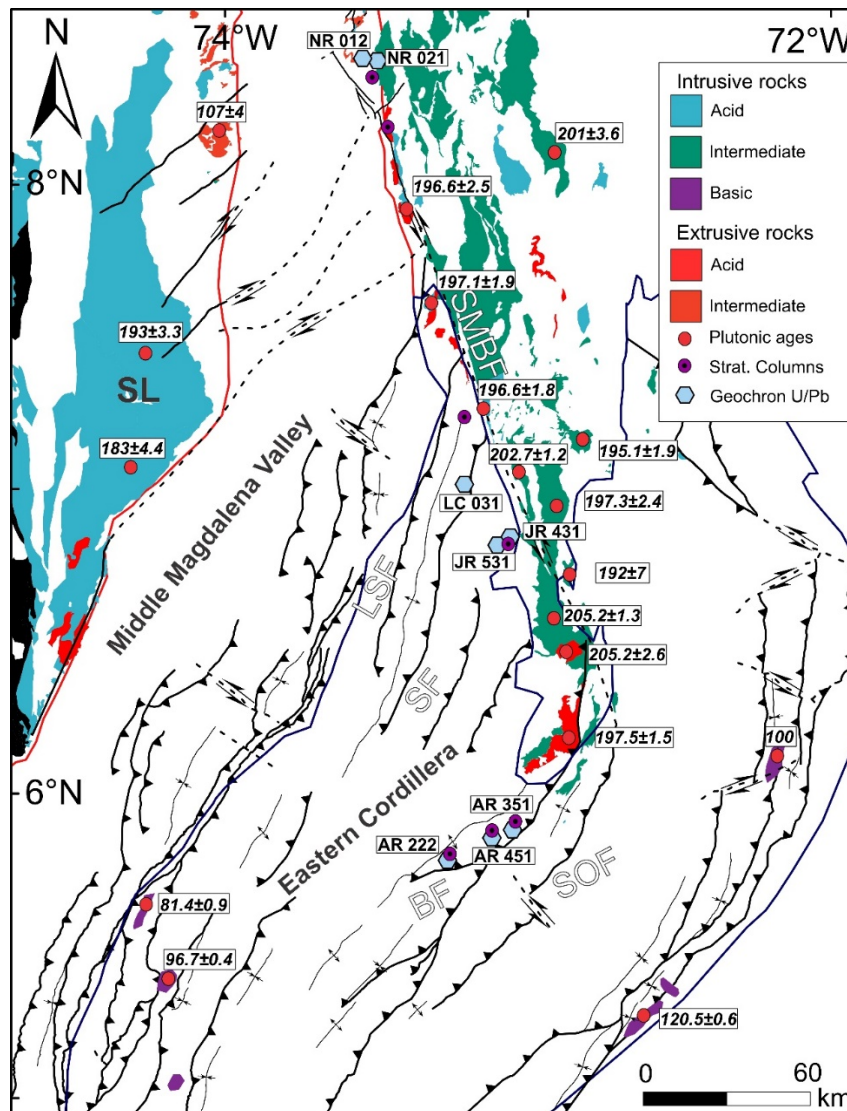


Figure 2-14. Mesozoic magmatic bodies of the Eastern Cordillera and Middle Magdalena valley (after Bayona et al. 2020; Rodriguez-Garcia et al. 2020). Note the alignment of intrusions parallel to the strike of the Bucaramanga-Santa Marta strike slip fault (SMBF). See [Figure 2.1](#) for abbreviations of sub-basins in the Eastern Cordillera as well as folds and faults.

2. Sinemurian – Pliensbachian (199.3-182.7 Ma)

The major density of plutonism in the Eastern Cordillera and Middle Magdalena Valley occurred during Sinemurian-Pliensbachian according to the U/Pb ages obtained by (González et al. 2015; Arango et al. 2016; Zapata et al. 2016; 2018; Rodriguez et al. 2018) on the diverse Early Jurassic magmatic bodies. Most of the Early Jurassic plutons are aligned with the main structural feature of Santa Marta-Bucaramanga strike slip fault. Still, large plutons are also present on the western side of the Middle Magdalena Valley. Based on this observation and according to Wilson (1993), the geometry of the slab probably affected the amount of magma generation ([Figure 2.15b](#)). The majority of the bodies during the Sinemurian are associated with type I granites, where some of them present variations to type S, and can be classified as quartz monzonites and monzogranites like the Pescadero, Santa Barbara, Rionegro and Norosí, described by González et al. (2015), Arango et al. (2016), Zapata et al. (2016) and Rodriguez et al. (2018) respectively (Fig 14). The plutons are characterized by SiO₂ contents that oscillate between 61% to 78%. Rodriguez et al. (2018) suggests that the origin of this plutonism must be related to a typical magmatic arc where the continental crust plays an important role. Furthermore, the presence of the San Martin tonalite (Rodriguez et al. 2017b) and El Uvo Rhyolite (Zapata et al. 2018), defined as type I granites with variations to type S, allow a correlation between the plutonism for that time with a magmatic arc associated with a subduction zone where the slab angle increases ([Figure 2.15b](#)). Following work from Arango et al. (2016), all the rocks were generated from the partial fusion of the continental crust under oxide conditions. During the Pliensbachian, the plutonism recorded a decrease of the number of plutons to two principal bodies, Granodiorite of Guamoco (González et al. 2015) and La Malena Dacite (González et al. 2015), principally located to the western side of the study area. These plutons are categorized as I-type granites, with the content of SiO₂ ranging from 58 to 70% and related to the plutonic event in the eastern border of the Central Cordillera (González et al. 2015).

The Jordán Fm. was defined as Sinemurian based on the U-Pb ages obtained from the welded tuffs (Alarcón et al. 2020) The new samples from this study with suggested Sinemurian to Pliensbachian age from the Jordán Fm. show two ages between 187 and 200 Ma, which supports the age proposed by Alarcón et al. (2020). In sample JR-431 from the welded tuffs layer, the age value is 195±1.3 Ma. According to the stratigraphic position and structural evidence (Fig. 12a), the Jordán Fm. underlies the Girón Fm. in this location.

Possible explanations for the older ages obtained from the Girón Fm. include: (1) a volcanoclastic origin that would imply that: the older ages in the younger stratigraphic deposits of Girón in the hanging wall of Suarez fault may suggest that the sample dated in this work comes from a volcanoclastic deposit that reworked older volcanic material. This interpretation is consistent with the absence of glass and the increase of quartz in the mineralogical composition, in contrast with the welded tuffs that contain glass matrix and typical pyroclastic texture. (2) The Jordán Fm. is a lateral equivalent of part of the Girón Fm. As the ages were obtained on samples from different locations, the Jordán Fm. could represent laterally equivalent facies within the Girón Fm., rather than an older unit underlying it. The Jordán unit was probably deposited associated with a structural high within the basin, and in the area where the Girón Fm. was deposited, the basin experienced major subsidence at a structurally deeper point ([Figure 2.2](#)).

The older zircon values obtained for the Girón Fm. suggest that it is stratigraphically older than the Jordán Fm. Therefore, this impedes the generation of a definitive conclusion about their stratigraphic relationship. We consider that the sample of Girón is associated with volcanoclastic material that contains different grains from diverse sources, where the Mesozoic population could be attributed to the Rhaetian plutonism. In contrast, the sample from the Jordán Fm. is classified as a welded tuff and interpreted as the age of crystallization of this volcanic material in the study area. Nevertheless, the idea of integrating the Jordán inside the Girón as sub-member is still reliable and requires more stratigraphic information to confirm.

The cross section in the Chicamocha canyon ([Figure 2.12](#)) the Suarez Fault is illustrated once again in [Figure 12](#) as an inverted Mesozoic normal fault since it clearly controls thicker syn-rift units of the Girón Fm. (Rhaetian – Hettangian) to the west versus coeval units of the Jordán Fm. to the east. The presence of thicker units west of the Suarez Fault cannot be extrapolated from the cross section in [Figure 2.12](#) directly but the observed thickness in [Figure 2.12](#) is a projection to the cross-sectional plane from along-strike observations. Moreover, the very coarse grain size of the Jurassic units west of the fault suggests a short transport distance and therefore provenance from nearby topographic highs.

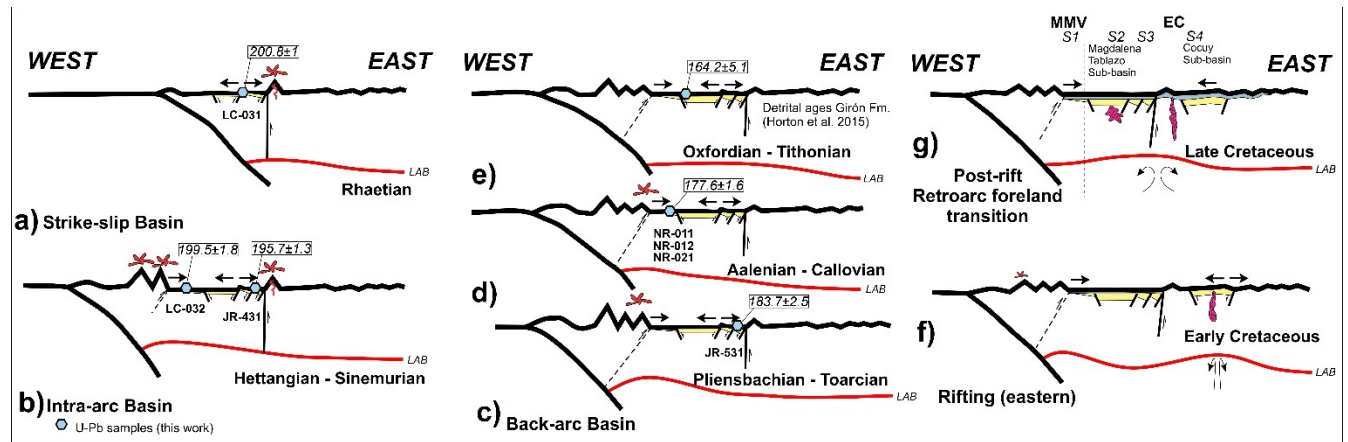


Figure 2-15. Tectonic evolution model for the Late Triassic to Late Cretaceous in the Northern Andes of Colombia. Illustrates the migration of the magmatic arc and the depositional environment in the Eastern Cordillera. see [Figure 2.2.](#) to the conventions of the sedimentary environments. Inspired in the tectonic evolution image style of Horton et al. 2010. The sample and cross sections are located in a regional scale.

3. Toarcian (182.7-174.1 Ma)

During this time, plutonism declines along the Eastern Cordillera and Middle Magdalena Valley. Nevertheless, according to Rodriguez-Garcia et al. (2020), small plutonic bodies of this age range occur in the south of Sierra Nevada de Santa Marta and north of the San Lucas range ([Figure 2.14](#) and [Figure 2.15c](#)). The samples analyzed in the Noreán Fm. belong to volcanoclastic deposits. Sample NR-012, located at the bottom of the sequence in the hanging wall of the Campana fault, has an age of 178.8 ± 1.2 Ma. The Sample NR-021 is recorded at 176.85 ± 0.83 Ma for the tuffaceous layer located at the top of the sequence in the hanging wall of the La Morena fault ([Figure 2.10a](#)). We interpret these ages as crystallization ages constraining the age of the Noreán Fm. A rough sedimentation rate of ~ 655 meters per million years is estimated based on the sample stratigraphic positions and the cross-section evidence.

In the cross section ([Figure 2.10](#)) we suggest a conceptual model of the Mesozoic rifting evolution of the Noreán region. According to the geological map and the unconformities exposed in the western border of the Middle Magdalena Valley, we inferred that the La Campana fault served as border fault that control the deposition of the Triassic rock units.

4. Middle Jurassic – Late Jurassic (174.1-145 Ma)

During the Middle Jurassic, the amount of plutonism decreased considerably in the Eastern Cordillera and Middle Magdalena basins. However, the Segovia (González et al. 2015) and Ibagué (Vesga and Barrero 1978; Bustamante et al. 2016) batholiths located in the Central Cordillera are categorized as two plutons of intermediate to acid composition ([Figure 2.14](#)), with a percentage of SiO₂ between 41 and 67 %, which are related with a magmatic arc as a result of a subduction zone domain with crustal contamination. This Volcanism has been described as a product of a back-arc extension (Aspden et al. 1987) ([Figure 2.15d](#)).

For the Late Jurassic, the plutonism ceases, and this change is argued by Bustamante et al. (2016) to be a consequence of oblique convergence, that generated a magmatic arc controlled by transtensional stresses ([Figure 2.15e](#)). This magmatic lull could be attributed to external events such as the break-up of Gondwana and its plate arrangement (Paterson and Ducea, 2015). Besides, tectonic processes such as shortening, underthrusting of the upper crust into the lower crustal arcs, thickening, exhumation, sedimentary erosion and magmatic flare-ups (DeCelles et al., 2009) are elements that could explain the magmatism lull in the Eastern Cordillera and Middle Magdalena during the Middle Jurassic and Late Jurassic.

5. Early Cretaceous – Middle Cretaceous (145.5-80 Ma)

At this time in the Eastern Cordillera and Middle Magdalena Valley, small mafic bodies have been reported by Vasquez and Altenberger (2005), and Vasquez et al. (2010). The mafic bodies include the Rio Nuevo, Pajarito, and the Rodrigoque and Rio Cravo Sur micro gabbro's ([Figure 2.14](#)) in the Cocuy sub-basin (Sarmiento 2001). Other reported magmatic bodies include the Rio Guacavía diorite, the Pacho gabbro, the Cáceres Puerto Romero intrusive, and the La Corona intrusive to the south of the Magdalena Tablazo sub-basin ([Figure 2.15f](#) and [Figure 2.15g](#)). According to Vasquez and Altenberger (2005), these mafic rocks vary from centimeters to meters with an SiO₂ content of 44 to 55%. Furthermore, the magmatism evolves from alkaline to tholeiitic. Based on the stratigraphic relations with the intrusives, the emplacement occurred during the Middle Cretaceous (Vasquez and Altenberger 2005) that coincides with the maximum stretching stage in the Eastern Cordillera (Sarmiento 2001). The genesis is supported by the enrichment of the mantle source to

the east and the contamination of the mantle region to the west, endorsed by the scarcity and abundance of metasomatized fluids (Vasquez and Altenberger 2005).

Nevertheless, in the northern side of the Middle Magdalena Valley, for a rock unit defined by Mantilla et al. (2006) as the Las Brisas extrusive, composed of porphyritic rocks with composition from diorite to andesite, K-Ar ages of 107 ± 4 Ma were obtained, corresponding to the Albian. This age and the documented variations in the magmatism, allow us to infer that these bodies were associated with a subduction setting that was probably linked to a magmatic arc. Nevertheless, more information and new fieldwork are required to further our understanding of the genesis of this unit.

6. Zircon Recycling

The volcanoclastic samples analyzed for the La Rusia and Montebel Fms. in the Arcabuco Anticline and the detrital sample in the Arcabuco unit ([Figure 2.13a](#)) were previously classified as Jurassic units according to their stratigraphic relations (Renzoni 1967). Nevertheless, the samples described in this work did not yield Mesozoic ages, and most of the values are related to Lower and Middle Ordovician ages. During the Early Ordovician the peak of the Caparonesis orogenic episode in South America occurred. At the end of this event during the Late Ordovician low to medium metamorphism occurred (Cediel 2019). However, the magmatism exposed during this time in the Eastern Cordillera is considered to be a product of a magmatic arc due to the subduction of the Pacific plate beneath South America (Van der Lelij et al. 2016; Cardona et al. 2016).

According to Leal-Mejia et al. (2019), the basin has experienced different pulses of Magmatism since the Early Paleozoic. Moreover, the shape and the evidence of fluids allow us to interpret the older grains as inherited material generated from metamorphic and magmatic events during the pre-Andean configuration.

To explain the absence of Mesozoic ages in the Jurassic units, we consider three hypotheses: (1) Dominant old source. According to the geographical distribution of the Triassic-Jurassic plutonism, and with the grain properties of each sample, we infer a possible re-working during the flow transportation which removed the signal from Mesozoic sources and created a predominance of old ages. (2) Magmatic inheritance is supported by the proportions of the age populations, where zircon crystals yielding Ordovician ages amount to as much as 90% of the analyzed populations and most crystals present magmatic geometries. Also, the contemporaneous plutonism in the study

area reflects similar zircon inheritance patterns, and High K calc-alkaline origin and negative EpsNd (Rodríguez-García et al. 2020). The Floresta massif (Ordovician) located in the axial zone of the Eastern Cordillera is the nearest magmatic Ordovician source of the Mesozoic magmatism in the region of the Arcabuco anticline.

(3) Based on its geometry and location the Arcabuco anticline can also be linked to the Floresta massif. The Permian-Triassic orogen is limited by the Boyacá fault (Tesón et al. 2013), while the southernmost part of the Arcabuco anticline is parallel to the trend of the Floresta massif in the east ([Figure 2.1b](#)) (Kammer and Sanchez 2006). This feature is observed to be a Late Paleozoic rift event and could also potentially be linked to the Ordovician – Devonian intrusives (Kammer and Sanchez 2006). The absence of volcanic Mesozoic grains suggests that this material comes from the Ordovician magmatic bodies of the Floresta Massif. We interpreted the Floresta Massif as part of the rift shoulders and the main material source of the Mesozoic volcanoclastic units in the Arcabuco region. However, to confirm the idea and constrain the evolution of the Arcabuco anticline, it is necessary to increase the detail of sampling to identify Mesozoic populations

In terms of extensional events and based on the values obtained during this work that refer to the Girón Fm. and the previous detrital analysis obtained by Horton et al. (2015) in the Middle Magdalena Valley, we interpret the onset of an extensional event in the northern region of the Eastern Cordillera in the Magdalena Tablazo sub-basin to have occurred during the Late Triassic. Additionally, the thickness variations and lithology are principally dominated by thick conglomerates and red bed layers, which are characteristic of a rift setting. According to the thermal subsidence of Sarmiento (2001), the Magdalena Tablazo sub-basin experienced extension until the Hauterivian. In the Middle Magdalena Valley, the analysis at the Noreán unit allowed us to infer that the extensional event started in the Early Jurassic.

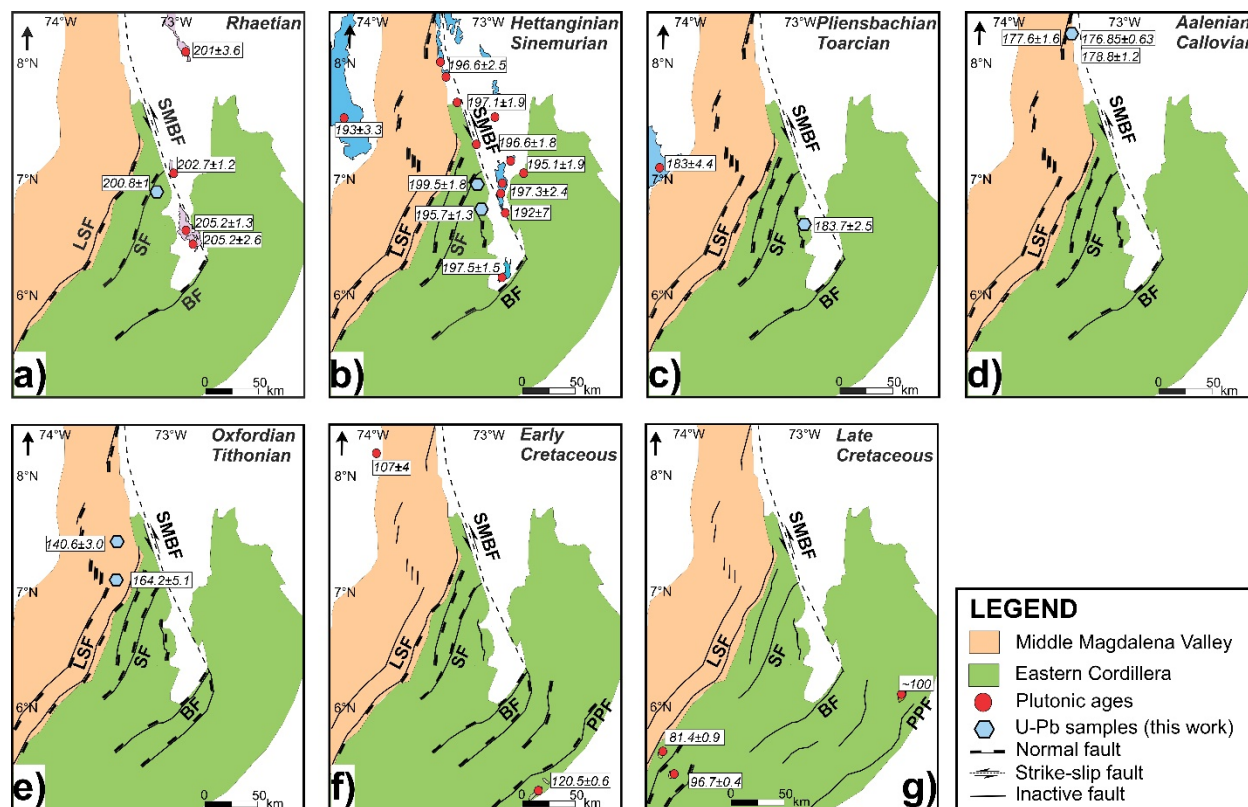


Figure 2-16. Mesozoic paleo structural maps of the Eastern Cordillera and Middle Magdalena Valley. Illustrates the development of the extensional structures as La Salina (LSF), Suarez (SF), Boyacá (BF), Paya-Pajarito (PPF) through the Mesozoic, the relation with the plutonism and the strike slip fault of Santa Marta Bucaramanga Fault (SMBF). The light blue hexagon reflects the geochronology samples dated in this work. Line faults without symbology show the inactivity for each time.

The ages obtained in this work from the Arcabuco anticline prevent the generation of extensional chronology in this area. The cross section in [Figure 2.13](#) illustrates that the absence of Jurassic and Triassic rock units east of the Boyacá Fault suggest that of coeval rock units (Jura-Triassic) west of that fault, are syn-rift units, where even these basal formations are preserved. However, the stratigraphic and field analysis carried by Kammer and Sanchez (2006) established that the Boyacá fault is a structure linked to a horsetail from the Bucaramanga fault, and the rifting activity occurred during the Late Triassic to Early Jurassic. Nevertheless, we consider that additional analysis in this area may allow researchers to refine the timing of the proposed extensional events.

At the southeastern region of the Eastern Cordillera Mora et al. (2006, 2009) suggest an Early Cretaceous (Berriasian to Barremian) age of rifting based on stratigraphic and structural

relationships. However, there is no evidence of older rift events in this structural domain (e.g., Mora et al., 2013).

Based on the structural analysis and new ages obtained in this paper, combined with those in previous studies, we present the distribution of the structures during the Mesozoic (Figure 2-16) since the Rhaetian, where a rift domain started in the Eastern Cordillera to the north of the basin (Figure 2-16a). The migration is apparently related with the magmatic activity that moved to the west and the structures that developed to the east of the magmatic arc during the initial events. However, the Cretaceous rifting development is mainly localized to the south and northeast of the Eastern Cordillera, while mafic magmatism is present in the paleo grabens (Figure 2-16f and Figure 2-16g).

In accordance with these observations, we infer two origins for these extensional events during the Cretaceous: 1) Back-arc widening, inferred based on the presence of the andesitic flows of the Las Brisas dated by Mantilla et al. (2006). As a result, this unit requires more studies to establish the chronology and redefine the origin. The mafic plutonism is the product of stretching as a consequence of the mechanical interaction. In general, this setting aligns more with the Early Cretaceous. 2) Different rifting regimes from the back-arc, based on the mafic plutonism.

In summary, we interpret that extension started in the Late Triassic and lasted until the Hauterivian in the Eastern Cordillera and Middle Magdalena Valley. Nonetheless, the development of the extension was differentiated in the sub-basins. In the northeast of the Eastern Cordillera – in the Cocuy region – the extensional event started in the Early Cretaceous. Following the volcanism dated by Vasquez and Altenberger (2005) and Vasquez et al. (2010), we infer that extension had different pulses and was not related to a unique extension event in the Late Triassic. If the widening back-arc theory is applied, we can identify a migration of the back-arc towards the southeastern side. Nevertheless, the other hypotheses are still possible and a clear difference between the types of magmatism allows us to identify two pulses, one associated with a back-arc domain (Late Triassic – Early Cretaceous) and another with the rift setting during the Cretaceous. However, further studies related to detailed Mesozoic subsidence analysis will help understanding the extensional processes in the basin.

Conclusions

New U-Pb zircon ages obtained from volcanic and volcanoclastic rock units, structural analysis, petrography and geochemistry from pluton bodies located in the Eastern Cordillera and Middle Magdalena basins helped to constrain the Mesozoic evolution in the eastern area of the northeastern Andes during the Mesozoic configuration. Our conclusions are as follows:

- Two stages of extension or rifting occurred. The first took place during the Late Triassic-Early Jurassic to Middle Jurassic and lasted for 37 Ma, while the second took place from the Early Cretaceous to middle Cretaceous and lasted for 40 Ma.
- The Eastern Cordillera and Middle Magdalena Valley preserve Late Triassic-Early Jurassic plutonism associated with a magmatic arc and subduction-related calc-alkaline signatures. At this initial stage, synchronous volcanism is registered in the continental strata deposited in rift basins produced by intra arc to back-arc extension.
- In the study area, a westward migration of arc magmatism is suggested by the distribution and ages of the plutonism. Nevertheless, this observation is not reflected through the entire Colombian Andes margin.
- During the Middle Jurassic – Late Jurassic, a significant cease in plutonism occurred in the Eastern Cordillera and Middle Magdalena Valley, which was probably the result of oblique convergence.
- During the Early to Middle Cretaceous, mafic alkaline to tholeiitic bodies and increasing water depth indicate maximum stretching of the basin.
- We consider that the extension is related to a back-arc setting. We defined the main extension phases according to the evolution of the magmas through time from calc-alkaline to alkaline and tholeiitic, assuming that magma was generated in an initial stage from a magmatic arc associated with subduction, and during the later stages due to the thinning of the lithosphere.
- Based on the ages obtained in the Noreán Fm. and Jordán Fm., volcanism may have migrated from north to south during the early stages of the extension. Only the ages obtained in the Arcabuco anticline do not conform to this pattern, whereas the Early Cretaceous structures located in the northeast of the Eastern Cordillera are consistent with southward migration.

3. MESOZOIC GEOMETRY AND STRUCTURAL STYLES IN THE MIDDLE MAGDALENA VALLEY AND THE WESTERN FOOTHILLS OF THE EASTERN CORDILLERA

This chapter is a preliminary version of the manuscript in preparation to submission.

Chapter Overview

This chapter refers to a geometrical analysis of the Middle Magdalena Valley and the western foothills. These analyses were performed employing seismic reflection data. In this chapter, we show how is the structural variation along the basin strike. The methodology is fundamentally based on geophysical interpretation and constraining with petrophysical and surface information of the Western Foothills area. Furthermore, we also compared different interpretations and the possible relationship with Mesozoic inheritance, and also we considered the foreland development models to complement our structural interpretation.

Abstract

The northern Andes experienced different events as consequence of the interaction between the Caribbean, Nazca, South American plates leading to stages of Mesozoic extension and Cenozoic compression and uplifting. The Middle Magdalena Valley basin preserved these changes. However, the Eastern Cordillera exposes the Mesozoic sequence in most of its area, and the Cenozoic sequence is just preserved in the synclines and it is almost eroded.

We aim to analyze and define the geometry of the Middle Magdalena Valley and the Western Foothills of the Eastern Cordillera basin. We conducted a detailed seismic interpretation and mapping of the subsurface geology, also we integrated it with the surface geology. Through this methodology we identified the thin and thick-skinned domains and analyzed the Mesozoic extension's influence on basin development. Besides this, we classified the different depozones in the basins and analyzed their variations along the strike.

Since the natural resources exploration began, those basins had been studied and analyzed through several tools such as geophysics, geochemistry, geochronology, and other methods to reconstruct the tectonic history. Furthermore, seismic reflection had been one of the most common methods to define geometry in the Middle Magdalena Valley. Notwithstanding, the quality of this seismic information is still poor, and geological knowledge is required to complement the seismic interpretation. Moreover, is important the correct tie-up between the surface and subsurface information. Based on that, we employed the different velocity logs to produce constrained pseudo-3D velocity models. Our methodology focused on reducing the uncertainty in the complex areas, i.e., thrust sheets or places with signal loss. We interpreted the 2D seismic reflection data in the Middle Magdalena Valley basin and the western foothills of the Eastern Cordillera; our objective was to define and identify the unconformities, stratigraphic variations, structural domains and add the foreland depozones concept to our outcomes.

The double vergence is linked up to the uplift of the Eastern and Central Cordilleras. However, this double vergence disappears southward, and the orogenic belt of the Eastern Cordillera became the principal tectonic load in the basin development to the south. Our observations allow us to infer that the changes in the thickness and tilting are the result of tectonic loading variations in size and weight along the strike. We localized the major depozones close to the footwall of the principal fold-thrust belts, such as the La Salina fault system in our seismic lines. The shortening is

directly conditioned by the thick to thin-skinned domains. In this region, the uplift of the western foothills is due to the tectonic inversion of Mesozoic structures.

Keywords: Foreland, Mesozoic Inverted structures, Geophysics, Interpretation, Velocity, Modeling.

Introduction

Basins due flexure are found in oceanic-continent collision zones such as the Andes of South America (Allen and Allen, 2013). The northeastern of the Andean range spreads from Western to Eastern cordilleras and splitting by intermountain basins orientated from North to South such as the Middle Magdalena Valley basin (see in [Figure 3.1a](#)). The Eastern Cordillera exposes a structural configuration between thick and thin skin domains due to the interlinkage between South American, Nazca, and Caribbean plates (Cooper et al., 1995; Mora et al., 2006;2009, 2010; Sanchez et al., 2012; Nemcok et al., 2013; Teixell et al., 2015).

During the Late Triassic – Cretaceous, the basin evolved from an extensive regime (Sarmiento 2001; Sarmiento-Rojas et al., 2006; Kammer and Sanchez 2006) associated to a back-arc rifting (Maze, 1984; Aspden et al., 1987, Teixell 2015) based on the magma geochemical signature. According to Restrepo-Pace et al. (2004), as stated by the field evidence in the western foothills of the Eastern Cordillera, the basin started to experience a compressional regime during the late Paleocene – early Eocene time. Nevertheless, values of (U-Th)/He in the hanging wall of the La Salina fault unveiled the initial exhumation during the middle Eocene – early Oligocene (Sanchez et al., 2012). Latterly, the structure propagation to the Middle Magdalena Valley occurred during the early – middle Miocene and the last stage of exhumation during Miocene – Pliocene (Parra et al., 2009; 2012, Sanchez et al,2012). Based on the classification of Williams (1989) the basin experienced positive inversion of the extensional domain during the Mesozoic (Cooper et al., 1995; Sarmiento 2001; Sarmiento-Rojas et al., 2006) due to the Andean Cenozoic Orogeny that implied the compressional regime (Mora et al., 2006;2010).

The Eastern Cordillera geometry is associated with a pop-up structure (Restrepo-Pace et al., 2004) bounded by the La Salina Fault to the west; this structure was responsible for the initial exhumation in the basin (Sanchez et al., 2012) and to the east by the Guaicaramo Mesozoic inverted fault system (Mora et al., 2008). The study area is located in the northeastern of the Eastern Cordillera in the Magdalena Tablazo sub-basin and central-western area of the Middle Magdalena Valley basin (see location in [Figure 3.1b](#)). The Magdalena Tablazo sub-basin corresponds to the northwestern area of

the Eastern Cordillera bounded by the frontal thrust of the La Salina fault and the Middle Magdalena Valley basin to the west and limited to the Floresta Massif to the northeast; the sub-basin exposed the main structural features and outcrops of the Los Corbades, Portones, and Arcabuco anticlines (see location in [Figure 3.1b](#)). Those structures are defined as Mesozoic inverted grabens (Kammer and Sanchez 2006) and in the Middle Magdalena Valley, the basin tilts to the west, exposing the Cenozoic units along the western foothills.

According to the different structural domains along the basins, with this work, we aimed to integrate surface and subsurface information available in the study area, and also establish and delimit the main structural features. This characterization contributes to understanding the transition between different structural domains, the origin, and the synchronism associate with the main Mesozoic extensive events. We defined the main geometries and structural domains by integrating seismic interpretation and surface from preexisting field maps in the study area. Additionally, we did the structural balancing and forward modeling in Move (©Petroleum Experts) software to validate the geometries and kinematics of the main structures. This work focus on identify the principal structures and the differences along the basin. We also aimed to discuss the transition between the structural domains and their relation with the shortening values.

Data and Methodology

Data

We collected field information from the Eastern Cordillera and Middle Magdalena Valley, comprised mainly of geological maps published from the Colombian Geological Survey, reports, and published papers until the present date. All of these data were filtered according to the relevance, validity, location, and geological meaning. Latterly this was uploaded in a Geographical Information System (GIS) database in ArcGIS (© ESRI software). Furthermore, the fieldwork was developed during two primary field campaigns during 2018 and 2019 to validate the stratigraphic thicknesses and main structures outcropping with main focus on the Mesozoic strata.

The subsurface information was uploaded and analyzed in Petrel (© Schlumberger software) through the geosciences core. The seismic lines analyzed were 144 seismic lines from 53 different surveys. Also, we used information from 32 boreholes, where 50% of these wells reached the Mesozoic rock units (Figure 3-2). All of these data were kindly provided by the Colombian National Hydrocarbons Agency (ANH).

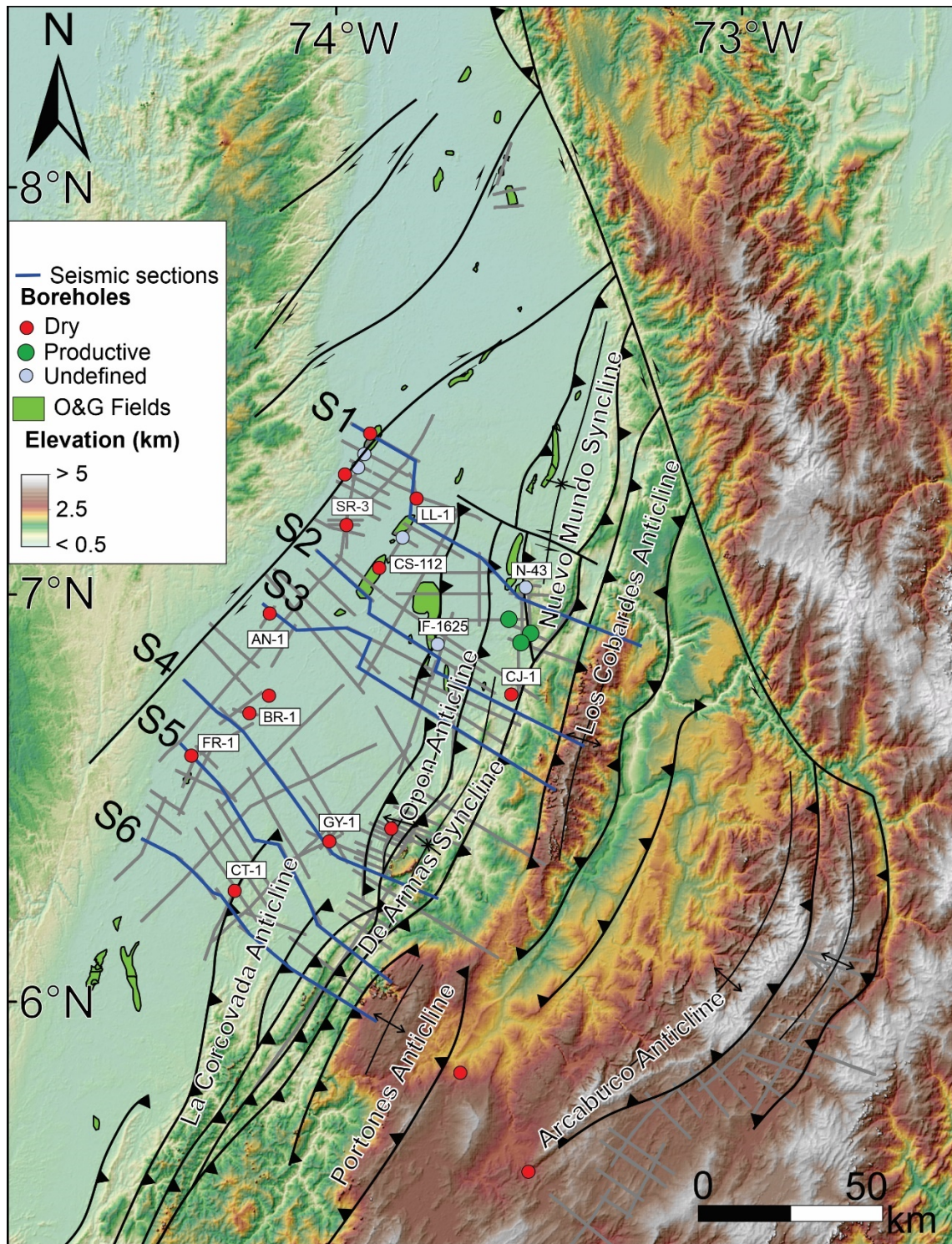


Figure 3-2. Digital elevation model of the study area showing the principal folds and faults, also the data employed to generate the seismic composite lines in blue. The boreholes that are projected in the composited seismic lines are labeled with their names.

Methodology

A massive seismic structural and stratigraphic interpretation has been carried out by Oil and Gas Companies during the exploration of the Middle Magdalena Valley basin. Defined as a mature and prolific basin, since the beginning of the 20th century. This massive exploration allows for generating a substantial amount of subsurface data towards the present.

The subsurface information used in this project was uploaded in Petrel (© Schlumberger) software. We defined the MAGNA-SIRGAS based on WGS1984 (World Geodetic Zone) 18 North as the Coordinate System to this project. The seismic information was analyzed, employing SeisSee (© Sergey I. Pavlukhin) to extract the headers and analyze the seismic quality.

We categorized the seismic following the next parameters 1. Seismic Reflector continuity 2. Loss of signal percentage 3. Acquisition year 4. Recent processing method if applicable. Afterward, we computed and qualified the parameters from 1 to 3, where 1 is high, 2 is medium, and 3 is low quality. The majority of the seismic lines are in the range between 2 and 3 according to these analyses.

Once the seismic quality control was done, we chose the datum of the project at 0 “zero” meters according to the average elevation in the Middle Magdalena Valley, where the majority of the seismic lines are located and processed, the replacement velocity employed in this project was 2000 m/s. Once the seismic lines were uploaded in Petrel (© Schlumberger), we applied the seismic attributes to each line separately to optimize the visualization. Finally, the topography was downloaded as DEM (Digital Elevation Model) directly from Global Mapper 21 (© Blue Marble Geographics software), with a size grid increment of 100 meters.

A seismic interpretation in the time domain was performed using the geophysics module of Petrel (© Schlumberger), These seismic lines were correlated with the velocity logs from 10 boreholes, and the principal geological horizons were identified. As a result, the main horizons and structures seismic response are highlighted in seismic lines. (See the global seismic response for all the units in [Figure 3-3](#)). The seismic composite lines were constructed with the seismic lines available in the study area, and in areas without information we projected the close and parallel seismic line to approach the structural setting.

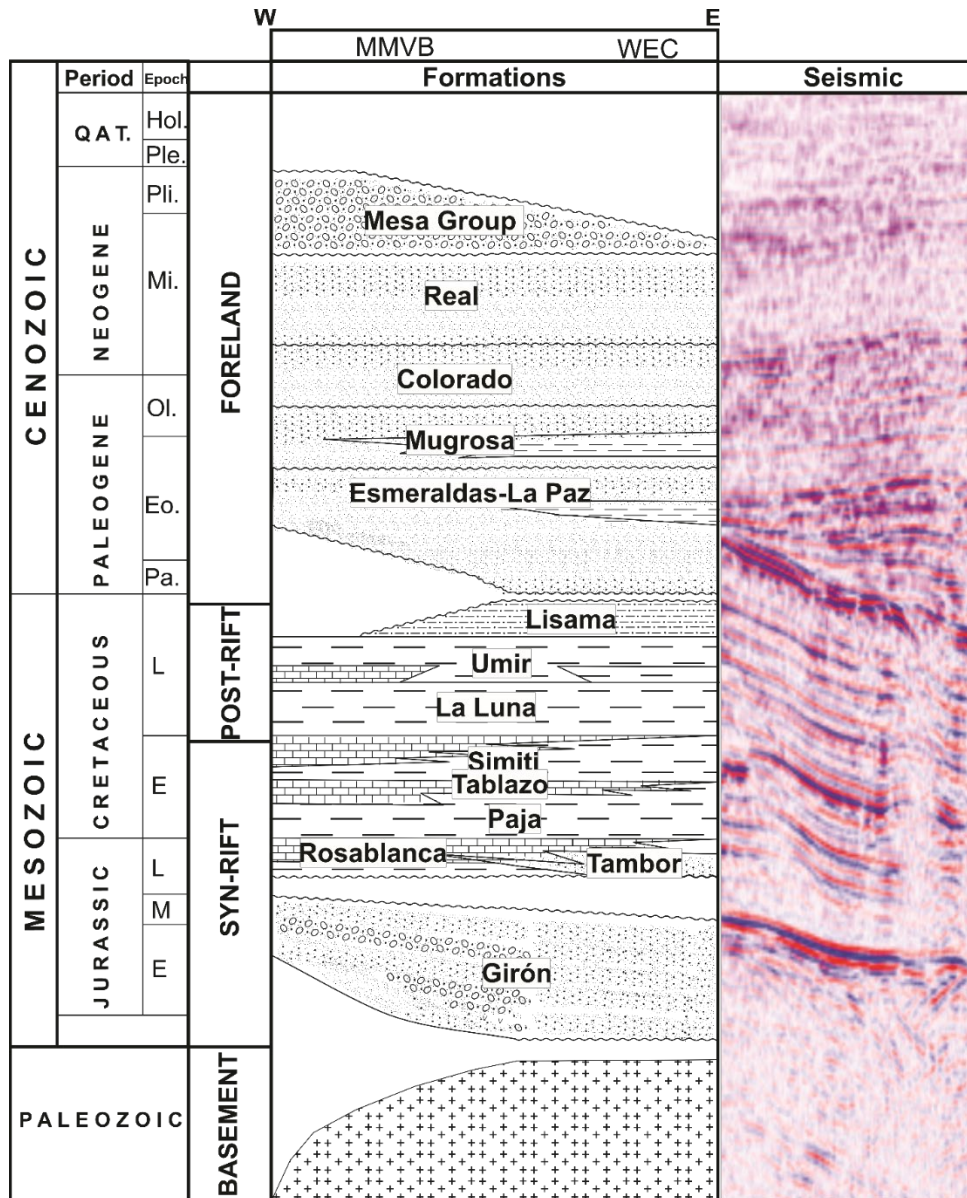


Figure 3-3. Generalized stratigraphic column of the Middle Magdalena Valley and western foothills of the Eastern Cordillera, showing the seismic response for the principal units.

Subsequently, the seismic lines were converted from time to depth; we employed the velocity values from the 10 boreholes containing velocity logs with their geological tops for this domain conversion. Furthermore, we employed depth maps published by Sarmiento (2011), to constraint the seismic conversion. Also, we did a seismic datum calibration employing the DEM in the time domain.

Ten boreholes from the total amount contain the VSP and check shot logs to seismic tie. The velocity depth conversion was performed according to the geological divisions made during the project execution. We divide the area where the seismic lines are depending on 1. Seismic response

2. Structural setting 3. Stratigraphy 4. Boreholes number with velocity logs. In the end, we generated 10 polygons; this amount was defined based on the previous features and with the primary aim to reduce the noise and the lack of data in some points related to the borehole distance.

Once the areas were delimited, we created the model zones based on our interest and the available information; usually, this zoning is based on the seismic response and geometry. Then the model is divided by layers and populated with their velocities. This division will be integrated with the interval velocities (representative values from one lithological layer). Therefore, we can calculate the average velocities to finalize the depth conversion model once we have the interval velocities.

$$V = d/t$$

Velocity equation to illustrate the relation between the different velocities employed during the seismic conversion.

$$V_{int} = \frac{da - db}{ttda - ttdb}$$

(Interval Velocity equation adapted from Stewart et al. 1984)

Where d means layer depth and a means the deeper value and b the upper one. tt means time, and a and b refer to lower and upper layers respectively. ([Figure 3.3](#) illustrates the velocity relationship).

$$V_{avg_n} = \frac{\sum_{j=1}^n V_{int}(j) \Delta ttdn}{\Delta ttdn}$$

(Average Velocity equation adapted from Veeken, 2007)

Where n means number of intervals and j means the position of that velocity interval. This is the only valid velocity to do the seismic depth conversion, and it is fundamentally based on the interval velocities. (See in [Figure 3-4](#) the relationship between interval and average velocities).

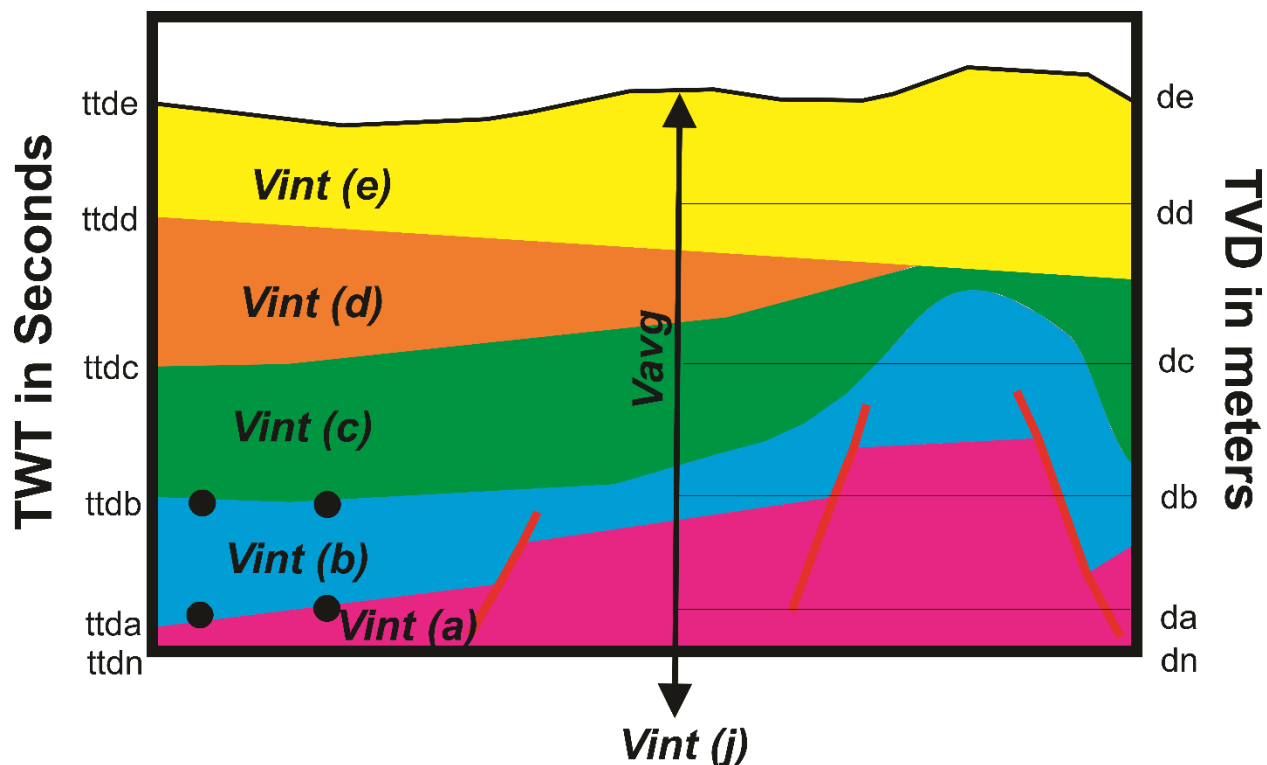


Figure 3-4. Diagram adapted from Veerke, 2007, showing the Vint (interval velocity) and Vavg (average velocity) relations and concepts.

The seismic lines were interpreted based on the seismic reflection techniques, such as the structure evidence (loss of signal, fault shallows), identifying the high and low seismic amplitudes for each seismic horizon, and defining the sequence boundaries as is proposed by Shaw et al. (2005) to interpret complex areas. This interpretation was done in depth domain to validate the geometry variations resulting from the domain conversion.

All the seismic lines and interpretations in depth were transferred to Move (© Petroleum Experts) software, where the structural analysis and validation was performed employing the steps proposed by Woodward et al. (1989) to build structural balanced cross-sections following the structural geometry principles of Dahlstrom (1969).

Those interpretations were analyzed regarding cut-off variations from north to south, thickness relations, and structural domains. The section lines were balanced employed the fault parallel flow and the flexural slip unfolding algorithms to test the geometry reliability. In this chapter, we present and compare the present-day basin geometry from north to south.

Results

Seismic Interpretation

The typical development scheme of the foreland basin provinces is composed of wedge-top, foredeep, forebulge, and backbulge (See the relation in [Figure 3-5a](#)). However, this scheme is affected by the local tectonic setting in the most fold and thrust belts (De Celles, 2012). The foreland basins are developed as a consequence of lithosphere flexural deflection in response to different loads, i.e., sublithospheric (static: slab pull or dynamic: mantle response) and supralithospheric (static: orogen, sediment, and water) (Catuneanu, 2004) (See in [Figure 3-5b](#) the deflection relationship). The subsidence in all the foreland basins responds to the adjacent orogenic belt (Jordán, 1981; Catuneanu, 2004).

The migration of the foreland basin through time depends on the re-organization of the orogenic loads (De Celles and Gilles, 1996); according to Cantuneanu (2004), the basin prograde towards the craton during the early stages of development and retrograde during the late stages. The present values of progradation in a basin-scale are between 100-200 km (Catuneanu, 2000). Nevertheless, the retrogradation is not just influenced by the re-organization of tectonic loads; this is also affected by the viscoelastic relaxation of the lithosphere through time, producing the deepening and narrowing of the foredeep (Beaumont et al., 1993) (See [Figure 3-5c](#)).

The seismic lines were interpreted following previous concepts and observations made from previous works such as (Caballero et al., 2013; Gomez et al., 2005; Guerrero et al., 2021; Moreno et al., 2013; Parra et al., 2012; Restrepo-Pace et al., 2004; Sanchez et al., 2012; Sarmiento, 2011). The interpretation conducted in the study area attempts to characterize the basin geometry according to the sedimentary infill and structural variations along the strike. The seismic lines are composed by different surveys originally in time domain, and all of these programs are located perpendicular to the primary structural trend NE-SW (See in [Figure 3-1](#) the location) in the EC and MMV. Six composite seismic sections are presented and described below.

Section S₁ (see in, [Figure 3-6](#)) which is a cross-section perpendicular to the La Salina Fault system strike and most of the Mesozoic inverted structures of the EC and MMV (NE-SW), show an atypical geometry of double vergence structures, with a basement high in the core of the seismic section. The section S₁ is composed by three main structural domains from west to east; in this section, we have the Cantagallo thrust east-verging fault as a boundary with the Central Cordillera or San Lucas

range; in this structure, a significant unconformity is evident in the hanging-wall between the Late Miocene (?) and Jurassic. The footwall of this fault contains east-verging structures preserving the angle of the major fault, the Cantagallo fault. Based on the seismic response and the thickness relations, the majority of these structures were inverted. Another relevant structure is a local thin-skinned thrust with a decollement during the Early Cretaceous but without significant displacement. The sedimentary infill in this area shows a thickening close to the thrust belt of the Cantagallo fault and a thinning to the middle of the cross-section. Based on the seismic response, a continuous seismic unconformity is identified and associated with the Esmeraldas-La Paz unit; from west to east, the older units are onlapping to the unconformity. In the center of this section is located the La Cira Basement-high (see Chapter 4, where we discuss the possible origin and compare it with previous interpretations); this is defined as the boundary between the east and west vergence structures. We have the Infantas inverted fault in this Basement-high, this fault is classified as high angle structure with small displacement <200 m. The footwall of this structure was previously described, and the hanging-wall is integrated by west-verging structures mainly; in general, the basin shows a thickening comparing with the east-verging block; this thickening is more notorious with the Cenozoic rock units. The Infantas hanging-wall contains inverted structures and non-reactivated structures; one of the major structures along the basin is the La Salina fault, this structure is defined as thick-skinned inverted fault, the total displacement of this structure in this section exceeds the >6 km, and the major sedimentary record is closer to the principal fold-thrust system.

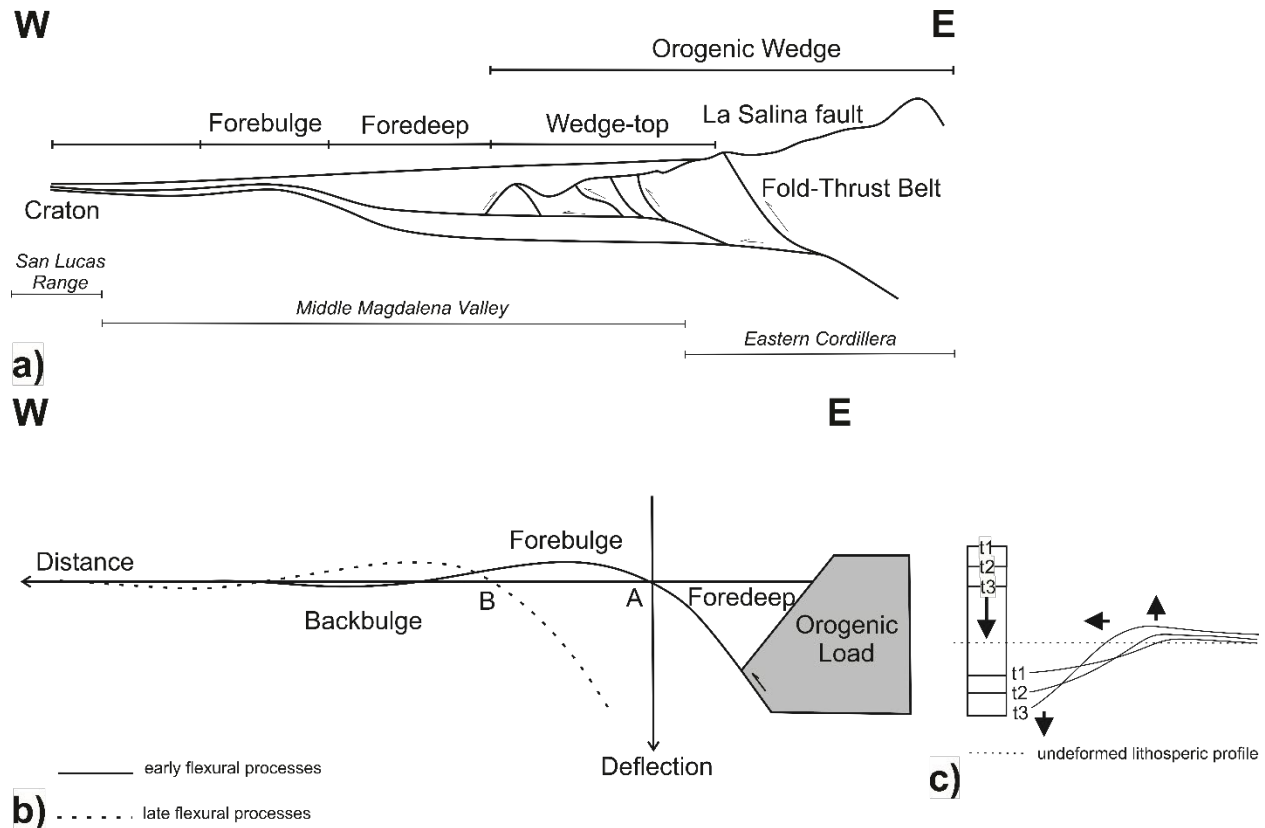


Figure 3-5. a) Schematic cross-section depicting a revised concept of a foreland basin system, with the wedge-top, foredeep, forebulge depozones shown at approximately true scale. (modified from DeCelles and Giles) This illustration shows the possible location of each depozone and its relation with the study area. . b) Foreland basin progradation through the time in response of an orogenic load migration (modified from DeCelles and Giles, 1996) c) Flexural response of a visco-elastic lithosphere that relaxes stress (modified from Catuneanu, 2004). In this diagram shows static loading in the fold-thrust belt, which leads to foredeep subsidence and forebulge uplift. The foredeep becomes deeper and narrower through the time.

Section S₂ (see [Figure 3-7](#)) shows the transition in the structural domain from Section S₁; in this section, the double vergence structures are scarce, and the principal structures are west-verging faults. From west to east, the section contains a Mesozoic horst structure that was not reactivated. Some inverted reverse structures with east-verging are less common but still present. The Infantas fault decreases its cut-off, and the La Cira Basement-high is almost absent. Toward the hanging wall of the Infantas fault, the faults preserved the same west vergence, and a significant thickening to the east is evident.

The principal fold-thrust of the La Salina fault splays it on different structures, preserving the geometry and basement involved structural style. Although in the footwall of the Arrugas fault, a buried thrust is interpreted as the mechanism to produce this onlapping and significant geometrical variation (See in Chapter 5 the kinematic restoration), but the thin sedimentary sequence compared with the closer deep footwall block westward of the section, allow us to generate a division between the two fold thrust systems. Moreover, another relevant structure is in the upper part of this thick sequence's hanging-wall, where the borehole IF-1625 is located. This structure is a back-thrust that are generating a piggyback basin. The general onlapping in this section is to the west, and the thickening in sediments is to the east where the major fold thrusts are located; but, as we mentioned above, the division between the higher thicknesses is due to the cut-off of the buried thrust system.

Section S₃ (see in [Figure 3-8](#)) presents two major structural domains; however, this section preserves the general geometry of section S₂. In this section, we have non-reactivated Mesozoic normal faults with a domino geometry, these structures keep the same displacement of ± 450 m mainly in the middle of the cross-section, different than the east where a normal fault increases the cut-off ± 900 m and affects the youngest sequence (Simití Fm.). Low angle west-verging structures characterize the east region, and the La Salina Fault redistributes the total displacement in the splay fault system. The buried thrust located in the hanging-wall of the La Salina fault reduces its cut-off significantly, and the thickness variations between the blocks are less notorious. Another important change is the widening of the Piggyback basin, and Mugrosa back-thrust reduces its displacement in relation with section S₂. In this section, the thickening is to the east and close to the major fold thrusts i.e., La Salina fault. The onlapping of this section is to the west; evidence of this unconformity relation is in the borehole AN-1, where we have Miocene rock units above the Jurassic sedimentary sequence.

Section S₄ (see in [Figure 3-9](#)) and S₅ (see in [Figure 3-10](#)) present almost the same structural geometry the only difference between these seismic cross-sections is regarding the sedimentary deposits and the ramp-flat relation of the San Fernando fault. In these cross-sections are west-verging structures the principal thrust related to the La Salina fault to the east of the section. To the west the San Fernando fault system, this thrust present a mixed thin-thick-skinned style, the structure detached from the Late Cretaceous formations. To the west of the section in the San Fernando footwall, a normal fault affects the Mesozoic sequence, this structure probably linked to

the previous normal fault described in section S-3. In section S4, the thick deposits are located in the footwall of the La Salina and San Fernando faults; but, in this section, the Cenozoic sediments overlaid the Mesozoic rock units unconformably. It is different from the case southward in the cross-section S5, where all the Cenozoic sequence is thinning and preserved. The fold structure associated with the San Fernando hanging-wall is widening to the south and steepening in the eastern limb. In general, both sections overlapped westward, reaching the major high in this direction. The southern section analyzed in this work refers to the S6 seismic composite line (see [Figure 3-11](#)). In this section, we have thin and thick-skinned domains. The structures from east to west are west-verging faults; the displacement is distributed along with the splay structures from the La Salina fault; near the orogen, the faults are primarily basement-involved structures. Westward to the basin La Corcovada and Dos Hermanos faults are characterized to detached at the Mesozoic level and are defined as thin skin structures. This section shows more fold-related faults in the hangingwall of the Dos Hermanos and El Ermitaño faults. The basin overlapped westward, and the thick deposits are located in the footwall of the principal structure of the La Salina fault.

Chapter 3. Mesozoic geometry and structural styles in the EC and MMV.

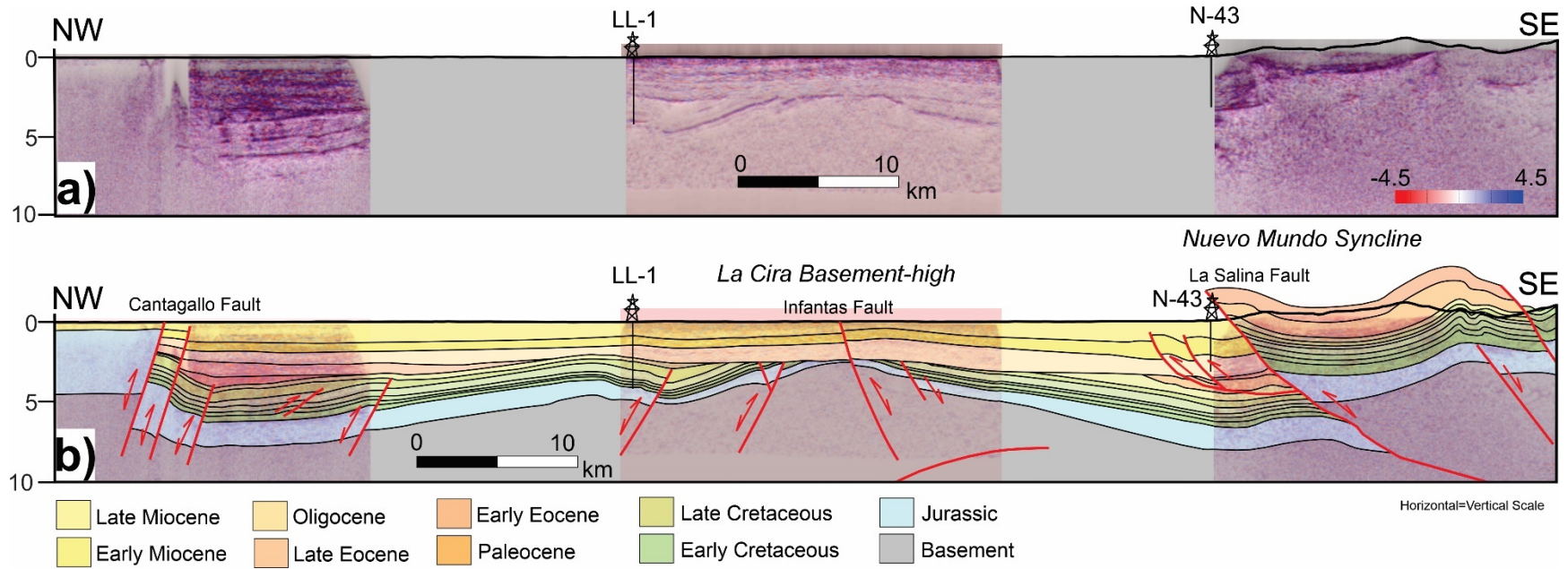


Figure 3-6. a) Uninterpreted composite seismic section S_1 in depth domain (the scale is in kilometers) and the colors scale bar refers the seismic amplitude. b) Interpreted seismic reflection line in depth domain. Showing the structural and stratigraphic relationship. The buried east-verging structure is discussed in the chapter 4. See Location in [Figure 3.1](#) and boreholes location in [Figure 3-2](#).

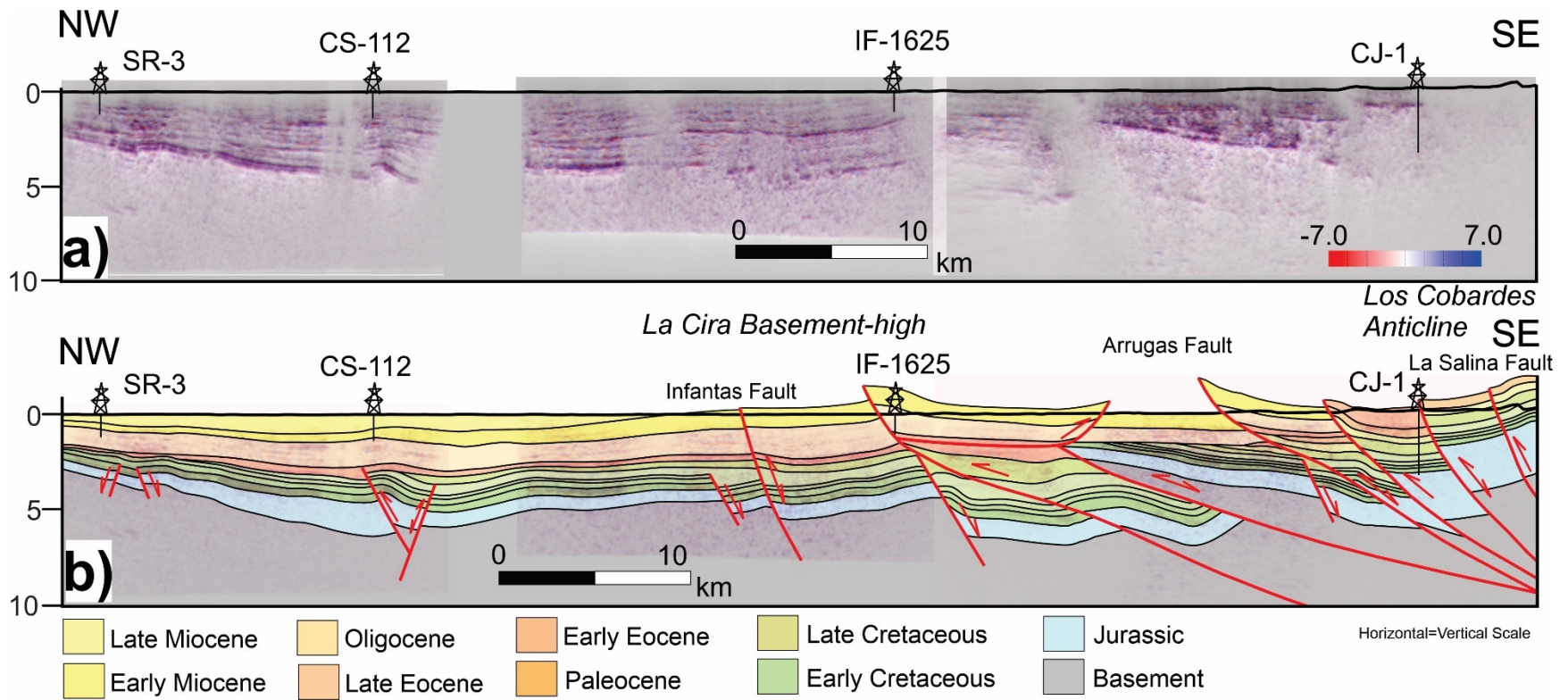


Figure 3-7. a) Uninterpreted composite seismic section S2 in depth domain (the scale is in kilometers) and the colors scale bar refers the seismic amplitude. b) Interpreted seismic reflection line in depth domain. Showing the structural and stratigraphic relationship. See Location in [Figure 3-1](#) and boreholes location in [Figure 3-2](#).

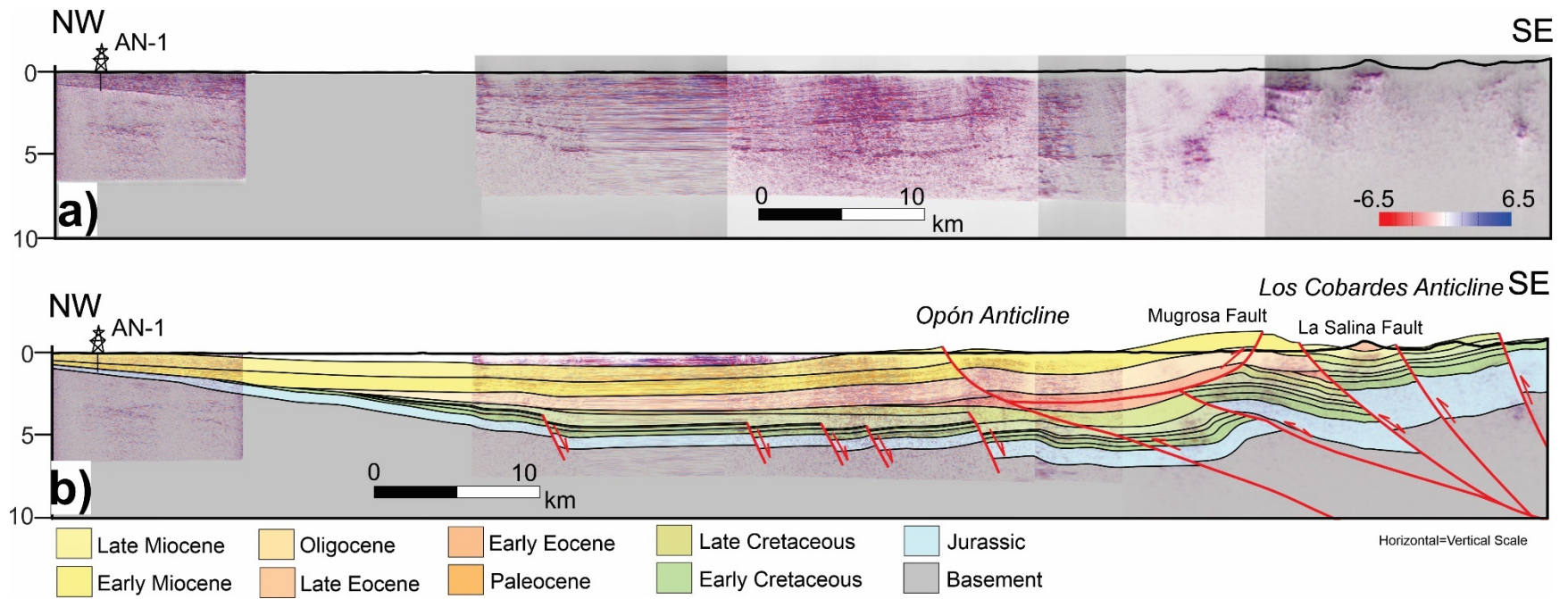


Figure 3-8 a) Uninterpreted composite seismic section S3 in depth domain (the scale is in kilometers) and the colors scale bar refers the seismic amplitude. b) Interpreted seismic reflection line in depth domain. Showing the structural and stratigraphic relationship. See Location in [Figure 3.1](#) and boreholes location in [Figure 3-2](#).

Chapter 3. Mesozoic geometry and structural styles in the EC and MMV.

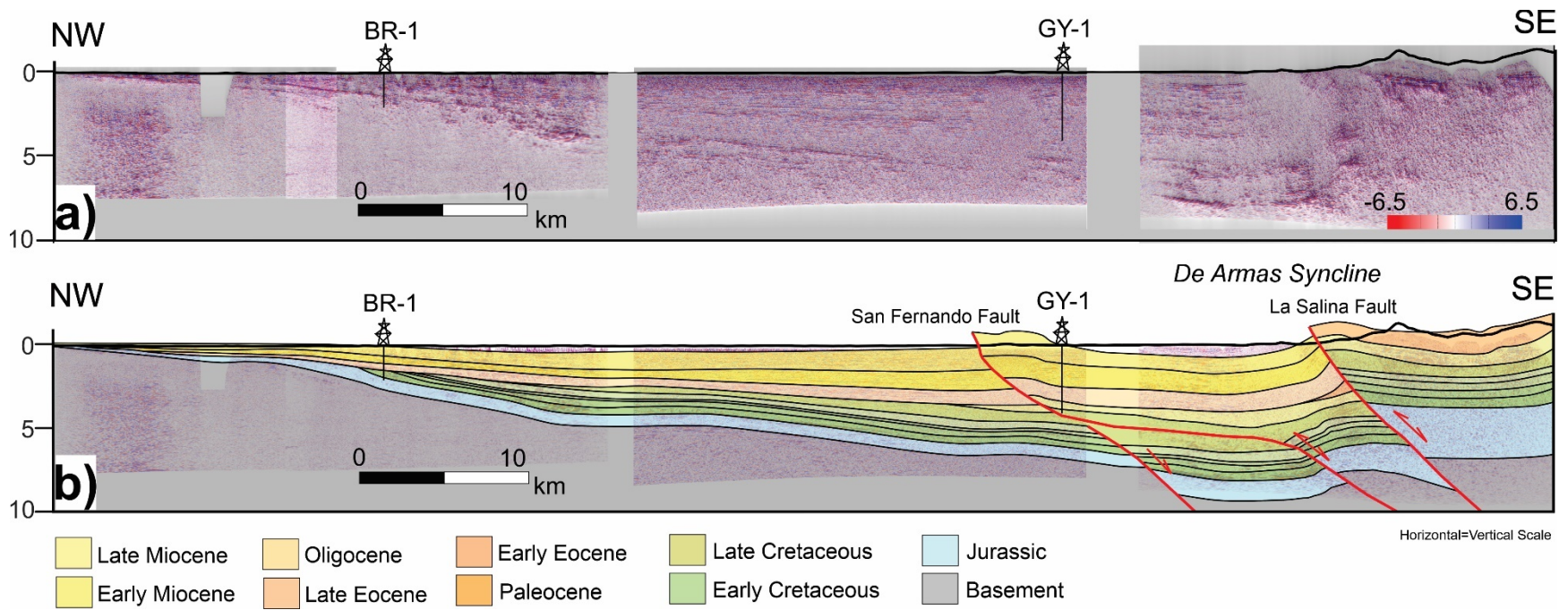


Figure 3-9 a) Uninterpreted composite seismic section S4 in depth domain (the scale is in kilometers) and the colors scale bar refers the seismic amplitude. b) Interpreted seismic reflection line in depth domain. Showing the structural and stratigraphic relationship. See Location in [Figure 3-1](#) and boreholes location in [Figure 3-2](#).

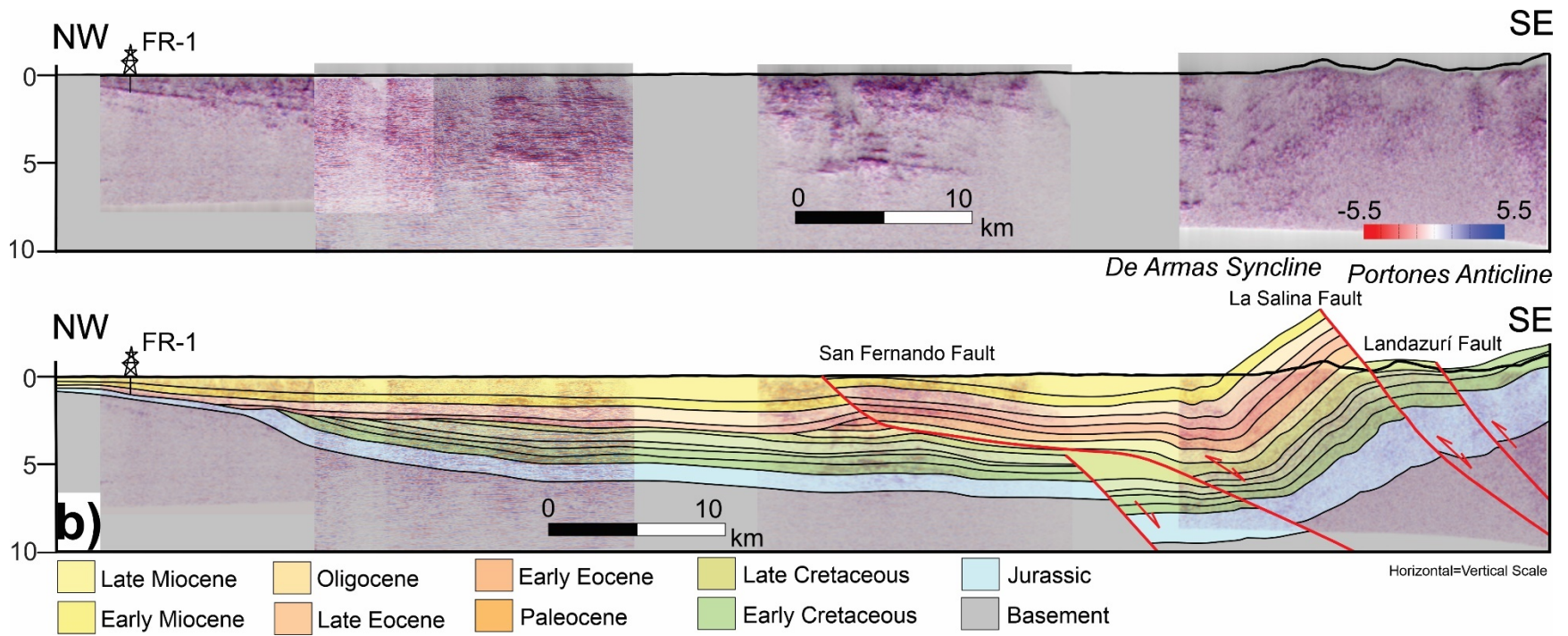


Figure 3-10 a) Uninterpreted composite seismic section S5 in depth domain (the scale is in kilometers) and the colors scale bar refers the seismic amplitude. b) Interpreted seismic reflection line in depth domain. Showing the structural and stratigraphic relationship. See Location in [Figure 3.1](#) and boreholes location in [Figure 3-2](#).

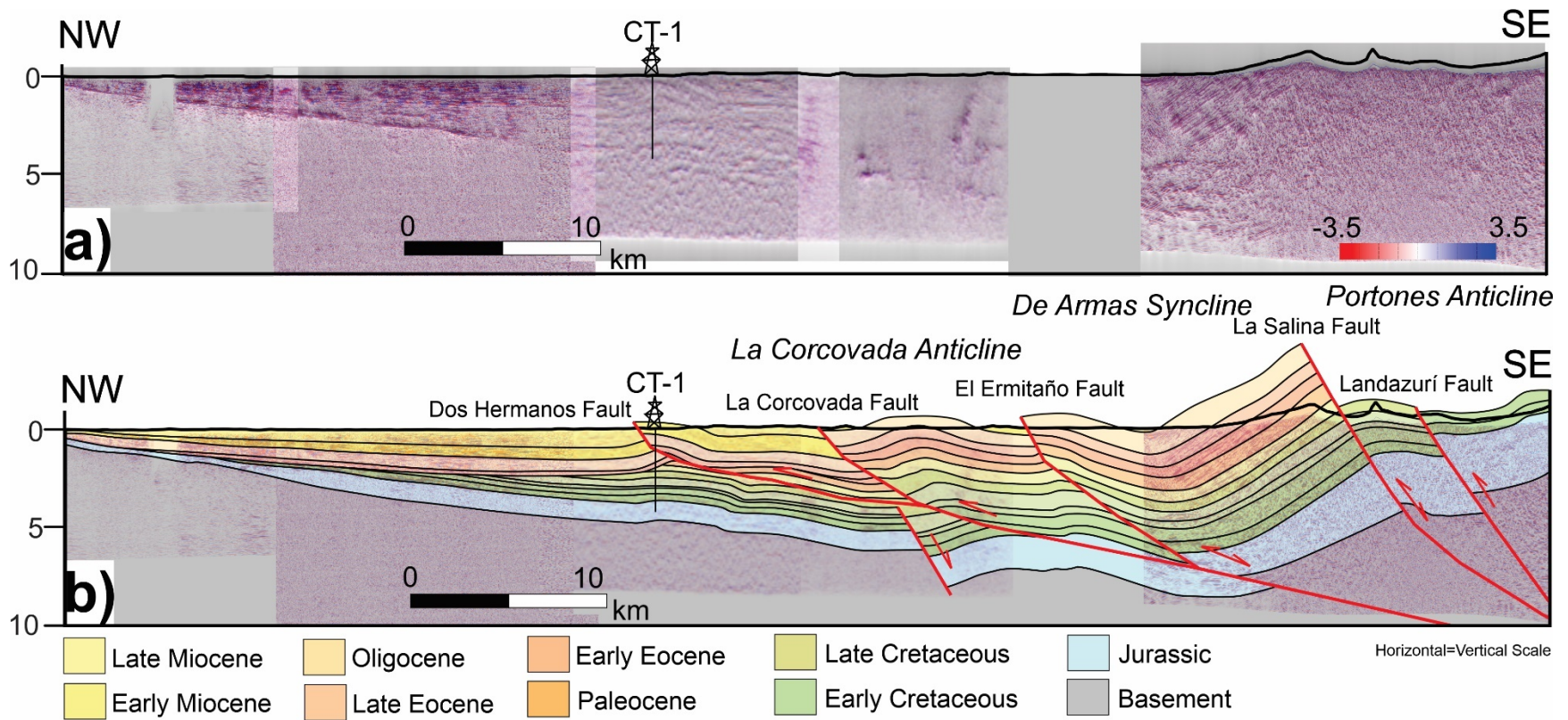


Figure 3-11. a) Uninterpreted composite seismic section S6 in depth domain (the scale is in kilometers) and the colors scale bar refers the seismic amplitude. b) Interpreted seismic reflection line in depth domain. Showing the structural and stratigraphic relationship. See Location in [Figure 3-1](#) and boreholes location in [Figure 3-2](#).

Discussion

This chapter showed six seismic composite lines and defined the main structural domains in the Middle Magdalena Valley basin and the western foothills of the Eastern Cordillera from north to south. Different deformation processes have affected the study area over time in response to the tectonic setting for each period. The Middle Magdalena Valley has been defined as an intermontane basin due to the uplift of the Eastern and Western Cordilleras (Parra et al., 2012; Caballero et al., 2013). The sedimentary infill is divided according to its tectonic domain; the cross-sections are interpreted in the depth domain and show the thickness variation and structural relation. The deepest formation is the Girón Fm. deposited in a continental environment; the basement is undifferentiated and underlays the Jurassic sedimentary sequence. According to Ward (1973); Restrepo-Pace (1997); Cochrane et al. (2014), the Paleozoic basement is composed mainly by metamorphic rocks, mainly schists, and gneiss. This basement is identified in the seismic lines following the non-continuous reflectors in the basal areas and classified as the acoustic basement as response of the seismic imaging (see Chapter 4, the seismic interpretation characterization).

DEPOZONES

In the S₁ section, we have an atypical structure composed by a basement-high bounded by double vergence structures. The prominent high is limited with the inverted fault to the east and a reverse east-verging structure to the west. The major depocenters are located close to the principal structures in the hanging wall of Cantagallo and La Salina faults, west to east, respectively. Thus, we have a double onlapping to the center of the basin where the high is located. Previous studies conducted by different authors in the study region, i.e., (Morales, 1958; Gomez et al., 2003; Parra et al., 2012; Kammer et al., 2020) had identified the opposite vergence of this structure through seismic interpretation.

The origin of this vergence had been attributed to the migration front of the Central Cordillera (Gomez et al., 2005; Moreno et al., 2011; Parra et al., 2012; Caballero et al., 2013). Parra et al. 2012 proposed that the minor inversion in some local faults in the MMV impedes the generation of major subsidence and accommodation space. The major depocenters are associated with inverted structures; in our cross-section S₁, we have two major depocenters linked to the Cantagallo fault and the la Salina fault; both structures are interpreted as Mesozoic inverted faults. Based on the model proposed by DeCelles and Giles (1996), these depocenters refer to the foredeep depozone of the foreland basin. For that reason, the La Cira high is a consequence of the long wave-length

migration due to the uplift of the Central Cordillera. However, the eastern side of the cross-section S₁ preserves almost the same geometry and thickness, allowing us to infer that the basin experienced a coeval loading during the basin development. Parra et al., (2012) obtained thermochronological ages of Paleocene in the western flank of the Los Cobardes Anticline; these values are associated with the initial deformation and cooling event in this region.

Southward, in section S₂, the basin thickening to the middle and west of the section. This thickening is interpreted as the structural closure of the La Cira Basement-high. In addition, the deepest and major accumulation is located near to the Arrugas fault. We considered that this thickening could be generated as a consequence of the variations in orogenic loading.

Due to these, the absence of east-verging structures is probably linked to the size and weight variations of the Central Cordillera orogenic load. Furthermore, the Mesozoic sequence presents, in general, a good continuity to the west. Based on these observations, we localized the Foredeep near the footwall of the La Salina fault; also, we considered that the Arrugas system played an important role in the depocenter development, and the orogenic wedge is associated with the La Salina Fault system. However, in this section, we do not have seismic evidence about the forebulge location.

The southern sections from S₃ to S₆ present a similar sedimentary infilling shape. The higher accumulations are mainly associated with the footwall of La Salina and San Fernando faults. The orogenic load of the Eastern Cordillera highly conditioned these depocenters. Furthermore, the basin deepened southward; this is reflected in the thickening and thickness changes. For these cross-sections, the Orogenic wedge is attributed to the western foothills of the Eastern Cordillera. The Foredeep is localized in the hanging wall of this frontal thrust mainly, these rock units are tilting to the west. The western area where the Jurassic sedimentary sequence is truncating with the Paleocene unconformity is defined as the forebulge.

According to Chase et al. (2009), the present Andean foreland dimensions are orogenic wedge, width: 50-70 km; Foredeep, width: 250-300 km; and buried forebulge without topographic expression. Although the basin dimensions are lower in our study area, we consider that the development in this basin is highly controlled by the uplift of Eastern and Central Cordilleras, furthermore, the proximity to the plutonic bodies that comprise the San Lucas Range. This plutonic body acts as a basin boundary and could behave as a craton following the model proposed by

DeCelles and Giles, 1996. Also Gomez et al. 2003; 2005 suggest that the MMV and Llanos basins were a single foreland system since the Central Cordillera uplift until the partitioning generated by the Eastern Cordillera uplift.

UNCONFORMITIES

The reflector truncations allowed us to identify the principal unconformities along the basin. Three major unconformities had been identified in these sections; the late Miocene – Jurassic; this unconformity is located in the hanging-wall of the Cantagallo fault, and appears in section S₁. This unconformity was identified with the seismic response and calibrated with borehole data. We assumed that this block was in a positive relief until the deposition of the Real Formation (late Miocene), where the Central Cordillera probably experience a tectonic quiescence.

Notwithstanding and based on thermochronological data, Sanchez et al. 2012 suggest that the Western Flank of the Eastern Cordillera experienced an accelerated exhumation during the Miocene- Pliocene.

The common known the Eocene Unconformity is the most notorious feature in the seismic lines (Sarmiento, 2001); nevertheless, the age of this unconformity was modified based on thermochronological data as late Paleocene-early Eocene (Parra et al., 2012) different than the age of late Eocene-early Oligocene proposed by Gomez et al. (2005) based on growth strata relation.

This unconformity is identified in all the seismic cross-sections due to its constant seismic response and truncation reflectors. Based on our interpretations from north to south, the Mesozoic rock units truncated this unconformity westward. But, in the S₁, the older deposits truncated westward and eastward, probably associated with the forebulge migration. From north to south, this truncation is moving westward. In addition, from section S₃ to the west, the Miocene deposits overlaid unconformably the Jurassic sedimentary sequence.

Guerrero et al. 2020 identified Mesozoic unconformities in the study area, and, based on well data, they classified in different events. In this work we focus on the structural features, and the unconformities for the Mesozoic were recognized in some areas, i.e., paleo-highs in (see [Figure 3-1](#)), the hanging wall of some inverted structures. However, we do not differentiate it due to the poor continuity of these reflectors and the bad seismic signal of some formations.

The last unconformity is defined as the Jurassic-Basement unconformity; we employed the borehole horizon markers to interpret the geometry, a high amplitude horizon is followed along the basin, and thicknesses are defined according to the basal response. The unconformities identified here allow us to define the present geometry and are part of the inputs to reconstruct the basin in previous stages.

GEOMETRY

The Middle Magdalena Valley and western foothills of the Eastern Cordillera provide an exceptional case of thin vs. thick-skinned domains; due to these from S₁ to S₆ section, we have different structural domains.

Through the seismic, well data, and field information integration, we constrained the different geometries. According to its seismic response, we split the study area into three domains that follow the same structural style along the strike.

The first domain is defined as the Eastern Domain. This is located along the western foothills of the Eastern Cordillera, and to the west of its orogenic wedge. The principal fault vergence in this area is to the west. This domain also has narrow anticlines and wide synclines, such as the Nuevo Mundo syncline (Sarmiento, 2011). The widening of these synclines is due to the generation of a Cenozoic taper in the depocenters areas before the thin-skinned deformation occurred (Moreno et al., 2013). The principal structures are high-angle faults; however we have low-angle reverse structures in sections S₂ and S₃, generating triangle zones. This domain is characterized as having the La Salina Fault considered a major basement involved structure along the strike. This structure decreases its shortening southward (see in [Figure 3-12](#) and percentages in [Figure 3-13](#)). It is defined as a principal fault system in the basin development of the western foothills and the footwall of the MMV. In [Figure 3-12](#), we can infer that the shortening behavior from the La Salina master Fault is transferred to the thin-skinned structures of Dos Hermanos and La Corcovada faults. The weak decollement layer could be associated with the Late Cretaceous Umir Formation.

Nevertheless, the Eastern Cordillera is defined mainly as a thick-skinned tectonic domain (Tesón et al., 2013). Local faults in the central-southern region of the MMV detached at the sedimentary cover. These faults generated imbrication structures, triangle zones, and duplexes (Restrepo- Pace et al., 2004). Moreno et al. 2013 argue that the absence of roof duplexes in the MMV is due to the scarce or null presence of syntectonic sediments that act as barriers. In addition to this, the same

authors considered that the rapid thinning to the west and the east dipping of the basement, are some reasons to impede the passive roof duplexes in the western foothills of the EC. Tesón et al., 2013 defined that the folding in the internal part of the EC is a consequence of buttressing effect, different than the external parts where the inverted Mesozoic structures play a fundamental role.

The second domain is located to the west, and we defined it as the Central Domain. We identified the La Cira Basement high in this area, and the principal structures are associated with buried Mesozoic inverted faults. According to Sarmiento (2011) the other paleohighs of Cachira and Cagui are also related to this trend, though the structural style changes dramatically from north to south. One example is that section S1 presents double vergence buried inverted structures, and southward in the section S2 the basement-high disappears, and the east-verging structures are scarce.

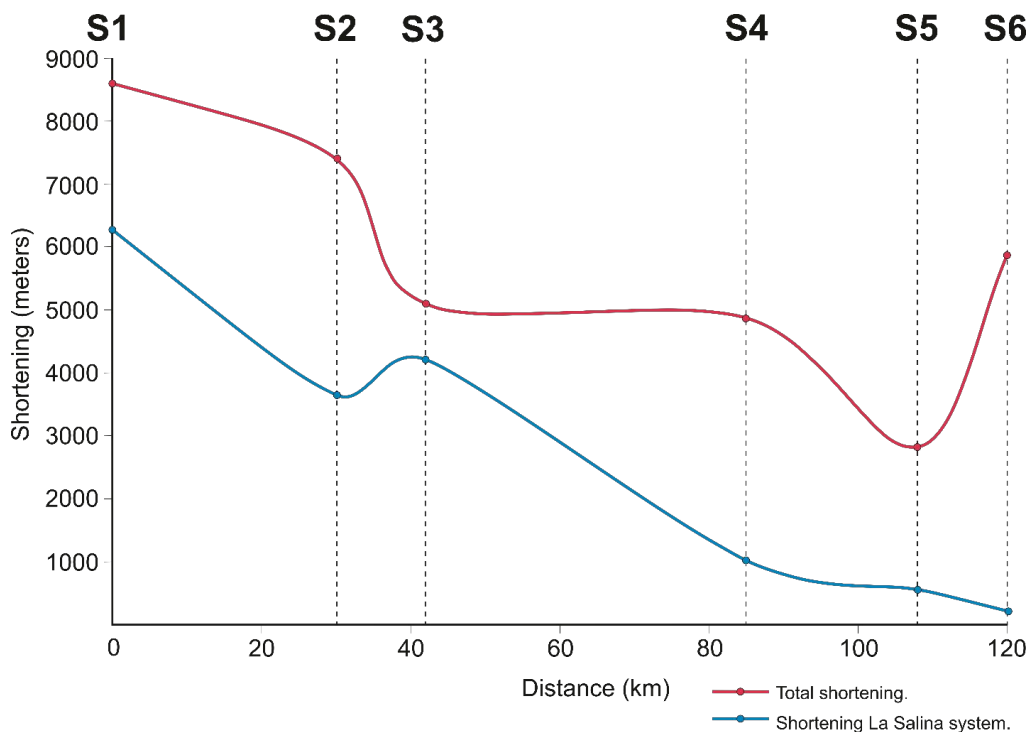


Figure 3-12. Shortening values along the strike from the different seismic cross sections. See in [Figure 3-1](#) the location of the different cross sections.

These buried structures were probably generated because sediment accumulation rates overpassed the rates of tectonic uplift in the MMV (Caballero et al., 2013). From section S3 to S6 the only family group is associated with the extensional Mesozoic non-reactivated faults. According to Mora et al. (2009) the selective inversion is not just defined by the orientation of the compressional stresses;

the fault growth also influences it. Decreasing tectonic rates during the early Eocene and coeval thrusting kept the normal stress of the Mesozoic structures in the MMV (Caballero et al., 2013).

The Last Domain is composed of the westernmost side of the cross-sections. This area is named as Western Domain. The sedimentary thinning of the basin characterizes it; the east-verging structures are present to the western side just between the section S₁ and S₂. The principal structure is the Cantagallo Fault, a thick-skinned structure thrusting the Mesozoic sequence over the Cenozoic deposits. This structure is considered an inverted structure and is defined by the Central Cordillera eastward migration (Gomez et al., 2005; Moreno et al., 2011; Caballero et al., 2013). Southward from section S₃ to S₆, faults in this region are rare, and the basin thinning is increasing. Based on thermochronological and provenance information, the burial history and the onlapping to the west were highly controlled by the loading of the EC (Caballero et al., 2013).

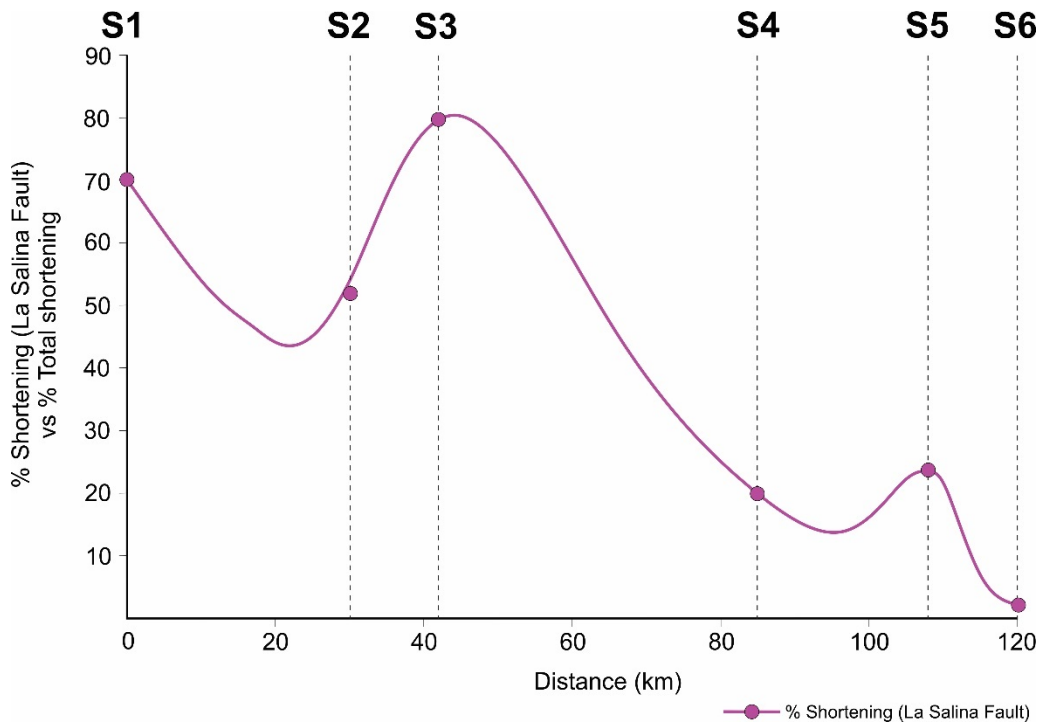


Figure 3-13. Percentage of shortening of the La Salina Fault vs. Total Shortening for each seismic composite line. See in [Figure 3-1](#) the location of the different cross sections.

Conclusion

In summary, we defined the basin geometry with the information presented in this chapter and the integration of previous works. The double vergence domain is associated with the uplift of the Central and Eastern cordilleras. Although, the denudation of these orogenic belts had started since the Late Cretaceous for the Central Cordillera (Gomez et al., 2005; Parra et al., 2012) and during the Paleocene-early Eocene (Parra et al., 2012; Caballero et al., 2013) for the western side of the Eastern Cordillera. However, our hypotheses are fundamentally based on coeval loading to produce the present-day configuration with two depocenters. For this reason, we suggest flexural modeling to analyze and constrained the previous interpretations. This basin evolved initially as a single foreland integrated by the MMV and Llanos foreland basin and was fragmented with the uplift of the Eastern Cordillera.

In this area, the Middle Magdalena Valley intermontane basin evolves with two sedimentary sources, initially from the Central Cordillera and later on from the Eastern Cordillera (Caballero et al., 2013). In our seismic interpretation, we identified that the major depocenters are close to the orogenic belts. Principally in the footwall of this Mesozoic inverted faults such as the La Salina Fault. The present major depocenters do not exceed the values of more than 8.5 km in thickness, and the westward onlapping is directly attributed to the deflection generated by the orogenic load of the EC.

The forebulge depozone is migrating to the west; though in section S₁ the basement high geometry could be associated with the long wave-length uplift of the regional forebulge. Notwithstanding, this geometry disappeared to the south. In the southern region, the forebulge is moved to the western side of the cross-sections. We hypothesize that this migration is directly associated with variations in size and weight in the orogenic load to the south.

In addition, we have the thick-skinned domain in the orogenic belt in the northern region, and the major shortening is related to thin-skinned structures such as the triangle zones of the section S₂ and S₃. This orogenic belt transports the deformation westward to the MMV basin, where these frontal thrust sheets develop thin-skinned structures. The shortening values allow us to define that the major rates are directly related to zones where we have weak sedimentary layers favoring the generation of thin-skinned structures.

The non-reactivated buried structures in the MMV allow us to infer that the sedimentary rates overpassed the tectonic uplift rates in this region, as was suggested by Caballero et al. (2013). The western foothills of the EC present fold-related fault but, as was defined by Tesón et al. (2013); Kammer et al. (2020) the EC basin is also affected by buckling in the axial region of the mountain range. In conclusion, we considered that the Mesozoic structures play a significant role in the basin development of the MMV and the EC. The reactivation and inversion of the major structures such as The La Salina or Cantagallo faults served as an orogenic wedge in the basin depocenter development. Furthermore, the areas with major displacement in the orogenic belts are also related to the higher depocenters. The non-reactivated structures in the MMV allow the definition of the extensional domain during the Mesozoic in some areas. We attributed the factors that controlled the selective reactivation to the fault length and style as was proposed by Mora et al. (2009); Caballero et al. (2013), nevertheless, the stress orientation also played a role in the reactivation of the Mesozoic structures (Cortes et al., 2005; Mora et al., 2006). According to Sarmiento (2011) the MMV was affected by compression and transpression events since the Late Cretaceous. Nevertheless, in the seismic data showed in this chapter, we cannot identify transpressive deformation evidence. The selective reactivation mechanism is still not clear and should be studied in more detail.

4. LA CIRA BASEMENT-HIGH, MIDDLE MAGDALENA VALLEY BASIN COLOMBIA

This chapter is a reorganized version of the manuscript published in the book “Andean Structural Styles: A Seismic Atlas” edited by G. Zamora and A. Mora.

Authors: Martin Reyes, Jonas Kley, Andrés Mora, Daniel Bello-Palacios, Andrés Felipe Vargas, Juan Carvajal-Torres, Jose Osorno.

Chapter Overview

In this chapter, we discuss the geometrical configuration of the La Cira Basement-high and the tentative evolution through time; the main objective here is to explore the influence of extensional structures in the present-day configuration and see the relation between the different theories to approach the origin of this high. We debate different interpretations made by different authors based on seismic reflection and tested its geometry. Also, in this chapter, we expose the limitations of our hypothesis and also consider the reliability of others.

Abstract

This chapter addresses the seismic interpretation of the La Cira Basement-high located in the central region of the Middle Magdalena Valley of Colombia. The La Cira Basement-high corresponds to a major basement anticline truncated by an Early Eocene unconformity, which truncates successively younger units east and west of the anticlinal axis. The unconformity surface and overlying Eocene to Neogene units form a much gentler anticline slightly offset towards the east. The basement high is bounded by an east-dipping normal fault to the east and to the west by an east-verging buried reverse fault. The Infantas inverted fault dissects its crest. Based on seismic data and borehole correlations, we mapped and interpreted the present-day structure of the La Cira Basement-high. We then tested different evolutionary scenarios of the paleohigh using forward modeling and a kinematic restoration and compared our results to previous interpretations. We propose that the La Cira Basement-high anticline is associated with a deep-seated, blind basement thrust that may have the same east vergence as the reverse faults we interpreted on the west flank of the La Cira Basement-high. Inversion of Early Cretaceous normal faults is evidenced by thickness changes and preserved normal offsets at deeper structural levels. Finally, we document Late Paleocene - early Eocene thrusting and folding that finalized when the sedimentation rates outpaced the rates of structural relief growth.

Keywords: Basement structures, Mesozoic Inverted structures, Eastern Cordillera, Seismic Interpretation, Northern Andes.

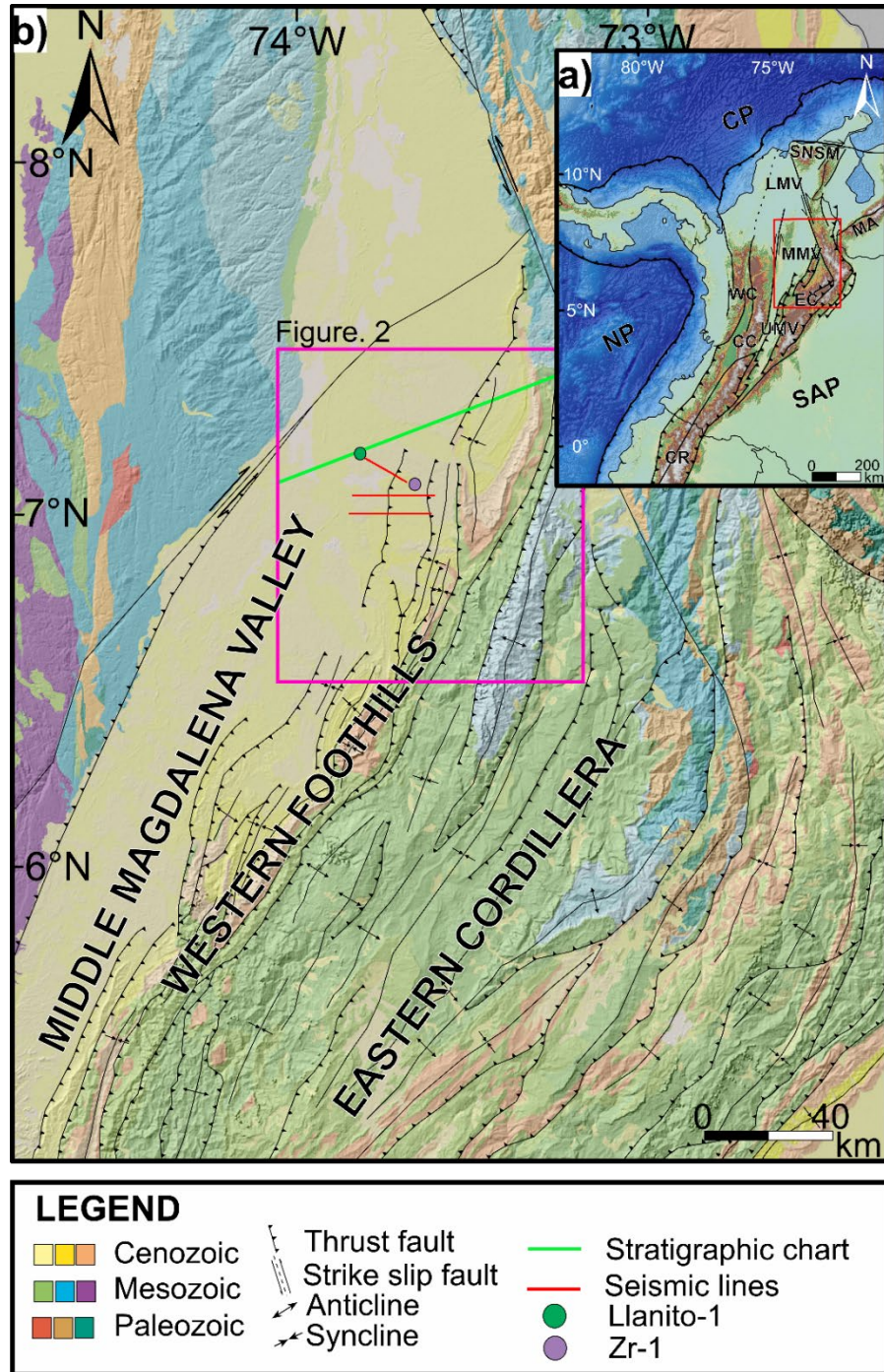


Figure 4-1. a) Regional tectonic map of the northern Andes. CP (Caribbean Plate), SAP (South American Plate), NP (Nazca Plate). Main structural elements are SNSM (Sierra Nevada de Santa Marta), LMV (Lower Magdalena Valley), MMV (Middle Magdalena Valley), MA (Merida Andes), EC (Eastern Cordillera), UMV (Upper Magdalena Valley), CC (Central Cordillera), WC (Western Cordillera) and CR (Cordillera Real). The red box shows the location of [Figure 4.1b](#). b)

Geological map of the central segment of the Eastern Cordillera and Middle Magdalena Valley, modified from Gomez et al. (2015). The purple box indicates location of the study area.

Introduction

We present a well-imaged buried basement high in the Middle Magdalena Valley, the La Cira Basement-high ([Figure 4.1](#) and [Figure 4.2](#)). The Middle Magdalena Valley Basin (MMVB) is an intramountain basin created as a consequence of the long-lasting structural and geomorphic interaction between two main branches of the Northern Andes: The Central and Eastern Cordilleras. The La Cira Basement-high is located close to the western front of the Eastern Cordillera. A buried east-verging, inversion-related reverse-fault system bounds the La Cira Basement-high to the west and an east-dipping normal fault bounds it to the east. The crest of the La Cira Basement-high coincides with the emergent inverted Infantas fault ([Figure 4.3](#) and [Figure 4.4](#)). The basement high trends NNE-SSW, has a length of ~16.3 km, a width of 4,2 km, and depth of ~1.2 km (where depth is defined here as the top of the Jurassic sequence) in its southern part (profile C-C”) at the level of the Girón Fm. (See this relationship in the 3D model of [Figure 4.5](#)). Different origins and geometrical evolutions of the La Cira Basement-high have been proposed in a number of studies based on subsurface interpretation (Morales 1958; Gomez et al., 2005; ANH 2006; Moreno et al., 2011; Kammer et al., 2020). In this work, we develop and discuss a structural model that honors the presently available data to provide a comprehensive structural and evolutionary interpretation for this area. Oil and gas exploration and development in the MMVB began in the early 20th Century with the discovery of the La Cira-Infantas field in 1917 (Dickey, 1992) The basin is considered one of the major hydrocarbon provinces in Colombia with an estimated amount of total recoverable MMboe (Million Barrels of Oil Equivalent) of 4626 and a total remaining 1356 Mmboe (IHS Markit, 2020). The La Cira-Infantas field is the largest oil field in the basin, with a STOIP (Stock tank oil-initially in place) of 762 MMboe (Sarmiento, 2011) while the main reservoir is in Oligocene fluvial sandstones of the Mugrosa Fm. ([Figure 4.6](#)). The principal source rock is constituted by Albian-Cenomanian calcareous shales (La Luna Fm.) (Dickey, 1992). ([Figure 4.6](#)).

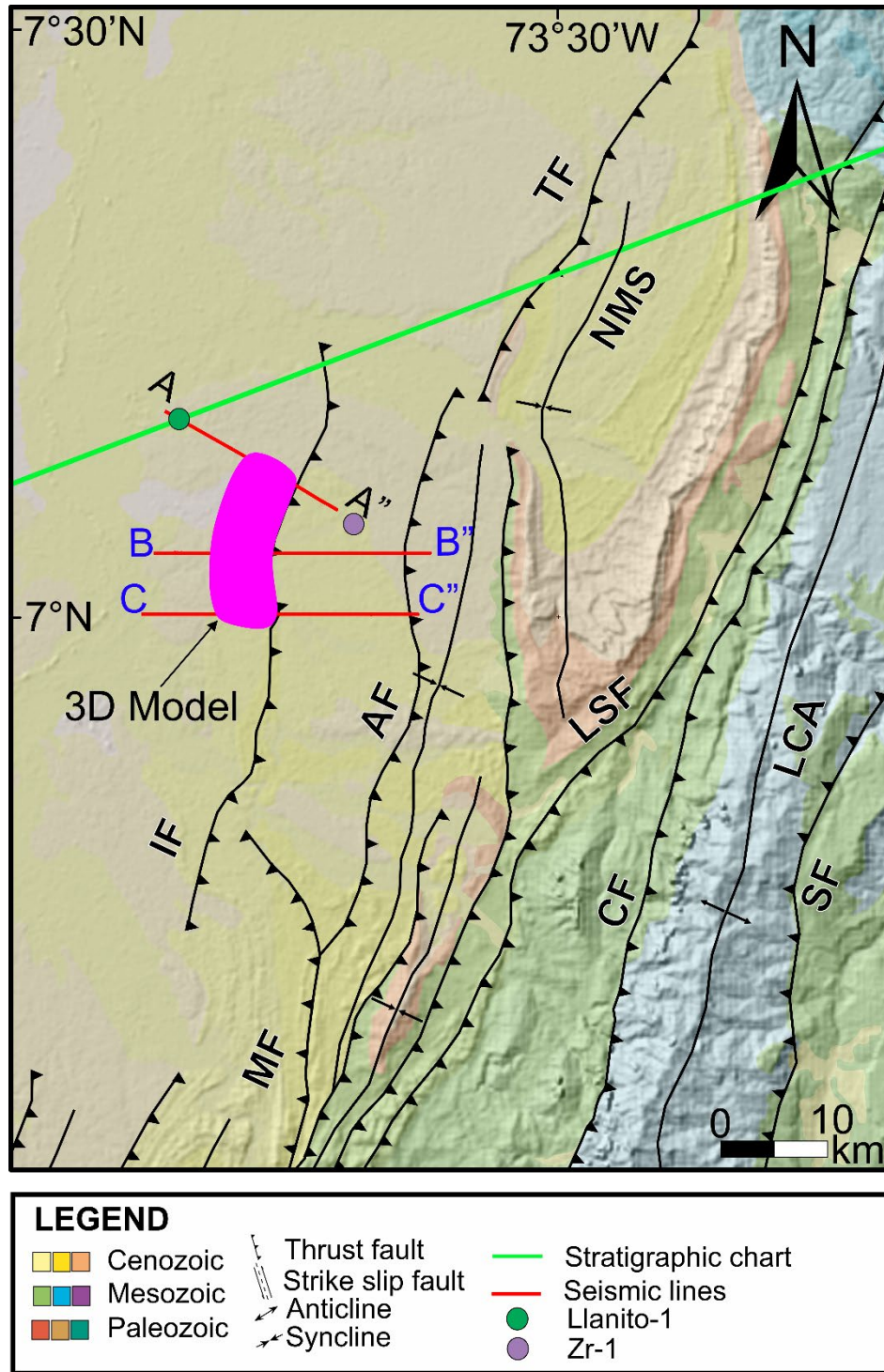


Figure 4-2. a) Geological map showing the main structural elements of the western foothills of the Eastern Cordillera. TF (La Tigra fault), LSF (La Salina fault), NMS (Nuevo Mundo syncline), AF (Arrugas fault), IF (Infantas fault), SF (Suarez fault), LCA (Los Cobardes anticline), CF (Carmen fault), MF (Mugrosa fault), The seismic lines are in red, and the purple polygon is the 3D model illustrated in [Figure 4.5](#).

Basin evolution began with initial rifting in the Mesozoic, probably during the Jurassic. This extensional phase dissected the basement and the Paleozoic sequences into a series of grabens and half-grabens, which were subsequently filled with Jurassic-Cretaceous coarse-grained continental to deltaic sediments (Cooper et al., 1995; Sarmiento, 2001; [Figure 4.6](#)) Many Mesozoic normal fault systems later became inverted during the Cenozoic Andean orogeny (Restrepo-Pace et al., 2004; Mora et al., 2010; Tesón et al., 2013).

The MMVB experienced polyphase shortening evidenced by both west- and east-vergent thrusting. (Restrepo-Pace et al., 2004; Mora et al., 2010; Tesón et al., 2013). Provenance analysis and thermochronological information in the Cenozoic units and structural modelling (Restrepo-Pace et al., 2004; Gomez et al., 2005; Parra et al., 2012; Caballero et al., 2013; Moreno et al., 2013; Reyes-Harker et al., 2015) suggest that the basin evolved as an intramountain foreland basin mainly controlled by the uplift of the adjacent Central and Eastern Cordilleras and their associated thrust systems. Different interpretations of the evolution and present-day structural configuration of the La Cira Basement-high include its development by (a) a west-verging thrust (Morales, 1958; Dickey, 1992), (b) an east-verging buried basement thrust (Gomez et al., 2005), (c) a thick-skin triangle zone (ANH, 2006), and (d) an inverted Mesozoic normal fault (tilted fault block) (Kammer et al., 2020). These options will be further discussed below.

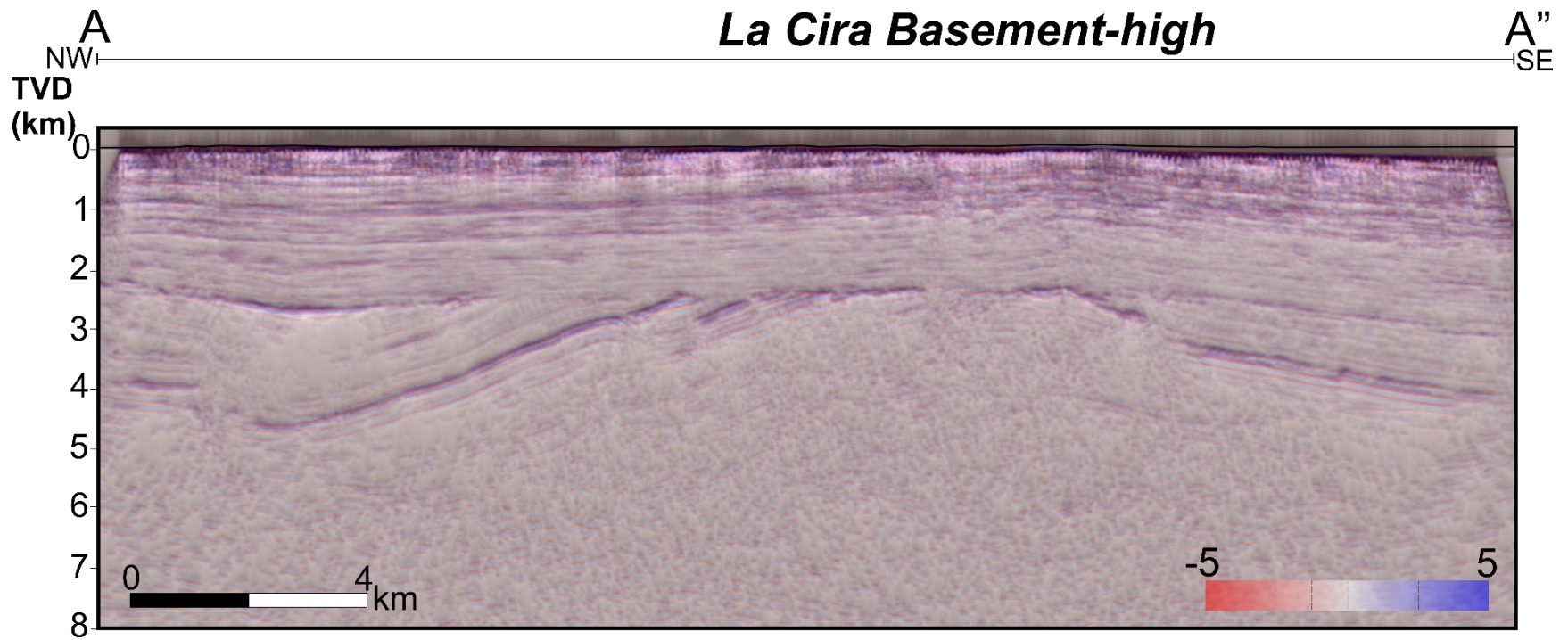


Figure 4-3. Uninterpreted seismic reflection profile A-A'' in depth domain. Location of seismic profile in [Figure 4.2](#). The color scale is in seismic amplitude units.

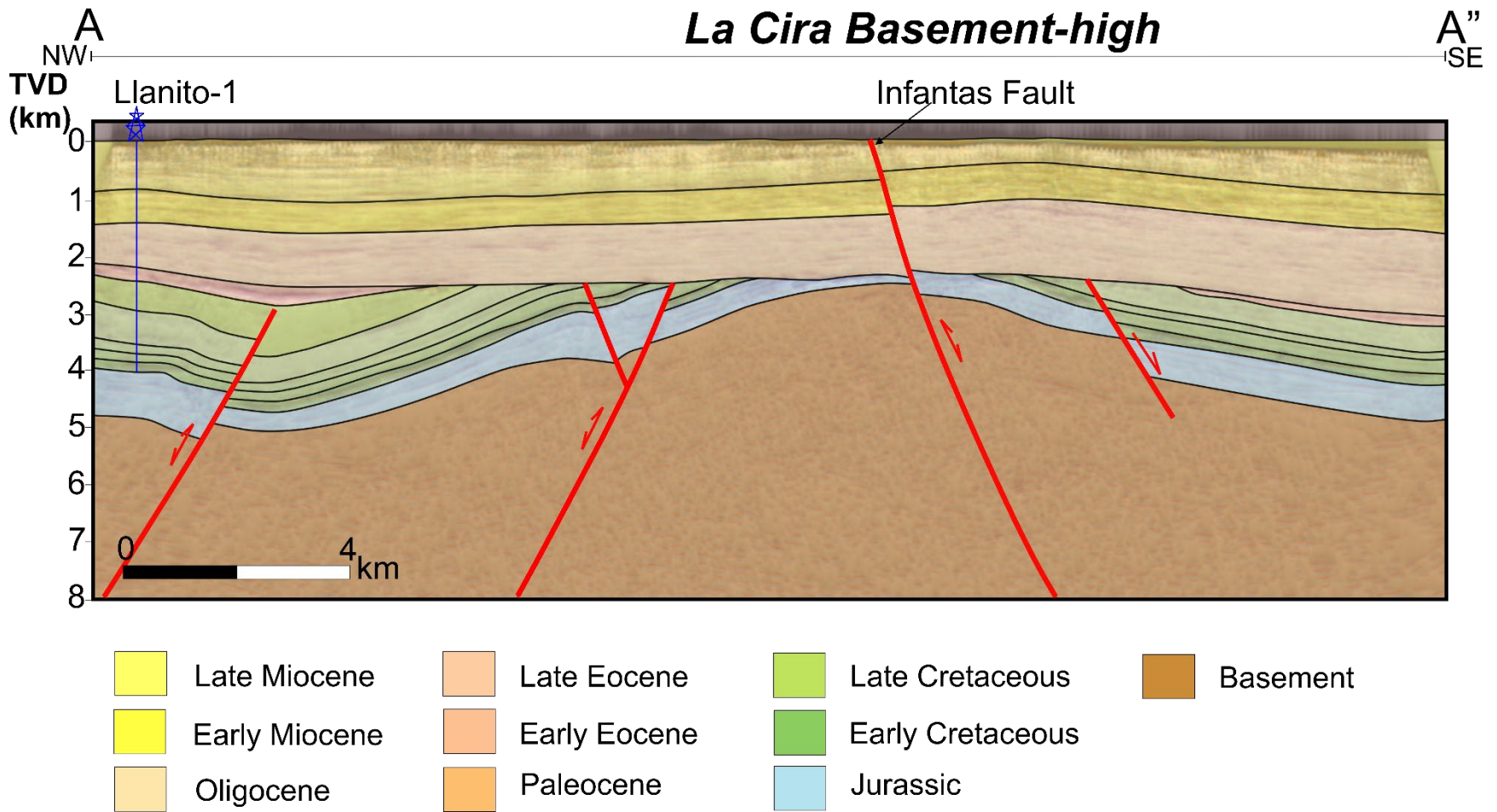


Figure 4-4. Interpreted seismic reflection profile A-A'' in depth domain. Location of seismic profile in [Figure 4.2](#).

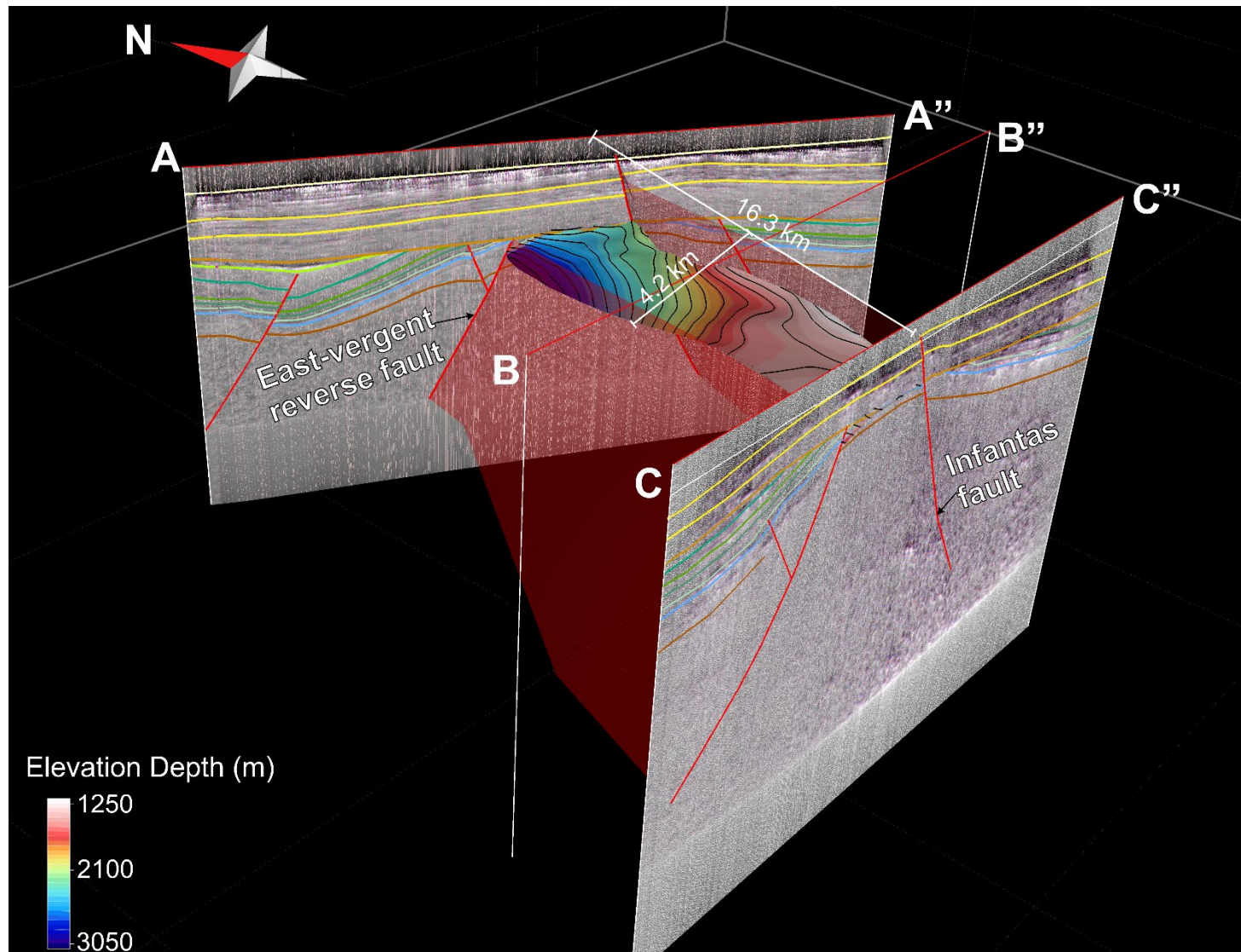


Figure 4-5. 3D Model of La Cira Basement-high. Contoured Early Jurassic horizon (top of Girón Fm.) bounded by the east vergent reverse fault system to the west and truncated by the inverted Infantas fault system to the east. No vertical exaggeration.

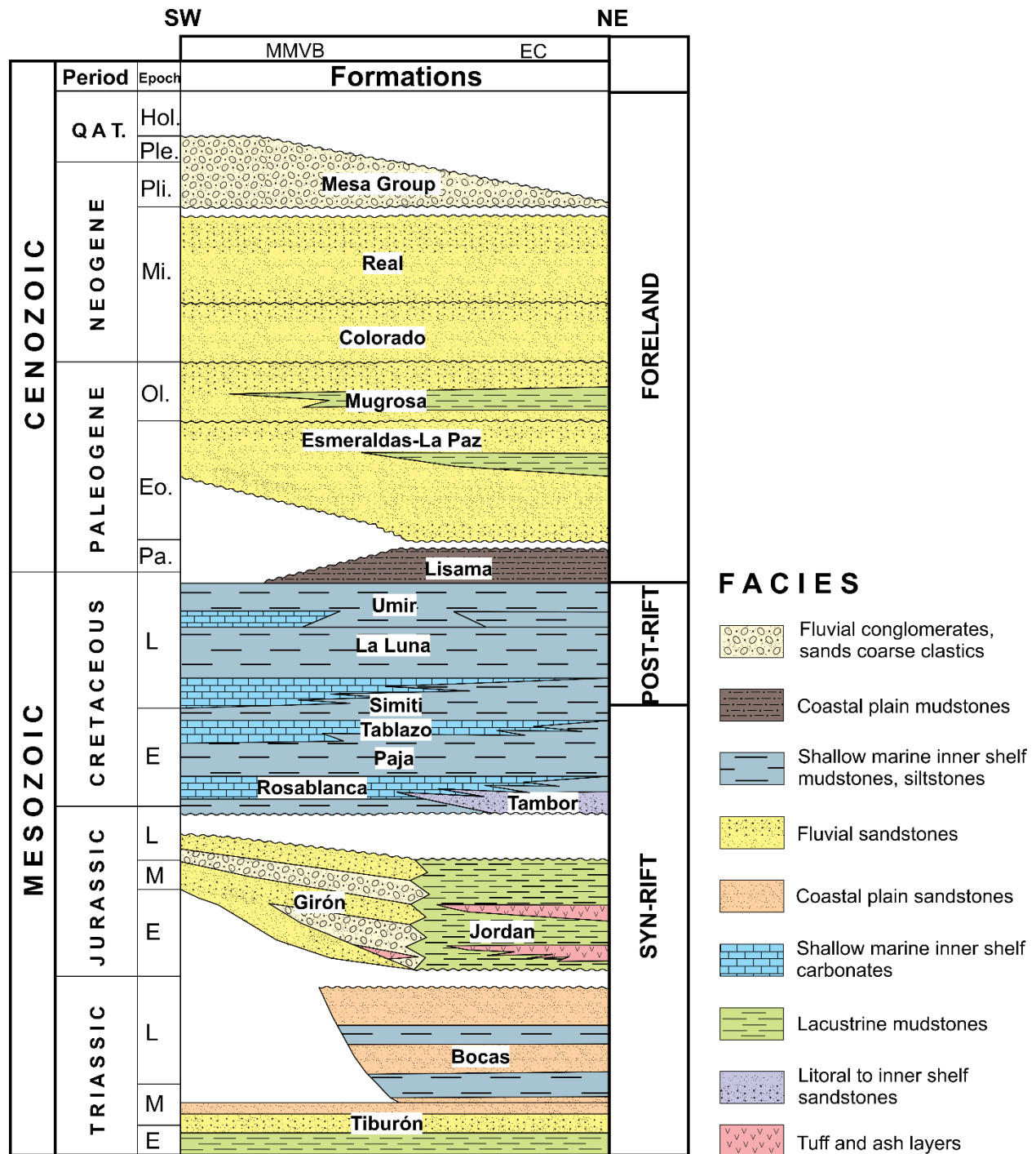


Figure 4-6. Regional stratigraphic chart of the Middle Magdalena Valley Basin and Eastern Cordillera (Modified from Caballero et al. 2013; location of transect in Figure 4.1)

Seismic Interpretation

We interpreted a grid of 2D seismic lines comprising a total length of ~204 km (See the uninterpreted seismic lines in [Figure 4.3](#) and [Figure 4.7](#)). First, we interpreted all seismic lines in time, and then we converted them to depth by employing velocity logs and generating a 3D velocity model in Petrel (© Schlumberger). The formation tops were taken from the Llanito-1 well and were used as control points during the depth conversion. (See the interpretation in [Figure 4.4](#), and see the horizon markers from the Llanito-1 in [Figure 4.8a](#)). Our interpretation of the seismic features was conducted with the aim of defining the main truncations and unconformities. Structural interpretation followed the workflow of Shaw et al. (2005), focused on defining (a) fault cutoffs, (b) kink bands or fold limbs, and (c) fault plane reflections with velocity variations. One of the most conspicuous features is a major unconformity that we used to subdivide our seismic profiles into a pre-unconformity (Jurassic to Paleocene sequence) and a post-unconformity domain (Eocene to Holocene sequences) ([Figure 4.7](#) and [Figure 4.8](#)).

The pre-unconformity domain is mostly characterized by low amplitudes in its deeper parts; however, some internal reflections are probably linked to basement features (see the seismic response in [Figure 4.3](#), [Figure 4.7](#), [Figure 4.8](#) and [Figure 4.9](#), and labelled and named as 6 Basement reflections in [Figure 4.8](#)). The Jurassic units are interpreted following the high amplitude reflections (see the seismic response in [Figure 4.3](#), [Figure 4.7](#) and [Figure 4.8](#), at 4-5 km depth on the sides, and in the core of the Basement-high at 3 to 1.2 km depth from north to south), and their thicknesses are defined according to the geometrical relationship of the over and underlying units and compared with measured values from nearby wells (see the boreholes location in [Figure 4.2](#)). In the upper sector of the pre-Eocene unconformity domain, high amplitudes are linked to Lower and Upper Cretaceous carbonates interbedded with low amplitude shale sequences (see the feature labelled and named as 2 High amplitude reflections in [Figure 4.8](#)). Reflection-free bands disrupting high-amplitude reflections were interpreted as faults (see the seismic response labelled as 4 and named as Loss of signal (Fault) in [Figure 4.8](#)). Fault dips and vergences were determined from associated folding and bisector extrapolation (This bisector relationship is showed in [Figure 4.8](#) in black dashed lines crossing the structures perpendicular). Three faults exclusively affect the pre-unconformity domain: In the west, two NW-dipping high-angle basement reverse faults and in the east a SE-dipping normal fault. (See the faults below the unconformity interpreted in the seismic profile A-A” in [Figure 4.4](#), [Figure 4.8](#) and [Figure 4.9a](#))

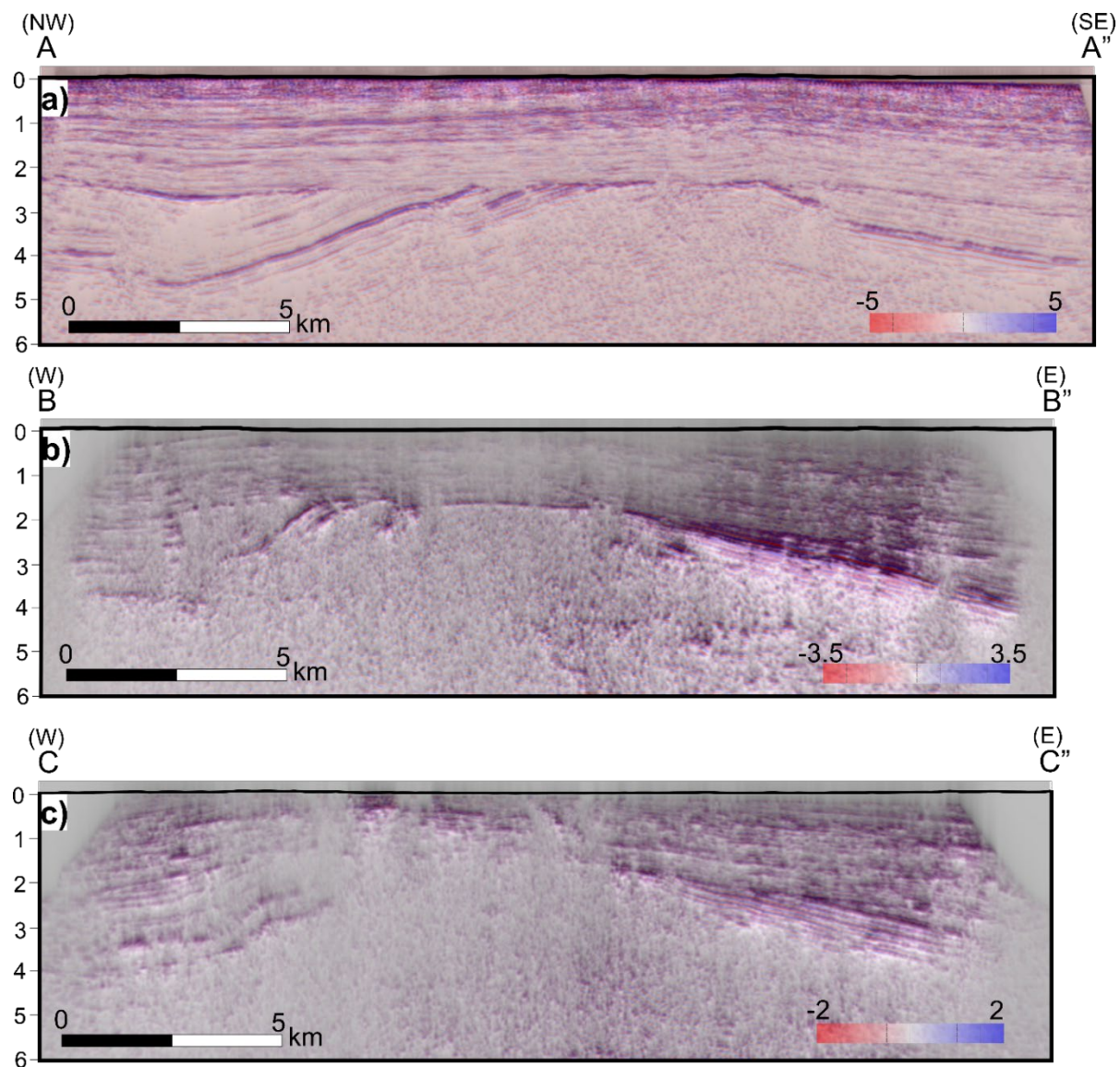


Figure 4-7. Uninterpreted seismic reflection profiles in depth domain. Showing the seismic features from north to south. Location in Figure 4.2.

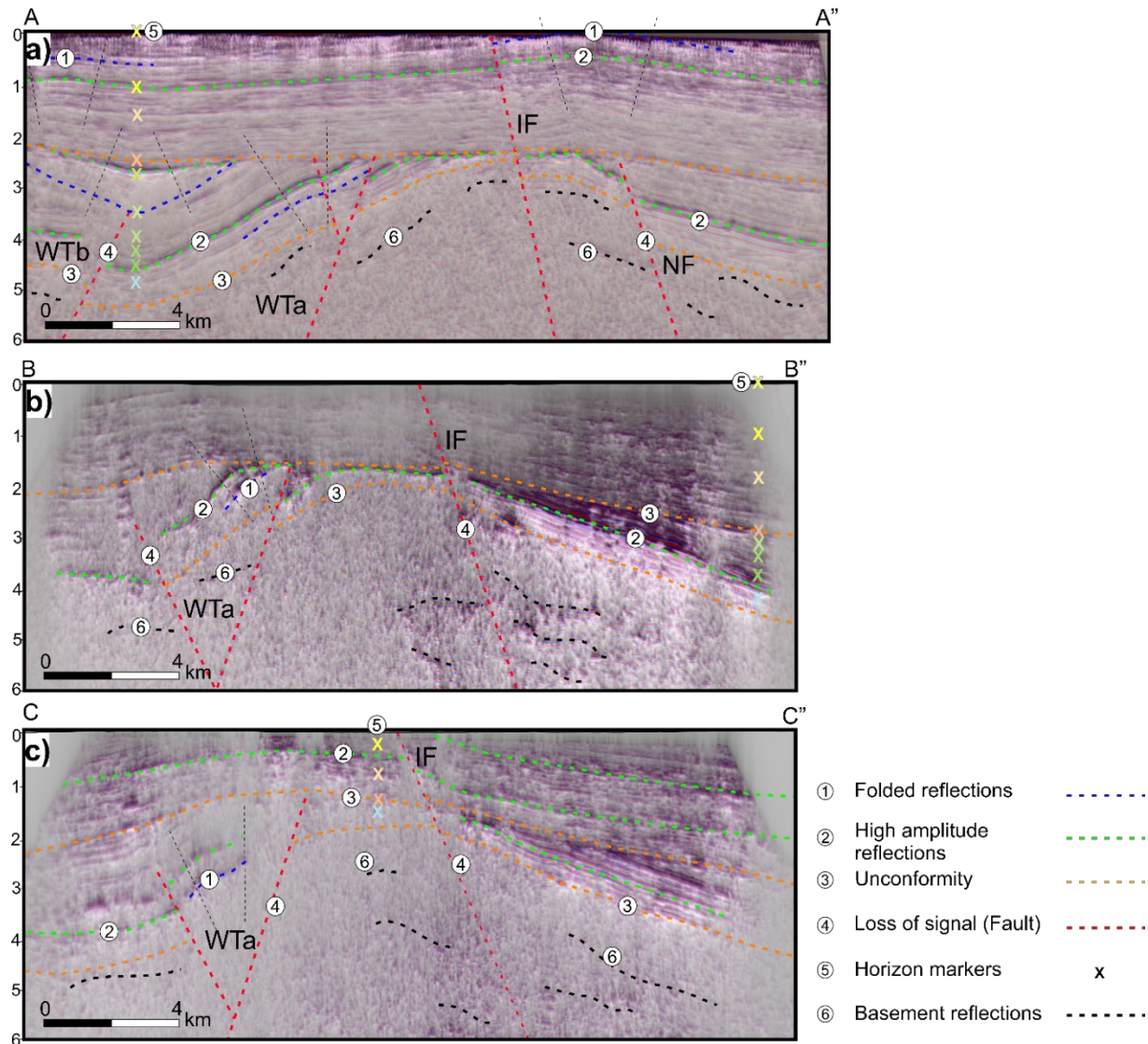


Figure 4-8. Three seismic reflection profiles from north to south in depth domain (km). Varying seismic quality as well as changing stratigraphic and structural relationships are evident. Location in [Figure 4.2](#). IF (Infantas fault) WTa(West thrust system a) and WTb (West thrust system b)...

The Late Paleocene- early Eocene unconformity abruptly truncates the dipping reflections of the lower domain and is covered by gently folded reflections that form a broad anticline (see the seismic response of the anticline in the eastern part of the Figure 4.3, [Figure 4.7](#), [Figure 4.8](#) and [Figure 4.9](#), see the bisector fold relationship in [Figure 4.8a](#) in the hanging-wall of the IF (Infantas fault)). This zone consists of well-stratified reflections with medium amplitude intercalated with remarkably high amplitudes linked to mudstone layers of fluvial origin. (See the features in the upper seismic sequence between 0 to 2 km depth, in [Figure 4.3](#), [Figure 4.7](#), [Figure 4.8](#) and [Figure 4.9](#); labelled and named as 2 High amplitude reflections in [Figure 4.8](#)). Folds affecting this succession reach the surface and are also evident in the digital elevation model, and the relationship between seismic geometry and topography (see the anticline soft topography expression in [Figure 4.2](#), and the seismic evidences in [Figure 4.3](#), [Figure 4.7](#), [Figure 4.8](#), and [Figure 4.9](#); this folds are labelled and named as 1 Folded reflections in [Figure 4.8](#)) Only one fault is evidenced by a loss of amplitude and clearly displaced reflections up to the top of the sequence (see the fault labeled as IF in [Figure 4.8a](#); IF means Infantas fault). The Infantas fault (IF in [Figure 4.8a](#)) is a steeply SE-dipping reverse fault that coincides with the crest of the La Cira Basement-high and has a gentle anticline in its hanging-wall.

Along the strike towards the southern section C-C” ([Figure 4.8c](#)), this anticline becomes less evident, while the high angle Infantas fault below is still apparent by a loss of seismic signal. According to this variation based on the seismic and topographic interpretation, we suggest that the La Cira Basement-high is bounded by an east-verging buried reverse fault to the west and Mesozoic normal faults to the east. Only in section A-A” are there two parallel normal faults: the Infantas fault with an emergent branch on the crest of the La Cira high and another to the east. This second normal fault labeled as NF in [Fig. 8a](#), probably merges with the Infantas fault between sections A-A” and B-B” ([Figure 4.3](#), [Figure 4.7](#), [Figure 4.8](#) and [Figure 4.9](#)).

However, other alternatives based on the anticline geometry in section A-A” for the Infantas fault ([Figure 4.3](#), [Figure 4.7a](#), [Figure 4.8a](#), [Figure 4.9a](#)) are possible, such as: a) a thin- skinned structure detached in the Jurassic or in the basement and an earlier normal fault that was not reactivated during the Cenozoic. b) Previous folding before the fault displacement, however this option is still more complex due to the timing of deformation and the fact that it is assumed to be a recent event.

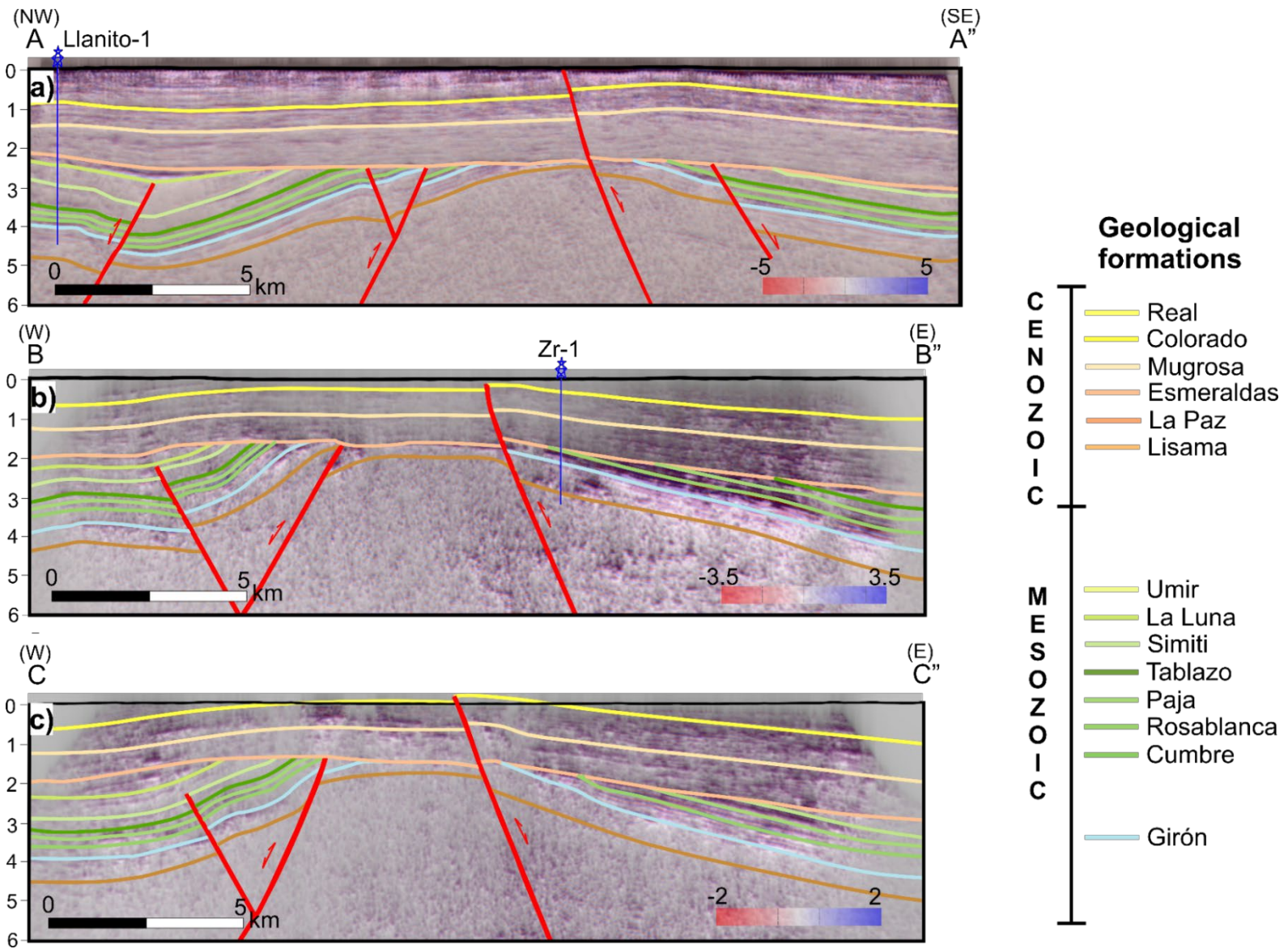


Figure 4-9. Interpreted seismic reflection profiles in depth domain. Showing the structural and stratigraphic relationship from north to south. Location in Figure 4.2

Kinematic Restoration

The present-day interpreted geometry of the highest quality seismic line ([Figure 4.3](#), [Figure 4.7a](#), [Figure 4.8a](#) and [Figure 4.9a](#)) was used as starting point for the kinematic restoration ([Figure 4.10](#)). We used the software MOVE (© Petroleum Experts) to create the kinematic restoration using the Fault Parallel Flow and Flexural Slip algorithms. Some temporal constraints are provided by the thermochronological data generated during the last two decades (Gomez et al., 2005; Mora et al., 2010; Parra et al., 2012; Caballero et al., 2013; Moreno et al., 2013). While the changing geometries were created by backward restoration, we present the results as geological evolution from Cretaceous time to the present in the following paragraphs and [Figure 4.10](#).

The evolution of the MMVB started with extensional faulting in the Mesozoic (Cooper et al., 1995; Sarmiento, 2001). Two different fault trends are present in the La Cira Basement-high, one dipping NW and the other SE ([Figure 4.3](#), [Figure 4.7](#), [Figure 4.8](#) and [Figure 4.9](#)) (Caballero et al., 2013). This configuration suggests a horst delimited on both sides by normal faults of opposite dips at that time ([Figure 4.10a](#)).

Once the extensional tectonics ceased, a regional transgression changed the depositional environment from fluvial continental (Jurassic) to marine (Middle Cretaceous). (Villamil, 1998; Sarmiento, 2001) ([Figure 4.4](#)). A relative sea-level fall began in the Maastrichtian as evidenced from coarser-grained deposition at this time. (Villamil, 1998, Gomez et al., 2005) ([Figure 4.6](#)).

According to unpublished reports from Ecopetrol, the respective unit (Umir Fm.) has good lateral continuity in the central and northern area of the MMVB; and is composed of shales and coarse-grained sandstones towards the top of the sequence, attributed to a coastal plain environment (Villamil, 1998; Restrepo-Pace et al., 2004). The Late Cretaceous (Umir Fm.) is mainly preserved in the cores of synclines, indicating deformation during or after its deposition. Nevertheless, Luis Ernesto Rojas (oral communication) argues based on subsurface evidence, that the Paleocene (Lisama Fm.) is syn-tectonic in those places, where the unit onlaps the flanks of synclines and does not cover the highs. ([Figure 4.6](#)). Moreover, during the Paleocene, the MMVB recorded its strongest regression event (Gomez et al., 2005; Sarmiento, 2011). Referring to these observations, we attribute the absence of Late Cretaceous to Paleocene deposits on the La Cira Basement-high to long wavelength minor surface uplift, probably associated with a regional Late Cretaceous forebulge and superimposed base-level variations ([Figure 4.10b](#), [Figure 4.10c](#)). Studies carried out by Parra et al. (2012) and Caballero et al. (2013) refined the timing of deformation and onset of exhumation of the

Central Cordillera. According to these authors, exhumation started to the northwest of the MMVB in the Late Cretaceous and accelerated during the Paleocene – Middle Eocene (60-50 Ma). The actual basin segmentation occurred coevally with rapid uplift of the Central Cordillera (Cooper et al., 1995; Sarmiento, 2001; Reyes-Harker et al., 2015). Based on mapping campaigns and structural analysis conducted by Restrepo-Pace et al. (2004), the La Paz Fm. was recognized as a syn-kinematic unit. Later, studies carried out by Moreno et al. (2013) and Reyes-Harker et al. (2015) established that the sedimentation occurred in piggyback basins during the Early Eocene (Esmeraldas-La Paz Fm.). Reyes-Harker et al. (2015) suggest a phase of tectonic quiescence during the Middle Eocene which supported the Paleogene deformation proposed by Parra et al. (2012) based on low temperature thermochronology.

Chapter 4. La Cira Basement-high, Middle Magdalena Valley basin – Colombia.

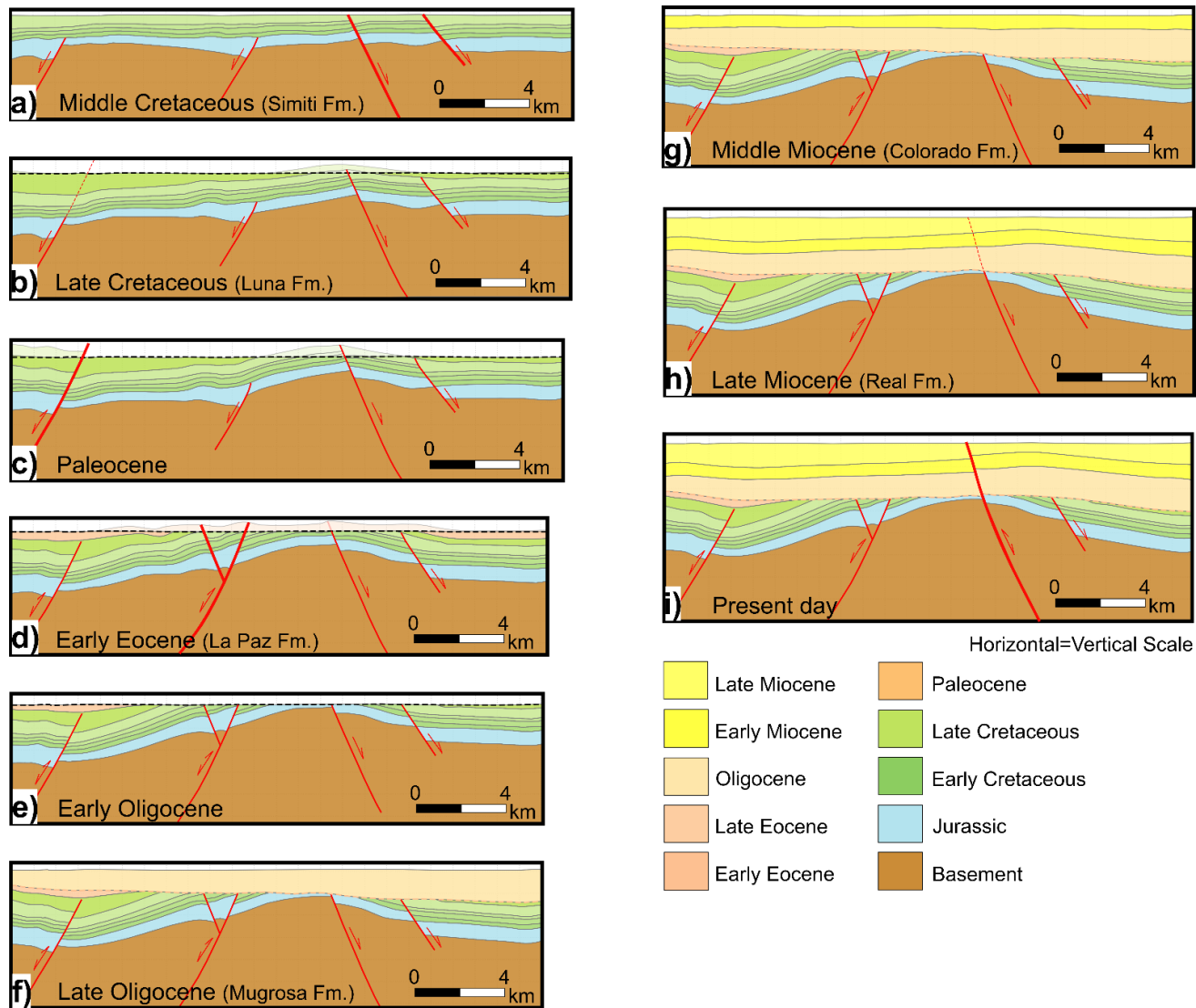


Figure 4-10. evolution of the La Cira Basement-high from middle Cretaceous to present-day configuration. The individual stages were created by stepwise kinematic restoration of [Figure 4.10.i](#)

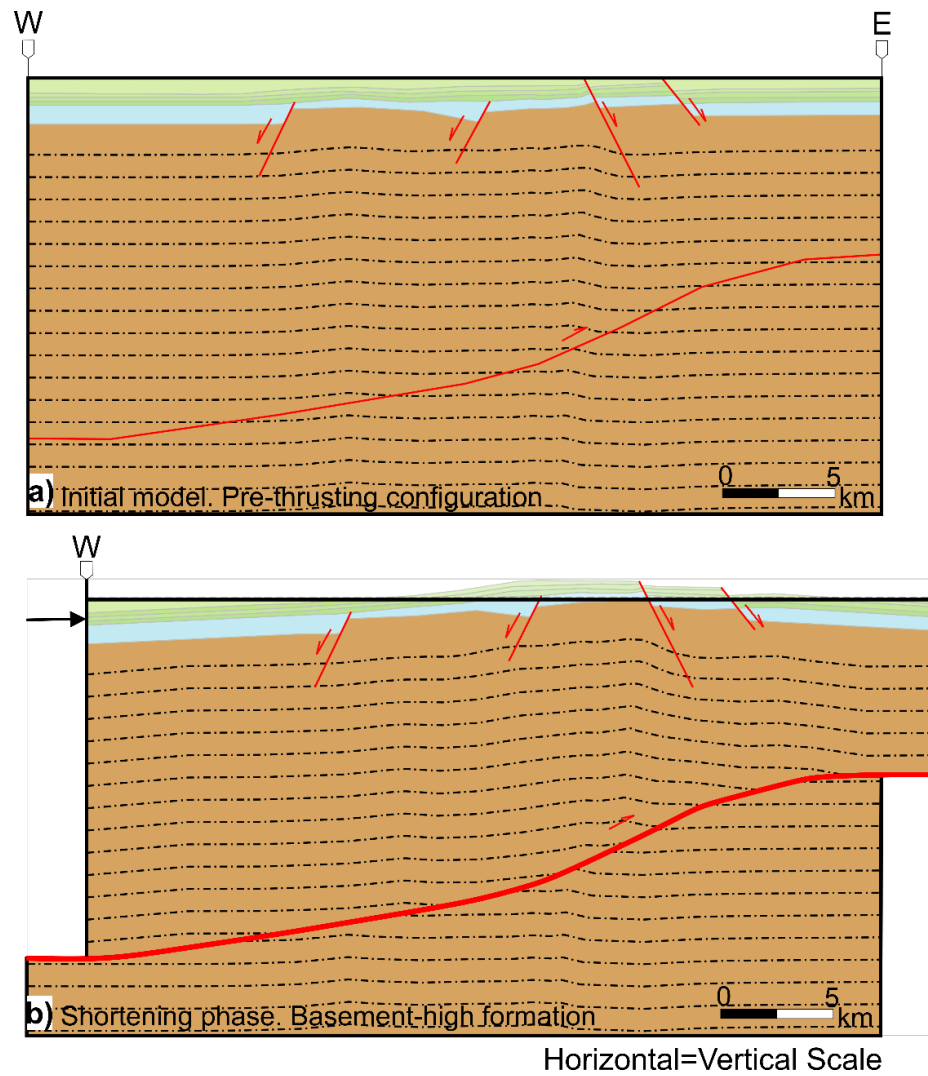


Figure 4-11 Forward model of La Cira Basement-high. a) Pre-thrusting configuration (middle Cretaceous). b) Initial compression with anticlinal folding and further uplift of pre-configured composite horst over the basement thrust fault. Material above the black dashed line is eroded in (b). The dashed dotted lines are a grid of markers drawn approximately parallel to top basement. These illustrate that the deformation of the basement but do not coincide with actual geologic contacts.

New sediment source areas have been documented within the Oligocene record of the MMVB (e.g., Moreno et al., 2011; Caballero et al., 2013; Moreno et al., 2013) which were not evident in the Eocene. Based on those results and constrained by the thermochronological information obtained by Mora et al. (2010), Parra et al. (2012), Caballero et al. (2013) and Moreno et al. (2013), these sources are interpreted to reflect erosional denudation of a deforming and rising Eastern Cordillera. Pre-Oligocene thrusts became inactive and buried in the MMVB during the Oligocene and Neogene (Figure 4.10f, g, h and i). This has been interpreted by Caballero et al. (2013) as being due to sedimentation outpacing crestal uplift rates in those sectors where most of the structures became inactive.

We have shown that the La Cira Basement-high is bounded on the west and east by middle Mesozoic normal faults. The eastern fault is located directly underneath the emergent Infantas reverse fault. Based on this observation we have interpreted the Infantas reverse fault to have dissected the Cenozoic strata upon reactivation of the eastern fault during Cenozoic compression. However, these faults alone cannot explain the entire shape of the La Cira Basement-high. Basement folding is required to form the wide, slightly asymmetric anticline whose growth is evident when Figs. 10a and 10d are compared. Forward modelling (see below) suggests that the shape of this anticline could be created by a deep-seated, east verging, probably blind thrust, likely belonging to the same system as the two east-verging thrusts imaged on the seismic section (Figure 4.10c, d). Nevertheless, the loss of signal below the core of the La Cira Basement-high does not permit the confirmation or rejection this idea, and the hypothetical fault is not shown in Figure 4.10. We have explored our hypothesis of thrust-related basement folding for the La Cira Basement-high with several forward models. For each version we employed the same stratigraphy with the thickness measured and interpreted for each block, testing different mechanisms that might generate the high. The geometries tested were reverse faults, fault-bend folds, fault-propagation folds and blind thrust faults, with east and west vergences detaching in the same depth range (+15 km). At the end we selected the east verging blind thrust as the best-fitting geometry to create the La Cira Basement-high (Figure 4.11). The final fault model has a smoothly curving flat-ramp geometry with a maximum dip angle of 30°. The upper flat may have merged with a precursor of the La Salina fault system generating a triangle zone (Figure 4.12). Shortening of approximately 2.5 km transferred from the west during initial compression is sufficient to generate the positive relief and erode the material missing from the elevated core of the La Cira Basement-high.

Chapter 4. La Cira Basement-high, Middle Magdalena Valley basin – Colombia.

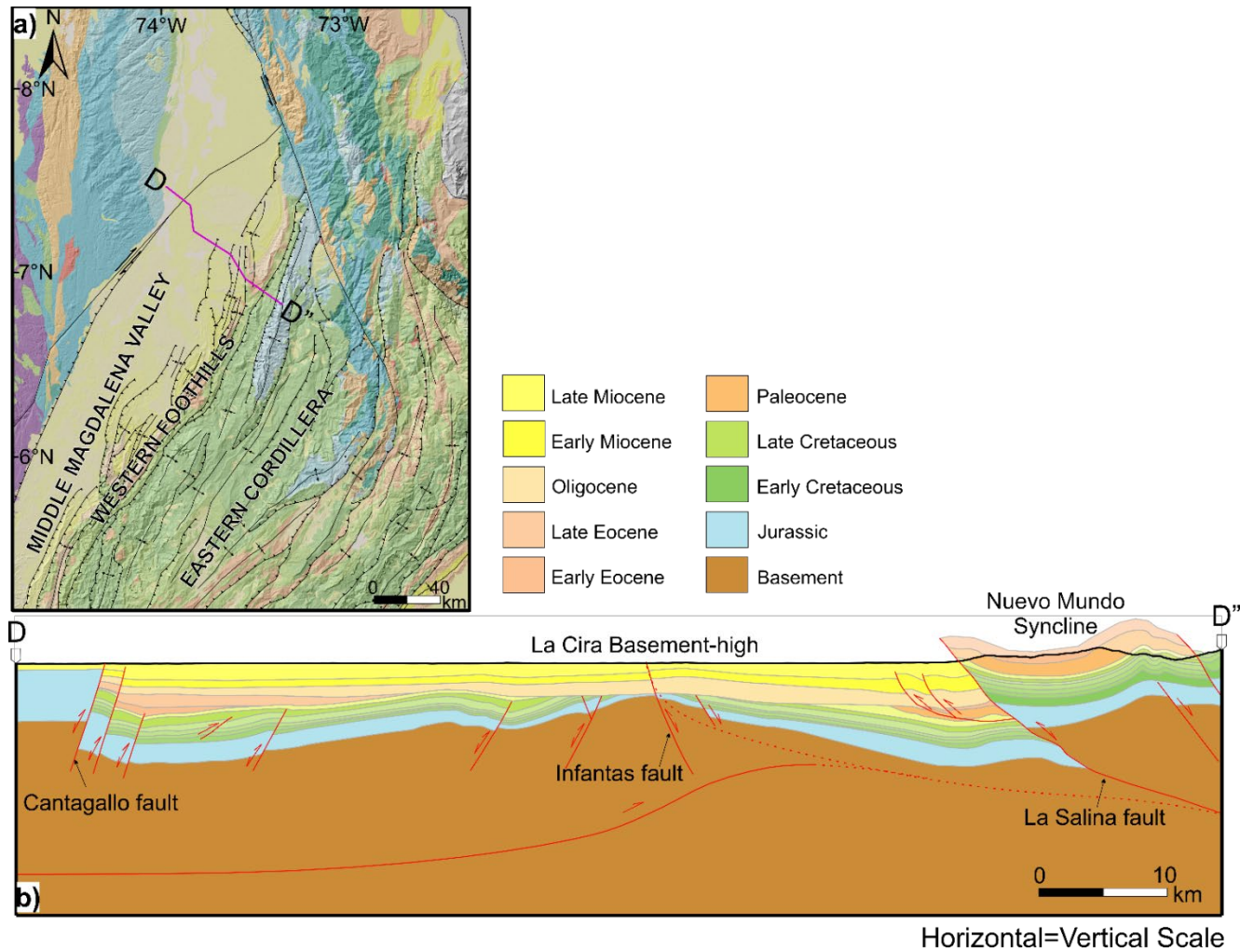


Figure 4-12. a) Regional geological map showing the location of the cross-section in (b) Regional cross-section of the MMVB between the Cantagallo fault in the west and the La Salina fault system in the east. The dashed fault between the La Cira Basement-high and La Salina fault is the upper detachment of the hypothetical blind basement thrust (see [Figure 4.11](#)). It is tentatively shown here to have undergone west-directed reactivation as a splay of the La Salina fault. This splay links up with the Infantas fault, inducing reverse reactivation of only its uppermost part in this scenario and creation of a new emergent branch across the Cenozoic cover.

Alternative models for the La Cira Basement-high

Earlier published studies related to the La Cira Basement-high proposed structural models different from ours. The first interpretation was developed by geologists from Standard Oil Co. (now ExxonMobil). Morales (1958) and Dickey (1992) considered the high to be linked to the Infantas fault which they classified as a high-angle thrust fault, affecting the basal Mesozoic deposits ([Figure 4.13b](#)).

Gomez et al. (2005) showed the La Cira Basement-high to be related with a blind, east-verging thrust fault. The Infantas fault is not shown by Gomez et al. (2005) ([Figure 4.13c](#)), however, the information acquired during recent years allows us to constrain the subsurface image and the evolution with more detail.

The interpretation proposed by the ANH (2006) is significantly different compared to the previous studies and the interpretation presented here. The very high number of faults interpreted and the abrupt thickness variations ([Figure 4.13d](#)) do not match the observations from our seismic profiles.

The model suggested by Kammer et al. (2020) shows the high bounded by the Infantas Mesozoic inverted fault to the east and to the west by a Mesozoic normal fault ([Figure 4.13e](#)). In general, Kammer et al.'s (2020) view of the structural style ([Figure 4.13e](#)) is the closest to the interpretation we present here (compare [Figure 4.4](#) with [Figure 4.13e](#)). However, we have used additional seismic evidence and borehole data to suggest that normal faults on the western flank of the La Cira Basement-high have been reactivated as reverse faults and that a partially inverted normal fault (Infantas fault) creates a structural relief on its eastern flank.

In agreement with previous seismic interpretations, we argue that Mesozoic extensional faults mainly controlled the evolution of the La Cira Basement-high during the initial stage. Nevertheless, part of its positive relief in our interpretation is due to a frontal thrust system of the Central Cordillera propagating to the east ([Figure 4.12](#)), evidenced in the previously mapped east-verging thrust and reverse fault systems and coeval uplift of the Central Cordillera.

Regarding the petroleum system and the trap formation for the La Cira-Infantas field, we analyzed the critical trap timing. According to Dickey (1992) the structure constitutes a faulted anticline with an oil accumulation from the footwall block (west) of the Infantas fault. This structure was formed during the post-Paleocene-pre-Pliocene, and the unconformity surface served as an oil migration channel to the east in areas where the Paleocene and the Cretaceous units were eroded. Nevertheless, our model suggests that this fault was formed during the

Mesozoic and the trap formation was post late-Miocene as a consequence of the Cenozoic orogeny.

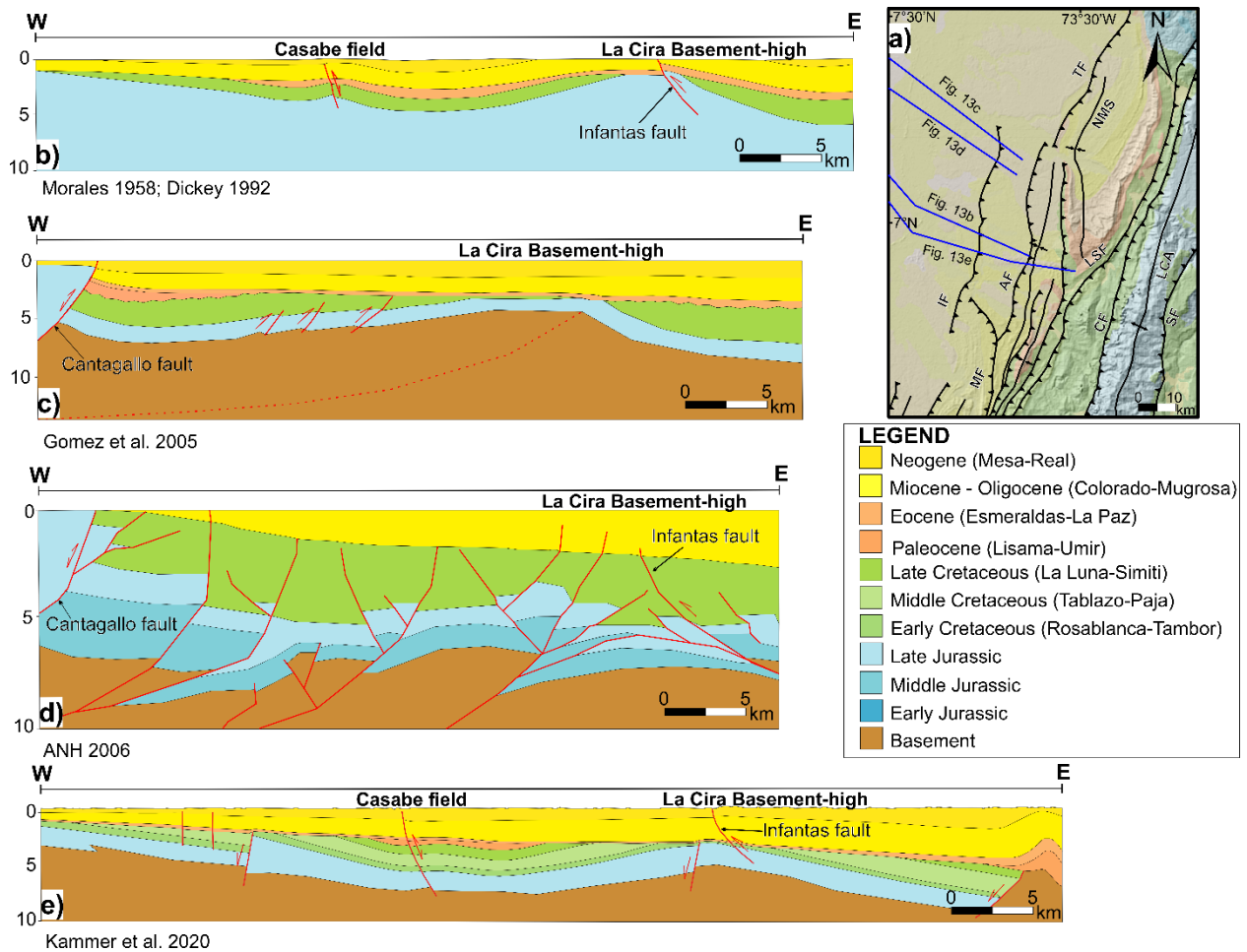


Figure 4-13. Alternative interpretations of the La Cira Basement-high. a) Geological map showing the main structural elements of the western foothills of the eastern cordillera. TF (La Tigra fault), LSF (La Salina fault), NMS (Nuevo Mundo syncline), AF (Arrugas fault), IF (Infantas fault), SF (Suarez fault), LCA (Los Cobardes anticline), CF (Carmen fault), MF (Mugrosa fault). b) Morales 1958; Dickey 1992: Basement anticline with west-verging thrust. c) Gomez et al., 2005: Basement high without emergent faults and probably linked to buried basement thrust (dashed line). Notice different vertical exaggeration. d) ANH 2006: Basement high associated with a thick-skin triangle zone. e) Kammer et al., 2020: Basement high linked to normal faulting (tilted block) with superimposed Infantas thrust fault.

Conclusions

The interpretation done in this study shows that the La Cira Basement-high is long wave-length anticline bounded by west and east verging faults active before the pervasive unconformity at the base of the Oligocene. Only the Infantas Fault has been reactivated recently, cutting and folding the Cenozoic sequence.

The kinematic restoration shows that Mesozoic normal faulting played an essential role in the basin segmentation. Fault dips and Cretaceous sedimentation suggest that the La Cira Basement-high initiated as a horst during this time. High Cenozoic sediment accumulation rates are probably associated with thrust-related uplift of the Eastern Cordillera and concomitant foredeep development in the Middle Magdalena Valley. The only associated deformation in our section is long-wavelength open folding and slight reverse reactivation of the Infantas Fault. Our forward modelling suggests the need to have a deep crustal blind thrust to obtain the present geometry of the La Cira Basement-high.

Our new interpretation reconciles many aspects of earlier ones: The role of Mesozoic normal faults in delimiting the basement high, pre-Eocene thick-skinned thrusting, and basement folding in the hanging-wall of a hypothetical, deep-seated thrust.

5. KINEMATIC RESTORATION OF THE MESOZOIC EXTENSIONAL BASINS IN THE MIDDLE MAGDALENA VALLEY AND THE EASTERN CORDILLERA

This chapter is a preliminary version of the manuscript in preparation to submission.

Chapter Overview

In this chapter, we approach the kinematics through the thermochronometers such as apatite fission-track (AFT) and zircon fission-track (ZFT) published and modeled during the last decade by different authors. We presented different composite cross-sections made with the subsurface information previously discussed in Chapter 3 and with the surface integration from the Eastern Cordillera. These cross-sections were tested geometrically following the structural balancing and restoration principles. The stepwise kinematic restoration was done in 8 steps; we presented the basin evolution from the middle Cretaceous until the present-day configuration.

Abstract

The present-day structural configuration of the Middle Magdalena Valley and Eastern Cordillera basins is associated with the inversion of the Mesozoic rift basin. The correct integration between the geometry evidence plus thermochronological and geochemical information constrains the mountain and basin development. Our main goal is to identify the extension and post-extension events that affected the basin development. To reconstruct the basin evolution, we employed AFT (apatite fission-track), ZFT (zircon fission-track) previously published and modeled by different authors from the Eastern Cordillera, palynological information from the southern localities, and structural constraints from previous works, i.e., shortening, geometry, vergences, cut-off analysis, dips, thicknesses.

This chapter shows six 2-D structural cross-sections located in the central region of the Middle Magdalena Valley and Eastern Cordillera basins. These cross-sections were constructed parallel to the fold-thrust belt propagation in order to reconstruct the Mesozoic configuration before of the Cenozoic orogeny.

Our stepwise kinematic restoration was defined according to the AFT age values from the fission track modeling and the paleo-elevation estimation from the palynological data generated south of our study area. Based on these, we estimated the tentative topography through the time to generate serial restoration in different stages

1. Syn-rift stage, previous ages to middle Cretaceous
2. Post-rift stage, Late Cretaceous to present-day
3. Major deformation, middle Miocene to present-day

This chapter focuses on the transition from the extensional domain to the exhumation onset; however, we analyzed the principal uplift events in the Eastern Cordillera, the variations along the strike, and the relationship with the faults involved.

Keywords: Restoration, Thermochronology, Inversion, Uplift, Mesozoic Inverted structures.

Introduction

The orogenic belts in the world have accumulated different extensional and compressional deformation phases through time. Several cases of orogenic belts and foreland basins are associated with the Cenozoic orogenesis as in the case of the Andes (Allen and Allen, 2013). The topography generated by the orogen uplift is eroded to fill the adjacent basins, i.e., the Middle Magdalena Valley Basin.

The Eastern Cordillera is an excellent case of a double verging inversion at orogenic level (Cooper and Warren, 2020). This orogen was defined as a pop-up structure characterized by thin and thick-skinned geometries. (Restrepo-Pace et al., 2004; Mora et al., 2006; 2010; Moreno et al., 2013).

Here, we present six balanced cross-sections from the Middle Magdalena Valley and Eastern Cordillera basins. These cross-sections were constructed based on seismic and borehole information kindly provided by the ANH; cartography carried out during the last decades by the Colombian Geological Survey at a scale of 1: 100 000, and structural, stratigraphic information published until now and new geological constraints collected during the previous fieldwork. These serial cross-sections are perpendicular to the strike of the Middle Magdalena Valley, Western Foothills, and the Eastern Cordillera, between latitude 6.50° and 7.50° north, and longitude 74° and 72.50° west, the higher topography values are located in the eastern region of the Eastern Cordillera. The lower relief or null values presented in the cross-sections are located in the Middle Magdalena Valley basin (See location in [Figure 5.1](#)).

Kinematic restorations are aimed to reconstruct the basin development through time. However, most of the orogens present-day configuration do not preserve the entire pre-deformation, syn-deformation, and post-deformation sequences.

The Eastern Cordillera have been affected by compressional stresses during the Cenozoic (Cooper et al., 1995; Sarmiento, 2001; Restrepo-Pace et al., 2004; Toro et al., 2004; Mora et al., 2006; 2008). Due to the last deformation stages in the Eastern Cordillera is rare and difficult to preserve growth strata (Mora et al., 2015). This growth strata facilitates the kinematic calibration through the timing and folding mechanism identification (Suppe et al., 1992; Zapata and Allmendiger, 1996; Vergés et al., 2002). Although, Gomez et al. 2003; 2005 and Moreno et al. 2011 indicated Eocene synorogenic sedimentation in the Nuevo Mundo syncline and Guaduas syncline based on growth strata analysis. The absence of growth strata along the strike of our study area impeded calibrating the cross-sections' kinematics.

Different structural works have been conducted in the Western Foothills of the Eastern Cordillera and Middle Magdalena Valley, employing surface and subsurface information (Restrepo-Pace et al., 2004; Toro et al., 2004; Parra et al., 2012; Sanchez et al., 2012; Mora et al., 2013; Moreno et al., 2013; Tesón et al., 2013).

In this work, we present six cross-sections restored backward from the present-day configuration to the middle Cretaceous. Our cross-sections were constructed using 2D seismic information in the Middle Magdalena Valley and with geological mapping from the Eastern Cordillera. With the main aim to assess the deformation timing and the basin evolution through time, we employed thermochronological data acquired in the last years (Parra et al., 2009, 2012; Mora et al., 2010; Ramirez-Arias et al., 2012; Sanchez et al., 2012; Caballero et al., 2013; Guerrero, 2018). Also, we integrated our information with the palynological data acquired by Hooghiemstra et al. (2006), to calibrate the paleo-topography according to the pollen zonation and the altimetry implication conducted in the southern axial region of the Eastern Cordillera. This chapter aims to approach and reconstruct the basin evolution; our goal is to identify the Mesozoic extensional inheritance (Sarmiento 2001; Kammer and Sanchez, 2006; Mora et al., 2009) and its influence on the basin development in the Middle Magdalena Valley and the Eastern Cordillera. The methodology of this work has been adapted from previous works conducted in the northern Andes (Sanchez et al., 2012; Mora et al., 2013; 2015; Costantino et al., 2020).

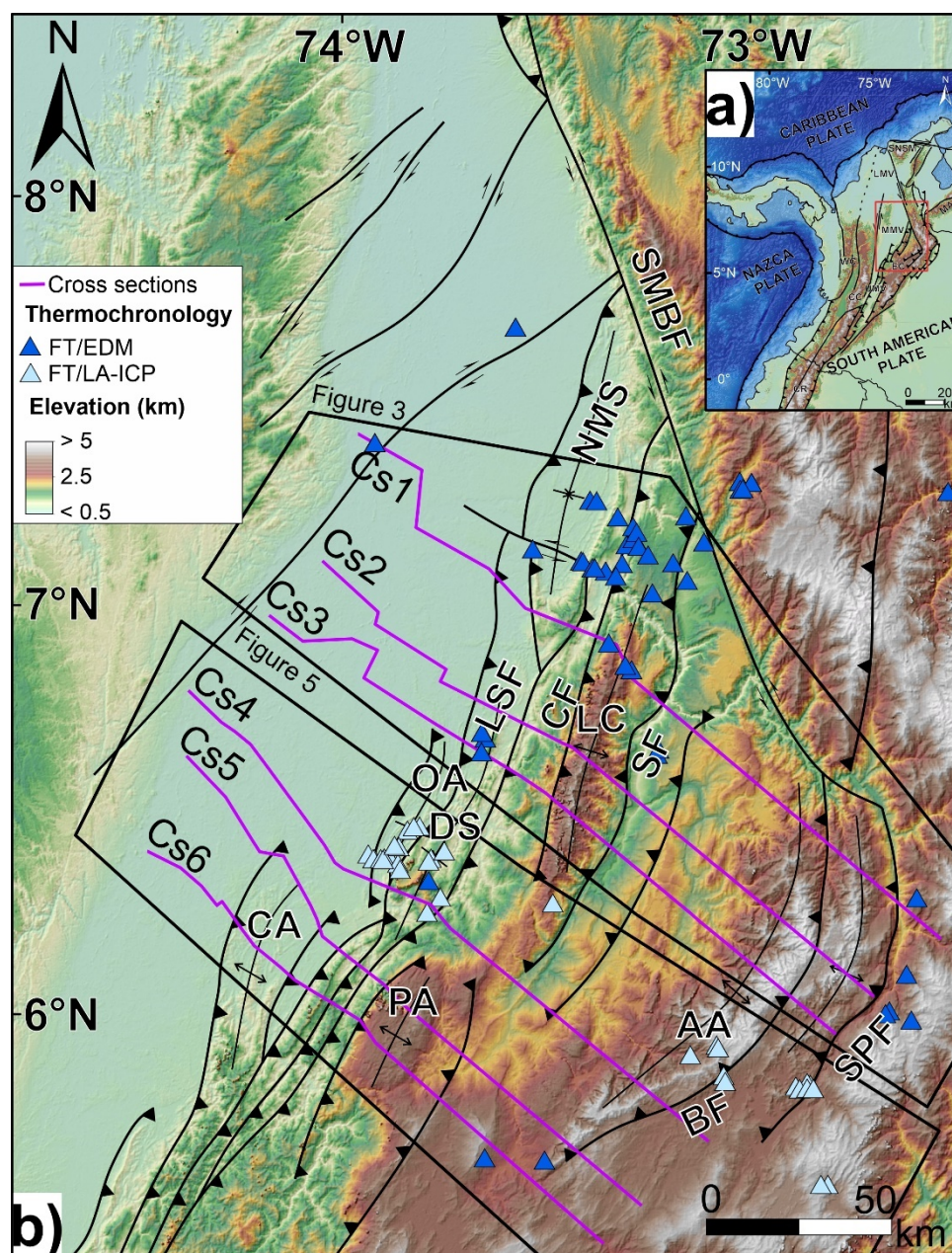


Figure 5-1. a) Present tectonic configuration of the northern Andes, showing the main tectonic features in the study area (orange box), MMV (Middle Magdalena Valley), WC (Western Cordillera), CC (Central Cordillera), EC (Eastern Cordillera). Orange box shows the study area location in [Figure 5.1b](#). b) Digital elevation model of the study area showing the principal folds and faults, distribution of the thermochronologic information and structural cross-sections. The main structural features are named in the map. NMS (Nuevo Mundo Syncline), LSF (La Salina Fault), CF (Carmen Fault), LC (Los Cobardes Anticline), SF (Suarez Fault), AA (Arcabuco Anticline), BF (Boyaca Fault), SPF (Soapaga Fault), PA (Portones Anticline), OA (Opon Anticline), DS (De Armas Syncline), CA (La Corcovada Anticline).

Data and Methodology

Data

In order to assess the structural basin evolution, we integrated different types of data from the Eastern Cordillera and Middle Magdalena Valley basins. First, the surface information was obtained from the public geological mapping of the Colombian Geological Survey at scale 1:1000000. Moreover, this surface information was uploaded and complemented with public information and new data described in the previous chapters. Second, the ANH gently provided the subsurface information, and this information was composed of seismic 2d reflection lines and boreholes (See chapter 4 for the analysis of this information). Third, thermochronological information was compiled from different works near to the study area obtained and published during the last years by Parra et al. (2009); (2012); Mora et al. (2010); Ramirez-Arias et al. (2012); Sanchez et al. (2012); Caballero et al. (2013); Guerrero (2018). Finally, the paleo-topography was constrained employing palynological zonation made by Hooghiemstra et al. (2006), from the southern region of the Axial Eastern Cordillera surrounding the La Sabana de Bogotá.

Methodology

Construction and Balancing Cross-sections

The seismic interpretation was made employing Petrel (© Schlumberger) initially in time domain, and latterly the interpretation and the seismic information was converted to depth domain (see in Chapter 4 more details about the time-depth conversion). Finally, the depth domain information was transferred to Move (© Petroleum Experts); in this software, we integrated the subsurface information such as seismic lines and interpretations, geological tops from different boreholes, and the surface information, i.e., dips, geological maps, thickness control points.

To reconstruct the basin evolution, we made six composite cross-sections following the next balancing steps from Woodward et al. 1989. The cross-sections are perpendicular to the major thrust systems, i.e., the La Salina Fault, parallel to the thrust movement direction. The thicknesses data was constrained employing borehole and field measurements. In our study area, the major folds such as the Los Cobardes anticline or the Arcabuco anticline were included, and a high number of dips were projected to approach the present-day geometry. Our basement depth calculation was determined through the seismic response together with the surface information. We projected the plunge information that is within the range of 2km away from each cross-section. The construction method employed was the kink-band (Fail, 1969); this method preserves the same thickness and inclination angle from the layers. Our methodology

to balance the cross-section was restoring the structures, identifying the mistakes and the fault displacement, and changing the angle of the fault, and trial and error until we approach the geometry. The algorithm that we employed was the fault parallel flow, this algorithm consists that all the hanging-wall moves parallel along the fault plane (Egan et al., 1997).

Thermochronology

A significant sampling density has increased along the Eastern Cordillera and Middle Magdalena Valley basins during the last two decades. In this chapter, we compiled the zircon fission-track (ZFT) and apatite fission-track (AFT) data available and published in our study area (Figure 5.1.).

Thermochronometers have been employed during the last decades to constrain the orogen thermal history, its deformation patterns, and its influence in the exhumation processes (Gallagher et al., 1998; Hurford, 1998; Reiners and Brandon, 2006).

The thermochronology dating methods are employed to understand the thermal history path of a mineral, rock, or geological area. This method is applied to radioisotopic systems (thermochronometers) composed of parental radioactive elements and daughter radiogenic elements (Dodson, 1973; Gallagher et al., 1998; Hurford, 1998; Reiners and Brandon, 2006).

Apatite and Zircon are the ideal minerals to date the cooling events rather than mineralization (Peyton and Carrapa, 2013); despite this, Dunkl et al. 2005 consider that zircon crystals are more mechanical and chemical stables than apatite crystals. Furthermore, the high uranium content allows to record of >100 tracks in a zircon crystal.

Fission tracks are crystal damage produced due to spontaneous nuclear fission decay of ^{238}U (Dodson, 1973; Fleischer et al., 1975; Gallagher et al., 1998). The fission tracks appear at low temperatures and may be annealed if the samples reached high temperatures. The partial annealing zone (PAZ) of apatite fission-track (AFT) are 60-120°C and 200-300°C for zircon fission-track (ZFT) (Green et al., 1989; Reiners and Brandon, 2006). This dating technique is ideally employed to reconstruct thermal histories from 0-300°, and at depths 0-10 km (Reiners and Brandon, 2006; Peyton and Carrapa, 2013). Moreover, according to Gleadow et al. (1986) the ages obtained through the Fission track are not absolute values and do not provide a geological meaning by themselves. Instead, the ages reveal a thermal story, and its integration with other techniques is necessary.

In the Eastern Cordillera and Middle Magdalena Valley basins AFT and ZFT have been applied in order to understand the basin development and its thermokinematic evolution (Mora et al.,

2010; 2013; 2015; Parra et al., 2009; 2012; Sanchez et al., 2012; Caballero et al., 2013; Carrillo et al., 2016; Guerrero, 2018).

We employed the previous results obtained and modeled from different authors in the study area; we compared the age variations and the main structures and analyzed different structural scenarios according to age values. In the end, we employed the AFT and ZFT to calibrate the stepwise kinematic restoration from the six cross-sections. Thus, our study area is divided into the northern and southern areas according to the structural domains and the available thermochronological information.

Thermokinematic Restoration

In this chapter, we employed the AFT and ZFT to constrain the thermal story for each sample, and we analyzed the possible cooling events and their relation with the fault kinematics and structural evolution for each step. Moreover, we employed the palynological results and analysis made by Hooghiemstra et al. (2006) to approach the topographic evolution and inferred the paleorelief and evolution of the Eastern Cordillera.

The paleoaltimetry is an essential input to calibrate the exhumation and cooling relation and see the evolution patterns. Although, the paleo-topography could be subject to errors and uncertainty depending on the proximity and quality of the data (Constantino et al., 2020). In this chapter we used the data from the la Sabana de Bogota, these samples were projected to the structural trend to obtain the average relief from each geological time in each cross-section. The paleoelevation in the la Sabana de Bogota constrained with pollen oscillates between 550-700 m during the Miocene, and the values above 2500 m during the Quaternary that fit with the present relief.

The algorithm employed for the kinematic restoration was fault parallel flow (Egan et al., 1997); we defined the ages according to the major tectonic events, but, in this sequential restoration, we started from the present-day to the middle Cretaceous configuration. Here we assumed the middle Cretaceous as part of the syn-extensional event in the study area. Our restoration follows the principles of ramp vs. flat of Wilkerson and Dicken, 2001. However, we consider that the model precision depending on many factors and constraints that limit the uncertainty. Despite this, the proper use and integration of the information collected in this chapter will allow us to approach the deformation through time. The stepwise kinematic restoration was conducted in Move (© Petroleum Experts) following the previously mentioned steps.

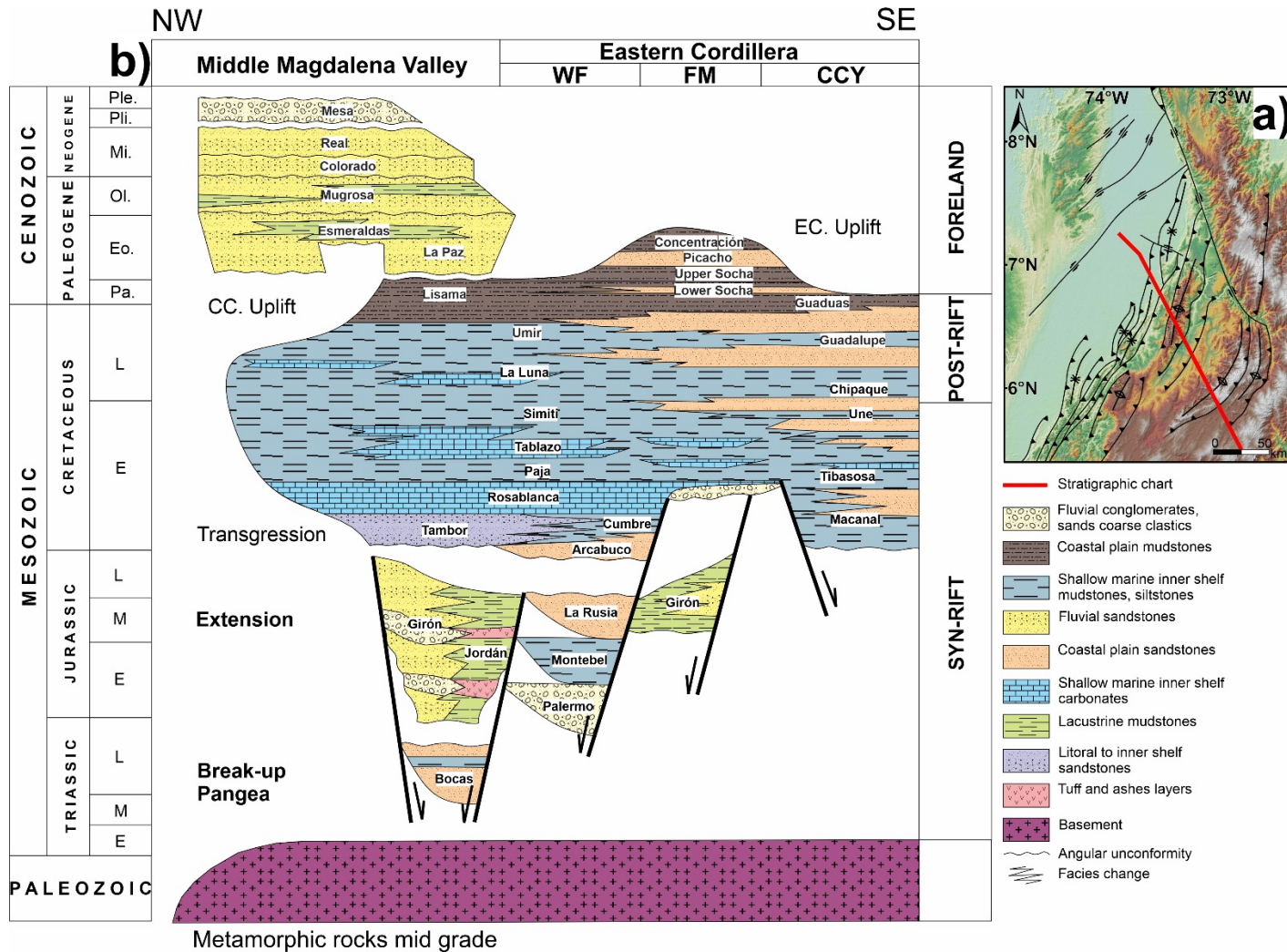


Figure 5-2. a) Digital elevation model of the study area showing the principal folds and faults, and the distribution of the stratigraphic chart described further in [Figure 5.2b](#) b) Regional stratigraphic chart modified from Moreno et al. 2013 comparing the stratigraphy of the Middle Magdalena Valley and the Eastern Cordillera, (WF) Western Foothills, (FM) Floresta Massif and (CCY) Cocuy sub-basin.

Stratigraphy summary

The Eastern Cordillera and Middle Magdalena Valley basins have been developed as a result of plates interactions in the northern Andes region. These basins are classified as an inverted Mesozoic basin during the Cenozoic and an intermontane basin, respectively (Cooper et al., 1995; Sarmiento, 2001; Toro et al., 2004; Kammer and Sanchez, 2006; Mora et al., 2006;2009;2010;2013; Parra et al., 2009;2012)

The stratigraphy infill in the study area comprises a syn-rift sequence from the Late Triassic to the middle Cretaceous and a post-rift sequence from the middle-Late Cretaceous to the present. (Figure 5.2) In this chapter, we describe the sequence from older to younger geological formations. The basement in this region is not differentiated between it. The basement comprises Precambrian-early Paleozoic medium to high-grade metamorphic complex (Ward et al., 1973; Restrepo-Pace et al., 1997; Cochrane et al., 2014; van der Leijj et al., 2016). These rocks are underlying disconformably the Mesozoic sequence; this unconformity is based on the age relationship between the basement and the upper formation.

The initial basin development is attributed to the basin extension during the Triassic-Jurassic; the sedimentary record was mainly continental with volcanoclastic deposits, i.e., Girón or Noreán formations. However, the basin experienced local transgression events, as in the shallow marine Montebel Formation. (Renzoni, 1967; Cediél, 1968; Cooper et al., 1995; Clavijo, 1996; Sarmiento, 2001; Kammer and Sanchez, 2006)

This deposition occurred in narrow <150km asymmetrical grabens along the Eastern Cordillera and bounded by the Mesozoic structures such as La Salina, Boyacá, Suarez faults. (Cooper et al., 1995; Sarmiento, 2001; Sarmiento et al., 2006), the higher deposition occurred in the western side of the Eastern Cordillera in the Magdalena Tablazo sub-basin and the western central axial part of the Eastern Cordillera. (Fabre, 1983; Cooper et al., 1995) During the Early Cretaceous, the basin experienced a widening, and the sediments were deposited in >180km asymmetrical rifts based on thickness and continuity of the geological formations (Sarmiento, 2001; Toro et al., 2004). The Early Cretaceous sedimentation occurred mainly in a shallow marine environment (Cooper et al., 1995; Villamil, 1998; Sarmiento, 2001).

The post-rift and thermal subsidence occurrence with the basin cooling this event had been attributed to the middle Cretaceous, according to Fabre (1983). Nevertheless, Sarmiento (2001) associated the thermal subsidence to the end of the Early Cretaceous. Parra et al. (2012) determined the initial uplift of the western side of the Eastern Cordillera as Late Cretaceous–Paleocene, more recently Carvajal-Torres (oral communication) through the sequence

stratigraphic analysis identified an event during the Late Cretaceous associated to the positive relief and the development of the actual foreland configuration.

The basin inversion occurred during the Late Cretaceous and is associated with the uplift of the Cordilleras. Initially from the Central Cordillera and afterward with the Eastern Cordillera, this event occurred in different stages along the time and have been analyzed and constrained with thermochronological, stratigraphy, and structural data during the last years (Gomez et al., 2003; 2005; Parra et al., 2009; 2012; Caballero et al., 2013; Mora et al., 2006; 2010; 2013; 2015). The sedimentation occurred mainly in a continental environment, starting with a regression associated with the initial Cenozoic orogenic (Cooper et al., 1995); but, the grain size variation corresponds to syntectonic geological formations. The absence of deposition in the Eastern Cordillera and the principal unconformities are mainly associated with the relief development in the Eastern Cordillera, and the Concentración Formation main constituted the foredeep deposits about 23 Ma (Mora et al., 2010).

Results

We present the six 2D structural cross-sections constructed following the previous methodology and restored in eight stages according to the thermochronology AFT and ZFT data. The north zone comprises the cross-sections from Cs₁ to Cs₃ (Figure 5.3). This region is characterized by the wide synclines as the Nuevo Mundo and the Mesozoic structures related to the bounded anticlines as the La Salina, Suarez, and Boyacá faults that bounded the Los Cobardes and the Arcabuco anticlines.

In this northern region, we have the double vergence structures in the Middle Magdalena Valley and two major depocenters associated with the La Salina footwall and the Cantagallo faults (Figure 5.4).

According to the structural domain, the southern region is composed of sections Cs₄ to Cs₆ (Figure 5.5). In this region, we identified tight folds such as the Opón syncline and broad anticlines such as the Los Portones, nevertheless in this region, the absence of Jurassic outcrops allows us to infer the widening of the extensional phase during the Cretaceous. In this region, the structures are thick and thin-skinned, and in the western foothills of the Eastern Cordillera, the folding is mainly related to faulting. Rather than the core of the Eastern Cordillera, where the folding is produced mainly by buckling. (Tesón et al., 2013; Kammer et al., 2020) (Figure 5.6)

We employed the cross-sections Cs₁ (Figure 5-4) and Cs₄ (Figure 5.6) to calibrate the northern and southern kinematic restoration. The AFT and ZFT values employed for the calibration are

summarized in (Table 5.1). This chapter summarized the structural evolution in three main tectonic phases; the first is related to the rifting or extensional phase; we presented the syn-rift event since the middle Cretaceous in the cross-sections.

However, we determined the extensional onset events according to the magmatism in Chapter 2, and based on our new data; we dated as Late Triassic in some areas. The second event is associated with thermal subsidence and cooling. This event is related to the post-rift stage. We classified it from the Late Cretaceous to the middle Eocene, where the basin allows the accommodation until the Concentración Formation in the Eastern Cordillera (Figure 5.2). The last deformation stage is associated with the inversion and uplift of the Eastern Cordillera from the Oligocene to the present-day configuration (Mora et al., 2015).

Kinematic Restoration

The sequential stepwise kinematic restoration was conducted following thermochronological AFT and ZFT values obtained from previous works (See in Table 5.1) (Parra et al., 2009, 2012; Mora et al., 2010; Ramirez-Arias et al., 2012; Sanchez et al., 2012; Caballero et al., 2013; Guerrero, 2018) and the palynological information from Hooghiemstra et al. 2006 in the La Sabana de Bogotá region (Figure 5.7). To calibrate our interpretation and identify the reset and annealed samples, we plot the AFT values from the hanging wall and footwall of the main structures, i.e., La Salina, Boyacá, and Cantagallo faults together with the stratigraphic age for the northern section Cs1 (Figure 5.4) and the southern region (Figure 5.6).

Syn-rift domain

The basin was developed in a narrow rifting during the Triassic-Jurassic in a continental environment (Cediel, 1968; Cooper et al., 1995; Clavijo, 1996; Sarmiento, 2001; Kammer and Sanchez, 2006). During the Early Cretaceous, the basin experienced a transgression process, and the basin deepened during the Coniacian -Turonian when the basin reached the major depth (Villamil, 1998). According to the data from AFT and ZFT until the middle Cretaceous, the basin did not experience any compressional event and was under the extensional domain; according to our thickness measurements database, we can infer that this was the time associated with the sag or the rift ending.

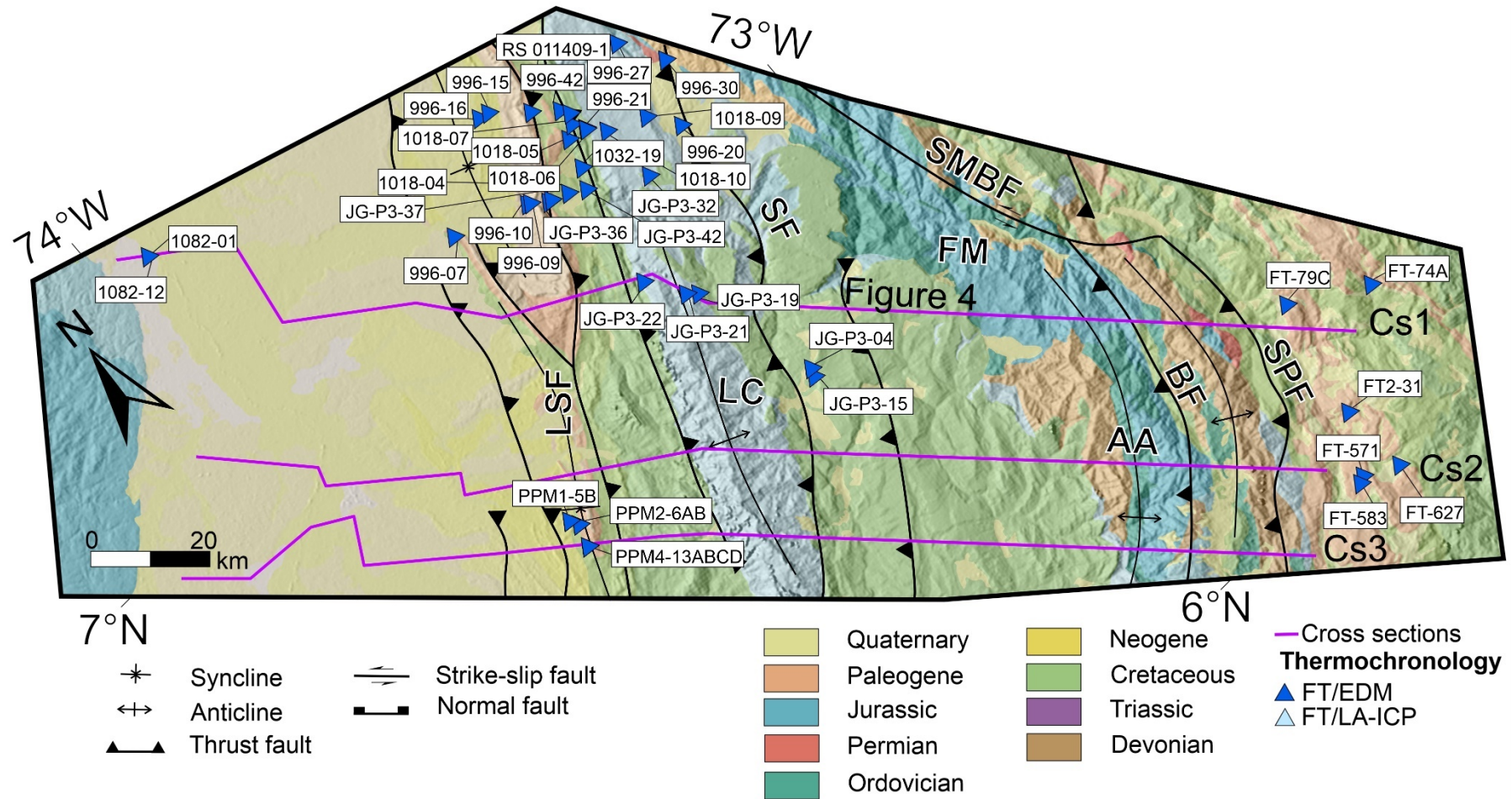


Figure 5-3. Geological map of the northern region, showing the AFT and ZFT samples and the northern cross-sections. Main structural features are showed in the map LSF (La Salina Fault), LC (Los Cobardes Anticline), SF (Suarez Fault), AA (Arcabuco Anticline), SMBF (Santa Marta Bucaramanga strike slip fault), BF (Boyaca Fault), SPF (Soapaga Fault). See location in [Figure 5.1](#).

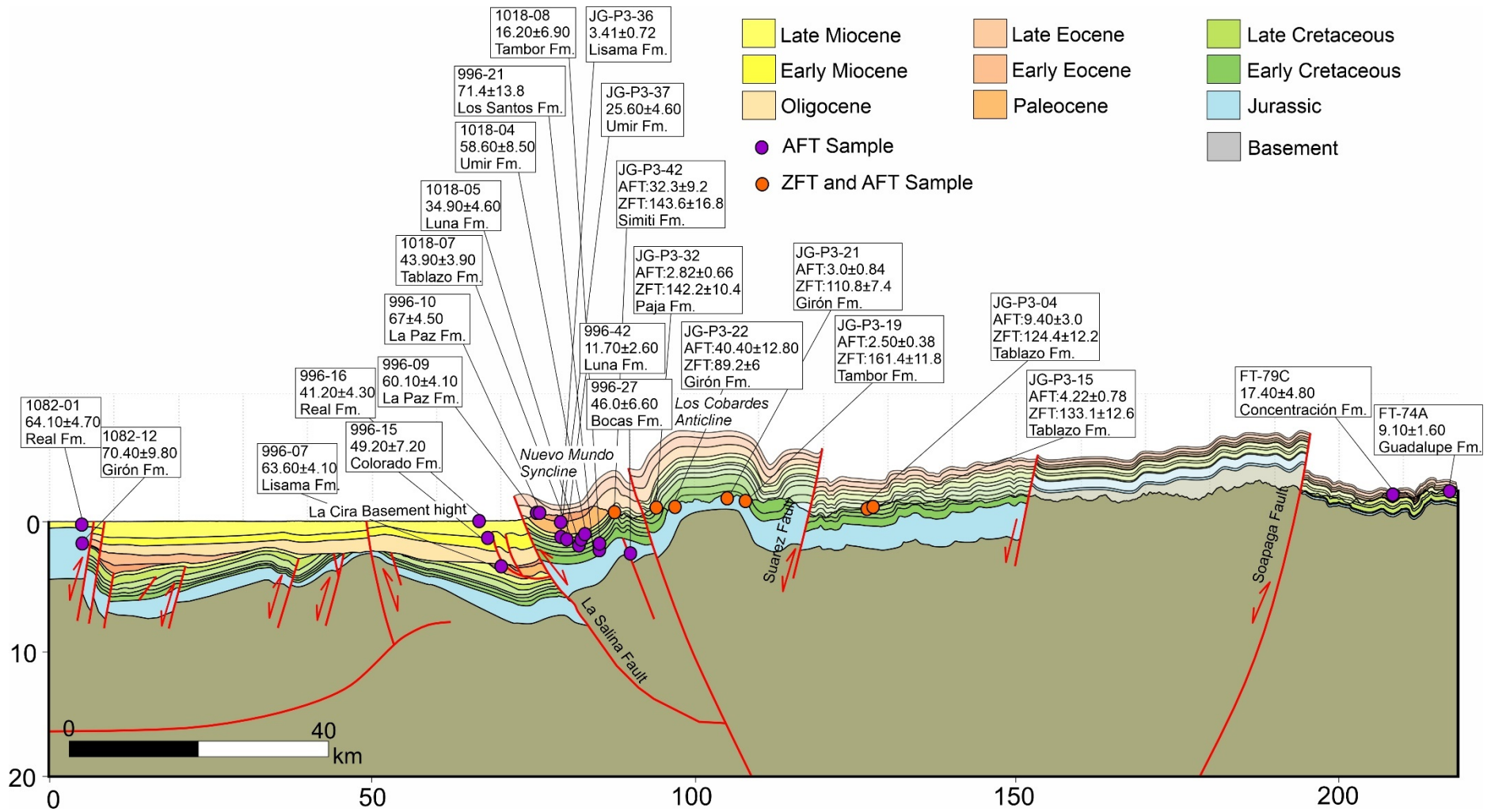


Figure 5-4. Structural cross-section Cs1 located in the northern region. Showing the major structural features and the projection of the AFT and ZFT samples in the northern region. See location in Figure 5.3. Vertical exaggeration 2x.

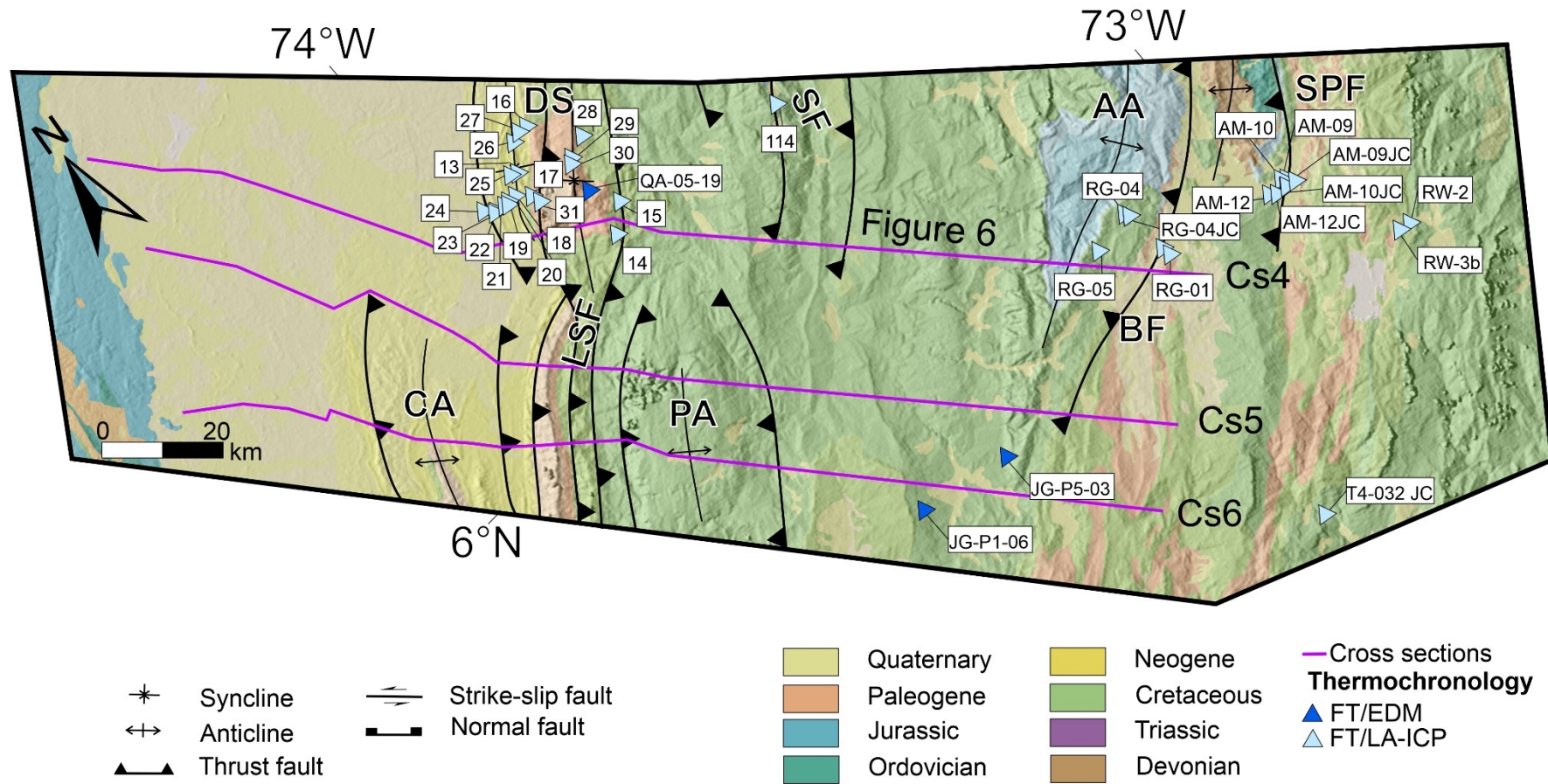


Figure 5-5. Geological map of the southern region, showing the AFT and ZFT samples and the northern cross-sections. Main structural features are shown in the map LSF (La Salina Fault), PA (Portones Anticline), SF (Suarez Fault), AA (Arcabuco Anticline), BF (Boyaca Fault), SPF (Soapaga Fault), DS (De Armas Syncline), CA (La Corcovada Anticline). See location in [Figure 5.1](#).

Chapter 5. Kinematic restoration of the Mesozoic extensional basins

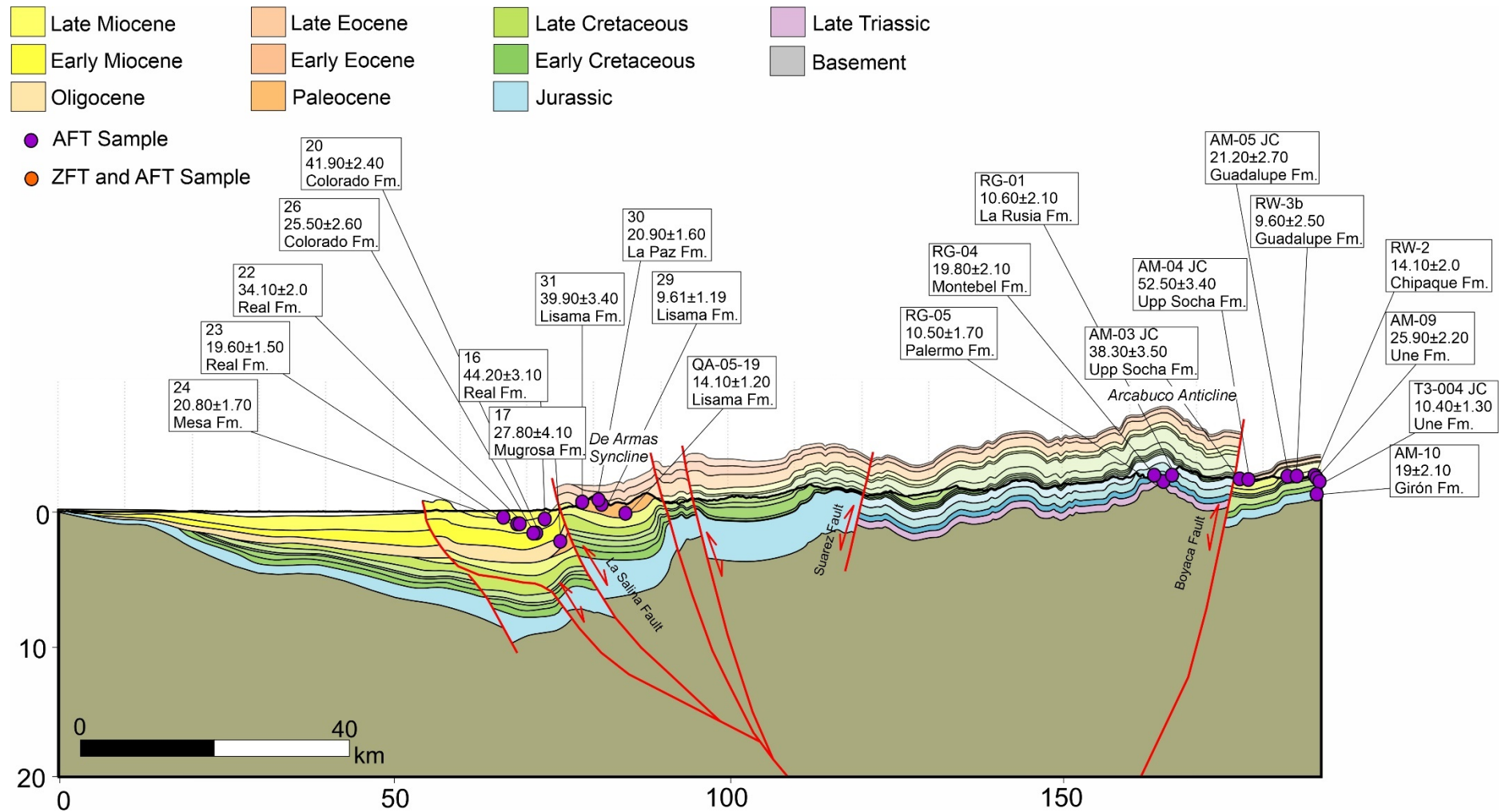


Figure 5-6. Structural cross-section Cs4 located in the southern region. Showing the major structural features and the projection of the AFT and ZFT samples in the northern region. See location in Figure 5.5. Vertical exaggeration 2x

Chapter 5. Kinematic restoration of the Mesozoic extensional basins

Table 5-1. AFT (Apatite Fission Track) and ZFT (Zircon Fission Track) samples employed in this chapter from different sources (Parra et al., 2009; 2012; Mora et al., 2010; Ramirez-Arias et al., 2012; Sanchez et al., 2012; Caballero et al., 2013; Guerrero, 2018). See location in [Figure 5.3](#) northern region and [Figure 5.5](#) southern region. The elevation values are in meters and negative values are from the boreholes in depth (samples highlighted in gray).

Name	Formation	Longitude	Latitude	Elevation (m)	Age	Sigma	Source
RG-01	Rusia	-73.071	5.850	3022	10.6	2.1	Mora et al. 2010
RG-04	Montebel	-73.084	5.918	2886	19.89	2.09	Parra et al. 2009
RW-3b	Guadalupe	-72.834	5.584	2744	9.6	2.5	Parra et al. 2009
AM-05 JC	Guadalupe	-73.385	5.217	2728	21.2	2.7	Ramirez-Arias et al. 2012
RW-2	Chipaque	-72.817	5.584	2656	14.1	2	Parra et al. 2009
RG-05	Palermo	-73.152	5.902	2600	10.5	1.7	Parra et al. 2009
FT-74A	Guadalupe	-72.479	6.229	2536	9.1	1.6	Mora et al. 2010
AM-03 JC	Upper Socha	-73.418	5.217	2529	38.29	3.5	Ramirez-Arias et al. 2012
AM-09	Une	-72.852	5.819	2525	25.89	2.2	Parra et al. 2009
AM-04 JC	Upper Socha	-73.401	5.219	2471	52.5	3.4	Ramirez-Arias et al. 2012
T3-004 JC	Une	-73.368	5.169	2386	10.39	1.29	Ramirez-Arias et al. 2012
FT-79C	Concentración	-72.599	6.283	2322	17.39	4.8	Mora et al. 2010
JG-P3-21	Girón	-73.309	6.854	1932	3	0.83	Guerrero 2018
JG-P3-19	Tambor	-73.294	6.843	1865	2.5	0.38	Guerrero 2018
AM-10	Girón	-72.868	5.832	1513	19	2.1	Mora et al. 2010
JG-P3-15	Tablazo	-73.232	6.636	1305	4.21	0.77	Guerrero 2018
JG-P3-22	Girón	-73.349	6.909	1303	40.4	12.8	Guerrero 2018
JG-P3-04	Tablazo	-73.228	6.649	1217	9.39	3	Guerrero 2018
JG-P3-32	Paja	-73.243	7.031	1173	2.81	0.66	Guerrero 2018
30	Lower La Paz	-73.790	6.376	984	20.89	1.6	Sanchez et al. 2012
31	Upper Lisama	-73.860	6.356	838	39.9	3.4	Sanchez et al. 2012
JG-P3-42	Simiti	-73.332	7.072	803	32.29	9.19	Guerrero 2018
QA-05-19	Lisama	-73.790	6.328	775	14.1	1.2	Mora et al. 2010
29	Middle Lisamma	-73.784	6.383	735	9.6	1.19	Sanchez et al. 2012
996-9	La Paz	-73.417	7.110	680	60.09	4.09	Caballero et al. 2013 (a)
996-10	La Paz	-73.412	7.108	680	67	4.5	Caballero et al. 2013 (a)
996-16	Real	-73.395	7.258	0	41.2	4.3	Caballero et al. 2013 (a)
JG-P3-36	Lisama	-73.389	7.092	-21	3.41	0.72	Guerrero 2018
1082-01	Real	-73.921	7.399	-152	64.09	4.69	Caballero et al. 2013 (b)
24	Lower Mesa	-73.937	6.393	-390	20.79	1.7	Sanchez et al. 2012
16	Middle Real	-73.812	6.460	-475	44.2	3.09	Sanchez et al. 2012
1018-04	Umir	-73.357	7.085	-830	58.59	8.5	Parra et al. 2012
22	Middle Real	-73.922	6.382	-831	34.09	2	Sanchez et al. 2012
23	Middle Real	-73.925	6.381	-905	19.6	1.5	Sanchez et al. 2012
JG-P3-37	Umir	-73.384	7.092	-1017	25.6	4.59	Guerrero 2018
1018-05	Luna	-73.306	7.149	-1148	34.9	4.59	Parra et al. 2012
996-15	Colorado	-73.378	7.256	-1180	49.2	7.19	Caballero et al. 2013 (a)
996-42	Luna	-73.290	7.192	-1268	11.69	2.59	Caballero et al. 2013 (a)
20	Upper Colorado	-73.899	6.384	-1395	41.9	2.4	Sanchez et al. 2012
26	Upper Colorado	-73.842	6.452	-1457	25.5	2.59	Sanchez et al. 2012
1082-12	Girón	-73.921	7.399	-1524	70.4	9.8	Caballero et al. 2013 (b)
1018-07	Tablazo	-73.281	7.179	-1551	43.9	3.9	Parra et al. 2012
1018-08	Tambor	-73.276	7.145	-1764	16.2	6.9	Parra et al. 2012
996-21	Los Santos	-73.276	7.147	-1953	71.4	13.8	Caballero et al. 2013 (a)
17	Lower Mugrosa	-73.865	6.370	-2107	27.79	4.09	Sanchez et al. 2012
996-27	Bocas	-73.160	7.219	-2484	46	6.59	Caballero et al. 2013 (a)
996-07	Lisama	-73.535	7.139	-3557	63.59	4.09	Caballero et al. 2013 (a)

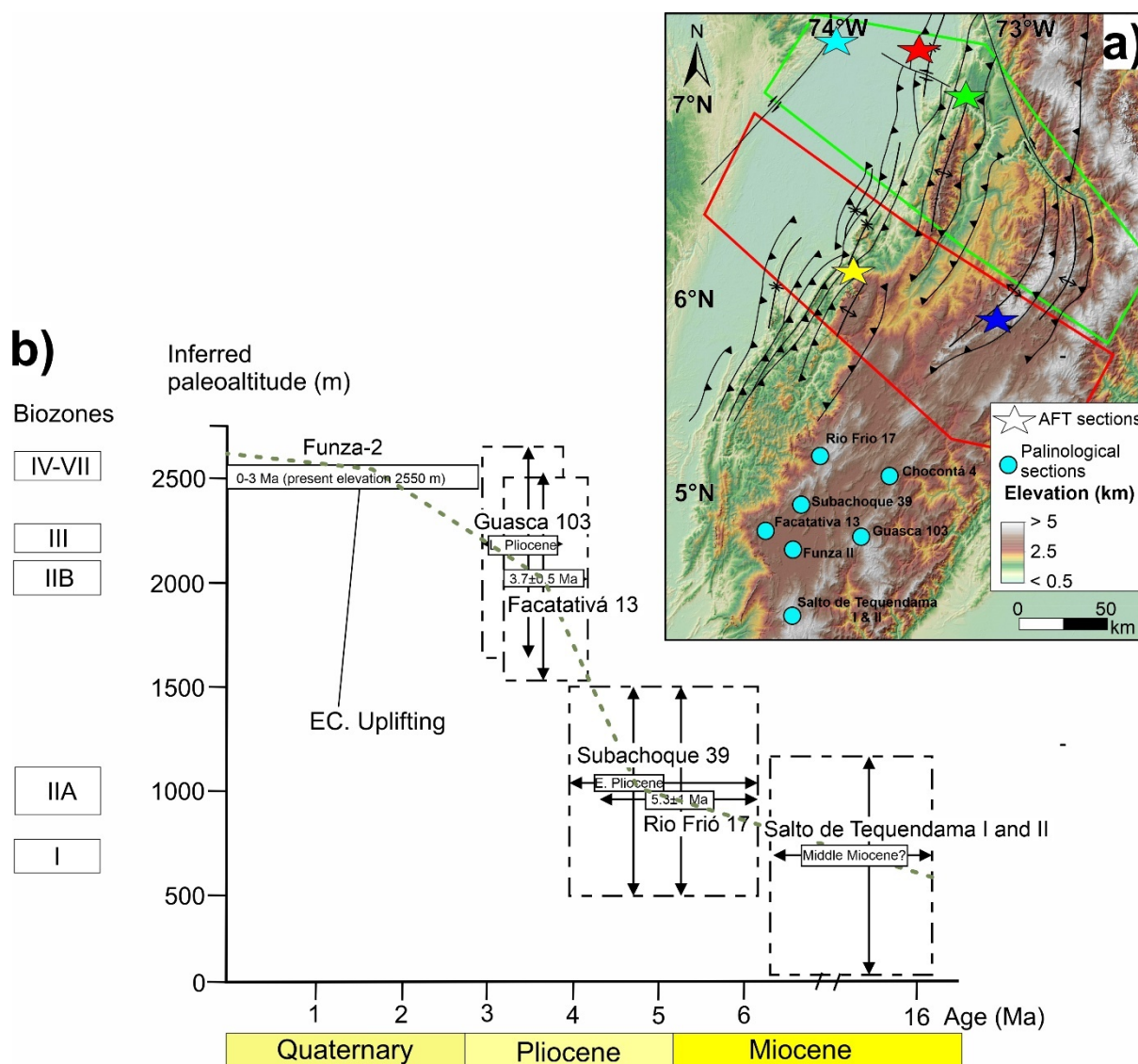


Figure 5-7. a) Digital elevation map of the study area showing the northern and southern regions vs the pollen samples location and AFT sections modeled and compiled from different authors. b) Paleo elevation estimation based on pollen data collected by Hooghiemstra et al. (2006).

Post-rift Domain

In the northern region in section Cs1 (Figure 5.4), the sample 1082-12 from the Jurassic Girón Formation yields an AFT age of 70.40 ± 9.80 Ma, and this value was modeled by Caballero et al. (2013) where he suggested an initial cooling during the Late Cretaceous. In the hanging wall of the Cantagallo Fault, the values of 64.10 ± 4.7 Ma obtained for the sample 1082-01 from the Miocene Real Formation are interpreted as detrital AFT age (Caballero et al., 2013) (Figure 5.8).

AFT Samples were obtained from the hanging wall and footwall of the La Salina Fault. The sample 996-21 from the Early Cretaceous Los Santos Formation has an AFT age of 67 ± 4.50 Ma; according to the time-temperature paths, the onset of the cooling in the hanging-wall of the La

Salina Fault and the northern region of the Los Cobardes anticline started during the Late Cretaceous ± 71 Ma (Caballero et al., 2013). The sample 1018-04 from the upper Late Cretaceous Umir Formation has an AFT age of 58.60 ± 8.50 Ma, and the sample 1018-05 from the Late Cretaceous La Luna Formation has an AFT age of 34.90 ± 4.60 Ma. These ages are interpreted as the early stage of shortening related to the Cenozoic inversion (Parra et al., 2012). Furthermore, the sample 1018-04 was calibrated with R_o vitrinite reflectance inverse modeling, which indicated a cooling event earlier than 55 Ma (Parra et al., 2012). Moreover, the ages from the sample 996-21 and 996-27 from the Los Santos Early Cretaceous Formation and the Bocas Jurassic Formation yielded values between 71.4 ± 13.18 to 46.0 ± 6.60 Ma, respectively. These values are interpreted as the onset of the cooling event in the Los Cobardes region, inverse modeling of the sample 996-21 yielded Late Cretaceous-early Paleocene ages interpreted as the exhumation onset in this region (Caballero et al., 2013) and confirmed the age suggested previously.

Nevertheless, Guerrero, 2018 obtained AFT values from the JG-P3-22 Jurassic Girón Formation with AFT age of 40.40 ± 12.80 Ma and younger AFT values from the basal Cretaceous formations in samples JG-P3-19, JG-P3-32, JG-P3-36, which have AFT age values of 2.50 ± 0.38 to 3.41 ± 0.72 Ma. According to Guerrero (2018) these ages are linked to a Neogene cooling event proposed by Sanchez et al. (2012) in the southern region.

The values obtained from the footwall of the La Salina Fault from the Lisama Paleocene Formation from sample 996-07 yielded values of 63.60 ± 4.10 Ma, and from the upper formation samples 996-15 and 996-16 from Colorado early Miocene and Real late Miocene formations have values of 49.20 ± 7.20 and 41.20 ± 4.30 Ma respectively. Thus, this block has older AFT ages than the stratigraphic ages, probably linked to the partial annealing zone (PAZ) exhumation (Caballero et al., 2013).

In the western region, the uplifting of the Santander massif occurred during the late Eocene based on AFT and ZHe ages (Caballero et al., 2013), nevertheless, AFT ages were obtained from the same authors in the pre-Devonian Silgara Formation and one intrusive of the Bucaramanga gneiss yielded AFT ages of 13.5 ± 2.1 to 15.7 ± 1.7 and 21.4 ± 4.2 Ma, based on these the uplifting event was underway during the late Oligocene-early Miocene (Caballero et al., 2013)

Farther west appeared the Soapaga thrust and the Santander Massif in the hanging wall. The samples FT-74A and FT-79C obtained from the hanging wall of the Soapaga thrust from the Late Cretaceous Guadalupe Formation and the middle Eocene Concentración Formation have AFT ages of 9.10 ± 1.60 and 17.40 ± 4.80 Ma, respectively. According to Mora et al. (2010) the footwall

of the Soapaga fault started its denudation in the late Oligocene-early Miocene, but based on the absence of major faults between the sample locations and the late Miocene AFT ages obtained from the Late Cretaceous samples, they suggested an early Miocene onset of exhumation in this region.

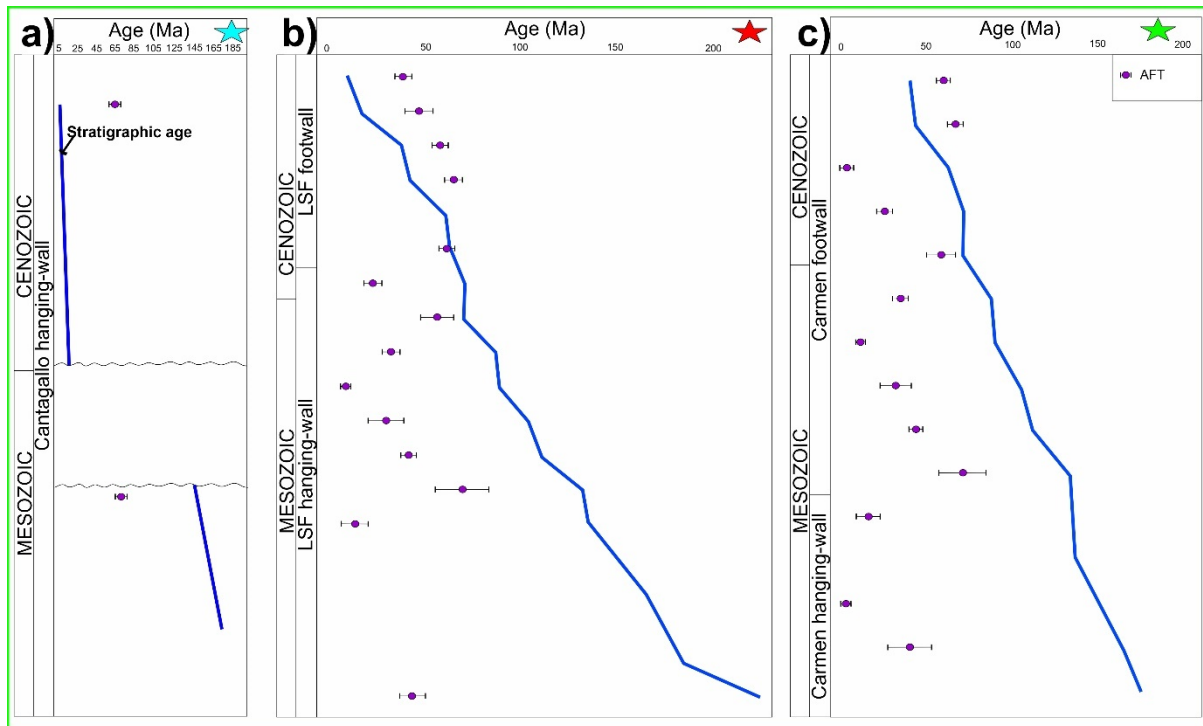


Figure 5-8. Samples from the northern section projected to cross-section Cs₁ (Figure 5.4 and see location in Figure 5-7a) a) Plot of the AFT vs depositional ages from the Cantagallo Fault. b) Plot of the AFT vs depositional ages from the La Salina Fault. c) Plot of the AFT vs depositional ages from the Carmen Fault. HF (hanging wall), FW (footwall).

In the southern region in section Cs₄ (Figure 5.6), different samples were projected to the cross-section to identify and correlate the kinematics and the exhumation evolution in this area. The samples 31, QA-05-19 and 29 obtained from the La Salina Fault hanging wall from the Paleocene Lisama Formation yielded AFT ages of 39.90 ± 3.40 , 14.10 ± 1.20 , and 9.61 ± 1.19 Ma, respectively. Sample 31 is partially reset, and the thermal inversion modeling and Ro vitrinite reflectance indicate the onset of the exhumation during the middle Eocene- early Oligocene at paleotemperatures $\sim 110^\circ\text{C}$, probably associated with the initial displacement of the La Salina Fault (Sanchez et al., 2012). The middle Miocene values obtained from the QA-05-19 were interpreted initially by Mora et al. (2010) as the onset of the thrust induced denudation of the La Salina hanging wall block. However, this hypothesis is fundamentally complemented by the new AFT ages obtained by Sanchez et al. (2012) in the De Armas syncline and interpreted as the ongoing exhumation. (Figure 5.9)

Sample 17 from the Oligocene Mugrosa Formation yields an AFT age of 27.80 ± 4.10 Ma, this value was plotted vs. the depositional age, and its proximity is interpreted as a partially reset sample and represent the PAZ (Sanchez et al., 2012). Nevertheless, the samples (16,20,22, 23, 24, 26) of the upper Cenozoic sequence in the La Salina Fault hanging wall have older AFT ages than the stratigraphic ages are interpreted as non-reset samples (Sanchez et al., 2012). Furthermore, thermal modeling from samples 17 and 20 indicates initial cooling events during early-middle Miocene for the Mugrosa Formation sample and slow cooling since middle Miocene-Pliocene for the Colorado Formation sample (Sanchez et al., 2012).

Westward to the cross-section, the samples were obtained from the hanging wall and footwall of the Boyacá Fault in the Arcabuco region. The values obtained by Parra et al. (2009) in the samples RG-01, RG-05, and RG-04 yield AFT middle-early Miocene ages interpreted as reset ages. However, just the sample RG-04 has enough number of grains to do the inverse modeling. Based on the vitrinite reflectance from the hanging wall of the Boyacá Fault, the samples exceed the 240°C burial temperatures, values not related to the early-middle Miocene onset of exhumation (Mora et al., 2010). The inversion thermal modeling for the RG-04 sample suggested an initial onset exhumation during the middle Eocene-early Oligocene (Mora et al., 2010). In the footwall of the Boyacá Fault, all the samples are partially reset, and just the AM-04 JC sample from the middle Paleocene Upper Socha Formation has an AFT age of 52.50 ± 3.40 Ma. (Figure 5.9)

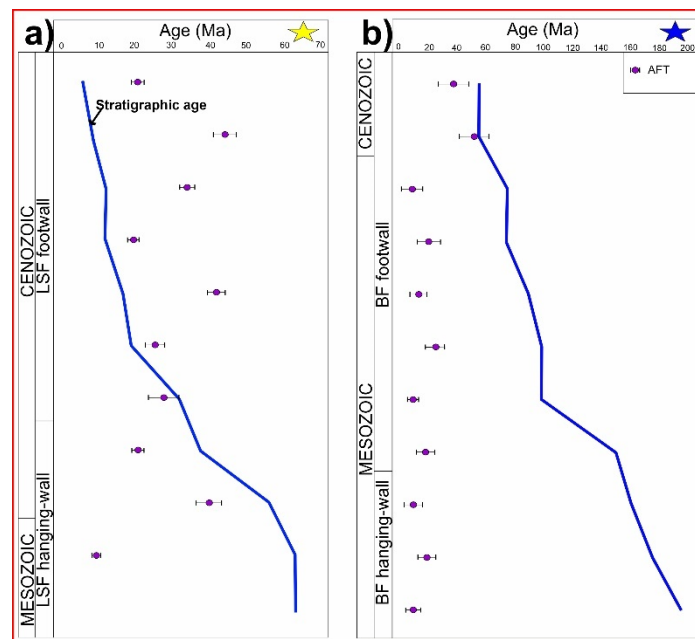


Figure 5-9. Samples from the southern section projected to cross-section Cs4 (Figure 5.6 and see location in Figure 5-7a) a) Plot of the AFT vs depositional ages from the La Salina Fault. b) Plot of the AFT vs depositional ages from the Boyacá Fault. HF (hanging wall), FW (footwall).

Chapter 5. Kinematic restoration of the Mesozoic extensional basins

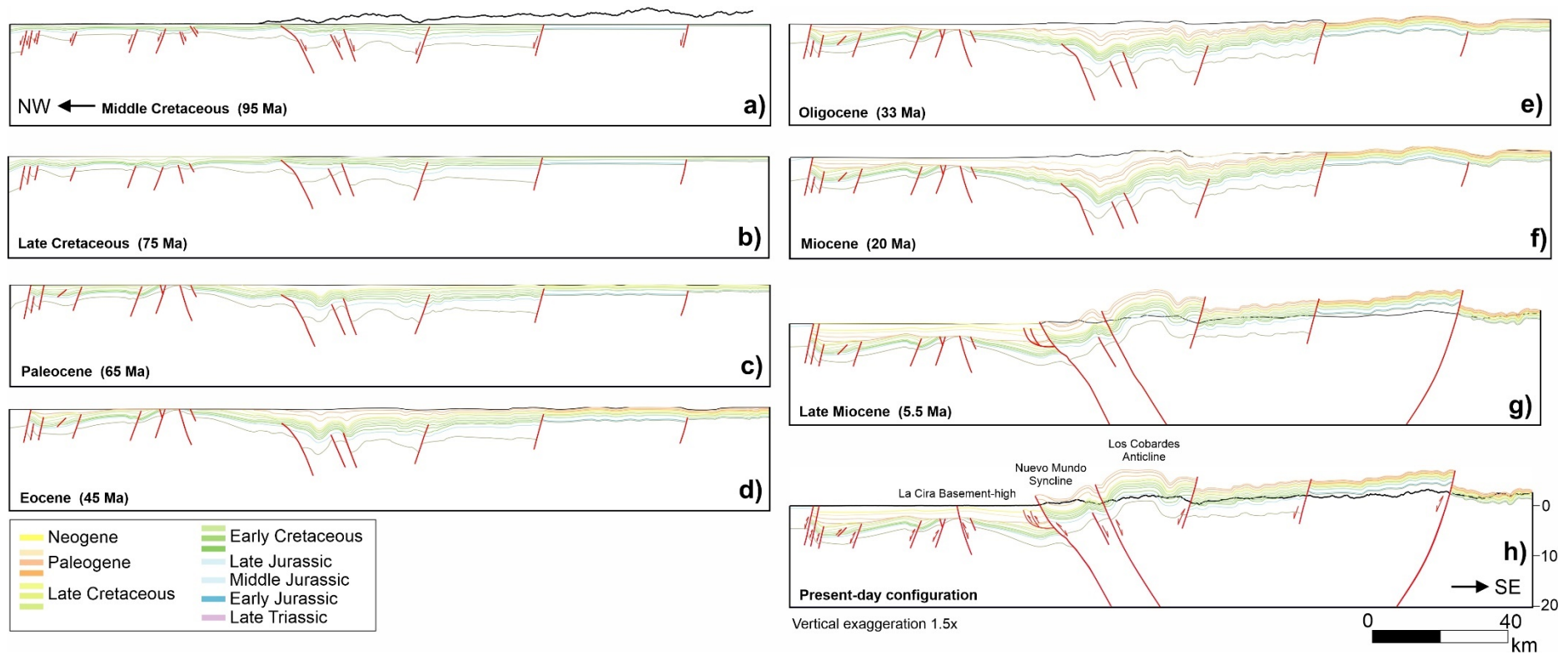


Figure 5-10. Geologic evolution of the northern region cross-section Csi from middle Cretaceous to present-day configuration. The individual stages were created by stepwise kinematic restoration of [Figure 5.10h](#). See Location in [Figure 5.3](#).

Chapter 5. Kinematic restoration of the Mesozoic extensional basins

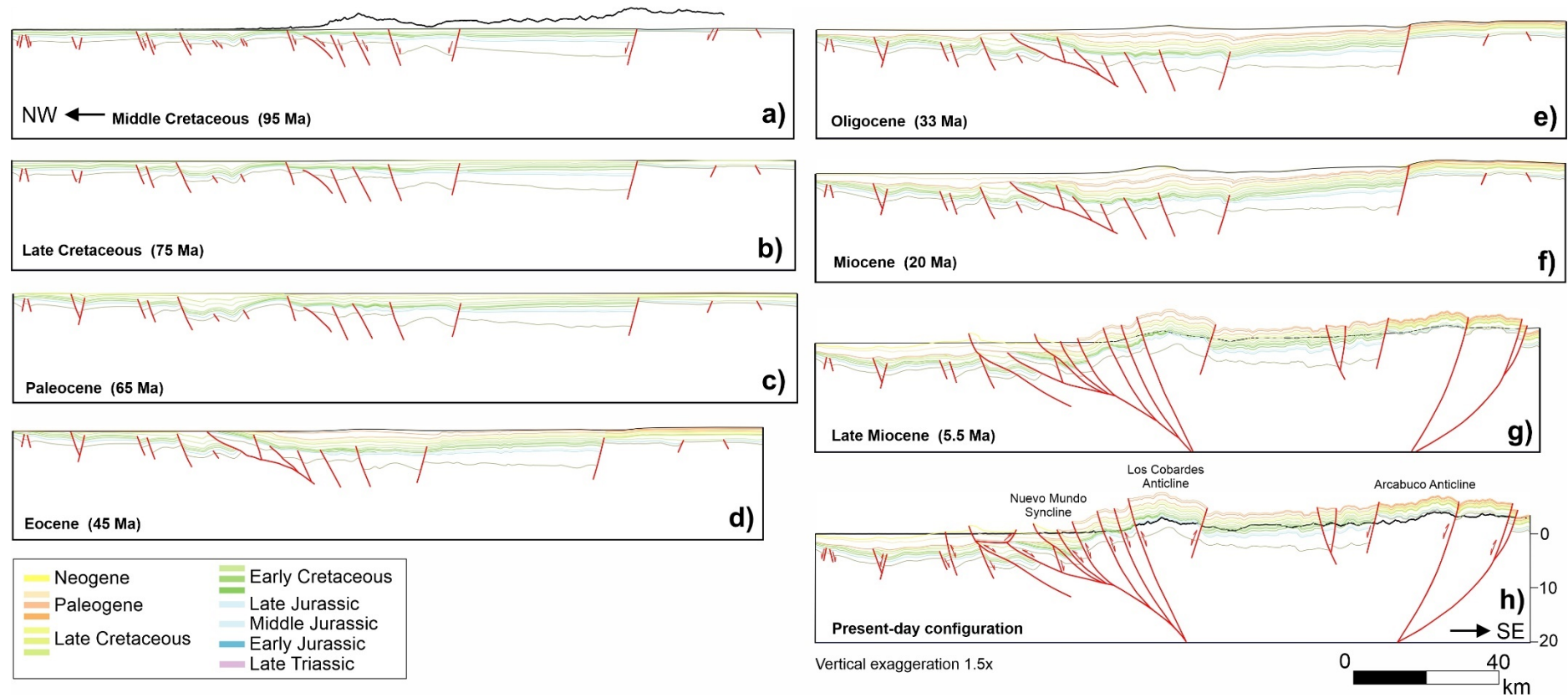


Figure 5-11 Geologic evolution of the northern region cross-section Cs2 from middle Cretaceous to present-day configuration. The individual stages were created by stepwise kinematic restoration of [Figure 5.11h](#). See Location in [Figure 5.3](#).

Chapter 5. Kinematic restoration of the Mesozoic extensional basins

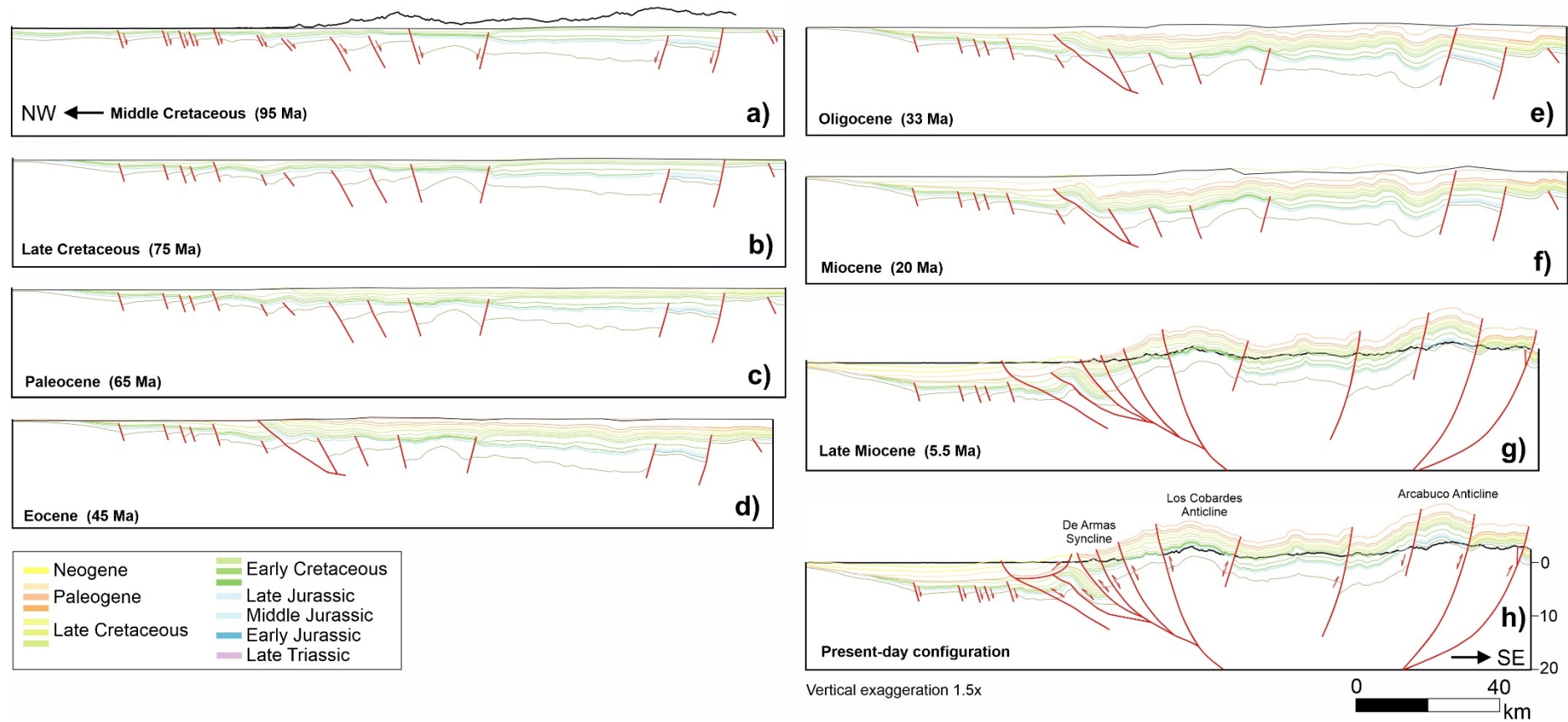


Figure 5-12. Geologic evolution of the northern region cross-section Cs3 from middle Cretaceous to present-day configuration. The individual stages were created by stepwise kinematic restoration of [Figure 5.12h](#). See Location in [Figure 5.3](#).

Chapter 5. Kinematic restoration of the Mesozoic extensional basins

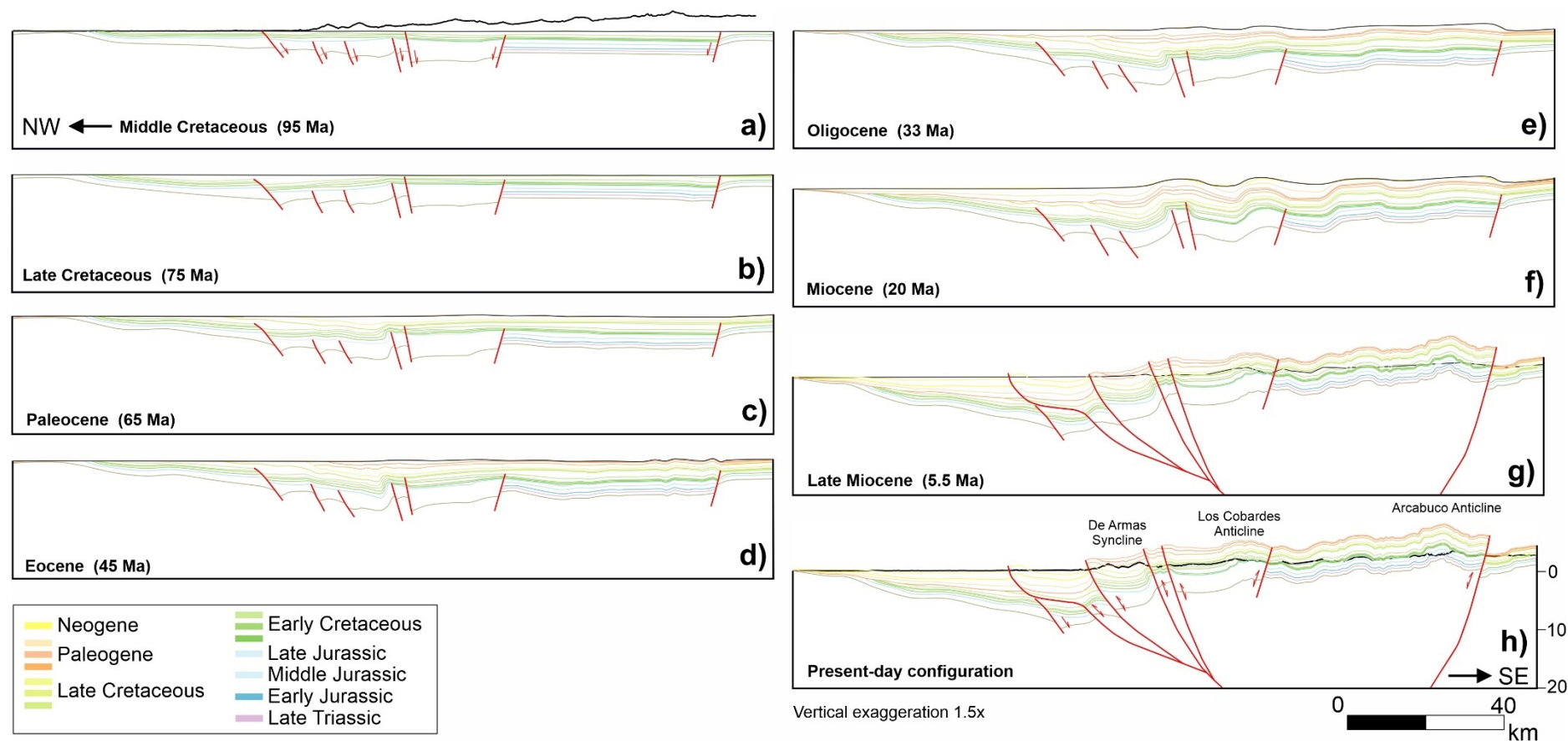


Figure 5-13. Geologic evolution of the southern region cross-section Cs₄ from middle Cretaceous to present-day configuration. The individual stages were created by stepwise kinematic restoration of [Figure 5.13h](#). See Location in [Figure 5.5](#)

Chapter 5. Kinematic restoration of the Mesozoic extensional basins

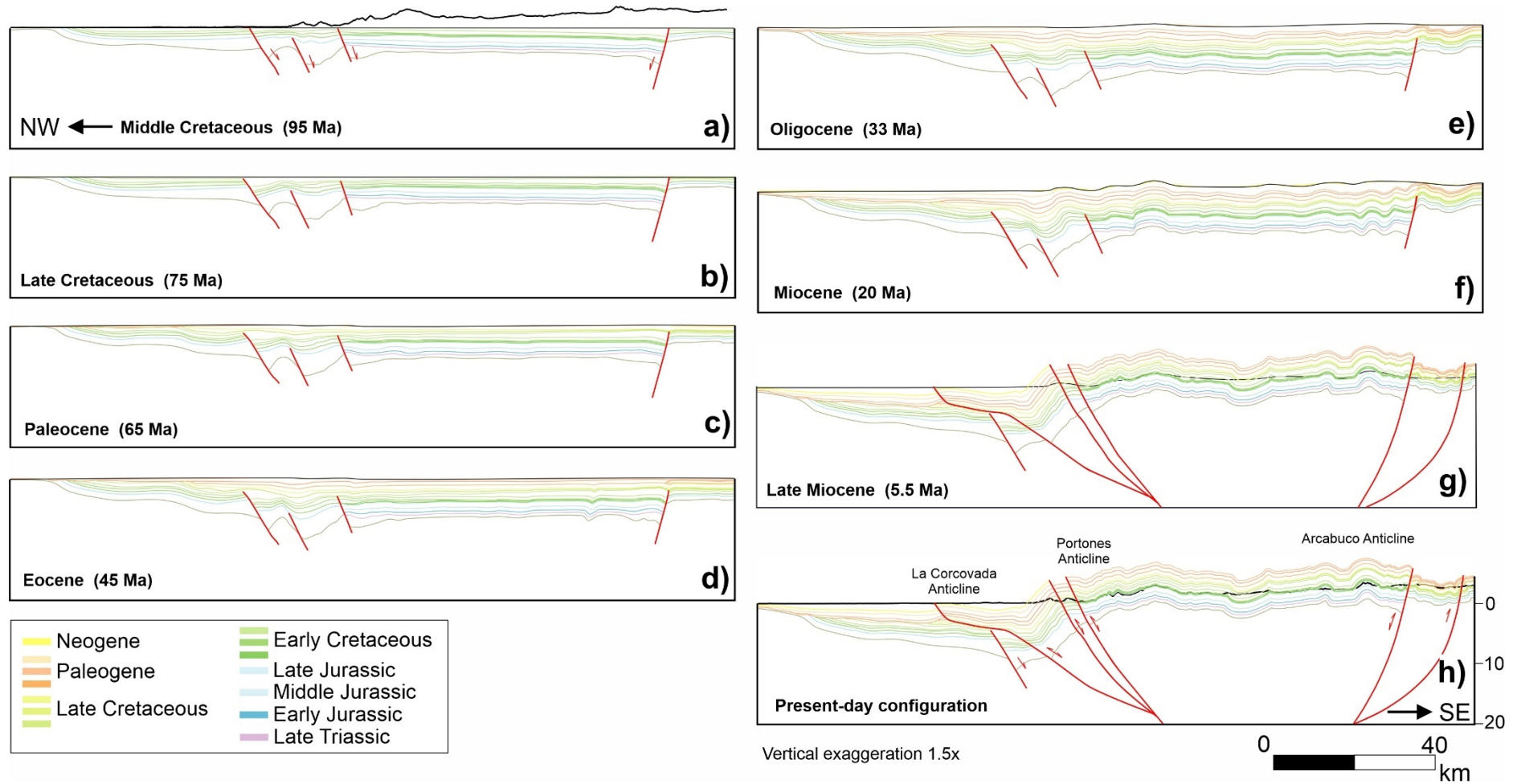


Figure 5-14. Geologic evolution of the southern region cross-section Cs5 from middle Cretaceous to present-day configuration. The individual stages were created by stepwise kinematic restoration of [Figure 5.14h](#). See Location in [Figure 5.5](#)

Chapter 5. Kinematic restoration of the Mesozoic extensional basins

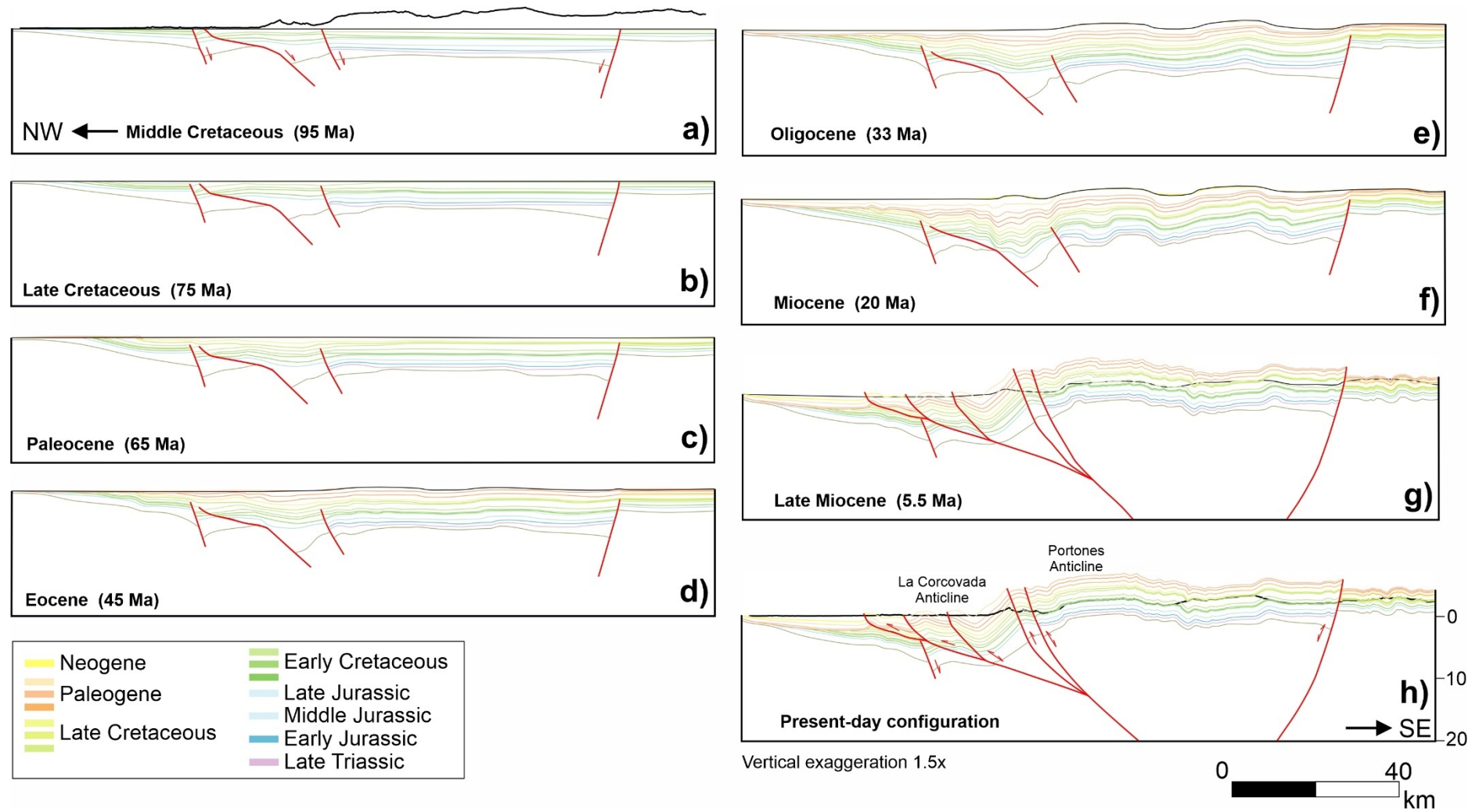


Figure 5-15. Geologic evolution of the southern region cross-section Cs6 from middle Cretaceous to present-day configuration. The individual stages were created by stepwise kinematic restoration of Figure 5.15i. See Location in Figure 5.5

Conclusions

This chapter summarizes the kinematic evolution of the Eastern Cordillera and Middle Magdalena valley from the middle Cretaceous to the present-day configuration.

Based on our kinematic restorations from [Figure 5.10](#) to [Figure 5.15](#), we identified that the major shortening is distributed along the western foothills and is highly controlled by the basement involved structures. Nevertheless, the major displacements are attributed to thin-skinned and triangle-zones structures. According to our kinematic restorations, the major shortening rates occurred during the last deformation stages during the early – late Miocene.

The initial basin development occurred in an extensional domain, and according to the thermochronometers analyzed from different authors, the basin experienced the exhumation onset after the middle Cretaceous. However, the cross-sections in the early stages reflect some folding probably linked to buckling and preserved basement anisotropies.

In the Northern area in the Los Cobardes region, the exhumation onset started in the Late Cretaceous-early Paleocene. Furthermore, the samples from the Cantagallo Fault are related to the onset of the exhumation at the Late Cretaceous for the eastern region of the San Lucas range. Following the kinematic restoration in all the cross-sections from north to south, the Late Cretaceous preserved a constant thickness, and the gentle relief is developed in the western area, where the La Salina Fault system is located. In Contrast, in the southern region, the basin started its exhumation in the middle Eocene-Early Oligocene.

The values obtained farther west in the northern region allow us to interpret that the exhumation in this region was gradually firstly developed in the western foothills and Los Cobardes and propagating to the east until the early Miocene in the footwall of the Soapaga Fault. In the southern region, the values obtained from (Sanchez et al., 2012) infer that the deformation propagates westward during the early Miocene associated with wedge propagation. The last Cenozoic cooling event is attributed to the east back thrust during the late Miocene-early Pliocene.

6. BASIN MODELING OF THE MESOZOIC EXTENSIONAL BASINS IN THE MIDDLE MAGDALENA VALLEY AND THE EASTERN CORDILLERA

This chapter is a preliminary version of the manuscript in preparation to submission.

Chapter Overview

This chapter addresses the basin and temperature behavior through geological time, this chapter considered previous results obtained during this work and external works.

This chapter integrates the previous outcomes such as the basin geometry, timing of the extension plus external vitrinite reflectance, total organic matter, and heat flow values. Also, this basin modeling considered thickness variations and oil and gas information.

The aim of this chapter is identifying the influence of the temperature in the basin maturity and oil and gas generation, see when was the critical point and why we preserved in some areas rather than others. Also show the calibration between different methods to approach the basin understanding in mature basins as methodology for frontier basins.

Abstract

The Middle Magdalena Valley and Eastern Cordillera basins were initially developed during the Mesozoic as a unique basin and subsequently inverted and divided during the Cenozoic.

The Eastern Cordillera in most of its central area is considered non-productive and primarily due to the incomplete petroleum system, i.e., improper reservoirs, eroded material and not enough lithostatic charge, overcooked kitchen, are some of the arguments to consider the majority of this area as non-productive. Different from the Middle Magdalena Valley that had been one of the most prospective basins in Colombia and is currently considered a mature basin after a century of extensive exploration.

This chapter shows the thermal evolution of the basin with four heat flow scenarios. In addition, compare the influence of the temperature in the organic matter transformation rate and the vitrinite reflectance. This comparison is shown in two cross-sections to reconstruct the initial basin extension, inversion, and last deformation stage to the present-day configuration. We also identify the key elements and the influence of the structures in hydrocarbon accumulation. Finally, we constrained these oil accumulations with the oil and gas discovered fields crossed by the cross-sections in both regions.

In the northern region, the basin modeling suggests that the significant subsidence accumulation is located in the Middle Magdalena Valley, and this value does not exceed 5 km. The heat flow in scenario A shows the feasible patterns to the present accumulations in the Middle Magdalena Valley; according to the transformation rate in the organic matter, the initial generation started in the Paleocene. Nevertheless, during scenarios C and D, the possible generation started since the Eocene and middle Eocene. In the Southern region, the basin modeling results show the generation started since the Paleocene. Nevertheless, heat flow scenarios A, C, and D, are optimal for generating hydrocarbons. However, the source rock thinned significantly. We attributed different factors that conditioned the oil and gas accumulation in this fold complex structures. In the synchronism between the generation and trap formation, the temperature usually plays an important role, and in this back-arc extension, the inverted basin is an essential input for understanding the generation. We proposed that the multidisciplinary approach is the key to reducing the risk in such complex tectonic settings as the sub-Andean basins.

Introduction

The correct understanding of the basin thermal evolution is crucial to reducing the uncertainty exploration in fold-thrust belts and associated basins like the Middle Magdalena Valley intermontane basin. Understanding the heat flow through time also allows identifying and constraining the evolution of the prospective areas due to its significant influence in resource generation such as geothermal and hydrocarbon energies. (Bjørlykke, 2010)

The thermal history is not just affected by the petrophysical properties such as thermal conductivity and radiogenic heat. (Ranalli, 1991) The thermal history is also affected by several factors that conditioned the basin development such as geological processes, paleowater depth, burial history, and basal heat flow variations, which are the parameters that equally affect the basin temperature through time. (Yalçın et al., 1997; Allen and Allen, 2013)

This chapter provides 2D basin modeling in the northern and southern regions ([Figure 6.1](#)) of the Middle Magdalena Valley and the western foothills of the Eastern Cordillera. We tested different 4 scenarios of heat flow and analyzed the outcomes in terms of vitrinite reflectance and transformation organic matter rate variations. This paper intends to identify the critical timing and its relation with heat flow changes in terms of source maturation and generation.

Fold and thrust belts are complex basins due to the timing between the generation and the trapping formation mainly linked to the inversion and compression stages. Therefore, the correct understanding and characterization between the thin and thick-skinned geometries in fold-thrust belts are essential to estimate possible petroleum accumulations (Cooper and Warren, 2020).

The Eastern Cordillera is a great example to understand the petroleum systems in complex areas such as the sub-Andean basins as the Middle Magdalena Valley. (Mora et al., 2010) Different authors had analyzed the thermal evolution in the western foothills of the Eastern Cordillera and Middle Magdalena Valley through 2D kinematic cross-section modeling and pseudo-3D modeling. (Restrepo- Pace et al., 2004; Toro et al., 2004; González et al., 2020)

In this chapter, we integrated information from the subsurface, such as the 2D seismic reflection lines and exploration boreholes, together with the surface information obtained during the last years by the Geological Survey and published data that allow generating the structural composite cross-sections in the northern and southern regions. This information was also compared with the oil and gas discoveries in the Middle Magdalena Valley mainly. Our goal was

to approach the evolution links between the migration, reservoir, and temperature along the western foothills of the Eastern Cordillera, the Middle Magdalena Valley.

Our project was carried out along the Mesozoic inverted basin composed of complex structures as the western foothills, range that contains triangle zones, duplexes, and thin and thick-skinned structures along its strike. In this chapter, we applied the integration of different methodologies to model the basin, estimate the critical timing in hydrocarbon generation, and identify the influence of different tectonic settings in the basin temperature through time.

The reconstruction of the thermal basin history in complex settings such as fold and thrust belts is still challenging and requires a vast database to approach geological evolution. These are due to the orogenic loading, changes in sedimentation, paleowater influence, and the structural variations along the strike (Toro et al., 2004; González et al., 2020). However, the correct integration of the existing data in the basin accoupled with the kinematic restorations allows to approach the basin infill and development and estimate when was the critical point in the hydrocarbon generation.

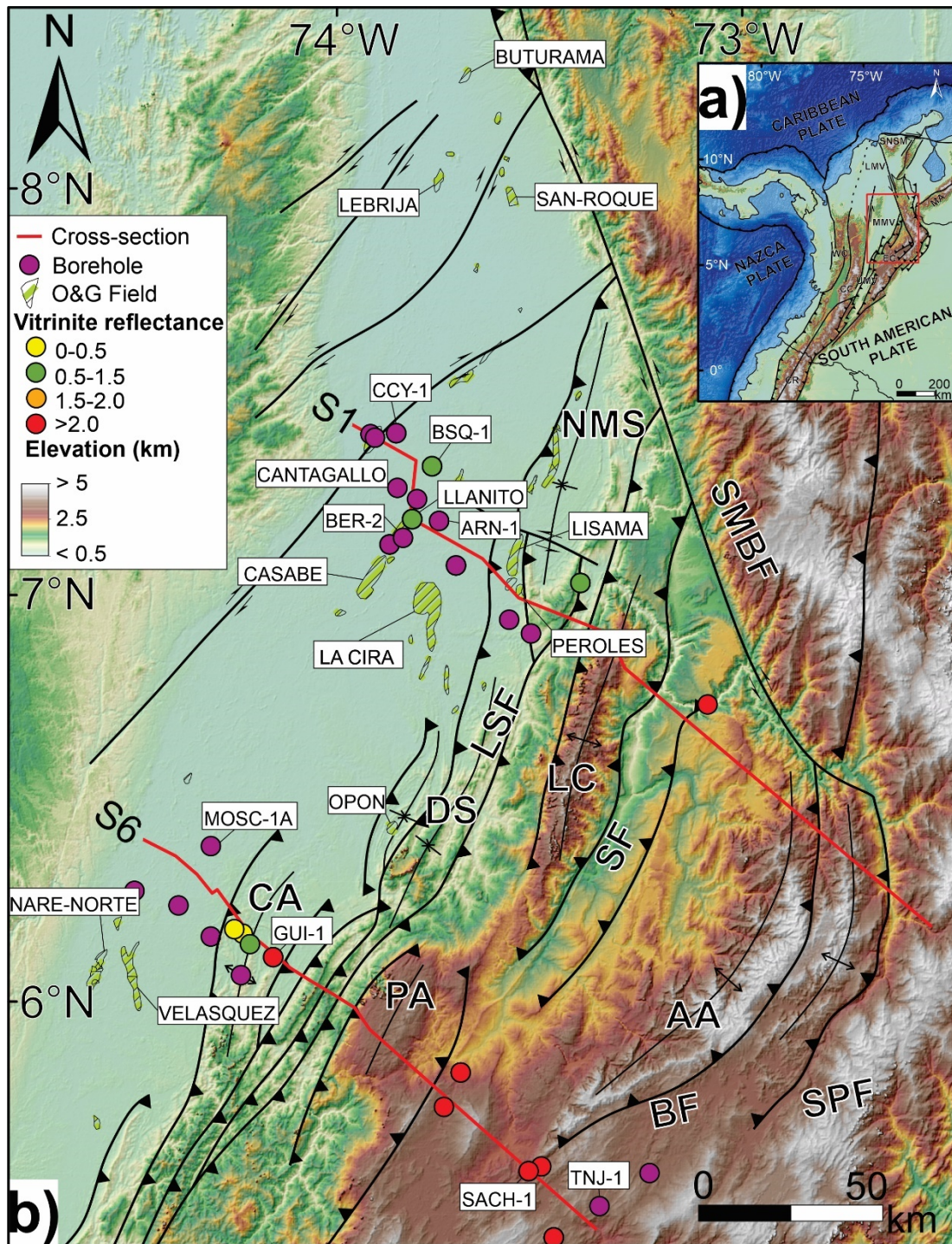


Figure 6-1. a) Present tectonic configuration of the northern Andes, showing the main tectonic features in the study area (orange box), MMV (Middle Magdalena Valley), WC (Western Cordillera), CC (Central Cordillera), EC (Eastern Cordillera). Orange box shows the study area location in [Figure 6.1b](#). b) Digital elevation model of the study area showing the principal oil and gas fields, distribution of the vitrinite reflectance and boreholes employed in this chapter. S1 cross-section northern region. S6 cross-section southern region. Also the main structural features are labeled. NMS (Nuevo Mundo Syncline), LSF (La Salina Fault), SMBF (Santa Marta Bucaramanga Fault), LC (Los Cobardes Anticline), SF (Suarez Fault), DS (De Armas Syncline), CA (La Corcovada Anticline), PA (Portones Anticline), AA (Arcabuco Anticline), BF (Boyaca Fault), SPF (Soapaga Fault).

Methodology

For the basin modeling we employed the Tec-Link module of Petromod (©Schlumberger) for complex tectonic settings where the model of McKenzie, 1978 is not suitable due to the complexity of compressional regimes, where different tectonic settings affected the basin evolution.

The cross-sections were previously constructed, balanced and restored in Move (©Petroleum Experts) we defined the most important stages based on thermochronological data. The initial development during the Mesozoic associated to an extensional regime, at the end of the Cretaceous the initial development of the compressional regime and probably the inversion onset, and during the last stage during the late Miocene a rapid deformation and exhumation.

This information was transferred directly to Petromod (©Schlumberger) where was conducted the calibration and the geometrical definition. This geometrical definition consists in split the fault blocks in the cross-section following the structural parameters but also avoiding the double depth values in the same block for the same horizon. Gonzalez et al., 2020 suggest the employment of standard backstripping under rigorous analysis to avoid the thicknesses errors. However, we agree with this statement that works perfectly in areas such as the Middle Magdalena Valley but is more complex in settings such as the Eastern Cordillera where thin and thick-skinned domains are present.

In this chapter we included 8 restoration stages from the ending of the extensional regime to the present-day configuration for the northern and southern cross-sections. The software followed the geometry to do the backstripping from the extensional regime to the initial basin development. Afterward, in Petromod (©Schlumberger) we populated the horizon layers with the standard mixed lithologies from Hantschel and Kauerauf, 2009 already loaded in Petromod (©Schlumberger). The cross-sections restored in 8 stages started from the present-day geometry with the eroded material but considered the evolution of the erosion through time linked to the fault activity and uplifting of the Eastern Cordillera.

The boundary conditions are essential parameters in terms to calibrate the basin model, such as heat flow, sediment water interface temperature (SWIT). The heat flow is defined as the variation of temperature in response to depth and lithology through geological time. (Bjørlykke, 2010) In addition, the heat flow in sedimentary basins is also affected by the underlying basements, where granitic rocks with high content of potassium and uranium produced high radiogenic heat flow rather than basic rocks (Yalçın et al., 1997; Bjørlykke, 2010). The basins are divided according their paleo geothermal history in three groups: basins with normal or near paleogeothermal history, cooler than normal basins, and hotter than normal basins. (Robert,

1988) The hotter basins (200- 65 mWm^{-2}q) are found in areas of lithospheric stretching such as rift, back-arc basins, the heat flow in internal arcs is elevated due to the volcanic activity, as is the case of the Andean range (Allen and Allen, 2013).

We defined 4 heat flow scenarios following the main tectonic settings in the area. The scenario A was extracted from Gonzalez et al. 2020 and this heat flow values were calculated from borehole measurements, i.e., thermal conductivity vs. geothermal gradient, these values were employed in the Fourier equation. The maximum heat flow of 80 mWm^{-2}q during the middle Cretaceous and minimum heat flow of 30 mWm^{-2}q in the present-day. The heat flow variations were attributed to the cooling and compressional events in the basin. For the other scenarios we tested several alternatives according to the previous results from the other chapters such as the onset of the extension and its ending, also considering external values from fission-tracks to constraint the inversion onset and the last uplifting of the Eastern Cordillera. The values employed for each scenario were following the standard according to sedimentary basins proposed by Allen and Allen (2013). Also, we employed similar range values to the calibrated heat flow values calculated by Gonzalez et al. (2020).

We analyzed the different heat flow scenarios in relation to the vitrinite reflectance R_o measurements mainly from boreholes in the Middle Magdalena Valley and outcrops from the Eastern Cordillera published during the last decades. At the end we calibrate thermally the heat flow vs the vitrinite reflectance values compiled previously employing the Sweeney and Burnham, 1990 kinetic model. The SWIT was calculated automatically following the principle suggested by Wygrala (1989) generating the sea level temperature including the global temperature and the latitude.

The source and organic matter evaluation was conducted for the Cretaceous formations. In our model we evaluated the traditional source rocks in the basin and the basal Cretaceous group that could be potential source rocks. The organic matter properties such as type of kerogen, total organic content (TOC), hydrogen index (HI) (Table 6.1 and Table 6.2) were defined according the measurements obtained from different authors (Ramon and Dzou, 1999; Rangel et al., 2000; 2002; Sarmiento, 2011) and based in the average calculation between the values, and the proximity to the cross-sections presented in this work. With the aim to approach the transformation evolution of the organic matter, we selected the kinetics of Behar et al., 1997 according to the original kerogen type for each formation.

Table 6-1. Organic geochemistry parameters from the source rocks employed in the northern region S₁ cross-section. (See location in [Figure 6.1](#))

Name	Age	Lithology	Kerogen	(Average) TOC %	HI (mgHC/g TOC)
Rosablanca	Barremian	Limestone	II and III	0.75	100
Paja	Aptian	Siltstone	II and III	1.24	55
Tablazo	middle Aptian	Limestone	II and III	3.36	80
Tablazo	middle Aptian	Siltstone	II and III	3.36	80
Simiti	Cenomanian	Siltstone	II	1.1	88
Luna	Santonian	Limestone	II and III	2.73	450
Luna	Santonian	Siltstone	II and III	2.73	450
Luna	Santonian	Shale	II and III	2.73	450
Umir	Maastrichtian	Siltstone	III	1	200

Table 6-2. Organic geochemistry parameters from the source rocks employed in the southern region S₆ cross-section. (See location in [Figure 6.1](#))

Name	Age	Lithology	Kerogen	(Average) TOC %	HI (mgHC/g TOC)
Paja	Aptian	Siltstone	II and III	1.35	60
Tablazo	middle Aptian	Limestone	II and III	1.56	200
Tablazo	middle Aptian	Siltstone	II and III	1.56	200
Luna	Santonian	Limestone	II and III	3.63	800
Luna	Santonian	Siltstone	II and III	3.63	800
Luna	Santonian	Shale	II and III	3.63	800

Results

We present two cross-sections, the S₁ for the northern region and the S₆ for the southern region. We initially analyzed the burial history from the northern and southern regions. Afterward, we presented the different heat flow scenarios and the relationship between the transformation rate and its influence on vitrinite reflectance values. Finally, we concluded this analysis with the thermally constraint heat flow plot vs. vitrinite reflectance, observing the hydrocarbon accumulations and the possible relation with the location of previous oil and gas discoveries.

Burial History

The basement in the study area is defined as Precambrian-early Paleozoic metamorphic rocks with medium to high metamorphism grade. (Ward et al., 1973; Restrepo-Pace et al., 1997; Cochran et al., 2014) However, the presence of different Mesozoic granitoid bodies along the Eastern Cordillera was reported, as is the case of the San Lucas granitoid (Clavijo et al., 2008). The major depocenters were identified through the seismic interpretation described in Chapter

3; these depocenters are located in the frontal footwall block of the orogenic wedge. In this analysis, the primary deposition occurred in the footwall of the La Salina Fault and did not exceed the 8.5 km in the most profound areas of the cross-sections analyzed in this work.

Northern region

Figure 6.2 shows the northern cross-section S₁ with five 1D burial history models from the west to the east to analyze the transition from the intermontane basin to the orogenic belt.

Model A is located on the western side of the cross-section in the footwall of the Cantagallo east-verging Fault. (Figure 6.2) the burial history plot allows us to identify the low subsidence rate since the beginning of basin development, probably during the Late Triassic – Early Jurassic; this rate is almost continuous until the Early Cretaceous (~135 Ma), which a total thickness of ~1000 m. was deposited. From the Early Cretaceous to the middle Cretaceous (~100 Ma), a subsidence increasing occurred, and a total amount of ~1000 m sedimentary record was deposited during this period. Following this event during the middle Cretaceous to the Late Cretaceous, the basin experience almost no subsidence, and at the end of the Late Cretaceous (Maastrichtian)-Paleocene, the subsidence rate increase with a preserved thickness of ~400m followed by a short period of constant subsidence until the early Eocene (~50 Ma) when the fast subsidence began depositing a total sedimentary record of ~3000 m. From the middle Miocene (~11 Ma) to the present day, the subsidence rate decreases significantly. A total of ~5500 meters of sediments were deposited at this point. In general terms, model B, located in the footwall of the La Salina west-verging Fault, resembles model A's subsidence behavior; the only difference is the total amount of sediments ~7700 m deposited through time. In this analysis, the primary deposition occurred in the footwall of the La Salina Fault and did not exceed the 8.5 km in the most profound areas of the cross-sections analyzed in this work.

Eastward in the hanging wall of the La Salina Fault, model C shows since the Late Triassic (~210 Ma) to the Early Cretaceous major subsidence than the previous models described before, with a total deposition of ~3300m. From the Early Cretaceous (~115 Ma) to the Paleocene occurred a low subsidence rate and just ~300 m was deposited, followed by major subsidence event registered since the Paleocene (~60Ma) to early Miocene, which deposited ~4500 m. Finally, at the beginning of the early Miocene (~20Ma), the curve reflects an uplifting event decreasing the subsidence from the maximum burial depth of ~8500 m to ~4500 m at the present-day configuration.

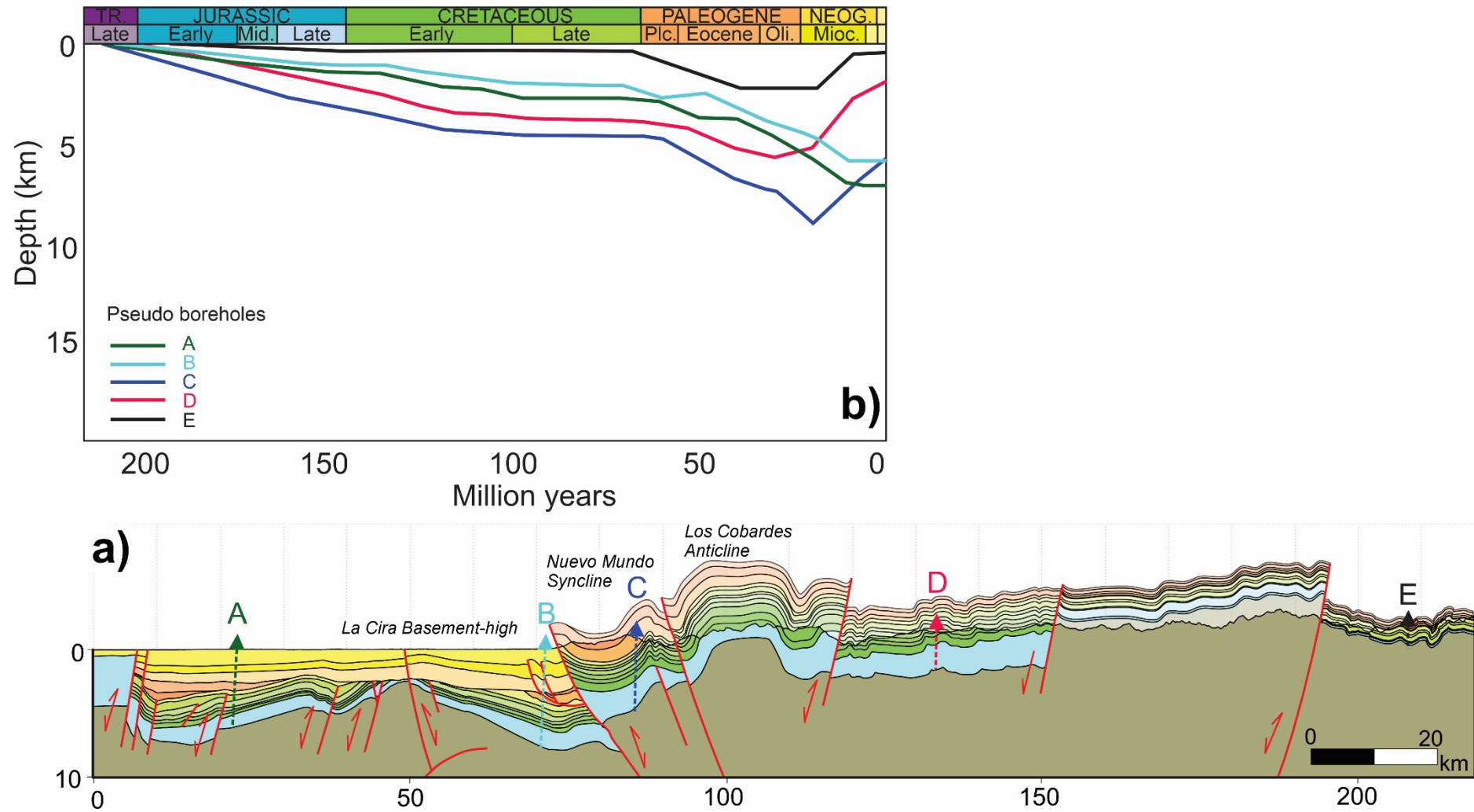


Figure 6-2. a) Cross-section S1 from the northern region (see location in Figure 6.1) showing the location of the 1D burial models (A, B, C, D, E) extracted from the 2D basin model, from west to east respectively. b) Subsidence curves from the different pseudo boreholes extracted from the cross-section S1.

Model D is located in the axial area of the Magdalena-Tablazo sub-basin in the footwall of the Suarez reverse inverted Fault. In this location, the subsidence plot shows extended initial subsidence from the Late Triassic (~210 Ma) to the middle Cretaceous (~103 Ma) and with a total of ~3600 m sediments accumulated during this time. From the middle Cretaceous (~103 Ma) to the Late Cretaceous, the subsidence rate decreases notably, and the sedimentary thickness deposited during this time does not exceed the ~200 m. Following this event occurred the major subsidence event recorded ~3000 m during the Late Cretaceous to early Oligocene, experiencing a steepening from the middle Eocene (~40 Ma) to the early Oligocene. This event was followed by a slow erosive event from the early Oligocene (~29 Ma) to the early Miocene, when the major erosion event started. This event occurred from the early Miocene (~19 Ma) to the middle Miocene from burial depth ~ 6400 m to ~ 2400 m; since the middle Miocene (~10 Ma), the model shows a gradual uplifting and one estimated erosion of ~ 1000m to the present day preserved sedimentary record.

Model E is located to the west in the footwall of the Soapaga fault; the subsidence curve reflects a meager subsidence rate from the Middle Jurassic (~185 Ma) to the middle Cretaceous (~103Ma) which a total of ~ 250 m were deposited. The major subsidence event recorded in the plot is from the Late Cretaceous (~68 Ma) to the middle Eocene with a preserved thickness of ~ 1500 m. afterward, the plot shows an erosive steeped event that started from the middle Eocene (~40 Ma) to the middle Miocene; this event eroded more than ~1000 m sedimentary thickness. Finally, the curve reflects a low gradual erosive event from the middle Miocene (~10 Ma) until the present-day configuration.

Southern region

The four 1D burial history models obtained from the southern region in the cross-section S6 were employed to understand the basin infill in different locations and the evolution through time ([Figure 6.3](#)).

Model A located in the forebulge (?) of the Middle Magdalena Valley, shows a continuous low subsidence rate from the Middle Jurassic (~175 Ma) to the Late Cretaceous, with a steeped initial during the Jurassic. The total sedimentary record deposited during this time does not exceed ~780m. The basin recorded an erosive event during the Paleocene (~65 Ma), and afterward, the main deposition event occurred from middle Eocene (~40 Ma) to middle Miocene, recording a total thickness of ~1000 m during this time. Since the middle Miocene (~10 Ma), the curve shows a shallow erosion to the present-day configuration.

Farther east the model B, located in the hanging wall of the La Salina Fault system, comprises the major depocenter in the basin. The subsidence began from the middle Jurassic (~175 Ma) to the Late Jurassic, during which ~1000 m of sedimentary record was deposited. A high subsidence rate occurred from the Early Cretaceous (~145 Ma) to the middle Cretaceous. An estimated amount of ~1700 m was deposited during the Cretaceous. Followed by a low subsidence rate until the Late Cretaceous (~70 Ma) during this time, the sedimentation does not exceed the ~250 m. From the Late Cretaceous (~70 Ma) to the middle Paleocene (~60 Ma), the subsidence rate increases as is reflected in the curve steepening and the high sedimentation of ~1600 m during this time. This event was followed by the low subsidence rate from the middle Paleocene (~60 Ma) to the early Eocene (~55 Ma). At the end of the previous low subsidence rate started the major subsidence in this model from the early Eocene to the early Miocene, depositing ~4000 m. the last subsidence event registered in this plot is low subsidence rate from the early Miocene (~20 Ma) to the present-day.

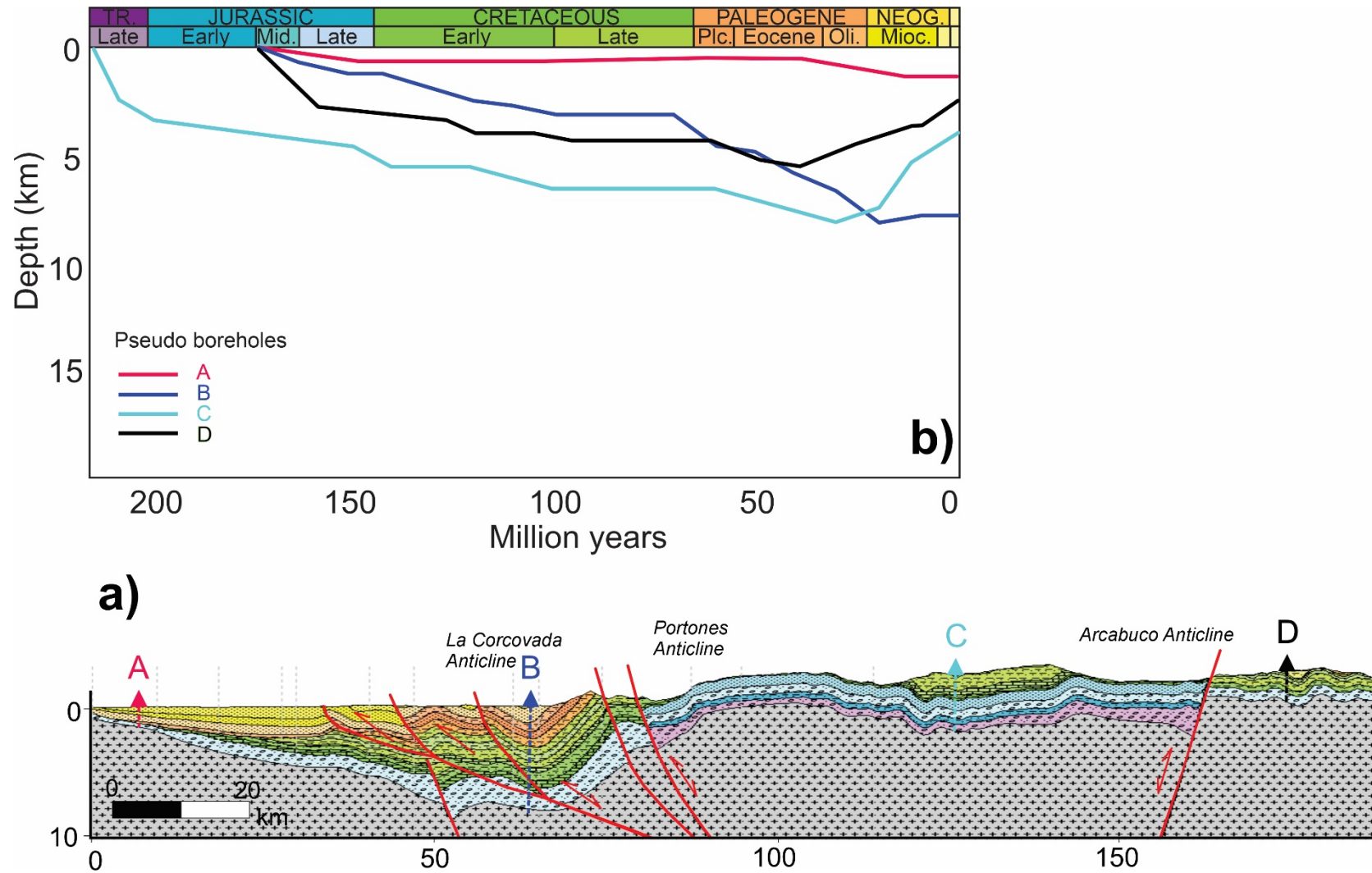


Figure 6-3. a) Cross-section S6 from the southern region (see location in Figure 6.1) showing the location of the 1D burial models (A, B, C, D) extracted from the 2D basin model, from west to east respectively. b) Subsidence curves from the different pseudo boreholes extracted from the cross-section S1.

Model C is located in the axial area of the Arcabuco anticline in the hanging wall of the Boyacá Fault. The gradual subsidence rate started from the Late Triassic (~210 Ma) to the Early Cretaceous; during this time, ~3000 m of sediments were deposited. Followed this event, a decrease in the subsidence rate is reflected from ~ 145 Ma to ~ 120 Ma during the Early Cretaceous and when the sedimentation did not overpass the ~ 600 m. After this event, subsidence increased from a low to gradual subsidence rate during the Early Cretaceous (~ 120 Ma) to middle Cretaceous with sedimentation during this time of ~1000 m. Then a low subsidence rate from the middle Cretaceous to the Late Cretaceous. Afterward, a rapid erosive event occurred during the Late Cretaceous-Paleocene, and since the middle Paleocene (~60 Ma) began the major subsidence event in this area until the middle Oligocene, depositing ~2000 m. Followed these high subsidence rates, an erosive event started from the middle Oligocene (~30 Ma) to the middle Miocene, when the erosion event increases significantly to ~4000 m until the Present-day.

Westward in the footwall of the Boyacá Fault, the model D shows gradual subsidence rates from the middle Jurassic (~175 Ma) with increasing subsidence rates during the Early Cretaceous ~130Ma to ~120 Ma depositing ~ 600 m, another subsidence rate increment occurred at the end of the Early Cretaceous with ~700 m sediments deposited during this time. Followed these gradual events occurred the major subsidence rate from the Paleocene (~60 Ma) to the middle Eocene (~40 Ma), during which a total of ~1600 m were deposited. Since the middle Eocene (~40 Ma), the curve reflects an erosive event that keeps the trend until the Present-day with an estimated erosion rate of ~ 3000 m.

Heat flow analysis

The heat flow scenarios described in this chapter comprise different constraints to see the heat flow's influence on the basin evolution. Also, the different heat flow graphs were analyzed, compared, and calibrated with vitrinite reflectance values to identify the most feasible scenario.

Scenario A

This scenario was defined by Gonzalez et al. (2020) based on the heat flow obtained from the Fourier equation. This curve plot analyzed a vast database of temperatures from different borehole measurements. According to this analysis, the heat flow began from 60 mWm⁻²q, gradually rising during the Mesozoic until the middle Cretaceous when the basin experienced the highest peak of 80 mWm⁻²q. Following this high, the basin experienced a gradual decrease until the early Eocene with ~70 mWm⁻²q. From the early Eocene to the middle Miocene, the heat flow decreased to 50 mWm⁻²q, and since the middle Miocene, a fast event occurred until it

reaches the present-day heat flow of $\sim 30 \text{ mWm}^{-2}$. They suggested different tectonic events associated with the heat flow variations from the Late Triassic – middle Cretaceous (extension event); middle Cretaceous to early Eocene (cooling or thermal subsidence); early Eocene – middle Miocene (compression event), and during the last stage a fast uplifting and major deformation occurred since the Late Miocene to the present-day ([Figure 6.4a](#) and [Figure 6.5a](#)).

Our models showed the heat flow influence concerning the source generation and vitrinite reflectance evolution.

Within the heat flow curve defined in this scenario, Section S1 (northern region) and S6 (southern region) began the hydrocarbon generation in terms of transformation ratio ([Figure 6.4b](#) and [Figure 6.5b](#)) since ($\sim 60 \text{ Ma}$) Paleocene. The first-generation pulse is associated with the Rosablanca Formation (Barremian). In the northern region, this generation occurred in folded depth areas in the central and western sides of the cross-section; regarding the southern section, the generation was primarily localized in the central region of the cross-section

Chapter 6. Basin modeling of the MMV and EC

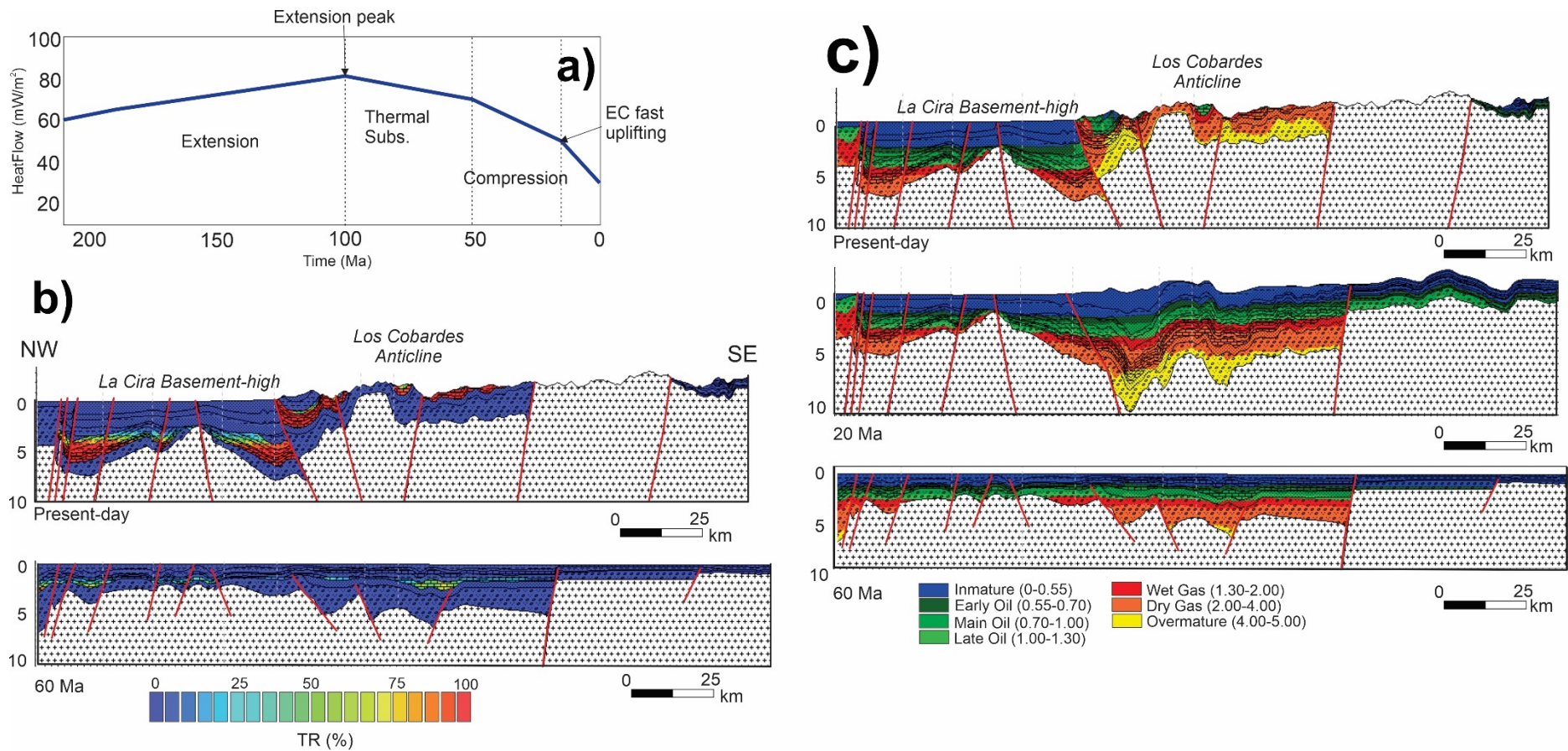


Figure 6-4. a) Heat flow curve for the scenario A modified from (Gonzalez et al., 2020) b) Transformation ratio reconstruction for the Paleocene and the Present-day configuration (TR<=50% are considered optimal to generate hydrocarbon during this time). c) Vitrinite reflectance reconstruction for the Paleocene, early Miocene and Present-day configuration. All those models are from the cross-section S₁ (see location [Figure 6.1](#)) testing the scenario A. Vertical exaggeration 3x.

Chapter 6. Basin modeling of the MMV and EC

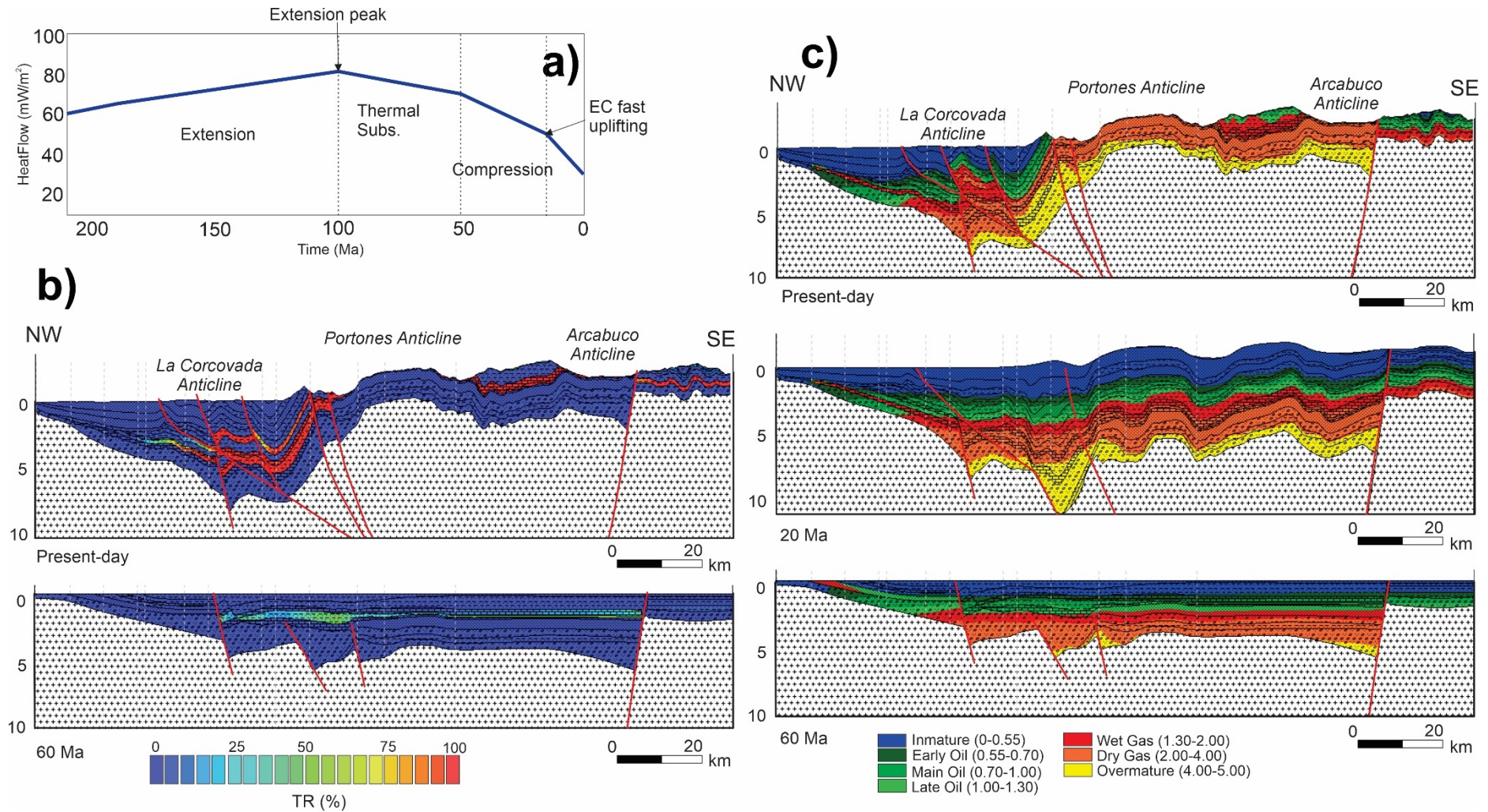


Figure 6-5. a) Heat flow curve for the scenario A modified from (Gonzalez et al., 2020) b) Transformation ratio reconstruction for the Paleocene and the Present-day configuration (TR<=50% are considered optimal to generate hydrocarbon during this time). c) Vitrinite reflectance reconstruction for the Paleocene, early Miocene and Present-day configuration. All those models are from the cross-section S6 (see location [Figure 6.1](#)) testing the scenario A. Vertical exaggeration 3x.

Subsequently, different generation pulses occurred from the Paleocene to the Present-day, where both sections show that most of the source rocks reached the organic transformation previously, however in the distal upper parts of the deposits, primarily in steeped source layers as the onlaps, the upper source rocks are generating hydrocarbons at this point.

The vitrinite reflectance response in both sections ([Figure 6.4c](#) and [Figure 6.5c](#)) shows an oil generation window during the Paleocene for the basal Cretaceous group. However, the last oil generation began in the late Oligocene – early Miocene for the Late Cretaceous rocks such as the La Luna Formation.

Scenario B

Scenario B ([Figure 6.6a](#) and [Figure 6.7a](#)) was constructed following the previous values range proposed by Gonzalez et al. (2020) for Scenario A, but the major constraints in this plot were the integration of previous results such as volcanism dating, uplifting events, and the major deformation phases in the Eastern Cordillera based on thermochronological data (Mora et al., 2006; 2010; 2013; 2015; Parra et al., 2009; 2012; Sanchez et al., 2012; Caballero et al., 2013). This plot started at $\sim 60 \text{ mWm}^{-2}\text{q}$ during the Late Triassic, and a gradual increasing heat flow follows it until it reached the maximum heat flow of $\sim 85 \text{ mWm}^{-2}\text{q}$ in the middle Jurassic. After this peak, the basin experienced a gradual cooling until the Late Cretaceous $\sim 70 \text{ mWm}^{-2}\text{q}$. From the Paleocene to the middle Miocene, the heat flow reached $\sim 50 \text{ mWm}^{-2}\text{q}$. Finally, during the middle Miocene to the Present-day, the temperature decreased to $\sim 25 \text{ mWm}^{-2}\text{q}$. We defined the following tectonic settings from Late Jurassic-middle Cretaceous (back-arc extensional regime); the maximum peak during the middle Jurassic is attributed to the major volcanism. We considered that thermal subsidence started from the middle Cretaceous to the Late Cretaceous. Then the basin experienced a compressional and inversion onset from the Late Cretaceous-early Paleocene to the middle Miocene. Finally, the last stage from the middle Miocene to the present-day is defined as the fast-uplifting phase.

Scenario B resembles Scenario A; however, the transformation ratio reconstructions ([Figure 6.6b](#) and [Figure 6.7b](#)) reflect some local differences in the cross-section S₁ where the initial generation is higher than the scenario A transformation ratio. The difference between this peak and the previous one is $\sim 10\text{-}20 \text{ TR}\%$, having almost a similar response in the northern region for both scenarios. Unlike the southern region, where the increment is $\sim 50 \text{ TR}\%$, the initial source generation for this scenario is located in the central part and generates from the eastern and western sides of the cross-section. Significant changes occurred in the southern region where the Rosablanca Formation reached the maximum transformation ratio during the Paleocene.

According to the transformation ratio restoration, the source rocks experienced different generation pulses; the major generation pulse presumably occurred during the middle Eocene. However, the shallow and onlapped source rocks are still generating hydrocarbons in the last deformation phase.

In terms of vitrinite reflectance and maturity in relation to the heat flow ([Figure 6.6c](#) and [Figure 6.7c](#)), the northern and southern regions show similarities with the scenario A, tiny changes are located in the Eastern Cordillera, especially in the deep depocenters such as the hanging wall of the La Salina Fault and the footwall of the Suarez Fault, where Jurassic formations are overmature at the present-day configuration. However, in general terms, the maturity in response to heat-flow behaves similar to scenario A where the basal Cretaceous are in oil window generation during the Paleocene, and later on, is mature until the present-day where most of those deposits present high vitrinite reflectance values.

Chapter 6. Basin modeling of the MMV and EC

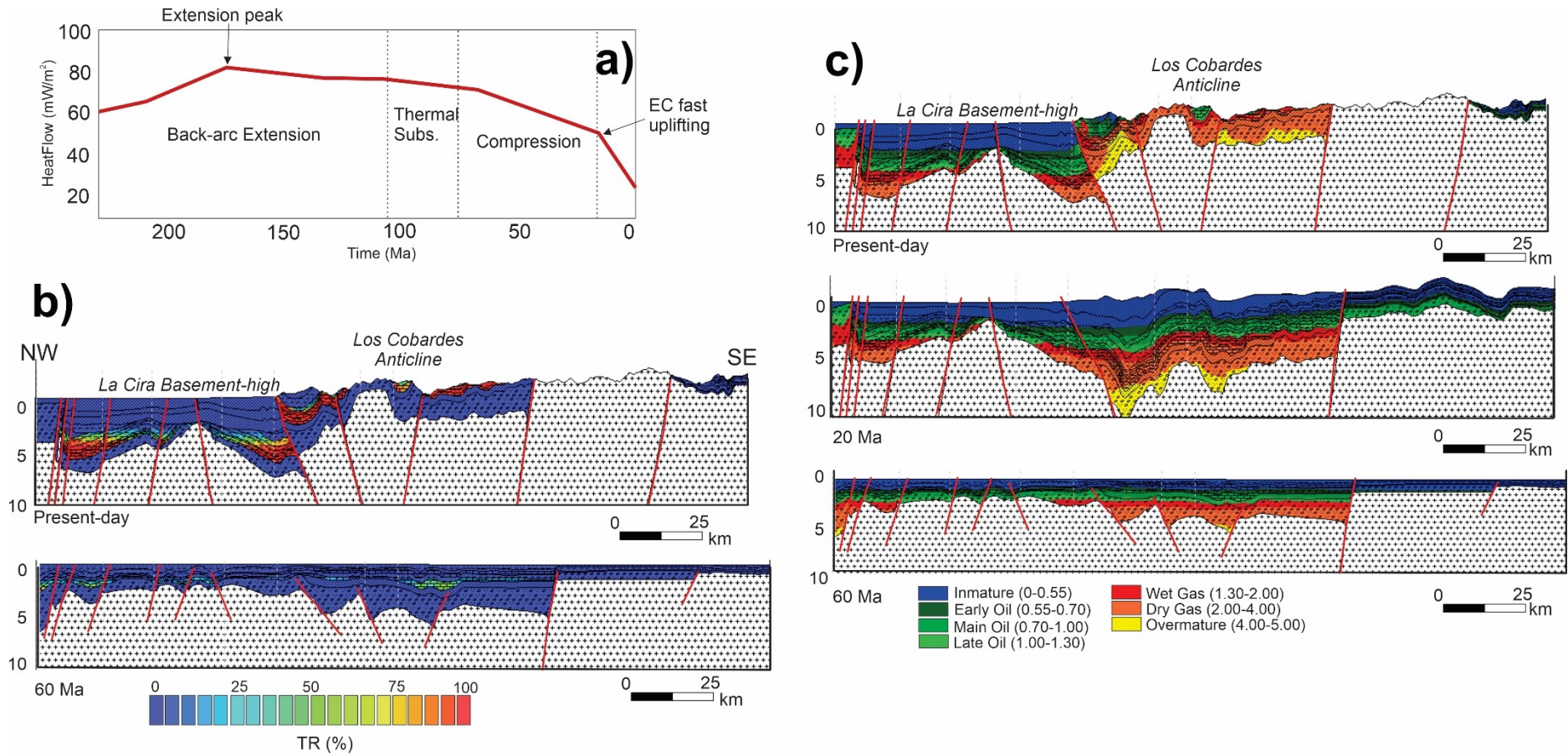


Figure 6-6. a) Heat flow curve for the scenario B b) Transformation ratio reconstruction for the Paleocene and the Present-day configuration (TR<=50% are considered optimal to generate hydrocarbon during this time). c) Vitrinite reflectance reconstruction for the Paleocene, early Miocene and Present-day configuration. All those models are from the cross-section S1 (see location [Figure 6.1](#)) testing the scenario B. Vertical exaggeration 3x.

Chapter 6. Basin modeling of the MMV and EC

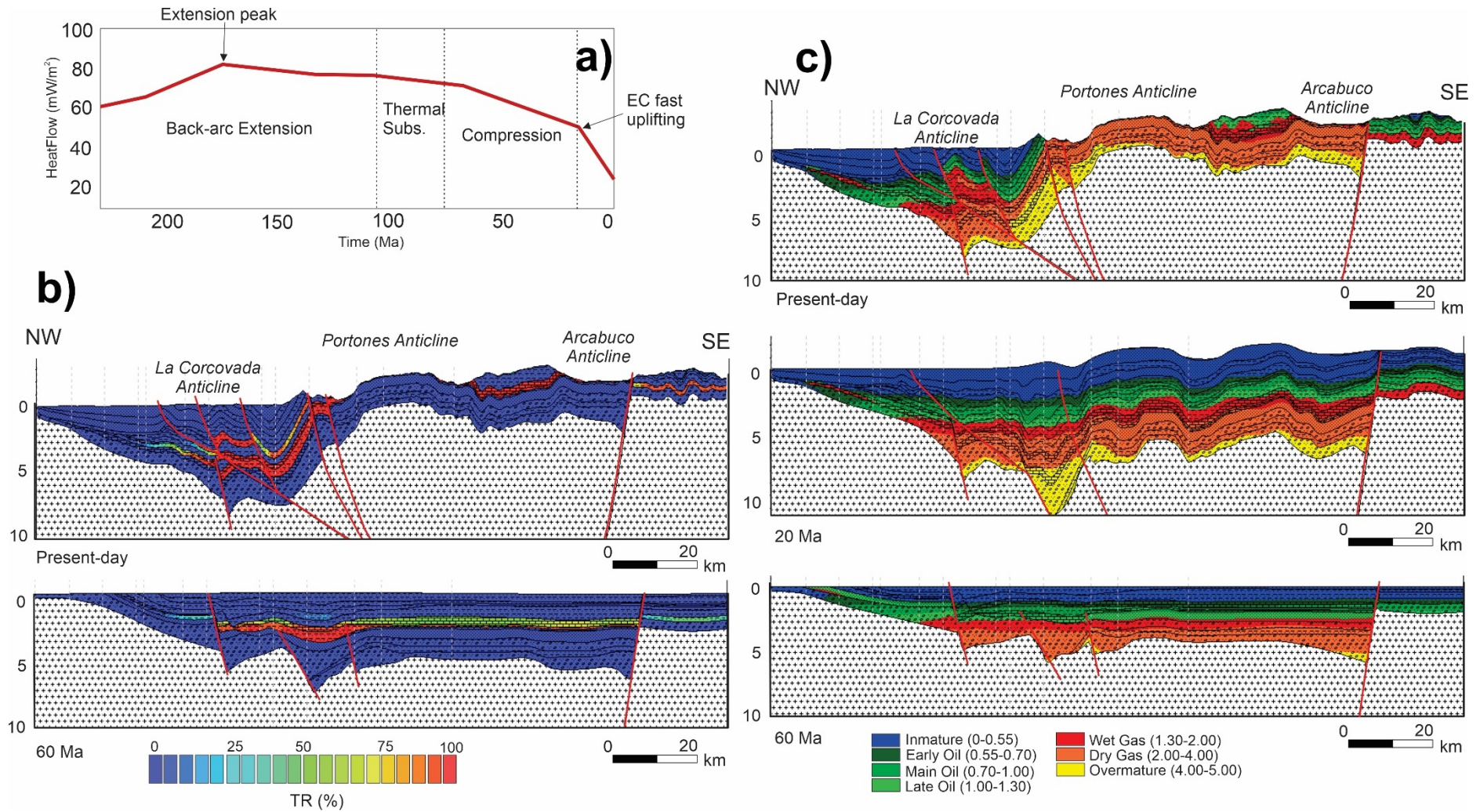


Figure 6-7. a) Heat flow curve for the scenario B b) Transformation ratio reconstruction for the Paleocene and the Present-day configuration (TR<=50% are considered optimal to generate hydrocarbon during this time). c) Vitrinite reflectance reconstruction for the Paleocene, early Miocene and Present-day configuration. All those models are from the cross-section S6 (see location [Figure 6.1](#)) testing the scenario B. Vertical exaggeration 3x.

The upper Cretaceous group, composed of La Luna and Umir formations are in the oil window since the late Oligocene-early Miocene to the Present-day in some localized areas.

Scenario C

The heat flow from this scenario ([Figure 6.8a](#) and [Figure 6.9a](#)) started at $\sim 60 \text{ mWm}^{-2}\text{q}$ from the Late Triassic until the middle Jurassic where the curve shows the first and major peak $\sim 80 \text{ mWm}^{-2}\text{q}$, different than the previous scenarios A and B, this peak shows a flat between the Early Jurassic and Middle Jurassic. Afterward, the heat flow decreased to $\sim 60 \text{ mWm}^{-2}\text{q}$ until the Early Cretaceous, when a slight rising of $5 \text{ mWm}^{-2}\text{q}$ is evident until the middle Cretaceous. After that, a heat flow reduction occurred from the middle Cretaceous to the Late Cretaceous, reaching $\sim 50 \text{ mWm}^{-2}\text{q}$. Then a progressive heat flow decreasing of $\sim 20 \text{ mWm}^{-2}\text{q}$ occurred between the Paleocene to the middle Miocene. During the last heat flow event, a steeped change occurred between the middle Miocene and Present-day heat flow $\sim 25 \text{ mWm}^{-2}\text{q}$. We divided according to the tectonic events recorded in the basin, Late Triassic – Early Cretaceous (back-arc extension), major peak associated with the volcanism during the Middle Jurassic, the second peak plotted is associated with the mafic bodies reported by Vasquez et al. (2010). Since the middle Cretaceous – Late Cretaceous, the basin experienced a short and fast thermal subsidence. Then the Paleocene, a compressional event probably linked to the Cenozoic inversion ongoing until the middle Miocene when the basin experienced major deformation.

The initial transformation ratio reached the levels of hydrocarbon generation since the Eocene ([Figure 6.8b](#) and [Figure 6.9b](#)) in both regions. Concerning the previous scenarios analyzed previously, in the northern region, the transformation ratio decreased considerably $\sim 30\text{-}50 \text{ TR}\%$ in all the stages since the generation started. According to this presumption, the Late Cretaceous source rocks generated primarily on the central part of the basin, and the last pulse of generation showed in the previous scenarios is very weak for this scenario. Regarding the southern region, the cross-section S6 shows a significant decrease in TR% for the Late Cretaceous as the case of the La Luna Formation. According to this Scenario, the La Luna Formation reached its major TR% during the last deformation stage in the deepest areas.

In summary, the major peak of generation occurred during the Oligocene where the basal Cretaceous formations reached 100 TR%, and the upper Cretaceous group is also in conditions to generate. However, the generation pulse is weak, and the transformation ratio is not equally distributed along the cross-sections.

The vitrinite reflectance models obtained from the northern and southern regions ([Figure 6.8c](#) and [Figure 6.9c](#)) with this scenario show that most of the Cretaceous source rocks are in oil window generation from the Eocene until the early Miocene. Also, in some local areas, the source rocks are mature, but with this scenario are most of the source rocks in oil window generation since the Eocene.

Scenario D

The last scenario ([Figure 6.10a](#) and [Figure 6.11a](#)) began at the Late Triassic with a lower heat flow of $\sim 45 \text{ mWm}^{-2}$ than the previously described scenarios A, B, and C. The maximum peak is reached at the Middle Jurassic $\sim 75 \text{ mWm}^{-2}$. After it, a slight decrease to $\sim 60 \text{ mWm}^{-2}$ occurred until the Early Cretaceous. During the Early Cretaceous, the heat flow shows a low variation that occurred until the middle Cretaceous $\sim 60 \text{ mWm}^{-2}$. The major heat flow decreasing was during the middle Cretaceous to early Paleocene from $\sim 60 \text{ mWm}^{-2}$ to $\sim 35 \text{ mWm}^{-2}$. From the Paleocene to the Present-day the heat flow variation does not exceed the $\sim 5 \text{ mWm}^{-2}$.

Chapter 6. Basin modeling of the MMV and EC

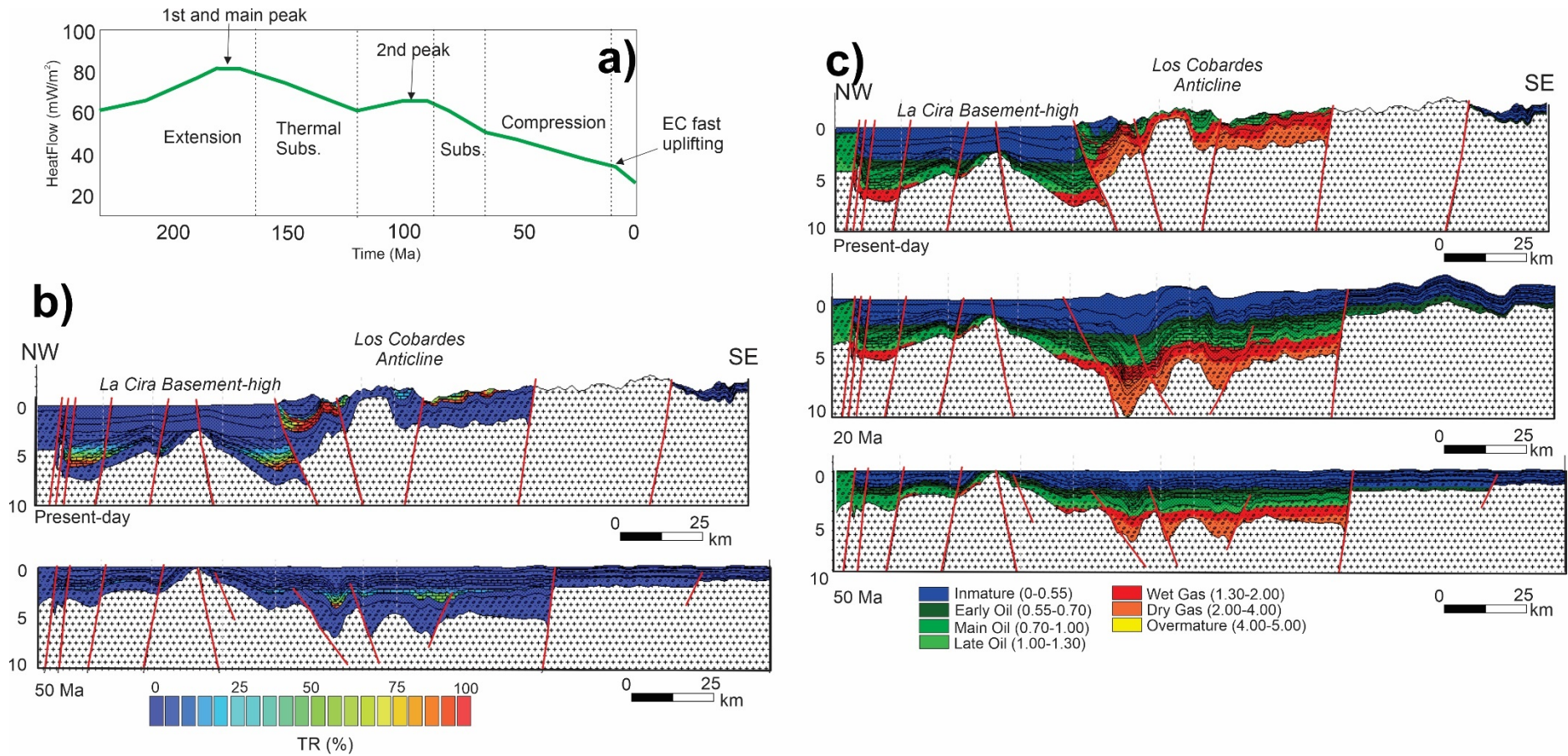


Figure 6-8. a) Heat flow curve for the scenario C b) Transformation ratio reconstruction for the Eocene and the Present-day configuration (TR<=50% are considered optimal to generate hydrocarbon during this time). c) Vitrinite reflectance reconstruction for the Eocene, early Miocene and Present-day configuration. All those models are from the cross-section S1 (see location [Figure 6.1](#)) testing the scenario C. Vertical exaggeration 3x.

Chapter 6. Basin modeling of the MMV and EC

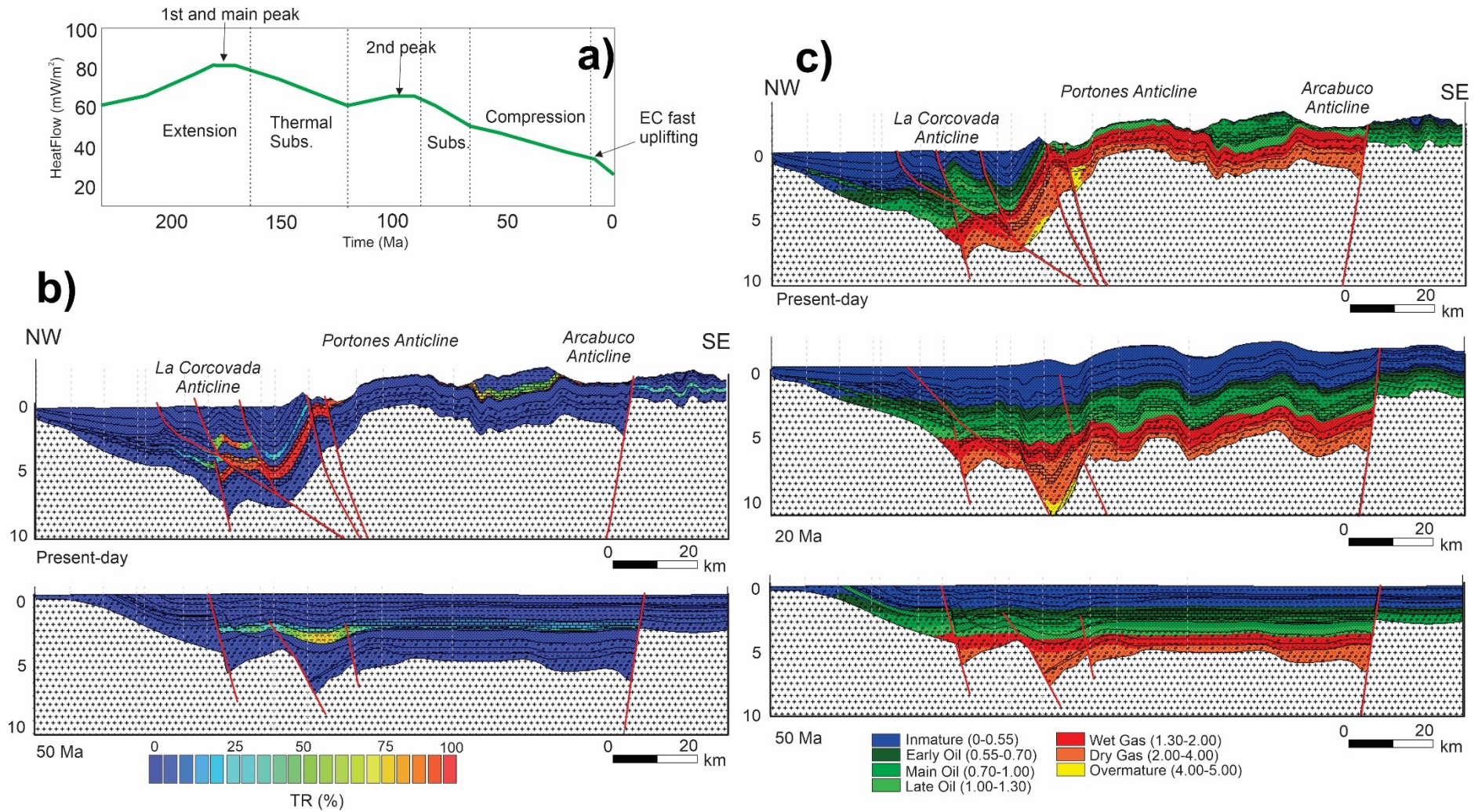


Figure 6-9. a) Heat flow curve for the scenario C b) Transformation ratio reconstruction for the Eocene and the Present-day configuration (TR<=50% are considered optimal to generate hydrocarbon during this time). c) Vitrinite reflectance reconstruction for the Eocene, early Miocene and Present-day configuration. All those models are from the cross-section S6 (see location [Figure 6.1](#)) testing the scenario C. Vertical exaggeration 3x.

The possible tectonic scenarios to obtain this heat flow are Late Triassic-middle Cretaceous (back-arc extension), the major peak of heat flow Middle Jurassic linked to the volcanism. Thermal subsidence event since the middle Cretaceous to the Paleocene. From Paleocene to middle Miocene, a constant heat flow during the compressional event and from the middle Miocene to the Present-day a fast deformation event.

The source rocks reached the transformation ratio to hydrocarbon generation since the middle Eocene ([Figure 6.10b](#) and [Figure 6.11b](#)) being the earliest onset of generation related to the other heat flow scenarios. Furthermore, most of the source rocks do not reach the transformation ratio to generated hydrocarbons with this heat flow scenario. Therefore, according to the models, the major peak of generation occurred during the late Oligocene, and the primary generation source is located in deeper areas during the early Miocene.

According to this heat flow vs. the vitrinite reflectance models ([Figure 6.10a](#) and [Figure 6.11a](#)), the hydrocarbon generation in the basin reached the oil window maturity since the middle Eocene and continued until the Present-day.

Chapter 6. Basin modeling of the MMV and EC

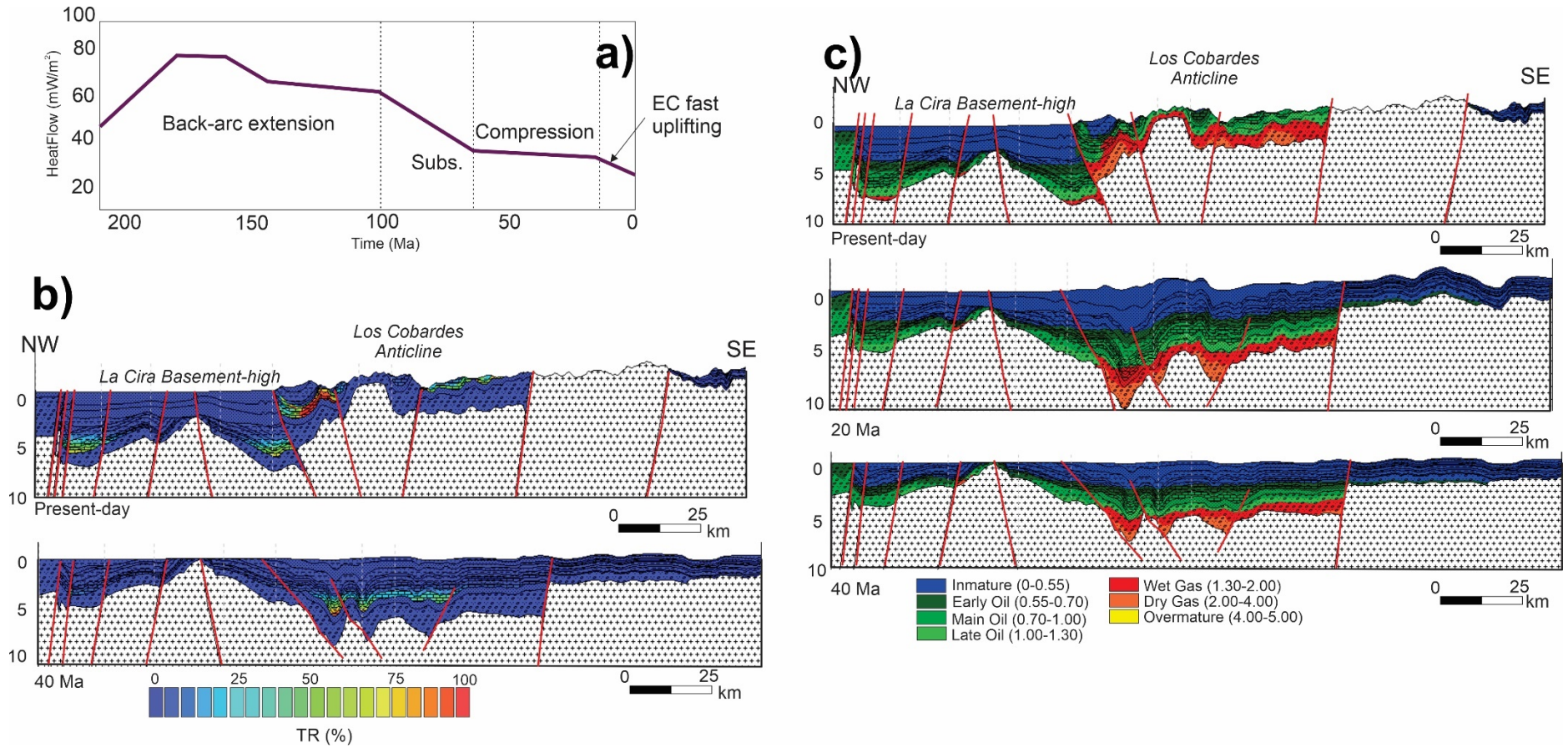


Figure 6-10. a) Heat flow curve for the scenario D b) Transformation ratio reconstruction for the Eocene and the Present-day configuration (TR<=50% are considered optimal to generate hydrocarbon during this time). c) Vitrinite reflectance reconstruction for the Eocene, early Miocene and Present-day configuration. All those models are from the cross-section S1 (see location [Figure 6.1](#)) testing the scenario D. Vertical exaggeration 3x.

Chapter 6. Basin modeling of the MMV and EC

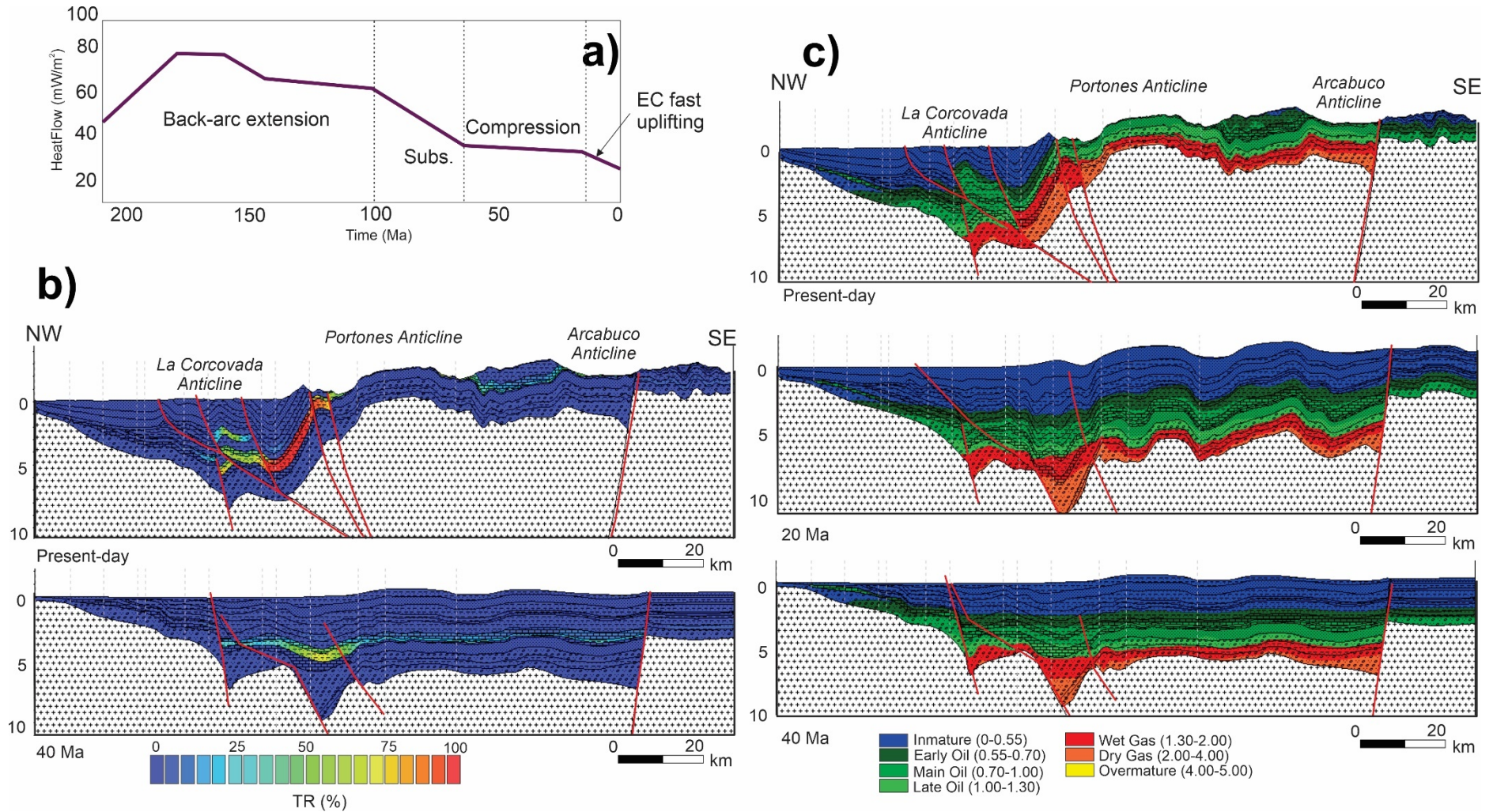


Figure 6-11. a) Heat flow curve for the scenario D b) Transformation ratio reconstruction for the Eocene and the Present-day configuration (TR<=50% are considered optimal to generate hydrocarbon during this time). c) Vitrinite reflectance reconstruction for the Eocene, early Miocene and Present-day configuration. All those models are from the cross-section S6 (see location [Figure 6.1](#)) testing the scenario D. Vertical exaggeration 3x.

Possible Accumulations

We analyzed all the scenarios against the vitrinite reflectance to identify the best fit calibrated model. Afterward, we ran a migration model without the field information details, i.e., pore pressures, Darcy flow, petrophysical parameters, and detailed information that allows calibrating the outcomes.

According to the vitrinite reflectance analysis in different heat flow scenarios ([Figure 6.12](#)), Scenario B is the most suitable, with values between $\sim 85 \text{ mWm}^{-2}\text{q}$ to the approximated present value of $\sim 25 \text{ mWm}^{-2}\text{q}$.

With this model, we can evaluate possible hydrocarbon saturations based on the previously mentioned parameters and the source conditions employed. Based on these, we recognized that this model does not have the detail and precision of the reservoir migration model. However, we consider this alternative as a powerful exploration tool to define target zones.

It is essential to highlight that the petroleum system is not in an optimal condition in this area, especially in terms of seal for the Cenozoic reservoirs; moreover, the trap formation is a critical factor in the hydrocarbon accumulations.

The northern cross-section S1 ([Figure 6.13](#)) has some interesting accumulation areas; the first is located into the west, in the hanging wall block of an east-verging fault, the potential reservoir is the Mugrosa Formation (Oligocene) nevertheless some Eocene formations have hydrocarbon shows, and the seal is the Top of the reservoir formation. To the east in the hanging wall of the La Salina Fault, we have an accumulation to the same geological formation. Other places could be charged and accumulated hydrocarbons, but the weakness in seal and generation could affect the accumulation.

Southward in the cross-section S6, the accumulations are scarce with this model. Nevertheless, we identified a slight accumulation in the western area in a pinch out of the Cretaceous against the Paleocene unconformity. This accumulation could be attributed to the hydrocarbon show presented in the borehole Acacia Este- 1 drilled by Kappa in 2007 (Sarmiento, 2011).

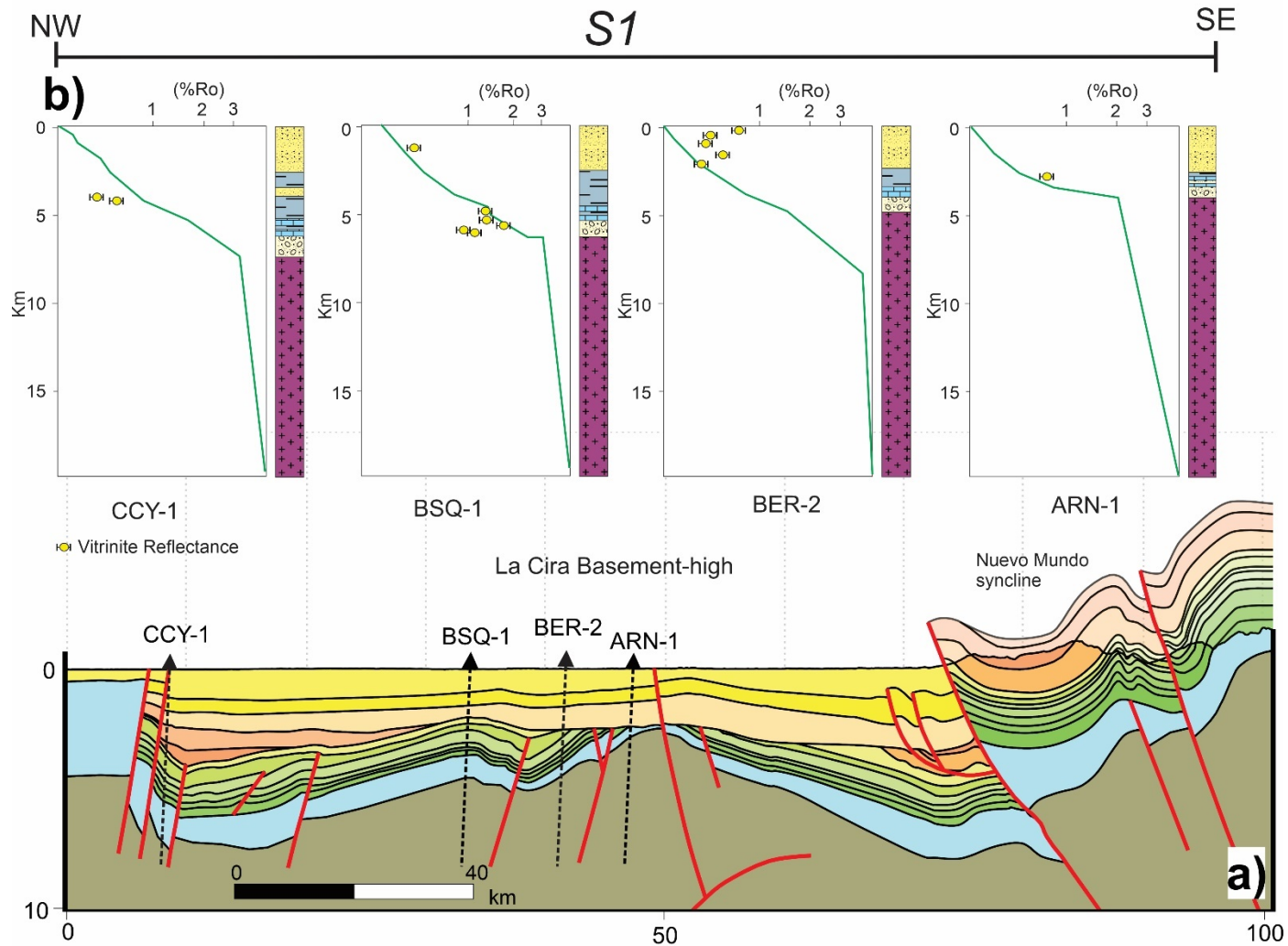


Figure 6-12. a) Western side of the cross-section S₁ with the projected boreholes with vitrinite reflectance (Ro%) (See location in [Figure 6.1](#)). b) Vitrinite reflectance (Ro%) vs depth, showing the expected vitrinite reflectance (green line from Sweeney and Burnham, 1990) vs measured vitrinite reflectance.

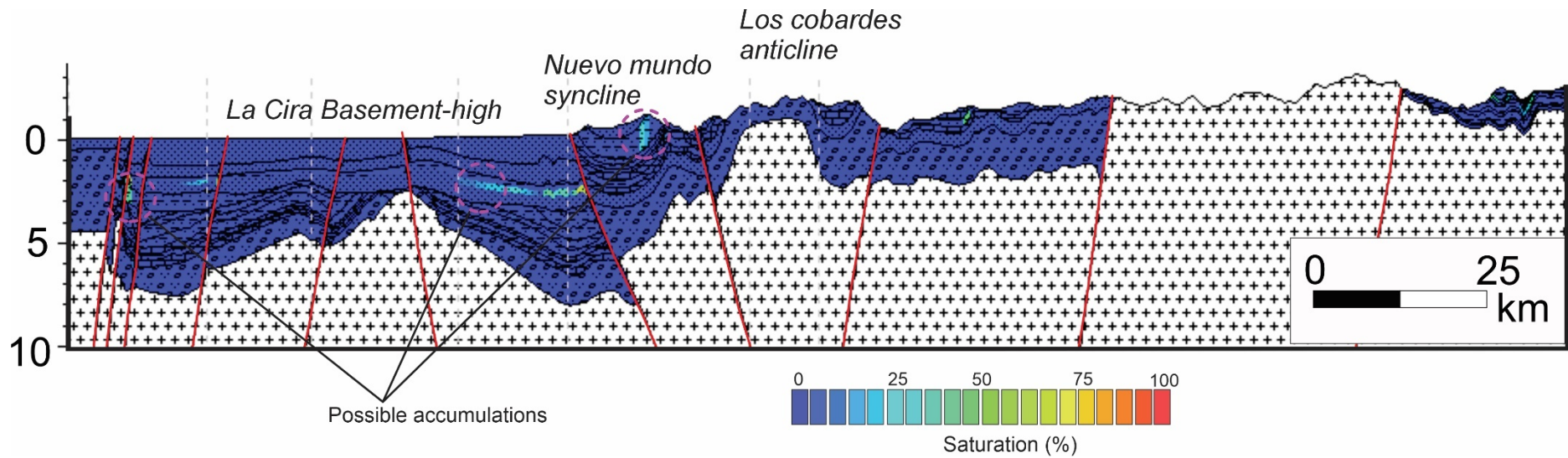


Figure 6-13. Petroleum saturation model in cross-section S1. Dashed purple circles highlight the possible hydrocarbon accumulations.

Conclusions

In summary, and based on the previous subsidence models from the northern and southern regions, we can evidence different sedimentation rates associated with tectonic events over time.

1. (Early Jurassic- Early Cretaceous) during this time occurred the initial deposition related to basin stretching, the subsidence is at a slow rate.
2. (Middle Cretaceous-Late Cretaceous) the subsidence during this time could be associated with the thermal cooling after the initial stretching event. Nevertheless, the distinction of this change is more evident in the Middle Magdalena Valley than the Eastern Cordillera.
3. (Late Cretaceous -Paleocene) a steeped change occurred during this time concerning the previous ages. This is attributed to the inversion onset. Moreover, in some areas, this curve is more inclined and shows a fast subsidence behavior.
4. (Paleocene-middle Miocene) the subsidence rates show a significant increment in deposition, especially in the foreland areas, where the foredeep zones were modeled.
5. (Middle Miocene-Present-day) the foreland models show a low or null deposition in contrast with the Eastern Cordillera in that the curves reflect an erosive event during this time.

Based on the heat flows, we can observe and test the relation and influence with hydrocarbon generation.

According to the best-calibrated models from Scenario A and B, the initial generation occurred from the Paleocene. Latterly, the basin is still generating hydrocarbons until the last phase. Although, nevertheless, source rocks were generating hydrocarbons in the early stages, at late stages are mature or overmature, how is the case of basal kitchens.

In general terms, the high heat flow scenarios modeled in this chapter could overcook some of the source rocks with good conditions to generate hydrocarbons as the Tablazo Formation. Therefore, it is essential to highlight the different TOC (total organic content) and features that are conditioning the generation at different stages from all the source rocks.

The evolution generation model suggested a maximum peak during the Oligocene when all the source rocks had reached the TR% to generate or were reached from previous stages such as the Rosablanca Formation in the Paleocene.

The hydrocarbon accumulations identified in this analysis fit perfectly with the oil and gas discoveries in the study area. Although in this evolutive model, we recognized that the generation started since the Paleocene, in contrast, the trapping generation occurred during and until the last stages of deformation; this assumption allows us to consider the trap formation as one of the critical elements in the petroleum system.

GENERAL CONCLUSIONS

In summary, in this thesis, we analyzed the tectonostratigraphic evolution in the Eastern Cordillera and the Middle Magdalena Valley. We primarily interpreted stratigraphic, structural, petrographic, geochemical and geophysical data. First, we integrated all the information provided and compiled from different sources, with the new outcomes obtained during the development of this project in a Geo-database, next to a summary of the main observations or conclusions obtained during the development of this work.

- According to the new U-Pb zircon ages, we interpreted the onset of extension during the Late Triassic-Early Jurassic.
- The relation between magmatism and extensional events is identified through geochronological data from plutons and volcanoclastic layers. Based on these, we classified the major volcanic events as 1. Late Triassic-Early Jurassic; 2. Middle Jurassic-Late Jurassic, and 3. Early to middle Cretaceous (based on published data, Vasquez et al. 2010).
- Our results support the hypothesis of back-arc extension triggering rifting, primarily based on the calc-alkaline geochemical signature of volcanic ashes and the timing of the extension.
- Early activity of the Bucaramanga-Santa Marta strike-slip fault from the Triassic is suggested by the distribution plutonism, which allows us to interpret a coeval activity.
- There is no clear evidence for a progradation in the extension. Nevertheless, the data obtained from the Noreán and Jordán formations suggest to us that testing the hypothesis of a north to south migration with more geochronological data would be warranted, especially with ages from the Arcabuco and la Rusia highlands.
- Ages obtained from the Girón and Jordán formations contradict their commonly assumed stratigraphic order, suggesting that the Jordán formation could be a lateral equivalent to parts of the Girón formation. Additional detailed stratigraphic information and analysis in the field is required to confirm or dismiss this hypothesis.
- According to the Ordovician ages obtained through Geochronological U-Pb dating in the Arcabuco anticline for the Mesozoic units, detrital zircon ages obtained from volcanoclastic units in the Arcabuco anticline indicate a source in the Floresta massif, suggesting it was part of the rift shoulder.
- In the northernmost part of the project region, the MMV basin subsided between the Central Cordilleran and EC thrust fronts of opposing vergence. We propose coeval

Recommendations

activity of both thrust belts and interpret the main uplift phase of the La Cira basement-high to be related to this shortening event. Thermochronological data (Parra et al., 2012) suggest a Late Cretaceous-Paleocene age for this tectonic event.

- The primary deposition occurred mainly in the hanging wall of the orogenic belts, and the westward onlapping of the pre-Paleocene units is interpreted as an orogenic load response.
- The forebulge is migrating to the west during the Late Cretaceous-Paleocene, and we interpret that it played an essential role in long wave-length uplift.
- The major shortening at shallow structural levels is accumulated in thin-skinned domains, where there are triangle zones and duplexes structures. The deformation is migrated to the west of the MMV from the Western Foothills of the Eastern Cordillera where the frontal sheets developed the thin-skinned structures.
- We identify an important role of Mesozoic inverted structures in the evolution of depocenters. Non-reactivated normal faults in the MMV allow to constrain the timing of Mesozoic extension, nevertheless, the poor seismic quality at deeper levels, near the base of the Mesozoic succession, limits the temporal resolution.
- We propose that present-day geometry of the La Cira Basement-high was largely generated by a blind basement thrust; this structure probably was activated during the uplift of the Central Cordillera. Nevertheless, the forebulge migration as a consequence of coeval orogenic load.
- The west and east verging structures bounding the La Cira Basement-high were active before the pervasive Paleocene unconformity.
- According to kinematic restoration, the Mesozoic inverted structures played an essential role in the basin segmentation; one example is the initial geometry of the La Cira Basement-high as horst during the Cretaceous.
- Kinematic restorations suggest that most shortening is accumulated along the western foothills of the EC and is controlled by the basement-involved structures. The highest fault offsets are associated with triangle zones and duplexes and were mostly obtained during the last stage of deformation in early-late Miocene time.
- The basin development began in an extensional setting from the Late Triassic-Early Jurassic; according to our kinematic restorations and thickness analysis, this tectonic regime lasted until the middle Cretaceous in some areas, after this time, in most of the area the basin transitioned to thermal subsidence.

Recommendations

- According to thermochronological ages obtained by different authors (Gomez et al., 2003; 2005; Mora et al., 2006; 2010; 2013; 2015; Parra et al., 2009;2012; Ramirez-Arias et al., 2012; Sanchez et al., 2012; Caballero et al., 2013; Guerrero, 2018); we interpreted that the initial exhumation occurred in the northern region of the Eastern Cordillera in the Los Cobardes anticline, and according to the values obtained in the Opon region, this uplifting started from the middle Eocene-Early Oligocene. This assumption allows us to infer a gradual uplift southward propagation. Nevertheless, in the northern region, the values obtained suggest a gradual uplifting propagating to the east, in contrast with the southern region where the values obtained by Sanchez et al. (2012) suggested an westward migration of uplift.
- We identified five phases in the subsidence history: (1) Early Jurassic-Early Cretaceous: initial deposition at slow subsidence rate; (2) middle Cretaceous-Late Cretaceous: probably cooling and thermal subsidence; (3) Late Cretaceous-early Paleocene: onset of inversion recorded in the steeped and fast subsidence change; (4) Paleocene-middle Miocene: main subsidence particularly recorded in the foredeep areas); (5) middle Miocene-Present day: slow subsidence in the depocenter areas, erosion in the axial part of the Eastern Cordillera.
- According to the best-fitting heat flow models, the basin began its hydrocarbon generation from the Paleocene, and progressively reached the peak of generation during the Oligocene.
- The high heat flow compared to other conventional extensional models of McKenzie, 1978, where the temperature reached a high temperature peak and afterward experienced a cooling event, in our case the basin is affected by maximum peak of temperature, and different cooling events as consequence of inversion and compression. Based on these features the basin probably was affected the generation conditions of the Tablazo Formation, a potential source rock of probably sufficiently high organic content to generate hydrocarbons.
- We constrained the roles of different petroleum system elements in developing an accumulation; our models can predict and visualize the accumulations and their evolution through time. Based on our model runs with varying heat flow scenarios and organic contents, we found that the most critical elements are the timing of trap formation and the seal conditions.

RECOMMENDATIONS

- We recommend acquiring more geochronological data, especially for the Jurassic and Triassic units, in key areas for the extensional period in the northern Andes. In our study area, we have the challenge to confirm or reject the idea of the Floresta massif influence in the development and the absence of Mesozoic grains in these samples; based on this uncertainty, intensive fieldwork at higher detail to identify more volcanoclastic layers is highly recommended.
- In this work, we compiled different datasets and assessed their importance to reach viable models; nevertheless, stratigraphic detail could be increased in some areas, especially with the Mesozoic units, in order to validate or reject the idea of Jordán and Girón as belonging to the same formation.
- Numerical flexure modeling is highly recommended to understand the crustal behavior and constrain possible crustal evolution models in complex areas such as the double vergence zone characterizing the northern region. Flexure modelling would also help to identify the influence of variable orogenic loading and its impact on the depocenter zone, possibly revealing additional processes affecting the generation of uplift and depozone subsidence such as dynamic topography.
- The amount of available data is high and allowed us to approach most problems suitably. Nevertheless, we consider that some areas could benefit from additional thermochronology data, especially in the southern region, to support or improve the uplift evolution model. Another exciting project could be to trace the thermal evolution of boreholes in the Middle Magdalena Valley and Eastern Cordillera using different thermochronometers to calibrate the burial and cooling history.
- Reprocessing of the seismic data is an excellent alternative for improving the seismic quality without new acquisition. Nevertheless, most seismic campaigns were run in the 60s when there were other exploration targets with the imaging focused on shallow Cenozoic deposits. For increased quality and resolution in the basal deposits new 2D and 3D seismic data need to be acquired. More and more detailed fieldwork along the western foothills where the seismic imaging is challenging would be helpful.
- In a next step of kinematic restoration, our new results could be integrated with existing cross-sections from the eastern side of the Eastern Cordillera to analyze the evolution of deformation patterns and especially uplift and exhumation for the entire mountain chain.

Recommendations

- Basin modeling as a tool to explore frontier and mature basins such as the Middle Magdalena Valley is a solid methodology for identifying interest zones, increasing the level of detail, and supporting exploration ideas. Our models produce realistic results that match oil and gas discoveries. Nevertheless, these models could become even more realistic, reliable and accurate with more detailed information on TOC, Ro% from boreholes, petrophysical properties.

REFERENCES

- Alarcón CM, Clavijo-Torres J, Mantilla-Figueroa LC, Rodríguez JG. (2020) Nueva propuesta de edades para el registro sedimentario de las formaciones Bocas y Jordán y su relación con el desarrollo de la actividad magmática del Grupo Plutónico de Santander (cordillera Oriental, Colombia). *Rev. Acad. Colomb. Cienc. Ex. Fis. Nat.* 44(173):1137-1151. doi: <https://doi.org/10.18257/raccefyn.1208>
- Allen P, Allen R, (2013) *Basin analysis: Principles and Applications to Petroleum Play Assessment*, Third Edition. Publications, Blackwell Scientific.
- ANH., (2006) Línea Sísmica Trasandina ANH-TR-2006-4A, VMM-Cordillera Oriental, Informe Sismopetrol-Inforpetrol, 91 p. Bogotá -Colombia.
- Arango M, Rodríguez G, Zapata G, Correa A, (2016) Monzogranito de Rionegro. Catálogo de unidades litoestratigráficas de Colombia. Servicio Geológico Colombiano, 128 p. Medellín.
- Aspden J, McCourt W, Brook M, (1987). Geometrical control of subduction-related magmatism: the Mesozoic and Cenozoic plutonic history of Western Colombia. *Journal of the Geological Society* 144 (6), 893-905.
- Ballesteros C, (1989) Petrographic study of the Lower Cretaceous, Arcabuco, Cumbre and Rosablanca Formations, Sabanagrande-El Penon- Hoya de Panama area, Departamento de Santander, Colombia. - (MS Thesis) University of South Carolina, 60 p.
- Bayona G, Rapalini A, Costanzo-Alvarez V, (2006) Paleomagnetism in Mesozoic rocks of the Northern Andes and its implications in Mesozoic Tectonics of Northwestern South America. *EPS* 58 (10), 1255-1272.
- Bayona G, Bustamante C, Nova G, Salazar-Franco A, (2020) Jurassic evolution of the northwestern corner of Gondwana: Present knowledge and future challenges in studying Colombian Jurassic rocks. In: Gómez J, Pinilla-Pachon A, (editors), *The Geology of Colombia, Volume 2 Mesozoic*. Servicio Geológico Colombiano, *Publicaciones Geológicas Especiales* 36, 37 p. Bogotá. <https://doi.org/10.32685/pub.esp.36.2019.05>
- Beaumont C, Quinlan G, Stockmal G, (1993) The evolution of the Western Interior Basin: causes, consequences and unsolved problems. In: Caldwell, W.G.E., Kauffman, E.G. (Eds.), *Evolution of the Western Interior Basin*, Special Paper 39. Geological Association of Canada, pp. 97-117.

References

- Behar F, Vandenbroucke M, Tang Y, Marquis F, Espitalié J, (1997) Thermal cracking of kerogen in open and closed systems: determination of kinetic parameters and stoichiometric coefficients for oil and gas generation. *Organic Geochemistry* 26, 321–339
- Bjorlykke K, (2010) Heat transport in sedimentary basins, in Bjorlykke K, (Editor), *Petroleum Geoscience: From Sedimentary Environments to Rock Physics*: New York, Springer, p. 253–260
- Branquet Y, Cheilletz A, Cobbold P, Baby P, Laumonier B, Giuliani G, (2002) Andean deformation and rift inversion, eastern edge of Cordillera Oriental (Guatèque – Medina area), Colombia: *Journal of South American Earth Sciences*, v. 15, p. 391–407
- Bürgl H, (1954) El cretáceo inferior en los alrededores de Villa de Leiva, Boyacá. *Bol. Geológico, Serv. Geol. Nal.*, v.2, n.1, ps.5-22, 4 ls., Bogotá.
- Bürgl H, (1961) Historia geológica de Colombia. *Revista de la Acad. Colomb. de Ciencias Exac. Fis. y Nat.*, v, 11, n, 43, ps, 137.191, 41 fs., Bogota.
- Bustamante C, Archanjo C, Cardona A, Vervoort J, (2016) Late Jurassic to Early Cretaceous plutonism in the Colombian Andes: A record of long-term arc maturity. *Geological Society of America Bulletin*, 128(11–12): 1762–1779. <https://doi.org/10.1130/B31307.1>
- Caballero V, Parra M, Mora A, (2010) Levantamiento de la Cordillera Oriental de Colombia durante el Eoceno Tardío- Oligoceno Temprano: Proveniencia sedimentaria en el Sinclinal de Nuevo Mundo, cuenca Valle Medio del Magdalena. *Boletín de Geología* ISSN: 2145-8553 ed: Cefac Universidad Industrial De Santander, v.32 fasc.1 p.45 – 77p.
- Caballero V, Parra M, Mora A, López C, Rojas L, Quintero I, (2013). Factors controlling selective abandonment and reactivation in thick-skin orogens: a case study in the Magdalena Valley, Colombia. *Geological Society, London, Special Publications*, 377(1), 343–367. <https://doi.org/10.1144/SP377.4>
- Cáceres C, Cediel F, Etayo-Serna F, (2003) Maps of Sedimentary Facies Distribution and Tectonic Setting of Colombia through the Proterozoic and Phanerozoic. *Ingeominas*: Bogotá.
- Cardona A, Valencia V, Lotero A, Villafañez Y, Bayona G, (2016) Provenance of middle to late Paleozoic sediments in the northeastern Colombian Andes: Implications for Pangea reconstruction. *International Geology Review*, 58(15): 1914– 1939. <https://doi.org/10.1080/00206814.2016.1190948>
- Carrillo E, Mora A, Ketcham R, Amorocho R, Parra M, Costantino D, Robles W, Avellaneda, W., Carvajal, J.S., Corcione, M.F., Bello, W., Figueroa J, Gómez J, González

References

- J, Quandt D, Reyes M, Rangel A, Román I, Pelayo Y, Porras J, (2016) Movement vectors and deformation mechanisms in kinematic restorations: A case study from the Colombian Eastern Cordillera. *Interpretation*, 4(1): T31–T48. <https://doi.org/10.1190/INT-2015-0049.1>
- Casero P, Salel J, Rossato A, (1997): Multidisciplinary correlative evidence for polyphase geological evolution of the foot-hills of the Cordillera Oriental (Colombia). IV Simposio Bolivariano “Exploración Petrolera en la Cuencas Subandinas”, T. 1, pp 119-128.
 - Catuneanu O, Sweet A, Miall A, (2000) Reciprocal stratigraphy of the Campanian–Paleocene Western Interior of North America. *Sedimentary Geology* 134 (3–4), 235–255
 - Catuneanu O, (2004) Retro-arc foreland systems evolution through time. *Journal African. Earth Sciences*. 38, 225–242.
 - Cediél F, (1968) El grupo Girón, una molasa mesozoica de la Cordillera Oriental. *Boletín Geológico, INGEOMINAS, Bogotá*, 16, pp. 5–96.
 - Cediél F, Shaw R, Cáceres C, (2003) Tectonic assembly of the northern Andean Block. In: Bartolini C, Buffler R, Blickwede J, (editors), *The circum-Gulf of Mexico and the Caribbean: Hydrocarbon habitats, basin formation, and plate tectonics*. American Association of Petroleum Geologists, Memoir 79, p. 815–848. Tulsa, USA.
 - Cediél F, Shaw R, 2018 *Geology and tectonics of Northwestern South America, the Pacific, Caribbean, Andean conjunction*, F. Cediél and R. P. Shaw, Eds. Springer. https://doi.org/10.1007/978-3-319-76131-2_16
 - Chase C, Sussman A, Coblentz D, (2009) Curved Andes: geoid, forebulge, and flexure. *Lithosphere*, 1, 358–363. doi: 10.1130/L67.1.
 - Clavijo J, (1996) Mapa geológico de Colombia, Plancha 75 – Aguachica. INGEOMINAS. Memoria explicativa, Bucaramanga, 1:48 pág.
 - Clavijo, J, Mantilla, L, Bernal, P, Perez, A, (2008) Evolución geológica de la Serranía de San Lucas, Norte del Valle Medio del Magdalena y Noroeste de la Cordillera Oriental. *Boletín de Geología, Universidad Industrial de Santander*, 30, 45–62.
 - Cochrane R, Spikings R, Gerdes A, Winkler W, Ulianov A, Mora A, Chiaradia M, (2014) Distinguishing between in-situ and accretionary growth of continents along active margins. *Lithos*, 202–203: 382–394. <https://doi.org/10.1016/j.lithos.2014.05.031>
 - Colletta B, Hebrard F, Letouzey J, Werner P, Rudkiewicz J, (1990) Tectonic style and crustal structure of the eastern Cordillera (Colombia) from a balanced cross-section, in Letouzey J, (editor), *Petroleum and tectonics in mobile belts*: Paris, Technip, p. 81–100.

References

- Cooper M, Addison R, Alvarez M, Coral R, Graham S, Hayward J, Martinez J, Naar R, Peñas A, Pulham J, Taborda A, (1995) Basin development and tectonic history of the Llanos Basin, eastern Cordillera, and Middle Magdalena Valley, Colombia: AAPG Bulletin, v. 79, p. 1421–1443.
- Cooper M, Warren M, (2020) Chapter 10 - Inverted fault systems and inversion tectonic settings in Scarselli N, Adam J, Chiarella D, Roberts D, Bally A (editors) Regional Geology and Tectonics, Volume 1 (Principles of Geology Analysis). Elsevier <https://doi.org/10.1016/C2017-0-00442-1>
- Correa–Martínez A, Rodríguez G, Arango M, Zapata G, Bermúdez J, (2016) Batolito de Mogotes. Catálogo de unidades litoestratigráficas de Colombia. Servicio Geológico Colombiano, 110 p. Medellín.
- Correa–Martínez A, Rodríguez G, Bermúdez J, Arango M, Zapata G, (2018) Riolitas del Alto Los Cacaos. Catálogo de unidades litoestratigráficas de Colombia. Servicio Geológico Colombiano, 54 p. Medellín.
- Costantino D, Paton D, Mora A, (2021) Structural Style and Kinematic History of the Colombian Eastern Cordillera. *Frontiers Earth Sciences*. Special research topic: Active Fold-and-Thrust Belts: From Present-Day Deformation to Structural Architecture and Modelling.
- Cross T, Pilger R, (1982) Controls of Subduction Geometry, Location of Magmatic Arcs, and Tectonics of Arc and Back-arc Regions, *Geol. Soc. Amer. Bull.* 93, 545–562.
- Dahlstrom C, (1969) Balanced cross sections: *Canadian Journal of Earth Sciences*, v.6, p. 743-757
- DeCelles P, (2012) Foreland basin systems revisited: variations in response to tectonic settings. In: Busby, C., Azor, A. (Eds.), *Tectonics of Sedimentary Basins: Recent Advances*. Wiley-Blackwell, Oxford, UK, pp. 405–426.
- DeCelles P, Giles K, (1996) Foreland basin systems. *Basin Research*. 8, 105–123. doi:10.1046/j.1365-2117.1996.01491.x
- DeCelles P, Ducea M, Kapp P, (2009). Cyclicality in Cordilleran orogenic systems. *Nature Geosciences* 2, 251–257 <https://doi.org/10.1038/ngeo469>
- Dengo C, Covey M, (1993) Structure of the Eastern Cordillera of Colombia: Implications for trap styles and regional tectonics. *American Association of Petroleum Geologists Bulletin*, 77(8): 1315–1337. <https://doi.org/10.1306/BDFE8E7A-1718-11D7-8645000102C1865D>

References

- Dickey P, (1992) La Cira-Infantas Field Δ Colombia, Middle Magdalena Basin. In: Beaumont E, Foster N, (Editors.), Structural Traps VII. American Association of Petroleum Geologists Treatise of Petroleum Geology: Atlas of Oil and Gas Fields, A-25, pp. 323-347.
- Dodson M, (1973) Closure temperature in cooling geochronological and petrological systems: Contributions to Mineralogy and Petrology, v. 40, p. 259-274.
- Dunkl I, Mikes T, Simon K, von Eynatten H, (2008) Brief introduction to the Windows program Pepita: data visualization, and reduction, outlier rejection, calculation of trace element ratios and concentrations from LA-ICP-MS data. In: Laser ablation ICP-MS in the Earth Sciences: Current practices and outstanding issues. Mineralogical Association of Canada, Short Course (Edited. by Sylvester P) 40, 334-340.
- Dunkl I, Kuhlemann J, Reinecker J, Frisch W, (2005): Cenozoic relief evolution of the Eastern Alps – constraints from apatite fission track age-provenance of Neogene intramontane sediments. Austrian Journal of Earth Sciences, 98, 92-105.
- Egan S, Buddin S, Kane S, Williams G, (1997) Three-dimensional modelling and visualisation in structural geology: New techniques for the restoration and balancing of volumes. Proceedings of the 1996 geoscience information group conference on geological visualisation. Electron Geology, 1:67-82
- Etayo-Serna F, (1964) Posición de las faunas en los depósitos cretácicos colombianos y su valor en la subdivisión cronológica de los mismos. Bol. Geol., Univ. Ind. Santander, n° 16-17, pp. 5-141, 8 fig., Bucaramanga.
- Etayo-Serna F, (1968), El sistema Cretáceo en la región de Villa de Leiva y zonas próximas. Geología Colombiana, Bogotá, 5: 5-74.
- Fabre A, (1983) Geología de la extremidad sur de La Sierra Nevada de El Cocuy y los alrededores de La Salina y Sacama, Plancha 153 -Chita, Boyacá, Arauca y Casanare. Informe No.1911. Informe No.1911. Bogotá, Colombia.
- Fail R, (1969) Kink band structure in the Valley and Ridge Province, central Pennsylvania: Geological Society America Bulletin, V. 80, p. 2539-2550.
- Frei D, Gerdes A, (2009) Precise and accurate in situ U-Pb dating of zircon with high sample throughput by automated LA-SF-ICP-MS. Chemical Geology 261, 261-270.
- Frost R, Barnes C, Collins W, Arculus R, Ellis D, Frost C, (2001) A geochemical classification for granitic rocks. Journal of Petrology, 42(11): 2033- 2043.
- Gallagher K, Brown W, Johnson C, (1998) Geological applications of fission track analysis: Annual Review of Earth and Planetary Sciences, v. 26, p. 519-572.

References

- Geyer O, (1969) La fauna de amonitas del perfil típico de la Formación Morrocoyal (Liásico Inferior). I Congreso Colombiano de Geología. Bogotá, Colombia.
- Geyer O, (1982) Comparaciones estratigráficas y faciales en el Triásico Norandino. *Geología Norandina*, Bogotá, 5: 27-31
- Gómez E, Jordán T, Allmendinger R, Hegarty K, Kelley S, Heizler M, (2003) Controls on architecture of the late Cretaceous to Cenozoic Southern Middle Magdalena Valley Basin, Colombia. *Geological Society of America Bulletin*, 115, 131-147.
- Gómez E, Jordán T, Allmendinger R, Hegarty K, Kelley S, (2005) Syntectonic Cenozoic sedimentation in the northern middle Magdalena Valley Basin of Colombia and implications for exhumation of the Northern Andes. *Bulletin of the Geological Society of America*, 117(5-6), 547-569. <https://doi.org/10.1130/B25454.1>
- Gómez J, Montes N, Nivia Á, Diederix H, (2015) Geological Map of Colombia 2015. Scale 1:1 000 000. Servicio Geológico Colombiano, 2 sheets. Bogotá.
- González H, Maya M, Tabares L, Montoya A, Palacio A, Sánchez C, Barajas A, Vélez W, (2015) Elaboración de la cartografía geológica de un conjunto de planchas a escala 1:100.000 ubicadas en cuatro bloques del territorio nacional, identificados por el Servicio Geológico Colombiano. Plancha 118-San Francisco. Servicio Geológico Colombiano.
- González R, Suárez C, Higuera I, Rojas L, (2020) Alternative workflow for three-dimensional basin modeling in areas of structural complexity: Case study from the Middle Magdalena Valley, Colombia. *AAPG Bulletin*. Volume 104 (1): 1-19. <https://doi.org/10.1306/0415191612917185>
- Gleadow A, Duddy I, Green P, Lovering J, (1986) Confined fission track lengths in apatite: a diagnostic tool for thermal history analysis. *Contributions to Mineralogy and Petrology* 94, 405-415.
- Green P, Duddy I, Laslett G, Hegarty K, Gleadow A, Lovering J, (1989) Thermal annealing of fission tracks in apatite: 4. Quantitative modelling techniques and extension to geological timescales: *Chemical Geology*, v. 79, p. 155-182.
- Guerrero J, (2018) Pre-andean tectonic events from albian to eocene in the middle Magdalena valley and situation of the western flank of the proto-eastern cordillera (Colombia). PhD thesis, Universidad Nacional de Colombia - Sede Bogotá.
- Guerrero J, Montes L, Jaillard E, Kammer A, (2021) Seismic interpretation of the Cretaceous unconformities and sequences in the Middle Magdalena Valley and the western margin of the Eastern Cordillera, Colombia *Comptes Rendus. Géoscience*, Volume 353 no. 1, pp. 155-172.

References

- Haas O, (1960): Lower Cretaceous Ammonites from Colombia, South America. The American Museum of Natural History No. 2005.
- Hantschel T, Kauerauf A, (2009) Fundamentals of basin and petroleum systems modeling. Springer, Berlin, 475pp.
- Hooghiemstra H, Wijninga V, Cleef A, (2006) The paleobotanical record of Colombia: Implications for biogeography and biodiversity. *Annals of the Missouri Botanical Garden*, 93(2): 297–325. [https://doi.org/10.3417/0026-6493\(2006\)93\[297:TPROCI\]2.o.CO;2](https://doi.org/10.3417/0026-6493(2006)93[297:TPROCI]2.o.CO;2)
- Horton B, Saylor J, Nie J, Mora A, Parra M, Reyes-Harker A, Stockli D, (2010) Linking sedimentation in the Northern Andes to basement configuration, Mesozoic extension, and Cenozoic shortening: evidence from detrital zircon U–Pb ages, Eastern Cordillera, Colombia. *Geological Society of America Bulletin*, 122, 1423–1442.
- Horton B, Anderson V, Caballero V, Saylor J, Nie J, Parra M, Mora A, (2015) Application of detrital zircon U–Pb geochronology to surface and subsurface correlations of provenance, paleo drainage, and tectonics of the Middle Magdalena Valley Basin of Colombia. *Geosphere* 11, 1790–1811. <https://doi.org/10.1130/GES01251.1>
- Hubach E, (1957) Estratigrafía de Sabana de Bogotá y alrededores. *Inst. Geol., Nal., Bol. Geol.*, 5(2). Bogotá
- Hurford, J (1998) Zeta: the ultimate solution to fission-track analysis calibration or just an interim measure? In: P. van den Haute and F. De Corte (Editors), *Advances in fission-track geochronology*, pp. 19–32, Kluwer Academic Publishers
- IHS Markit, (2020) Middle Magdalena Basin, basin summary report.
- INGEOMINAS – UIS, (2006) Cartografía geológica de 9.600 KM² de la Serranía de San Lucas: planchas 55 (El Banco), 64 (Barranco de Loba), 85 (Simití) y 96 (Bocas del Rosario).
- Jackson S, Pearson N, Griffin W, Belousova E, (2004) The application of laser ablation-inductively coupled plasma-mass spectrometry to in situ U–Pb zircon geochronology. *Chemical Geology* 211, 47–69.
- Jaillard E, Soler P, Carlier G, Mourier T, (1990) Geodynamic evolution of the northern and central Andes during early to middle Mesozoic times: a Tethyan model. *Journal Geological Society of London*, 147, 1009–1027, 9 figs. London.
- Jaillard E, Hérail G, Monfret T, Diaz-Martinez E, Baby P, Lavenu A, Dumont J.-F, (2000) Tectonic evolution of the Andes of Ecuador, Peru, Bolivia and northernmost Chile. In: Cordani U, Milani E, Thomaz F, Campos D, (Editors) *Tectonic Evolution of South*

References

- America. Proceedings of the 31st International Geological Congress, Rio de Janeiro, 481–559
- Jarrard R, (1986) Relations among subduction parameters. *Reviews of Geophysics*, 24, 217–284.
 - Jordán T, (1981) Thrust loads and foreland basin evolution, Cretaceous, western United States: *American Association of Petroleum Geologists Bulletin*, v. 65, p. 2506–2520
 - Julivert M, (1958) La morfoestructura de la zona de mesas al SW de Bucaramanga. *Boletín de Geología* 1: 9-43.
 - Julivert M, (1963) Nuevos datos sobre la dinámica del ámbito del Macizo de Santander durante el Secundario (Cordillera Oriental, Colombia). *Ibid.*, nº 12, pp. 45-49, 2 fig., Bucaramanga.
 - Kammer A, (1996) Estructuras Y Deformaciones Del Borde Oriental Del Macizo De Floresta. *Geología Colombiana*, 21, 65–80. Bogotá.
 - Kammer A, (1999) Observaciones acerca de un origen transpresivo de la Cordillera Oriental. *Geología Colombiana*, 24: 29-53. Bogotá.
 - Kammer A, Sánchez J, (2006) Early Jurassic rift structures associated with the Soapaga and Boyacá faults of the eastern Cordillera, Colombia: Sedimentological inferences and regional implications: *Journal of South American Earth Sciences*, v. 21, p. 412–422.
 - Kammer, A., Piraquive, A., Gómez, C., Mora, A., Velásquez, A., (2020) Structural styles of the Eastern Cordillera of Colombia. In: Gómez, J., Mateus-Zabala, D. (editors), *The Geology of Colombia, Volume 3 Paleogene – Neogene*. Servicio Geológico Colombiano, *Publicaciones Geológicas Especiales* 37, p. 143–183. Bogotá.
 - Lagenheim J, (1961) Late Paleozoic and early Mesozoic fossil plants from the Cordillera Oriental of Colombia and correlation of the Girón Formation. *Boln. geol. Bogotá*, 8, (1-3), 95-132.
 - Leal-Mejía H, Shaw R, Melgarejo J, (2011) Phanerozoic granitoid magmatism in Colombia and the tectono-magmatic evolution of the Colombian Andes. In: Cediél F (ed) *Petroleum Geology of Colombia. Regional Geology of Colombia*, vol 1. Agencia Nacional de Hidrocarburos (ANH) – EAFIT, p 109–188
 - Leal-Mejía H, Shaw R, Melgarejo J, (2019) Spatial/temporal migration of granitoid magmatism and the phanerozoic tectono-magmatic evolution of the Colombian Andes. In: Cediél F and Shaw RP (eds). *Geology and Tectonics of Northwestern South America: The Pacific Caribbean-Andean Junction*, Springer, pp 253–397.

References

- Ludwig K, (2012) User's manual for Isoplot 3.75: A geochronological Toolkit for Microsoft Excel. Berkeley Geochronology Center Special Publication, no. 4, p. 70.
- Mantilla L, Bernal L, Clavijo J, Osorio J, Pinto J, Castro E, Quintero I, Perez A, Ibañez D, Paez L, Correa K, Lopez E, Garcia C, Serrano J, Casas R, Niz L, Castellanos O (2006) Cartografía geológica de 9.600 KM² de la Serranía de San Lucas: planchas 55 (El Banco), 64 (Barranco de Loba), 85 (Simití) y 96 (Bocas del Rosario). INGEOMINAS-UIS. Informe Final Plancha 64, 201 p.
- Mantilla L, Bissig T, Cottle J, Hart C, (2012) Remains of early Ordovician mantle-derived magmatism in the Santander Massif (Colombian Eastern Cordillera). *Journal of South American Earth Sciences* 38:1–12.
- Maze W, (1984) Jurassic La Quinta Formation in the Sierra de Perija, northwestern Venezuela: geology and tectonic environment of red beds and volcanic rocks. - *Geol. Soc. Am. Mem.*, 162, 263-82.
- McCourt W, Aspden J; Brook M, (1984) New geological and geochronological data from the Colombian Andes: continental growth by multiple accretion. *Journal of the Geological Society, London*, 141, 831-45.
- McKenzie D, (1978) Some remarks on the development of sedimentary basins: *Earth and Planetary Science Letters*, v. 40, no. 1, p. 25–32, doi:10.1016/0012-821X(78) 90071-7.
- Metcalf R, Smith E, (1995) Introduction to Special Section: Magmatism and Extension, *J. Geophys. Res.*, 100(B6), 10249– 10253, <https://doi:10.1029/95JB00759>.
- Mojica J, Kammer A, (1995) Eventos jurásicos en Colombia. *Geología Colombiana*, 19, pgs. 165-172, 2 Figs., Santa Fé de Bogotá.
- Mojica J, Kammer A, Ujueta G, (1996) El Jurásico del Sector Noroccidental de Suramerica y Guías de la Excursión al Valle Superior del Magdalena (Nov. 1-4/95), *Regiones de Payandé y Prado, Departamento del Tolima, Colombia*. -*Geología Colombiana No.21*, p. 3-40, 18 Figs., 3 Láminas, Santafé de Bogotá.
- Mora A, Parra M, Strecker M, Kammer A, Dimate C, Rodriguez F, (2006) Cenozoic contractional reactivation of Mesozoic extensional structures in the eastern Cordillera of Colombia: *Tectonics*, v. 25, TC2010, <https://doi:10.1029/2005TC001854>.
- Mora A, Parra M, Strecker M, Sobel E, Hooghiemstra H, Torres V, Jaramillo J, (2008) Climatic forcing of asymmetric orogenic evolution in the Eastern Cordillera of Colombia. *Geological Society of America Bulletin*, 120, 930–949.
- Mora A, Gaona T, Kley J, Montoya D, Parra M, Quiroz L, Reyes G, (2009) The role of inherited extensional fault segmentation and linkage in contractional orogenesis: A

References

- reconstruction of Lower Cretaceous inverted rift basins in the Eastern Cordillera of Colombia. *Basin Research* 21 (1), 111-137p.
- Mora A, Horton B, Mesa A, Rubiano J, Ketcham R, Parra M, Blanco V, Garcia D, Stockli D, (2010) Migration of Cenozoic deformation in the Eastern Cordillera of Colombia interpreted from fission track results and structural relationships: implications for petroleum systems. *American Association of Petroleum Geologists Bulletin* 94, 1543e1580.
 - Mora A, Parra M, Strecker M, Sobel E, Zeilinger G, Jaramillo C, Ferreira Da Silva, S., Blanco, M., (2010) The eastern foothills of the Eastern Cordillera of Colombia: An example of multiple factors controlling structural styles and active tectonics, *Geol. Soc. Am. Bull.*, 122: 1846-1864, <https://doi.org/10.1130/B30033.1>.
 - Mora A, Reyes-Harker A, Rodriguez G, Tesón E, Ramirez-Arias J, (2013) Inversion tectonics under increasing rates of shortening and sedimentation: Cenozoic example from the Eastern Cordillera of Colombia. *Geological Society, London, Special Publications* 377 (1), 411-442p.
 - Mora A, Parra M, Forero G, Blanco V, Moreno N, Caballero V, Stockli D, Duddu I, Ghorbal B, (2015) What drives orogenic asymmetry in the Northern Andes?: A case study from the Apex of the Northern Andean Orocline. *Mem. 108 Pet. Geol. Potential Colomb. Caribb. Margin* 547-586. <https://doi.org/10.1306/13531949M1083652>.
 - Mora A, Villagómez D, Parra M, Caballero V, Spikings R, Horton B, Mora-Bohórquez J, Ketcham R, & Arias-Martínez J, (2020) Late Cretaceous to Cenozoic uplift of the northern Andes: Paleogeographic implications. In: Gómez, J. & Mateus-Zabala, D. (editors), *The Geology of Colombia, Volume 3 Paleogene – Neogene*. Servicio Geológico Colombiano, *Publicaciones Geológicas Especiales* 37, p. 89-121. Bogotá. <https://doi.org/10.32685/pub.esp.37.2019.04>
 - Mora A, Casallas W, Ketcham R, Gomez D, Parra M, Namson J, Stockli D, Almendral A, Robles W, Ghorbal B, (2015) Kinematic restoration of contractional basement structures using thermokinematic models: a key tool for petroleum system modeling. *Bulletin* 99, 1575-1598. [doi:10.1306/0428141110](https://doi.org/10.1306/0428141110)
 - Mora A, Villagómez D, Parra M, Caballero V, Spikings R, Horton B, Mora-Bohórquez J, Ketcham R, Arias-Martínez J, (2020) Late Cretaceous to Cenozoic uplift of the northern Andes: Paleogeographic implications. In: Gómez J, Mateus-Zabala D, (editors), *The Geology of Colombia, Volume 3 Paleogene – Neogene*. Servicio Geológico Colombiano,

References

- Publicaciones Geológicas Especiales 37, p. 89–121. Bogotá.
<https://doi.org/10.32685/pub.esp.37.2019.04>
- Morales L, and the Colombian petroleum industry, (1958) General geology and oil occurrences of the Middle Magdalena Valley, Colombia. In: Habitat of Oil: A Symposium (edited by L.G. Weeks). American Association of Petroleum Geologists, Special Publication, 641-695
 - Moreno J, (1990) Stratigraphy of the Lower Cretaceous Rosablanca and Cumbre Formations, Utica Sandstone and Murca Formation, West Flank, Eastern Cordillera, Colombia -Geol. Colombiana, 17, pp. 65-86, 9 figs., Bogota.
 - Moreno, C.J., Horton, B.K., Caballero, V., Mora, A., Parra, M., Sierra, J., (2011) Depositional and provenance record of the Paleogene transition from foreland to hinterland basin evolution during Andean orogenesis, northern Middle Magdalena Valley Basin, Colombia. *Journal of South American Earth Sciences*, 32(3), 246– 263. <https://doi.org/10.1016/j.jsames.2011.03.018>
 - Moreno N, Silva A, Mora A, Tesón E, Quintero I, Rojas L, Lopez C, Blanco V, J. Castellanos J, Sánchez J, Osorio L, Namson J, Stockli D, Casallas W, (2013) Interaction between thin- and thick-skinned tectonics in foothill areas of an inverted graben: The Middle Magdalena foothill belt Colombia, in: Nemcok M, Mora A, Cosgrove J (Editors) *Thick-skin-dominated orogens: From initial inversion to full accretion: GSL Special Publications 377*, p. 221–255.
 - Navas G, (1963) Estudio Estratigráfico del Girón al W del Macizo de Santander (Cordillera Oriental, Colombia). *Boletín de Geología*. 12, 19–33.
 - Nemcok M, Mora A, Cosgrove J, (Editors) (2013) *Thick- skin-dominated orogens: From initial inversion to full accretion: GSL Special Publications 377*, 473 p.
 - Nova G, Bayona Chaparro G, Silva-Tamayo J, Cardona A, Rapalini A, Montaña Cortes P; Eisenhauer A; Dussan K, Valencia V, Ramirez V, Montes C, (2019) Jurassic break-up of the Peri-Gondwanan margin in northern Colombia: Basin formation and implications for terrane transfer. *Journal of South American Earth Sciences*. 89:92-117
 - Osorio-Afanador D, Velandia F, (2021) Late Jurassic syn-extensional sedimentary deposition and Cenozoic basin inversion as recorded in The Girón Formation, northern Andes of Colombia. *Andean Geol.* 48 (2), 237–266. <https://doi.org/10.5027/andgeoV48n2-3264>.
 - Parra M, Mora A, Sobel E, Strecker M, González R, (2009) Episodic orogenic front migration in the northern Andes: constraints from low- temperature thermochronology in the Eastern Cordillera, Colombia. *Tectonics* 28, a. doi:10.1029/2008tc002423

References

- Parra M, Mora A, Lopez C, Rojas L, Horton B, (2012). Detecting earliest shortening and deformation advance in thrust belt hinterlands: Example from the Colombian Andes. *Geology*, 40(2), 175–178. <https://doi.org/10.1130/G32519.1>
- Patarroyo P, (1997) Barremiano Inferior en la Base de la Formación Paja, Barichara, Santander -Colombia. - *GEOLOGIA COLOMBIANA*, 22, pgs. 135-138,2 Figs., Santafé de Bogotá.
- Peyton SL, Carrapa B, (2013) An introduction to low-temperature thermochronologic techniques, methodology, and applications, in C Knight. and J. Cuzella, eds., *Application of structural methods to Rocky Mountain hydrocarbon exploration and development: AAPG Studies in Geology* 65, p. 15–36. <https://doi.org/10.1306/13381688St653578>
- Pindell J, Kennan L, (2009) Tectonic evolution of the Gulf of Mexico, Caribbean and northern South America in the mantle reference frame: An update. In: James K, Lorente M, Pindell J, (Editors), *The origin and evolution of the Caribbean Plate*. Geological Society of London, Special Publication 328, p. 1–55. <https://doi.org/10.1144/SP328.1>
- Pupin J, (1980) Zircon and granite petrology *Contributions Mineralogy and Petrology*, 110, pp. 463-472.
- Ramon J, Dzou L, (1999) Petroleum geochemistry of the Middle Magdalena Valley, Colombia. *Organic Geochemistry* 30, 249–266
- Ramos V, Aleman A, (2000) Tectonic evolution of the Andes. In: Cordani UG, Milani EJ, Thomaz Filho A, Campos DA (Editors) *Tectonic evolution of South America*. Rio de Janeiro, pp 635–685
- Ramos V, Folguera A, (2009) Andean flat-slab subduction through time, in: Murphy J, Keppie J, Hynes A, (Editors), *GSL Special Publication* 327, p. 31–54.
- Ranalli G, (1991) Regional variations in lithosphere rheology from heat flow observations, in Cermak V, Rybach L, (Editors), *Terrestrial heat flow and the lithosphere structure*. Exploration of the deep continental crust: Berlin, Springer, p. 1–22, doi:10.1007/978-3-642-75582-8_1.
- Rangel A, Parra P, Niño C, (2000) The La Luna Formation: chemostratigraphy and organic facies in the Middle Magdalena basin: *Organic Geochemistry*, v. 31, p. 1267–1284.
- Rangel A, Moldowan J, Niño C, Parra P, Giraldo B, (2002) Umir formation: organic geochemical and stratigraphic assessment as cosource for Middle Magdalena Basin oil, Colombia. *AAPG Bulletin* 86 (12), 2069–2087.
- Reiners P, Brandon M, (2006) Using thermochronology to understand orogenic erosion: *Annual Review of Earth and Planetary Sciences*, v. 34, p. 419–466.

References

- Remy W, Remy R, Pfefferkorn H, Volkheimer W, Rabe E, (1975) Neueinstufung der Bocas-Folge (Bucaramanga, Kolumbien) in den Unteren Jura anhand einer Phleboterisbranneri und Classopollis-Flora. *Argumenta Palaobotanica* 4: 55-77, Munster.
- Renzoni G, (1962) Apuntes acerca de la litología y tectónica de la zona al este y sureste de Bogotá. *Serv. Geo. Nal. Bol. Geol.* 10(1-3). Bogotá.
- Renzoni G, (1967) Geología del Cuadrángulo J-12, Tunja: INGEOMINAS, *Boletín Geológico*, v. 24, 2, 31-48.
- Restrepo J, Ordóñez-Carmona O, Armstrong R, Pimentel M, (2011) Triassic metamorphism in the northern part of the Tahamí Terrane of the central cordillera of Colombia. *Journal South American Earth Sciences* 32(4):497-507
- Restrepo-Pace P, Ruiz J, Gehrels G, Cosca M, (1997) Geochronology and Nd isotopic data of Grenville-age rocks in the Colombian Andes: New constraints for late Proterozoic – early Paleozoic paleocontinental reconstructions of the Americas. *Earth and Planetary Science Letters*, 150(3-4): 427-441. [https://doi.org/10.1016/S0012-821X\(97\)00091-5](https://doi.org/10.1016/S0012-821X(97)00091-5)
- Restrepo-Pace P, Colmenares F, Higuera C, Mayorga M, (2004) A Fold and thrust belt along the western flank of the Eastern Cordillera of Colombia-Style, kinematics, and timing constraints derived from seismic data and detailed surface mapping, in: McClay, K.R., ed., *Thrust tectonics and hydrocarbon systems: AAPG Memoir 82*, p. 598-613.
- Restrepo-Pace P, Cediel F, (2010) Northern South America basement tectonics and implications for paleocontinental reconstructions of the Americas. *Journal of South American Earth Sciences*, 29(4): 764-771. <https://doi.org/10.1016/j.jsames.2010.06.002>
- Reyes-Harker, A., Ruiz-Valdivieso, C.F., Mora, A., Ramírez-Arias, J.C., Rodriguez, G., De La Parra, F., Blanco, V., (2015) Cenozoic paleogeography of the Andean foreland and retroarc hinterland of Colombia. *AAPG Bulletin* (Vol. 99).
- Robert P, (1988) *Organic Metamorphism and Geothermal History, Elf- Aquitaine and Reidel Publishing, Dordrecht*, 311pp.
- Rodríguez G, Correa A, Zapata G, Arango M, (2017a) Monzogranito de La Corcova. *Catálogo de unidades litoestratigráficas de Colombia. Servicio Geológico Colombiano*, 105 p. Medellín.
- Rodríguez G, Arango M, Zapata G, Correa-Martínez A, (2017b) Tonalita de San Martín. *Catálogo de las unidades litoestratigráficas de Colombia. Servicio Geológico Colombiano*, 55 p. Medellín.

References

- Rodríguez G, Zapata G, Arango M, Correa A, (2018) Monzogranito de Santa Bárbara. Catálogo de unidades litoestratigráficas de Colombia. Servicio Geológico Colombiano, 95 p. Medellín.
- Rodríguez-García G, Correa-Martínez A, Zapata-García G, Arango-Mejía M, Obando-Erazo G, Zapata-Villada J, Bermúdez J, (2020) Diverse Jurassic magmatic arcs of the Colombian Andes: Constraints from petrography, geochronology, and geochemistry. In: Gómez J, Pinilla-Pachon A, (Editors), *The Geology of Colombia, Volume 2 Mesozoic*. Servicio Geológico Colombiano, Publicaciones Geológicas Especiales 36, 54 p. Bogotá. <https://doi.org/10.32685/pub.esp.36.2019.04>
- Roeder D, Chamberlain R, (1995) Eastern Cordillera of Colombia: Jurassic-Neogene crustal evolution. In: Tankard A, Suarez S, Welsink H, (Editors.), *Petroleum Basins of South America*. AAPG Mem. 62, 633-645.
- Sánchez J, Horton B, Tesón E, Mora A, Ketcham R, Stockli D, (2012) Kinematic evolution of Andean fold-thrust structures along the boundary between the Eastern Cordillera and Middle Magdalena Valley basin, Colombia. *Tectonics*, [https://doi: 10.1029/2011TC003089](https://doi.org/10.1029/2011TC003089)
- Sarmiento L, (2001) Mesozoic Rifting and Cenozoic Basin Inversion History of the Eastern Cordillera Colombian Andes-Inferences from tectonic models. Vrije Universiteit Amsterdam. Tectonics Department. PhD thesis, 295p.
- Sarmiento, L.F.,(2011) Middle Magdalena Basin. Volume 11.194 p. In: Cediél, F., Ojeda, G. Y., and Colmenares, F., (eds) *Petroleum Geology of Colombia*. ANH, and Universidad EAFIT. Medellín, Colombia.
- Sarmiento-Rojas L, Van Wess J, Cloetingh S, (2006) Mesozoic transtensional basin history of the Eastern Cordillera, Colombian Andes: Inferences from tectonic models: *Journal of South American Earth Sciences*, v. 21, p. 383-411, [https://doi:10.1016/j.jsames.2006.07.003](https://doi.org/10.1016/j.jsames.2006.07.003).
- Schmid R, (1981). Descriptive nomenclature and classification of pyroclastic deposits and fragments: Recommendations of the IUGS Subcommittee on the Systematics of Igneous Rocks. *Geology*, 9(1), 41-43.
- Shaw, J.H., Connors, C.D., Suppe, J., (2005) *Seismic Interpretation of Contractional Fault-Related Folds*. AAPG Studies in Geology No. 53, American Association of Petroleum Geologists, Tulsa, Oklahoma.
- Siravo G, Fellin M, Faccenna C, Bayona G, Lucci F, Molin P, Maden C, (2018). Constraints on the Cenozoic deformation of the northern eastern cordillera, Colombia. *Tectonics* 37 (11), 4311-4337. <https://doi.org/10.1029/2018TC005162>

References

- Siravo G, Faccena C, G erault M, Becker T, Giuditta F, Herman F, Molin P, (2019). Slab flattening and the rise of the Eastern Cordillera, Colombia. *Earth and Planetary Science Letters*, 512, 100–110. <https://doi.org/10.1016/j.epsl.2019.02.002>
- Silva, A., A. Mora, V. Caballero, G. Rodriguez, C. Ruiz, N. Moreno, M. Parra, J. C. Ramirez-Arias, M. Ib a nez, and I. Quintero, 2013, Basin compartmentalization and drainage evolution during rift inversion: evidence from the Eastern Cordillera of Colombia: Geological Society, London, Special Publications, v. 377, p. 369.
- Sl ama J, Ko ler J, Condon D, Crowley J, Gerdes A, Hanchar J, Horstwood M, Morris G, Nasdala L, Norberg N, Schaltegger U, Schoene B, Tubrett M, Whitehouse M, (2008) Ple ovice zircon - A new natural reference material for U-Pb and Hf isotopic microanalysis. *Chemical Geology* 249, 1-35.
- Spikings R, Cochrane R, Villag omez D, Van der Lelij R, Vallejo C, Winkler W, Beate B, (2015) The geological history of northwestern South America: From Pangaea to the early collision of the Caribbean Large Igneous Province (290–75 Ma). *Gondwana Research*, 27(1): 95–139. <https://doi.org/10.1016/j.gr.2014.06.004>
- Streckeisen A, (1978). IUGS Subcommittee on the Systematics of Igneous Rocks: Classification and nomenclature of volcanic rocks, lamprophyres, carbonatites and melilitic rocks; recommendation and suggestions. *Neues Jahrbuch f ur Mineralogie - Abhandlungen*, 134, 1-14.
- Suppe J, (1983) Geometry and kinematics of fault- bend folding. *American Journal of Science*, 283, 684-721.
- Suppe J, (1985) *Principles of Structural Geology*. Prentice- Hall, Englewood Cliffs, NJ.
- Suppe J, Chou G, T., Hook S, C., (1992) Rates of folding and faulting determined from growth strata. In: McClay K, (Editor) *Thrust Tectonics*, Chapman & Hall, London, 105-123
- Sweeney J, Burnham A, (1990) Evaluation of a simple model of vitrinite reflectance based on chemical kinetics. *American Association Petroleum Geologists Bulletin*, 74, 1559–1570.
- Taboada A, Rivera L, Fuenzalida A, Cisternas A, Philip H, Bijwaard H, Olaya J, Rivera C, (2000) Geodynamics of the Northern Andes: Subduction and intracontinental deformation (Colombia): *Tectonics*, v. 19, no. 5, p. 787–813.
- Tchegliakova N, (1995) Los Foramin feros de la Formaci n Umir (Secci n Quebrada La Julia): Registro del Cret cico Superior cuspidal (Maastrichtiano) en el Valle Medio del Magdalena, Colombia. *Geolog a Colombiana*, 19, 109-130.

References

- Teixell A, Ruiz J, Tesón E, Mora A, (2015). The structure of an inverted back-arc rift: Insights from a transect across the Eastern Cordillera of Colombia near Bogotá. In Bartolini C, Mann P, (Editors.), *Petroleum geology and potential of the Colombian Caribbean margin*, AAPG Memoir (Vol. 108, pp. 499–516). <https://doi.org/10.1306/13531947M1083650>
- Tesón E, Mora A, Silva A, Namson J, Teixell A, Castellanos J, Casallas W, (2013) Relationship of Mesozoic graben development, stress, shortening magnitude, and structural style in the Eastern Cordillera of the Colombian Andes. *Geological Society, London, Special Publications* 377 (1), 257-283.
- Toro J, Roure F, Bordas-Le Floch N, Le Cornec-Lance S, Sassi W, (2004) Thermal and Kinematic Evolution of the Eastern Cordillera fold- and-thrust-belt, Colombia, in *Deformation, Fluid Flow and Reservoir Appraisal in Foreland Fold-and-Thrust Belts*, AAPG Hedberg Ser., vol. 1, edited by F. Roure and R. Swennen, pp. 79–115, Am. Assoc. ofPet. Geol., Tulsa, Okla.
- Toussaint J, (1995) *Evolución geológica de Colombia; 2 Triásico– Jurásico*. Universidad Nacional de Colombia, 94 p. Medellín
- Van der Lelij R, Spikings R, Ulianov A, Chiaradia M, Mora A, (2016) Palaeozoic to Early Jurassic history of the northwestern corner of Gondwana, and implications for the evolution of the Iapetus, Rheic and Pacific Oceans. *Gondwana Research* 31, 271–294.
- Van der Lelij R, Spikings R, Mora A, (2016) Thermochronology and tectonics of the Mérida Andes and the Santander Massif, NW South America. *Lithos*, 248–251: 220–239. <https://doi.org/10.1016/j.lithos.2016.01.006>
- Vásquez M, Altenberger U, (2005) Mid-Cretaceous extension-related magmatism in the eastern Colombian Andes. *Journal of South American Earth Sciences* 20, 193–210
- Vasquez M, Altenberger U, Romer R, Sudo M, Moreno-Murillo J, (2010) Magmatic evolution of the Andean Eastern Cordillera of Colombia during the Cretaceous: Influence of previous tectonic processes. *Journal of South American Earth Sciences* 29, 171-186
- Veeken P, (2007) *Seismic Stratigraphy, Basin Analysis and Reservoir Characterization*. Elsevier, Amsterdam. p. 453
- Vergés J, Marzo M, Muñoz J, (2002) Growth strata in foreland settings: *Sedimentary Geology*, v. 146, no. 1-2, p. 1-9.

References

- Vesga C, Barrero D, (1978) Edades K/Ar en rocas ígneas y metamórficas de la Cordillera Central de Colombia y su implicación geológica. II Congreso Colombiano de Geología, Resúmenes, Bogotá.
- Villamil T, (1998) Chronology, relative sea-level history and a new sequence stratigraphic model for basinal Cretaceous facies of Colombia. In: Pindell, J.L., Drake, C. (Eds.), *Paleogeographic Evolution and Non- Glacial Eustasy, Northern South America*, Society of Economic Paleontologists and Mineralogists Special Publication, 58, pp. 161-216.
- Villamil T, (1999) Campanian – Miocene tectonostratigraphy, dep- ocenter evolution and basin development of Colombia and western Venezuela. *Palaeogeography, Palaeoclimatology, Palaeoecology*, 153(1-4): 239-275. [https://doi.org/10.1016/S0031-0182\(99\)00075-9](https://doi.org/10.1016/S0031-0182(99)00075-9)
- Villagómez D, Spikings R, Magna T, Kammer A, Winkler W, Beltrán A, (2011) Geochronology, geochemistry and tectonic evolution of the Western and Central Cordilleras of Colombia. *Lithos*, 125(3-4): 875-896.
- Villagómez D, Spikings R, (2013) Thermochronology and tectonics of the Central and Western Cordilleras of Colombia: Early Cretaceous – Tertiary evolution of the northern Andes. *Lithos*, 160-161: 228-249. <https://doi.org/10.1016/j.lithos.2012.12.008>
- Vinasco C, Cordani U, González H, Weber M, Pelaez C, (2006) Geochronological, isotopic, and geochemical data from Permo-Triassic granitic gneisses and granitoids of the Colombian Central Andes. *Journal of South American Earth Sciences* 21:355-371.
- Ward D, Goldsmith R, Cruz B, Restrepo A, (1973) Geología de los Cuadrángulos H-12 Bucaramanga y H-13 Pamplona, Departamento de Santander: INGEOMINAS, Boletín Geológico, v. 21, 1-3, 132 p.
- Ward D, Goldsmith R, Jimeno A, Cruz J, Restrepo H, Gomez E, (1977) Mapa geológico del Cuadrangulo H- 12, “Bucaramanga”-Colombia: Instituto Nacional de Investigaciones Geológico-Mineras, 1:100,000
- Whalen J, Currie K, Chappell B, (1987) A-type granites: Geochemical characteristics, discrimination and petrogenesis. *Contributions to Mineralogy and Petrology*, 95(4): 407-419. <https://doi.org/10.1007/BF00402202>
- Wiedenbeck M, Allé P, Corfu F, Griffin W, Meier M, Oberli F, von Quadt A, Roddick J, Spiegel W, (1995) Three natural zircon standards for U-Th-Pb, Lu-Hf, trace element and REE analyses. *Geostandards Newsletter*, 19(1): 1-23. <https://doi.org/10.1111/j.1751-908X.1995.tb00147.x>

References

- Wilkerson M, Dicken C, (2001) Quick-look techniques for evaluating two-dimensional cross sections in detached contractional settings, AAPG Bull., 85, 1759–1770
- Williams G, Powell C, Cooper M, (1989) Geometry and kinematics of inversion tectonics. Geological Society Special Publications, Vol.44, p.3-15.
- Wilson M, (1993) Magmatism and the geodynamics of basin formation. Sedimentary Geology 86, 5–29.
- Woodward N, Boyer S, Suppe J, (1989) Balanced geological cross-sections: an essential technique in geological research and exploration: Washington, American Geophysical Union, 132 p. Short course in geology, volume 6.
- WYGRALA, B., 1989. Integrated study of an oil field in the southern Po basin, northern Italy. Doctoral thesis, Univ. Köln, Berichte Kernforschungsanlage Jülich, 2313, 217
- Yalçın M, Littke R, Sachsenhofer R, (1997) Thermal History of Sedimentary Basins. In: Welte D, Horsfield B, Baker D, (Editors) Petroleum and Basin Evolution. Springer, Berlin, Heidelberg. https://doi.org/10.1007/978-3-642-60423-2_3
- Zapata T, Allmendinger R, (1996) Growth stratal records of instantaneous and progressive limb rotation in the Precordillera thrust belt and Bermejo basin, Argentina. Tectonics 15, 1065–1083. <https://doi.org/10.1029/96TC00431>.
- Zapata G, Correa A, Rodríguez G, Arango M, (2016) Granito de Pescadero. Catálogo de unidades litoestratigráficas de Colombia. Servicio Geológico Colombiano, 54 p. Medellín.
- Zapata G, Arango M, Rodríguez G, Correa–Martínez A, (2018) Riolitas El Uvo. Catálogo de unidades litoestratigráficas de Colombia. Servicio Geológico Colombiano, 39 p. Medellín.

APPENDIX

1. U/PB LA-ICP-MS GEOCHRONOLOGY ON ZIRCONS FROM THE MESOZOIC FORMATIONS IN THE EASTERN CORDILLERA AND MIDDLE MAGDALENA.

Sample	Grain Code	Formation	Observation	U [ppm]	Pb [ppm]	<u>Th</u> U	²⁰⁸ Pb ²⁰⁶ Pb	²⁰⁶ Pb ²³⁸ U	±1S [%]	²⁰⁷ Pb ²³⁵ U	±1S [%]
JR-431-1	0 254	0 Jordán		[ppm] 212	[ppm] 144	0 0.689	0 0.2658	0 0.0320502	0.0 1.0	0 0.229035	0 2.8
JR-431-2	255	Jordán	high 208 Th/U >1	425	561	1.35	0.5264	0.0306561	0.9	0.225433	2.2
JR-431-3	256	Jordán		175	119	0.712	0.2576	0.0305408	0.9	0.213685	3.1
JR-431-4	257	Jordán		405	356	0.911	0.3356	0.0324305	0.8	0.228861	2.2
JR-431-5	258	Jordán	Th/U >1	311	385	1.308	0.4539	0.0322338	0.8	0.221783	2.2
JR-431-6	259	Jordán		428	363	0.907	0.317	0.0308546	0.8	0.208263	2.1
JR-431-7	263	Jordán		97	86	0.942	0.3283	0.032064	1.3	0.227505	4.4
JR-431-8	264	Jordán		119	88	0.78	0.2723	0.0314521	1.1	0.210217	3.8
JR-431-9	265	Jordán		525	424	0.857	0.3006	0.0316469	0.9	0.214742	2.2
JR-431-10	266	Jordán	Th/U >1	111	107	1.014	0.3608	0.0311784	1.1	0.216317	3.5
JR-431-11	267	Jordán	Th/U >1	539	577	1.127	0.3995	0.0319056	0.8	0.227405	1.9
JR-431-12	268	Jordán	Th/U >1	297	340	1.205	0.436	0.0304089	0.8	0.215839	2.3
JR-431-13	269	Jordán		113	85	0.79	0.2788	0.0309624	1.1	0.212369	3.8
JR-431-14	270	Jordán		615	329	0.566	0.2099	0.0309699	0.7	0.215667	1.8
JR-431-15	271	Jordán		44	27	0.641	0.2695	0.0306385	1.6	0.217552	6.2
JR-431-16	272	Jordán	high 208 Th/U >1	405	633	1.647	0.6043	0.0287974	1.1	0.220564	3.1

Appendix

JR-431-17	273	Jordán	high 208 Th/U >1	162	216	1.405	0.5014	0.0308959	0.9	0.216208	2.9
JR-431-18	274	Jordán	Th/U >1	162	217	1.403	0.4948	0.0311937	1.1	0.219382	2.6
JR-431-19	275	Jordán		340	308	0.953	0.1448	0.0836813	0.8	0.815638	1.7
JR-431-20	276	Jordán	high 208 Th/U >1	428	667	1.64	0.6003	0.0300629	0.9	0.221194	2.6
JR-431-21	277	Jordán		86	42	0.525	0.1835	0.0314145	1.3	0.23334	3.8
JR-431-22	278	Jordán	high 208 Th/U >1	196	265	1.422	0.5161	0.0312052	0.9	0.241596	3
JR-431-23	279	Jordán	high 208 Th/U >1	87	137	1.651	0.6074	0.0296319	1.4	0.220533	4.3
JR-431-24	283	Jordán	Th/U >1	295	287	1.024	0.3621	0.0307225	0.9	0.214541	2.1
Sample	^{207}Pb ^{206}Pb	$\pm 1\sigma$ [%]	rho	^{206}Pb ^{238}U	$\pm 2\sigma$ [Ma]	^{207}Pb ^{235}U	$\pm 2\sigma$ [Ma]	^{207}Pb ^{206}Pb	$\pm 2\sigma$ [Ma]	Disc. I. [%]	Disc. II. [%]
	0	0	0	[Ma]	$\pm 2\sigma$ [Ma]	[Ma]	$\pm 2\sigma$ [Ma]	[Ma]	$\pm 2\sigma$ [Ma]	0	0
JR-431-1	0.05183	2.6	0.36	203.4	4	209.4	10.6	277.9	59.9	2.9	26.8
JR-431-2	0.05333	2	0.42	194.7	3.6	206.4	8.4	343.1	46.5	5.7	43.3
JR-431-3	0.05074	3	0.28	193.9	3.3	196.6	11.2	229.3	69.1	1.4	15.4
JR-431-4	0.05118	2	0.36	205.7	3.1	209.3	8.2	249.1	46.8	1.7	17.4
JR-431-5	0.0499	2	0.39	204.5	3.4	203.4	8.1	190.5	46.9	-0.6	-7.4
JR-431-6	0.04895	2	0.36	195.9	2.9	192.1	7.4	145.7	46.7	-2	-34.5
JR-431-7	0.05146	4.2	0.3	203.5	5.4	208.1	16.7	261.6	96.8	2.3	22.2
JR-431-8	0.04847	3.6	0.3	199.6	4.5	193.7	13.4	122.6	84.8	-3	-62.8
JR-431-9	0.04921	2	0.39	200.8	3.4	197.5	7.9	158.1	47.4	-1.7	-27
JR-431-10	0.05032	3.3	0.31	197.9	4.2	198.8	12.6	209.8	77.1	0.5	5.7
JR-431-11	0.05169	1.7	0.43	202.5	3.2	208.1	7	271.9	38.8	2.7	25.5
JR-431-12	0.05148	2.1	0.34	193.1	3	198.4	8.2	262.4	49.4	2.7	26.4
JR-431-13	0.04975	3.6	0.29	196.6	4.3	195.5	13.4	183.2	83.6	-0.5	-7.3
JR-431-14	0.05051	1.7	0.41	196.6	2.8	198.3	6.5	218.4	38.5	0.8	10
JR-431-15	0.0515	6	0.26	194.5	6.3	199.9	22.6	263.3	137.2	2.7	26.1

Appendix

JR-431-16	0.05555	2.9	0.37	183	4.1	202.4	11.4	434.5	64.3	9.6	57.9
JR-431-17	0.05075	2.7	0.31	196.2	3.5	198.7	10.5	229.7	63.5	1.3	14.6
JR-431-18	0.05101	2.3	0.45	198	4.5	201.4	9.4	241.2	52.8	1.7	17.9
JR-431-19	0.07069	1.5	0.48	518.1	8	605.6	15.4	948.6	30.6	14.5	45.4
JR-431-20	0.05336	2.4	0.34	190.9	3.3	202.9	9.5	344.3	54.9	5.9	44.5
JR-431-21	0.05387	3.6	0.33	199.4	4.9	213	14.7	365.7	81.5	6.4	45.5
JR-431-22	0.05615	2.9	0.31	198.1	3.6	219.7	12	458.4	63.9	9.8	56.8
JR-431-23	0.05398	4	0.33	188.2	5.3	202.4	15.8	370.2	91.1	7	49.2
JR-431-24	0.05065	1.9	0.41	195.1	3.4	197.4	7.7	224.8	45.1	1.2	13.2
				U	Pb	Th	²⁰⁸Pb	²⁰⁶Pb	±1S	²⁰⁷Pb	±1S
Sample	Grain Code	Formation	Observation	[ppm]	[ppm]	U	²⁰⁶Pb	²³⁸U	[%]	²³⁵U	[%]
JR-531-1	245	Jordán		269	81	0.334	0.1063	0.171309	0.7	1.724704	1.3
JR-531-2	246	Jordán		232	47	0.224	0.0711	0.165066	0.7	1.669317	1.3
JR-531-3	247	Jordán		769	656	0.951	0.3322	0.0405854	0.7	0.286742	1.5
JR-531-4	248	Jordán		148	46	0.344	0.1114	0.1721383	0.8	1.747059	1.5
JR-531-5	249	Jordán		322	197	0.681	0.2321	0.0737482	0.8	0.573701	1.7
JR-531-6	250	Jordán		215	57	0.293	0.0933	0.1684624	0.8	1.702323	1.4
JR-531-7	251	Jordán	Th/U >1	134	137	1.14	0.385	0.1009634	0.9	0.848096	1.6
JR-531-8	252	Jordán		723	489	0.746	0.2562	0.0295261	0.9	0.206413	1.7
JR-531-9	253	Jordán		762	424	0.62	0.2121	0.039181	0.7	0.283013	1.6
JR-531-10	254	Jordán		406	135	0.366	0.1235	0.0441509	0.8	0.307669	2
JR-531-11	255	Jordán		328	174	0.59	0.1885	0.1683962	0.7	1.715718	1.3
JR-531-12	256	Jordán		126	52	0.461	0.1433	0.1678412	0.8	1.683651	1.7
JR-531-13	257	Jordán		102	37	0.402	0.132	0.1708917	0.9	1.702321	2
JR-531-14	258	Jordán		61	34	0.614	0.2107	0.0293474	1.3	0.202119	4.3
JR-531-15	259	Jordán		200	51	0.282	0.0903	0.1713257	0.7	1.71463	1.4
JR-531-16	263	Jordán		564	167	0.329	0.1077	0.1770444	0.7	2.180213	1.3
JR-531-17	264	Jordán		215	55	0.287	0.0915	0.1684161	0.7	1.700255	1.5
JR-531-18	265	Jordán		34	22	0.73	0.2398	0.1681002	1.1	1.664496	2.6

Appendix

JR-531-19	266	Jordán	64	25	0.442	0.1606	0.0407674	1.9	0.323473	6.5	
JR-531-20	267	Jordán	287	225	0.867	0.2972	0.0391333	0.8	0.278525	1.8	
JR-531-21	268	Jordán	81	26	0.355	0.1163	0.0431471	1	0.310014	3.3	
JR-531-22	269	Jordán	147	57	0.428	0.139	0.19032	0.8	2.068785	1.5	
JR-531-23	270	Jordán	42	22	0.574	0.2057	0.029434	1.7	0.199562	5.4	
JR-531-24	271	Jordán	316	64	0.227	0.074	0.1674043	0.7	1.681663	1.4	
JR-531-25	272	Jordán	155	52	0.375	0.1212	0.1926191	0.7	2.084026	1.4	
	²⁰⁷ Pb	±1s	rho	²⁰⁶ Pb	±2s	²⁰⁷ Pb	±2s	²⁰⁷ Pb	±2s	Disc. I.	Disc. II.
Sample	²⁰⁶ Pb	[%]		²³⁸ U	[Ma]	²³⁵ U	[Ma]	²⁰⁶ Pb	[Ma]	[%]	[%]
JR-531-1	0.07302	1.1	0.54	1019.3	13.3	1017.8	16.9	1014.5	23	-0.2	-0.5
JR-531-2	0.07335	1.1	0.53	984.9	13.1	996.9	17.2	1023.6	23.7	1.2	3.8
JR-531-3	0.05124	1.4	0.48	256.5	3.8	256	7	251.7	31.5	-0.2	-1.9
JR-531-4	0.07361	1.3	0.5	1023.9	14.4	1026.1	19.7	1030.8	27	0.2	0.7
JR-531-5	0.05642	1.6	0.44	458.7	6.7	460.4	12.9	469	34.8	0.4	2.2
JR-531-6	0.07329	1.2	0.55	1003.6	14.3	1009.4	17.9	1022	24	0.6	1.8
JR-531-7	0.06092	1.3	0.57	620.1	10.6	623.6	14.9	636.6	28.6	0.6	2.6
JR-531-8	0.0507	1.5	0.49	187.6	3.2	190.5	6.1	227.4	35.5	1.6	17.5
JR-531-9	0.05239	1.4	0.47	247.8	3.6	253	7.1	302.4	32.2	2.1	18.1
JR-531-10	0.05054	1.9	0.38	278.5	4.2	272.4	9.8	220	43.8	-2.3	-26.6
JR-531-11	0.07389	1.1	0.55	1003.3	13.3	1014.4	16.9	1038.6	22.8	1.1	3.4
JR-531-12	0.07275	1.5	0.47	1000.2	14.8	1002.4	21.7	1007.1	30.7	0.2	0.7
JR-531-13	0.07225	1.8	0.45	1017	16.7	1009.4	25.6	993	36.6	-0.8	-2.4
JR-531-14	0.04995	4.1	0.31	186.5	4.9	186.9	14.8	192.7	95.6	0.2	3.2
JR-531-15	0.07258	1.2	0.5	1019.4	13.6	1014	18.6	1002.4	25.8	-0.5	-1.7
JR-531-16	0.08931	1.1	0.55	1050.8	13.4	1174.7	17.6	1410.9	21	10.6	25.5
JR-531-17	0.07322	1.3	0.48	1003.4	13.5	1008.6	19.5	1020.1	27.5	0.5	1.6
JR-531-18	0.07181	2.4	0.41	1001.6	20	995.1	33.6	980.7	49.1	-0.7	-2.1
JR-531-19	0.05755	6.2	0.29	257.6	9.5	284.6	32.5	512.6	136.5	9.5	49.7
JR-531-20	0.05162	1.6	0.47	247.5	4.1	249.5	7.9	268.7	36.4	0.8	7.9

Appendix

JR-531-21	0.05211	3.1	0.31	272.3	5.5	274.2	15.9	290.3	71.8	0.7	6.2
JR-531-22	0.07884	1.3	0.53	1123.1	16.4	1138.5	20.8	1168.1	26	1.4	3.9
JR-531-23	0.04917	5.1	0.32	187	6.4	184.8	18.2	156.1	119.1	-1.2	-19.8
JR-531-24	0.07286	1.2	0.49	997.8	12.7	1001.6	17.8	1010	25.2	0.4	1.2
JR-531-25	0.07847	1.2	0.51	1135.5	15	1143.6	19.3	1158.8	24.4	0.7	2
				U	Pb	Th	²⁰⁸ Pb	²⁰⁶ Pb	±1S	²⁰⁷ Pb	±1S
Sample	Grain Code	Formation	Observation	[ppm]	[ppm]	U	²⁰⁶ Pb	²³⁸ U	[%]	²³⁵ U	[%]
NR-011-1	344	Noreán		54	40	0.764	0.2705	0.1969253	0.9	2.294958	1.8
			high 208								
NR-011-2	345	Noreán	Th/U >1	290	508	1.841	0.6551	0.0284361	0.9	0.194518	2.3
NR-011-3	346	Noreán		302	168	0.588	0.202	0.1646135	0.8	1.696333	1.4
NR-011-4	347	Noreán		540	194	0.378	0.085	0.1526521	0.8	1.883174	1.4
NR-011-5	348	Noreán		122	46	0.395	0.1347	0.1969555	0.8	2.134809	1.6
NR-011-6	349	Noreán		314	172	0.576	0.1982	0.1069301	0.7	0.918318	1.6
NR-011-7	350	Noreán		296	129	0.46	0.1574	0.164652	0.7	1.65571	1.4
NR-011-8	351	Noreán		265	82	0.328	0.1116	0.2102104	0.8	2.448877	1.4
			high 208								
NR-011-9	352	Noreán	Th/U >1	94	142	1.587	0.5636	0.0278394	1.2	0.18466	3.5
NR-011-10	353	Noreán	Th/U >1	110	111	1.062	0.3658	0.1647851	0.8	1.637445	1.8
NR-011-11	354	Noreán	Th/U >1	148	152	1.082	0.3789	0.0276678	1.1	0.180285	3.5
NR-011-12	355	Noreán		145	98	0.714	0.2569	0.2400542	0.8	3.046807	1.5
NR-011-13	356	Noreán		121	76	0.663	0.244	0.0393871	1	0.274194	3.2
NR-011-14	357	Noreán		91	25	0.284	0.0934	0.1812959	0.8	1.836121	1.8
NR-011-15	358	Noreán	Th/U >1	145	188	1.362	0.4961	0.0291956	1.1	0.216746	3.3
NR-011-16	359	Noreán		62	21	0.357	0.1169	0.2683835	0.9	3.574728	1.6
NR-011-17	363	Noreán		192	133	0.73	0.2512	0.0410942	1	0.29156	2.3
NR-011-18	364	Noreán		113	92	0.857	0.2827	0.1714374	0.8	1.728271	1.7
NR-011-19	365	Noreán		181	126	0.702	0.2561	0.0362246	1.1	0.250633	2.9
NR-011-20	366	Noreán		73	37	0.541	0.1828	0.1976479	0.8	2.150727	1.8

Appendix

NR-011-21	367	Noreán	Th/U >1	168	183	1.141	0.4061	0.0281262	1.1	0.188014	3.3
NR-011-22	368	Noreán		152	138	0.958	0.3563	0.028982	1.1	0.219937	2.9
NR-011-23	369	Noreán		77	44	0.606	0.2068	0.1921216	0.9	2.092289	1.9
NR-011-24	370	Noreán		186	74	0.419	0.1384	0.2694421	0.7	3.607633	1.4
NR-011-25	371	Noreán		195	153	0.827	0.2971	0.0319121	1	0.219539	2.9
NR-011-26	372	Noreán	high U high 208 Th/U >1	1293	1804	1.468	0.5383	0.0328395	0.7	0.230027	1.6
NR-011-27	373	Noreán		246	171	0.723	0.259	0.0276017	0.9	0.187059	2.7
	²⁰⁷ Pb	±1s	rho	²⁰⁶ Pb	±2s	²⁰⁷ Pb	±2s	²⁰⁷ Pb	±2s	Disc. I.	Disc. II.
Sample	²⁰⁶ Pb	[%]		²³⁸ U	[Ma]	²³⁵ U	[Ma]	²⁰⁶ Pb	[Ma]	[%]	[%]
NR-011-1	0.08452	1.5	0.51	1158.8	19.5	1210.7	25.5	1304.7	30.3	4.3	11.2
NR-011-2	0.04961	2.2	0.39	180.8	3.3	180.5	7.8	176.9	50.5	-0.2	-2.2
NR-011-3	0.07474	1.2	0.52	982.4	13.8	1007.2	18.6	1061.5	25.4	2.5	7.5
NR-011-4	0.08947	1.2	0.55	915.8	13.4	1075.2	19	1414.3	23.4	14.8	35.2
NR-011-5	0.07861	1.4	0.5	1158.9	17.3	1160.1	22.7	1162.4	28.6	0.1	0.3
NR-011-6	0.06229	1.4	0.46	654.9	9.2	661.5	15.5	684	30.5	1	4.3
NR-011-7	0.07293	1.2	0.51	982.6	13.3	991.7	18.2	1012.1	25.5	0.9	2.9
NR-011-8	0.08449	1.2	0.52	1229.9	16.9	1257.1	20.8	1303.9	24.4	2.2	5.7
NR-011-9	0.04811	3.3	0.35	177	4.3	172.1	11.2	104.6	78.4	-2.9	-69.2
NR-011-10	0.07207	1.6	0.45	983.3	15	984.7	23.1	987.9	33.5	0.1	0.5
NR-011-11	0.04726	3.3	0.33	175.9	4	168.3	10.8	62.4	77.8	-4.5	-181.9
NR-011-12	0.09205	1.3	0.5	1387	19.4	1419.4	23.7	1468.5	25.9	2.3	5.6
NR-011-13	0.05049	3	0.31	249	4.8	246	13.9	217.7	69.7	-1.2	-14.4
NR-011-14	0.07345	1.6	0.47	1074.1	16.8	1058.5	23.7	1026.5	32.3	-1.5	-4.6
NR-011-15	0.05384	3.1	0.33	185.5	3.9	199.2	11.8	364.6	69.7	6.9	49.1
NR-011-16	0.0966	1.3	0.6	1532.6	25.6	1543.9	25.1	1559.6	24.4	0.7	1.7
NR-011-17	0.05146	2.1	0.43	259.6	5	259.8	10.5	261.4	47.5	0.1	0.7
NR-011-18	0.07311	1.5	0.47	1020	15.2	1019.1	22.4	1017.2	31.5	-0.1	-0.3
NR-011-19	0.05018	2.7	0.37	229.4	4.8	227.1	11.8	203.4	62.5	-1	-12.8
NR-011-20	0.07892	1.6	0.47	1162.7	17.5	1165.3	24.5	1170.2	31.2	0.2	0.6

Appendix

NR-011-21	0.04848	3.1	0.32	178.8	3.8	174.9	10.7	122.9	74.2	-2.2	-45.5
NR-011-22	0.05504	2.6	0.37	184.2	3.9	201.9	10.5	413.9	59.3	8.8	55.5
NR-011-23	0.07898	1.6	0.48	1132.9	18.7	1146.3	25.7	1171.8	32.6	1.2	3.3
NR-011-24	0.09711	1.2	0.5	1538	19.6	1551.2	22.8	1569.4	23.8	0.9	2
NR-011-25	0.04989	2.7	0.34	202.5	3.9	201.5	10.5	190.1	63	-0.5	-6.5
NR-011-26	0.0508	1.4	0.46	208.3	2.9	210.2	6	231.9	32.6	0.9	10.2
NR-011-27	0.04915	2.6	0.33	175.5	3.1	174.1	8.7	155.1	60.1	-0.8	-13.2
				U	Pb	Th	²⁰⁸Pb	²⁰⁶Pb	±1S	²⁰⁷Pb	±1S
Sample	Grain Code	Formation	Observation	[ppm]	[ppm]	U	²⁰⁶Pb	²³⁸U	[%]	²³⁵U	[%]
NR-012-1	313	Noreán		247	55	0.233	0.0801	0.2508161	0.7	3.350833	1.3
NR-012-2	314	Noreán		198	91	0.488	0.1619	0.2864978	0.7	4.010071	1.3
NR-012-3	315	Noreán	high ²⁰⁸ Th/U >1	295	555	1.99	0.7701	0.0277105	1.4	0.20955	4.3
NR-012-4	316	Noreán	Th/U >1	230	261	1.202	0.4349	0.0281202	0.9	0.19216	2.8
NR-012-5	317	Noreán		240	190	0.837	0.3083	0.0279182	0.9	0.187692	2.6
NR-012-6	318	Noreán		187	64	0.36	0.1245	0.1689759	0.7	1.707345	1.6
NR-012-7	319	Noreán		81	16	0.209	0.0524	0.0786183	1.2	0.679327	2.4
NR-012-8	323	Noreán		175	123	0.737	0.259	0.0281637	0.9	0.186131	3
NR-012-9	324	Noreán		329	68	0.214	0.0957	0.064101	0.8	0.499532	1.8
NR-012-10	325	Noreán		80	40	0.521	0.1766	0.2464721	0.8	3.081147	1.6
NR-012-11	326	Noreán	high ²⁰⁸ Th/U >1	144	287	2.091	0.797	0.0285146	1.8	0.216185	8.6
NR-012-12	327	Noreán		43	25	0.599	0.2062	0.2347446	1	2.938283	1.8
NR-012-13	328	Noreán		435	146	0.355	0.1262	0.0732917	0.8	0.566787	1.8
NR-012-14	329	Noreán		254	45	0.188	0.0637	0.1699056	0.8	1.706554	1.5
NR-012-15	330	Noreán	high ²⁰⁸ Th/U >1	173	260	1.57	0.6049	0.0279573	1	0.18644	3.1
NR-012-16	331	Noreán		156	100	0.674	0.2505	0.0281397	0.9	0.201149	2.9
NR-012-17	332	Noreán		88	46	0.553	0.2003	0.0287873	1.3	0.190535	4.3

Appendix

NR-012-18	333	Noreán	high 208 Th/U >1	166	225	1.432	0.5062	0.0279541	1	0.18758	2.6
NR-012-19	334	Noreán		880	138	0.166	0.076	0.1822939	0.7	2.363978	1.3
NR-012-20	335	Noreán	Th/U >1	76	86	1.192	0.4323	0.0376559	1.2	0.266819	4
NR-012-21	336	Noreán		345	24	0.073	0.0299	0.0500403	0.8	0.35361	1.8
NR-012-22	337	Noreán	Th/U >1	175	171	1.024	0.3789	0.0281597	1	0.1874	3.4
NR-012-23	338	Noreán		191	110	0.605	0.2194	0.0317921	1.1	0.224709	2.8
NR-012-24	339	Noreán		134	120	0.947	0.3351	0.028343	1	0.200231	3.1
NR-012-25	343	Noreán		406	8	0.021	0.0088	0.1591463	0.7	1.554301	1.4
	²⁰⁷ Pb	±1σ	rho	²⁰⁶ Pb	±2σ	²⁰⁷ Pb	±2σ	²⁰⁷ Pb	±2σ	Disc. I.	Disc. II.
Sample	²⁰⁶ Pb	[%]		²³⁸ U	[Ma]	²³⁵ U	[Ma]	²⁰⁶ Pb	[Ma]	[%]	[%]
NR-012-1	0.09689	1.1	0.55	1442.7	19.2	1493	21.1	1565.2	21.7	3.4	7.8
NR-012-2	0.10151	1.1	0.53	1624	20.4	1636.2	22	1652	22	0.7	1.7
NR-012-3	0.05485	4.1	0.31	176.2	4.7	193.2	15.2	406	91.8	8.8	56.6
NR-012-4	0.04956	2.7	0.32	178.8	3.2	178.5	9.3	174.5	63.1	-0.2	-2.4
NR-012-5	0.04876	2.4	0.35	177.5	3.1	174.7	8.2	136.3	56.5	-1.6	-30.2
NR-012-6	0.07328	1.4	0.48	1006.5	13.9	1011.3	20	1021.8	28	0.5	1.5
NR-012-7	0.06267	2.1	0.49	487.9	11.4	526.4	20.2	697.1	45.5	7.3	30
NR-012-8	0.04793	2.8	0.31	179	3.3	173.3	9.4	96	66.5	-3.3	-86.5
NR-012-9	0.05652	1.7	0.45	400.5	6.4	411.4	12.6	472.9	36.9	2.6	15.3
NR-012-10	0.09067	1.4	0.52	1420.3	21.2	1428	24.8	1439.6	26.7	0.5	1.3
NR-012-11	0.05499	8.4	0.21	181.2	6.3	198.7	31.2	411.7	187.7	8.8	56
NR-012-12	0.09078	1.5	0.53	1359.3	23.4	1391.8	27.4	1442.1	29.5	2.3	5.7
NR-012-13	0.05609	1.6	0.43	456	6.6	455.9	12.9	455.9	35.4	0	0
NR-012-14	0.07285	1.3	0.51	1011.6	14.4	1011	19.5	1009.7	26.9	-0.1	-0.2
NR-012-15	0.04837	2.9	0.33	177.8	3.5	173.6	9.8	117.3	68.6	-2.4	-51.5
NR-012-16	0.05184	2.8	0.31	178.9	3.2	186.1	10	278.6	64.2	3.9	35.8
NR-012-17	0.048	4.1	0.29	183	4.6	177.1	14.1	99.5	98	-3.3	-83.9
NR-012-18	0.04867	2.4	0.39	177.7	3.6	174.6	8.4	131.9	56.9	-1.8	-34.7
NR-012-19	0.09405	1.1	0.55	1079.5	14.5	1231.8	18.9	1509.2	21.4	12.4	28.5

Appendix

NR-012-20	0.05139	3.8	0.31	238.3	5.7	240.1	17	258.4	86.6	0.8	7.8
NR-012-21	0.05125	1.7	0.42	314.8	4.7	307.4	9.7	252.2	38.4	-2.4	-24.8
NR-012-22	0.04827	3.2	0.31	179	3.7	174.4	11	112.4	76.7	-2.6	-59.3
NR-012-23	0.05126	2.6	0.38	201.8	4.2	205.8	10.5	252.7	59.8	2	20.2
NR-012-24	0.05124	3	0.31	180.2	3.5	185.3	10.7	251.6	68.9	2.8	28.4
NR-012-25	0.07083	1.2	0.51	952	13.1	952.2	17.9	952.7	25.8	0	0.1
				U	Pb	Th	²⁰⁸Pb	²⁰⁶Pb	±1S	²⁰⁷Pb	±1S
Sample	Grain Code	Formation	Observation	[ppm]	[ppm]	U	²⁰⁶Pb	²³⁸U	[%]	²³⁵U	[%]
NR-021-1	284	Noreán		81	63	0.81	0.292	0.0279166	1.2	0.192006	5
NR-021-2	285	Noreán		132	59	0.471	0.1717	0.027512	1	0.204765	3.2
NR-021-3	286	Noreán		211	135	0.678	0.2357	0.0274865	1	0.187041	2.6
NR-021-4	287	Noreán		138	75	0.576	0.205	0.0277088	1.1	0.200772	3.1
NR-021-5	288	Noreán	Th/U >1	246	246	1.043	0.4109	0.0288056	1	0.202236	2.6
NR-021-6	289	Noreán		114	84	0.789	0.2484	0.0262482	1.1	0.18476	4.5
NR-021-7	290	Noreán		212	149	0.74	0.2529	0.0282232	0.9	0.19484	2.6
NR-021-8	291	Noreán		459	259	0.593	0.2129	0.0277149	0.9	0.189926	2.2
NR-021-9	292	Noreán		135	76	0.591	0.2146	0.0276553	1	0.188318	3
NR-021-10	293	Noreán		132	106	0.848	0.3074	0.0274199	1.2	0.19063	3.5
NR-021-11	294	Noreán		43	33	0.806	0.299	0.0272918	1.7	0.190993	6.6
NR-021-12	295	Noreán		75	37	0.528	0.1964	0.0280907	1.3	0.19389	4.1
NR-021-13	296	Noreán	Th/U >1	169	193	1.206	0.4226	0.0268758	1	0.193278	3.1
NR-021-14	297	Noreán		128	103	0.842	0.3237	0.0293443	1.1	0.199757	3.6
NR-021-15	298	Noreán		125	75	0.629	0.2325	0.0283689	1.1	0.190733	3.3
NR-021-16	299	Noreán		35	17	0.505	0.1962	0.0284048	2.2	0.192487	9
NR-021-17	303	Noreán		640	343	0.564	0.2014	0.0276024	0.8	0.187166	2.1
NR-021-18	304	Noreán		162	88	0.572	0.2011	0.0272716	1	0.182977	3.3
NR-021-19	305	Noreán		87	58	0.698	0.2895	0.0281679	1.4	0.261942	4.2
NR-021-20	306	Noreán		419	241	0.607	0.2166	0.0277275	0.8	0.190188	2.4
NR-021-21	307	Noreán	Th/U >1	112	119	1.117	0.384	0.0273066	1.2	0.184091	4.1

Appendix

NR-021-22	308	Noreán		141	124	0.929	0.3241	0.027655	1.1	0.179711	3.2
NR-021-23	309	Noreán	high 208 Th/U >1	165	218	1.392	0.5163	0.0266491	0.9	0.176675	3.2
NR-021-24	310	Noreán		164	114	0.729	0.2636	0.027994	1.1	0.182282	3
NR-021-25	311	Noreán		121	95	0.824	0.2908	0.0278376	1	0.189994	3.3
NR-021-26	312	Noreán		67	46	0.721	0.2517	0.0272843	1.5	0.168867	5.5
Sample	²⁰⁷ Pb ²⁰⁶ Pb	±1s [%]	rho	²⁰⁶ Pb ²³⁸ U	±2s [Ma]	²⁰⁷ Pb ²³⁵ U	±2s [Ma]	²⁰⁷ Pb ²⁰⁶ Pb	±2s [Ma]	Disc. I. [%]	Disc. II. [%]
NR-021-1	0.04988	4.9	0.23	177.5	4.1	178.3	16.6	189.6	114.1	0.5	6.4
NR-021-2	0.05398	3	0.3	175	3.3	189.2	11	370.3	68.5	7.5	52.8
NR-021-3	0.04935	2.4	0.39	174.8	3.5	174.1	8.4	164.7	56.5	-0.4	-6.1
NR-021-4	0.05255	2.9	0.37	176.2	3.9	185.8	10.5	309.5	65.6	5.2	43.1
NR-021-5	0.05092	2.4	0.4	183.1	3.8	187	9	237.2	55.6	2.1	22.8
NR-021-6	0.05105	4.4	0.25	167	3.7	172.1	14.4	243.2	101.1	3	31.3
NR-021-7	0.05007	2.5	0.36	179.4	3.3	180.8	8.8	198.3	57.5	0.7	9.5
NR-021-8	0.0497	2	0.41	176.2	3.1	176.6	7.1	181.1	46.7	0.2	2.7
NR-021-9	0.04939	2.8	0.33	175.9	3.4	175.2	9.7	166.3	66.7	-0.4	-5.7
NR-021-10	0.05042	3.3	0.35	174.4	4.2	177.2	11.4	214.6	75.7	1.6	18.7
NR-021-11	0.05076	6.4	0.26	173.6	5.9	177.5	21.7	229.8	147.8	2.2	24.5
NR-021-12	0.05006	3.8	0.32	178.6	4.6	179.9	13.4	197.8	89.3	0.8	9.7
NR-021-13	0.05216	2.9	0.34	171	3.5	179.4	10.2	292.4	66.6	4.7	41.5
NR-021-14	0.04937	3.5	0.3	186.4	4	184.9	12.4	165.6	81.4	-0.8	-12.6
NR-021-15	0.04876	3.1	0.32	180.3	3.7	177.3	10.7	136.5	73.5	-1.7	-32.1
NR-021-16	0.04915	8.7	0.24	180.6	7.7	178.7	29.7	155	204.5	-1	-16.5
NR-021-17	0.04918	1.9	0.37	175.5	2.6	174.2	6.7	156.4	45.7	-0.8	-12.2
NR-021-18	0.04866	3.1	0.31	173.4	3.5	170.6	10.2	131.6	72.9	-1.7	-31.8
NR-021-19	0.06745	4	0.33	179.1	4.9	236.2	17.8	851.6	82.5	24.2	79
NR-021-20	0.04975	2.3	0.34	176.3	2.9	176.8	7.9	183.3	53.2	0.3	3.8
NR-021-21	0.04889	3.9	0.29	173.7	4.1	171.6	13	142.8	92.1	-1.2	-21.6
NR-021-22	0.04713	3.1	0.33	175.9	3.8	167.8	10	55.9	72.9	-4.8	-214.6

Appendix

NR-021-23	0.04808	3.1	0.29	169.5	3.2	165.2	9.9	103.4	73.2	-2.6	-64
NR-021-24	0.04723	2.8	0.36	178	3.8	170	9.4	60.7	66.4	-4.7	-193.2
NR-021-25	0.0495	3.1	0.31	177	3.5	176.6	10.7	171.6	73.4	-0.2	-3.1
NR-021-26	0.04489	5.3	0.27	173.5	5	158.4	16.1	0.1	0.2	-9.5	-173429.1
				U	Pb	Th	²⁰⁸ Pb	²⁰⁶ Pb	±1σ	²⁰⁷ Pb	±1σ
Sample	Grain Code	Formation	Observation	[ppm]	[ppm]	U	²⁰⁶ Pb	²³⁸ U	[%]	²³⁵ U	[%]
LC-031-1	343	Girón		201	175	0.97	0.337	0.0315262	2.1	0.236267	3.6
LC-031-2	344	Girón		812	281	0.379	0.1204	0.0748296	0.7	0.589586	1.4
LC-031-3	345	Girón		283	91	0.36	0.1182	0.1573042	0.8	1.591932	1.4
LC-031-4	346	Girón		413	242	0.653	0.2267	0.0412267	0.8	0.298993	1.9
LC-031-5	347	Girón		214	56	0.29	0.0991	0.2132265	0.7	2.514141	1.4
LC-031-6	348	Girón		536	289	0.596	0.2249	0.0326704	0.8	0.236228	1.8
LC-031-7	349	Girón		57	24	0.473	0.1608	0.0298509	1.6	0.206431	5.4
LC-031-8	350	Girón		293	6	0.025	0.009	0.2652064	0.8	3.478657	1.3
LC-031-9	351	Girón		132	67	0.57	0.1792	0.1536382	0.8	1.495745	1.6
LC-031-10	352	Girón		360	192	0.594	0.2053	0.073939	0.8	0.596967	1.6
LC-031-11	353	Girón		200	78	0.433	0.139	0.193856	0.8	2.108383	1.5
LC-031-12	354	Girón		420	235	0.623	0.2111	0.0758003	0.8	0.608501	1.5
LC-031-13	355	Girón		103	82	0.892	0.2814	0.0986531	0.9	0.818653	2.1
LC-031-14	356	Girón		748	155	0.235	0.0642	0.0706528	0.7	0.55919	1.4
LC-031-15	357	Girón		451	381	0.942	0.3162	0.0315532	0.8	0.221224	2.2
LC-031-16	358	Girón	Th/U >1 high U Th/U	275	346	1.399	0.4925	0.0321674	1.3	0.2378	4.1
LC-031-17	359	Girón		1058	1285	1.352	0.4204	0.0754079	0.7	0.604944	1.4
LC-031-18	363	Girón		466	20	0.047	0.0165	0.0758759	0.7	0.585099	1.4
LC-031-19	364	Girón		79	49	0.699	0.2271	0.165927	0.9	1.675423	1.9
LC-031-20	365	Girón		181	83	0.512	0.1715	0.0317958	1	0.216625	2.4
LC-031-21	366	Girón		78	34	0.491	0.157	0.1988422	0.9	2.233781	1.8
LC-031-22	367	Girón		198	34	0.195	0.0617	0.166143	0.8	1.672059	1.5

Appendix

LC-031-23	368	Girón		319	105	0.367	0.1221	0.0743486	0.8	0.582912	1.6
LC-031-24	369	Girón		451	361	0.89	0.3042	0.0316261	0.8	0.219063	2
LC-031-25	370	Girón		312	137	0.488	0.1644	0.0726492	0.7	0.543531	1.6
LC-031-26	371	Girón	Th/U >1	225	203	1.001	0.3277	0.1986926	0.8	2.20464	1.4
	²⁰⁷ Pb	±1σ	rho	²⁰⁶ Pb	±2σ	²⁰⁷ Pb	±2σ	²⁰⁷ Pb	±2σ	Disc. I.	Disc. II.
Sample	²⁰⁶ Pb	[%]		²³⁸ U	[Ma]	²³⁵ U	[Ma]	²⁰⁶ Pb	[Ma]	[%]	[%]
LC-031-1	0.05435	3	0.58	200.1	8.2	215.4	14.1	385.8	66.7	7.1	48.1
LC-031-2	0.05714	1.2	0.52	465.2	6.7	470.6	10.8	497.2	27.2	1.2	6.4
LC-031-3	0.0734	1.2	0.54	941.8	13.4	967.1	17.8	1025	24.8	2.6	8.1
LC-031-4	0.0526	1.7	0.44	260.4	4.2	265.6	8.7	311.6	38	2	16.4
LC-031-5	0.08552	1.1	0.55	1246	16.8	1276.1	19.7	1327.3	22.5	2.4	6.1
LC-031-6	0.05244	1.6	0.46	207.2	3.4	215.3	7.1	304.8	37.3	3.8	32
LC-031-7	0.05016	5.2	0.3	189.6	6.1	190.6	18.9	202.2	119.7	0.5	6.2
LC-031-8	0.09513	1.1	0.59	1516.4	21.4	1522.4	21.3	1530.7	21.2	0.4	0.9
LC-031-9	0.07061	1.4	0.49	921.3	13.2	928.7	19.1	946.2	28.3	0.8	2.6
LC-031-10	0.05856	1.4	0.49	459.8	6.7	475.3	11.9	550.7	30.2	3.3	16.5
LC-031-11	0.07888	1.2	0.57	1142.2	17.5	1151.5	20.2	1169.2	24.3	0.8	2.3
LC-031-12	0.05822	1.3	0.53	471	7.3	482.6	11.6	538.2	28.2	2.4	12.5
LC-031-13	0.06018	1.9	0.44	606.5	10.8	607.3	19.3	610.3	41.1	0.1	0.6
LC-031-14	0.0574	1.2	0.52	440.1	6.1	451	10.1	507.1	26.4	2.4	13.2
LC-031-15	0.05085	2.1	0.37	200.3	3.3	202.9	8.2	234.1	48	1.3	14.5
LC-031-16	0.05362	3.9	0.31	204.1	5.2	216.6	16.2	355	88.8	5.8	42.5
LC-031-17	0.05818	1.2	0.54	468.7	6.7	480.4	10.6	536.7	25.7	2.4	12.7
LC-031-18	0.05593	1.3	0.5	471.5	6.6	467.7	10.9	449.5	28.3	-0.8	-4.9
LC-031-19	0.07323	1.7	0.46	989.6	15.8	999.2	23.9	1020.5	33.9	1	3
LC-031-20	0.04941	2.2	0.41	201.8	3.9	199.1	8.8	167.5	51.7	-1.3	-20.5
LC-031-21	0.08148	1.6	0.48	1169.1	18.4	1191.7	25.2	1233	31.1	1.9	5.2
LC-031-22	0.07299	1.3	0.49	990.8	13.8	998	19.5	1013.7	27.4	0.7	2.3
LC-031-23	0.05686	1.4	0.5	462.3	7.1	466.3	11.8	486.3	30.3	0.9	4.9

Appendix

LC-031-24	0.05024	1.8	0.4	200.7	3.2	201.1	7.3	206	42.4	0.2	2.6
LC-031-25	0.05426	1.4	0.46	452.1	6.5	440.8	11.4	382	32.1	-2.6	-18.3
LC-031-26	0.08047	1.2	0.56	1168.3	17	1182.5	20.1	1208.7	24	1.2	3.3
				U	Pb	Th	²⁰⁸Pb	²⁰⁶Pb	±1S	²⁰⁷Pb	±1S
Sample	Grain Code	Formation	Observation	[ppm]	[ppm]	U	²⁰⁶Pb	²³⁸U	[%]	²³⁵U	[%]
LC-032-1	228	Girón	high ²⁰⁸ Th/U >1	243	326	1.492	0.507	0.0312663	0.9	0.222959	2.5
LC-032-2	229	Girón		360	251	0.774	0.2719	0.03301	0.9	0.222127	2
LC-032-3	230	Girón		660	305	0.514	0.1606	0.2502206	0.7	3.309022	1.2
LC-032-4	231	Girón		543	101	0.207	0.0685	0.0719619	0.7	0.55482	1.5
LC-032-5	232	Girón		452	104	0.257	0.0846	0.0732392	0.8	0.570332	1.5
LC-032-6	233	Girón		300	176	0.653	0.2267	0.2471514	0.7	3.601199	1.3
LC-032-7	234	Girón	Th/U >1	134	167	1.39	0.4828	0.0318509	1.2	0.224248	3.4
LC-032-8	235	Girón		204	73	0.396	0.127	0.2698776	0.7	3.666789	1.3
LC-032-9	236	Girón		257	142	0.608	0.2166	0.0791767	0.8	0.629127	1.8
LC-032-10	237	Girón		297	133	0.497	0.1719	0.0738192	0.8	0.586957	1.8
LC-032-11	238	Girón		284	201	0.789	0.2713	0.031356	0.8	0.217009	2.1
LC-032-12	239	Girón		243	165	0.75	0.2504	0.0726819	0.8	0.55492	1.7
LC-032-13	243	Girón		214	52	0.271	0.0937	0.0715264	0.8	0.560838	2
LC-032-14	244	Girón		215	128	0.666	0.2344	0.0314404	0.9	0.218546	2.1
	²⁰⁷Pb	±1S	rho	²⁰⁶Pb	±2S	²⁰⁷Pb	±2S	²⁰⁷Pb	±2S	Disc. I.	Disc. II.
Sample	²⁰⁶Pb	[%]		²³⁸U	[Ma]	²³⁵U	[Ma]	²⁰⁶Pb	[Ma]	[%]	[%]
LC-032-1	0.05172	2.3	0.35	198.5	3.4	204.4	9.2	273	53.2	2.9	27.3
LC-032-2	0.0488	1.8	0.44	209.4	3.6	203.7	7.3	138.5	41.7	-2.8	-51.2
LC-032-3	0.09591	1	0.55	1439.6	17.3	1483.2	19.1	1546.1	20	2.9	6.9
LC-032-4	0.05592	1.3	0.46	448	6	448.1	11	449.1	30.2	0	0.3
LC-032-5	0.05648	1.3	0.51	455.6	6.7	458.2	11	471.3	28.7	0.6	3.3
LC-032-6	0.10568	1.1	0.57	1423.8	19	1549.8	20.7	1726.2	20.3	8.1	17.5
LC-032-7	0.05106	3.2	0.34	202.1	4.6	205.4	12.7	243.7	74.1	1.6	17.1

Appendix

LC-032-8	0.09854	1.1	0.57	1540.2	20.3	1564.2	20.9	1596.7	20.8	1.5	3.5
LC-032-9	0.05763	1.6	0.45	491.2	7.6	495.6	14.2	515.7	35.7	0.9	4.7
LC-032-10	0.05767	1.6	0.45	459.1	6.9	468.9	13.2	517.2	34.8	2.1	11.2
LC-032-11	0.05019	1.9	0.39	199	3.2	199.4	7.6	204.1	44.8	0.2	2.5
LC-032-12	0.05537	1.4	0.5	452.3	7.2	448.2	12.1	427.4	32.4	-0.9	-5.8
LC-032-13	0.05687	1.9	0.38	445.3	6.6	452.1	14.7	486.5	41.2	1.5	8.5
LC-032-14	0.05041	1.9	0.45	199.6	3.7	200.7	7.8	214.2	44.3	0.6	6.8
				U	Pb	Th	²⁰⁸ Pb	²⁰⁶ Pb	±1S	²⁰⁷ Pb	±1S
Sample	Grain Code	Formation	Observation	[ppm]	[ppm]	U	²⁰⁶ Pb	²³⁸ U	[%]	²³⁵ U	[%]
AR-222-1	284	Arcabuco		221	92	0.462	0.1555	0.0704144	1	0.567715	1.8
AR-222-2	285	Arcabuco		282	112	0.442	0.1427	0.2091245	0.7	2.464037	1.3
AR-222-3	286	Arcabuco	Th/U >1	101	102	1.125	0.4139	0.0748893	0.9	0.592326	2.5
AR-222-4	287	Arcabuco		50	24	0.531	0.1776	0.1495933	1	1.441627	2.5
AR-222-5	288	Arcabuco		176	119	0.747	0.2157	0.0761048	1	0.756648	1.9
AR-222-6	289	Arcabuco		361	189	0.583	0.196	0.0740964	0.7	0.587501	1.4
AR-222-7	290	Arcabuco		367	173	0.524	0.1716	0.1668604	0.7	1.684115	1.3
AR-222-8	291	Arcabuco		320	60	0.209	0.0671	0.1698137	0.7	1.714951	1.4
AR-222-9	292	Arcabuco		151	65	0.481	0.1632	0.0772358	0.9	0.592631	2.2
AR-222-10	293	Arcabuco		652	337	0.576	0.1934	0.0750429	0.7	0.593373	1.4
AR-222-11	294	Arcabuco		426	127	0.331	0.1098	0.1590405	0.7	1.587166	1.3
AR-222-12	295	Arcabuco		218	120	0.602	0.2039	0.0748918	0.8	0.580499	1.7
AR-222-13	296	Arcabuco		215	141	0.726	0.2298	0.269184	0.8	3.835898	1.3
AR-222-14	297	Arcabuco		353	107	0.339	0.1048	0.2260266	0.7	2.804526	1.3
AR-222-15	298	Arcabuco		170	37	0.246	0.0808	0.167624	0.8	1.721061	1.5
AR-222-16	299	Arcabuco		331	248	0.832	0.2708	0.2473846	0.7	3.194478	1.3
AR-222-17	303	Arcabuco		115	57	0.554	0.187	0.0746119	0.9	0.599097	2.2
AR-222-18	304	Arcabuco		414	118	0.319	0.1081	0.2261414	0.7	2.906334	1.3
AR-222-19	305	Arcabuco		111	53	0.535	0.1791	0.1003383	1.1	0.848811	2.3
AR-222-20	306	Arcabuco		188	59	0.354	0.1167	0.1608974	0.8	1.598758	1.5

Appendix

AR-222-21	307	Arcabuco		252	211	0.934	0.3186	0.0753499	0.9	0.599618	1.9
AR-222-22	308	Arcabuco		140	105	0.833	0.2773	0.1922775	0.8	2.11201	1.5
AR-222-23	309	Arcabuco	high U	907	119	0.147	0.0154	0.1810524	0.7	1.982971	1.2
AR-222-24	310	Arcabuco		167	95	0.633	0.2079	0.259627	0.8	3.672627	1.3
AR-222-25	311	Arcabuco		691	192	0.309	0.1026	0.0805643	0.7	0.634393	1.4
AR-222-26	312	Arcabuco		271	134	0.551	0.1863	0.076315	0.8	0.59508	1.8
AR-222-27	313	Arcabuco		256	111	0.485	0.1724	0.0607366	0.8	0.465867	2.2
AR-222-28	314	Arcabuco	high U	1011	838	0.923	0.3353	0.0596197	0.8	0.482167	1.6
AR-222-29	315	Arcabuco		605	58	0.116	0.0356	0.076591	0.7	0.608342	1.4
AR-222-30	316	Arcabuco		272	93	0.38	0.12	0.2269879	1	2.914688	1.6
AR-222-31	317	Arcabuco		368	320	0.967	0.3205	0.0743148	0.8	0.589987	1.6
AR-222-32	318	Arcabuco		230	121	0.587	0.1905	0.0741445	0.8	0.577946	1.7
AR-222-33	319	Arcabuco		572	46	0.09	0.0303	0.0756254	0.7	0.591582	1.4
AR-222-34	323	Arcabuco		344	111	0.365	0.1217	0.0779974	0.7	0.598547	1.6
AR-222-35	324	Arcabuco		415	37	0.101	0.034	0.2393366	0.7	3.097977	1.3
AR-222-36	325	Arcabuco		625	323	0.576	0.192	0.0779278	0.8	0.615914	1.6
AR-222-37	326	Arcabuco	high U	962	382	0.446	0.1193	0.0550152	0.8	0.456223	1.6
AR-222-38	327	Arcabuco	high U	1052	496	0.526	0.1792	0.0701603	0.8	0.550941	1.4
AR-222-39	328	Arcabuco		78	35	0.507	0.1632	0.1673377	0.9	1.646339	1.9
AR-222-40	329	Arcabuco		188	77	0.458	0.1441	0.2965091	0.7	4.25231	1.3
AR-222-41	330	Arcabuco		227	54	0.267	0.0886	0.0911212	0.8	0.821147	1.6
AR-222-42	331	Arcabuco		123	30	0.275	0.0964	0.1746441	0.8	1.759745	1.7
AR-222-43	332	Arcabuco		250	63	0.281	0.0916	0.2382425	0.7	2.844097	1.4
AR-222-44	333	Arcabuco		97	33	0.382	0.1251	0.1670419	1	1.800923	1.9
AR-222-45	334	Arcabuco		80	57	0.783	0.2593	0.1998306	0.9	2.254473	1.8
AR-222-46	335	Arcabuco		80	49	0.685	0.2319	0.0761703	1	0.589067	2.6
AR-222-47	336	Arcabuco		171	78	0.509	0.1683	0.1700275	0.8	1.693663	1.5
AR-222-48	337	Arcabuco		515	37	0.079	0.0289	0.1792373	0.7	2.000029	1.3
AR-222-49	338	Arcabuco		218	52	0.268	0.0879	0.1675193	0.8	1.689992	1.4
AR-222-50	339	Arcabuco	high U	1560	178	0.127	0.0223	0.1779018	0.8	2.142489	1.4

Appendix

Sample	²⁰⁷ Pb	±1σ	rho	²⁰⁶ Pb	±2σ	²⁰⁷ Pb	±2σ	²⁰⁷ Pb	±2σ	Disc. I. [%]	Disc. II. [%]
	²⁰⁶ Pb	[%]		²³⁸ U	[Ma]	²³⁵ U	[Ma]	²⁰⁶ Pb	[Ma]		
AR-222-1	0.05847	1.5	0.56	438.7	8.7	456.5	13.6	547.6	33.9	3.9	19.9
AR-222-2	0.08546	1.1	0.53	1224.2	15.5	1261.5	19.1	1325.9	22.3	3	7.7
AR-222-3	0.05736	2.3	0.34	465.5	7.6	472.4	18.8	505.6	51.4	1.4	7.9
AR-222-4	0.06989	2.3	0.39	898.7	16.8	906.4	30.8	925.3	48.4	0.9	2.9
AR-222-5	0.07211	1.6	0.52	472.8	8.8	572.1	16.3	989	32.6	17.3	52.2
AR-222-6	0.05751	1.2	0.52	460.8	6.6	469.3	10.8	511	27.3	1.8	9.8
AR-222-7	0.0732	1.1	0.52	994.8	12.7	1002.5	17	1019.6	23.5	0.8	2.4
AR-222-8	0.07324	1.2	0.53	1011.1	13.8	1014.1	17.9	1020.8	24.4	0.3	1
AR-222-9	0.05565	2	0.42	479.6	8.7	472.5	17	438.5	45.6	-1.5	-9.4
AR-222-10	0.05735	1.2	0.52	466.5	6.5	473	10.7	505	26.9	1.4	7.6
AR-222-11	0.07238	1.1	0.55	951.4	12.6	965.2	16.1	996.7	22.3	1.4	4.5
AR-222-12	0.05622	1.5	0.49	465.6	7.5	464.8	12.8	461	33.5	-0.2	-1
AR-222-13	0.10335	1.1	0.6	1536.7	21.9	1600.3	21.7	1685.2	20.7	4	8.8
AR-222-14	0.08999	1.1	0.54	1313.6	16.9	1356.7	20	1425.4	22.1	3.2	7.8
AR-222-15	0.07447	1.3	0.52	999	14.6	1016.4	19.6	1054.2	26.6	1.7	5.2
AR-222-16	0.09365	1.1	0.55	1425	18.1	1455.8	19.8	1501.2	20.8	2.1	5.1
AR-222-17	0.05824	2	0.42	463.9	8.3	476.7	16.7	538.7	43.6	2.7	13.9
AR-222-18	0.09321	1.1	0.54	1314.2	16.9	1383.6	20.1	1492.2	21.8	5	11.9
AR-222-19	0.06135	2.1	0.47	616.4	13.1	624	21.9	651.7	44.4	1.2	5.4
AR-222-20	0.07207	1.3	0.54	961.8	14.5	969.7	19	987.9	26.4	0.8	2.6
AR-222-21	0.05772	1.7	0.47	468.3	8.2	477	14.7	519	37.5	1.8	9.8
AR-222-22	0.07966	1.3	0.51	1133.7	16.3	1152.7	21.3	1188.8	26.7	1.7	4.6
AR-222-23	0.07943	1	0.56	1072.7	13.5	1109.7	16.5	1183	20.5	3.3	9.3
AR-222-24	0.10259	1.1	0.58	1487.9	20.9	1565.4	21.6	1671.6	21	5	11
AR-222-25	0.05711	1.2	0.5	499.5	6.8	498.8	11.1	495.8	27.2	-0.1	-0.7
AR-222-26	0.05655	1.6	0.44	474.1	7.4	474.1	13.8	474.2	36.2	0	0
AR-222-27	0.05563	2	0.37	380.1	5.9	388.3	14.1	437.7	45.1	2.1	13.2

Appendix

AR-222-28	0.05866	1.4	0.48	373.3	5.6	399.6	10.6	554.4	31	6.6	32.7
AR-222-29	0.05761	1.2	0.51	475.7	6.7	482.5	10.9	514.9	27	1.4	7.6
AR-222-30	0.09313	1.3	0.6	1318.7	23.1	1385.7	24.5	1490.6	25	4.8	11.5
AR-222-31	0.05758	1.4	0.48	462.1	7	470.9	12.2	513.8	31.5	1.9	10.1
AR-222-32	0.05653	1.5	0.46	461.1	7.2	463.1	13	473.4	34.4	0.4	2.6
AR-222-33	0.05673	1.2	0.53	470	6.7	471.9	10.6	481.3	26.7	0.4	2.4
AR-222-34	0.05566	1.4	0.46	484.2	6.9	476.3	12.3	438.7	32.1	-1.6	-10.4
AR-222-35	0.09388	1	0.58	1383.2	18.5	1432.2	19.7	1505.7	20.5	3.4	8.1
AR-222-36	0.05732	1.4	0.5	483.7	7.3	487.3	12.2	504	30.4	0.7	4
AR-222-37	0.06014	1.4	0.5	345.2	5.5	381.6	10.5	608.8	31	9.5	43.3
AR-222-38	0.05695	1.2	0.54	437.1	6.4	445.6	10.1	489.7	26.3	1.9	10.7
AR-222-39	0.07135	1.7	0.48	997.4	16.6	988.1	23.9	967.6	34.1	-0.9	-3.1
AR-222-40	0.10401	1.1	0.56	1674	21.9	1684.2	22	1697	21.2	0.6	1.4
AR-222-41	0.06536	1.3	0.51	562.2	8.6	608.7	14.3	785.9	28.5	7.6	28.5
AR-222-42	0.07308	1.5	0.48	1037.6	15.1	1030.8	21.5	1016.2	29.9	-0.7	-2.1
AR-222-43	0.08658	1.2	0.53	1377.6	18.4	1367.3	21	1351.2	23.4	-0.8	-2
AR-222-44	0.07819	1.6	0.51	995.8	17.8	1045.8	24.8	1151.8	32.6	4.8	13.5
AR-222-45	0.08182	1.6	0.48	1174.4	18.5	1198.2	25.6	1241.4	31.6	2	5.4
AR-222-46	0.05609	2.4	0.4	473.2	9.4	470.3	19.7	455.9	53.3	-0.6	-3.8
AR-222-47	0.07224	1.2	0.54	1012.3	15	1006.1	19	992.9	25.8	-0.6	-2
AR-222-48	0.08093	1	0.56	1062.8	14	1115.5	17.2	1219.8	21.2	4.7	12.9
AR-222-49	0.07317	1.2	0.53	998.4	13.9	1004.8	18.1	1018.6	24.7	0.6	2
AR-222-50	0.08734	1.1	0.59	1055.5	16.4	1162.6	19.7	1368.2	22.6	9.2	22.9
				U	Pb	Th	²⁰⁸Pb	²⁰⁶Pb	±1S	²⁰⁷Pb	±1S
Sample	Grain Code	Formation	Observation	[ppm]	[ppm]	U	²⁰⁶Pb	²³⁸U	[%]	²³⁵U	[%]
AR-451-1	372	La Rusia		15	9	0.674	0.224	0.1709416	1.4	1.699388	3.4
AR-451-2	373	La Rusia		183	34	0.208	0.0693	0.1721642	0.8	1.721076	1.4
AR-451-3	374	La Rusia	high U high 208 Th/U >1	1056	1840	1.939	0.6451	0.0717537	0.7	0.579875	1.3

Appendix

AR-451-4	375	La Rusia		247	138	0.625	0.2121	0.0754802	0.8	0.580437	1.8
AR-451-5	376	La Rusia		166	54	0.362	0.1169	0.2011869	0.8	2.204259	1.4
AR-451-6	377	La Rusia		50	24	0.533	0.1824	0.2435878	0.9	3.11126	1.7
AR-451-7	378	La Rusia	Th/U >1	664	599	1.046	0.3461	0.0757374	0.8	0.590931	1.5
AR-451-8	379	La Rusia		119	36	0.34	0.1112	0.1680377	0.8	1.65484	1.7
AR-451-9	383	La Rusia		532	276	0.578	0.1947	0.0733656	0.7	0.571883	1.4
AR-451-10	384	La Rusia		223	113	0.564	0.1925	0.0744354	0.9	0.588174	1.8
AR-451-11	385	La Rusia		602	214	0.396	0.1321	0.0743753	0.8	0.586273	1.4
AR-451-12	386	La Rusia		91	64	0.777	0.2539	0.0791753	1	0.629402	2.6
AR-451-13	387	La Rusia	high 208 Th/U >1	151	222	1.626	0.5638	0.0726294	0.9	0.557458	2.2
AR-451-14	388	La Rusia		741	116	0.174	0.046	0.1182216	0.7	1.120593	1.4
AR-451-15	389	La Rusia	high U	930	370	0.443	0.15	0.0719582	0.7	0.558649	1.4
AR-451-16	390	La Rusia		411	78	0.212	0.0762	0.0775328	0.7	0.615053	1.6
AR-451-17	391	La Rusia		96	56	0.639	0.2189	0.0744882	1	0.591573	2.4
AR-451-18	392	La Rusia		260	145	0.621	0.2056	0.0729696	0.8	0.564023	1.8
AR-451-19	393	La Rusia		198	74	0.429	0.1372	0.2325348	0.9	3.136819	1.7
AR-451-20	394	La Rusia		86	29	0.379	0.1246	0.2524562	0.8	3.232251	1.6
AR-451-21	395	La Rusia		11	6	0.635	0.2162	0.1531559	1.5	1.420934	4.5
AR-451-22	2	La Rusia		627	395	0.709	0.2343	0.0736834	0.6	0.575168	1.6
AR-451-23	3	La Rusia		98	35	0.402	0.1284	0.1990894	0.7	2.146397	1.7
AR-451-24	4	La Rusia		114	27	0.265	0.086	0.1705623	0.7	1.727703	1.7
AR-451-25	6	La Rusia		496	224	0.507	0.1709	0.0768869	0.6	0.604505	1.7
AR-451-26	7	La Rusia		274	153	0.627	0.1999	0.0881489	0.8	0.739886	1.8
AR-451-27	8	La Rusia		56	20	0.403	0.1273	0.2470734	1	3.1451	1.8
AR-451-28	9	La Rusia		501	76	0.17	0.0419	0.1695411	0.6	1.853077	1.4
AR-451-29	11	La Rusia		721	308	0.479	0.1627	0.0770876	0.6	0.606017	1.6
AR-451-30	12	La Rusia		228	131	0.645	0.2194	0.0750639	0.7	0.586097	2
	²⁰⁷ Pb	±1σ	rho	²⁰⁶ Pb	±2σ	²⁰⁷ Pb	±2σ	²⁰⁷ Pb	±2σ	Disc. I.	Disc. II.
Sample	²⁰⁶ Pb	[%]		²³⁸ U	[Ma]	²³⁵ U	[Ma]	²⁰⁶ Pb	[Ma]	[%]	[%]

Appendix

AR-451-1	0.0721	3.1	0.42	1017.3	27.2	1008.3	44.1	988.9	63.1	-0.9	-2.9
AR-451-2	0.0725	1.2	0.52	1024	14.3	1016.4	18.7	1000.1	25.6	-0.7	-2.4
AR-451-3	0.05861	1.1	0.54	446.7	6.2	464.4	9.9	552.8	24.8	3.8	19.2
AR-451-4	0.05577	1.6	0.43	469.1	6.9	464.7	13.3	443.4	36	-0.9	-5.8
AR-451-5	0.07946	1.2	0.56	1181.7	17.4	1182.4	20.2	1183.7	24.1	0.1	0.2
AR-451-6	0.09264	1.4	0.53	1405.3	22.6	1435.5	26.3	1480.5	27.9	2.1	5.1
AR-451-7	0.05659	1.3	0.53	470.6	7.1	471.5	11.2	475.6	28.3	0.2	1
AR-451-8	0.07142	1.5	0.46	1001.3	14.3	991.4	21.1	969.6	30.4	-1	-3.3
AR-451-9	0.05653	1.2	0.5	456.4	6.3	459.2	10.5	473.5	27.5	0.6	3.6
AR-451-10	0.05731	1.6	0.47	462.8	7.6	469.7	13.6	503.5	35.1	1.5	8.1
AR-451-11	0.05717	1.2	0.54	462.5	6.7	468.5	10.5	498.2	26.3	1.3	7.2
AR-451-12	0.05765	2.4	0.39	491.2	9.6	495.7	20.5	516.7	52.8	0.9	4.9
AR-451-13	0.05567	2	0.39	452	7.5	449.9	15.9	439.2	44.6	-0.5	-2.9
AR-451-14	0.06875	1.1	0.53	720.3	9.7	763.3	14.6	891.2	24.2	5.6	19.2
AR-451-15	0.05631	1.2	0.53	447.9	6.5	450.6	10.3	464.5	26.8	0.6	3.6
AR-451-16	0.05753	1.5	0.44	481.4	6.7	486.7	12.7	512.1	32.5	1.1	6
AR-451-17	0.0576	2.2	0.42	463.1	9	471.9	18.2	514.6	48	1.9	10
AR-451-18	0.05606	1.6	0.43	454	6.9	454.1	13.3	454.8	36.5	0	0.2
AR-451-19	0.09784	1.4	0.56	1347.8	22.6	1441.8	25.8	1583.3	26.5	6.5	14.9
AR-451-20	0.09286	1.4	0.51	1451.1	21.2	1464.9	24.7	1485	26.4	0.9	2.3
AR-451-21	0.06729	4.3	0.33	918.6	25.4	897.8	54.8	846.8	89.4	-2.3	-8.5
AR-451-22	0.05661	1.5	0.39	458.3	5.6	461.4	12	476.6	33.1	0.7	3.8
AR-451-23	0.07819	1.6	0.42	1170.4	15.8	1163.9	24.3	1151.8	31.8	-0.6	-1.6
AR-451-24	0.07347	1.6	0.41	1015.2	13.4	1018.9	22.6	1026.9	32.6	0.4	1.1
AR-451-25	0.05702	1.5	0.38	477.5	5.8	480.1	12.7	492.5	34.2	0.5	3
AR-451-26	0.06088	1.7	0.41	544.6	7.9	562.3	16	634.9	36.6	3.2	14.2
AR-451-27	0.09232	1.5	0.53	1423.4	24.8	1443.8	28.3	1474.1	29.8	1.4	3.4
AR-451-28	0.07927	1.3	0.42	1009.6	11.5	1064.5	19.2	1179	26.4	5.2	14.4
AR-451-29	0.05702	1.5	0.38	478.7	5.7	481	12.5	492.2	33.4	0.5	2.7
AR-451-30	0.05663	1.8	0.37	466.6	6.7	468.4	14.9	477.2	40.8	0.4	2.2

Appendix

Sample	Grain Code	Formation	Observation	U	Pb	Th	²⁰⁸ Pb	²⁰⁶ Pb	±1S	²⁰⁷ Pb	±1S
				[ppm]	[ppm]	U	²⁰⁶ Pb	²³⁸ U	[%]	²³⁵ U	[%]
AR-351-1	13	Montebel	Th/U >1	36	42	1.322	0.4497	0.2139932	1	2.580808	2.5
AR-351-2	14	Montebel		104	64	0.689	0.2245	0.0749448	0.9	0.569667	2.7
AR-351-3	15	Montebel		162	109	0.752	0.2411	0.1998961	0.6	2.165358	1.6
AR-351-4	16	Montebel		618	235	0.426	0.1444	0.0751975	0.6	0.584134	1.5
AR-351-5	17	Montebel		43	23	0.591	0.1994	0.0761736	1.1	0.576381	3.4
AR-351-6	18	Montebel		137	67	0.552	0.1848	0.0745683	0.8	0.586393	2.2
AR-351-7	19	Montebel		273	105	0.429	0.1414	0.0766492	0.7	0.601625	1.9
AR-351-8	24	Montebel		461	208	0.503	0.1662	0.0769864	0.7	0.593949	1.7
AR-351-9	25	Montebel		542	94	0.194	0.0604	0.1669826	0.6	1.686478	1.4
AR-351-10	26	Montebel		223	64	0.318	0.1059	0.1680573	0.6	1.684026	1.6
AR-351-11	27	Montebel		656	332	0.569	0.1944	0.0732299	0.6	0.566569	1.6
AR-351-12	28	Montebel	high U	1666	439	0.296	0.0993	0.0770101	0.5	0.60121	1.4
AR-351-13	29	Montebel		61	18	0.338	0.1101	0.1726103	1	1.742342	2.4
AR-351-14	30	Montebel		74	38	0.572	0.1846	0.2512534	0.7	3.157252	1.8
AR-351-15	31	Montebel		172	52	0.342	0.1025	0.3071356	0.6	4.444721	1.4
AR-351-16	32	Montebel		45	11	0.277	0.086	0.2396053	0.9	2.809522	2.1
AR-351-17	33	Montebel		310	100	0.36	0.1191	0.1707842	0.6	1.752037	1.5
AR-351-18	34	Montebel		183	43	0.265	0.0886	0.1559727	0.7	1.492134	1.6
AR-351-19	35	Montebel		313	119	0.425	0.1384	0.1914827	0.6	2.075547	1.5
AR-351-20	36	Montebel		276	90	0.366	0.1188	0.1660652	0.6	1.662874	1.5
AR-351-21	37	Montebel		246	113	0.518	0.1691	0.0782707	0.7	0.608573	1.7
AR-351-22	38	Montebel		111	49	0.489	0.165	0.1682444	0.7	1.676773	1.6
AR-351-23	39	Montebel		270	35	0.144	0.0466	0.1592589	0.7	1.562379	1.6
AR-351-24	43	Montebel		168	34	0.23	0.0714	0.2359021	0.7	2.936512	1.5
AR-351-25	44	Montebel		335	186	0.623	0.1972	0.2611901	0.6	3.408541	1.4
AR-351-26	45	Montebel		278	65	0.262	0.0856	0.173965	0.6	1.750914	1.5
AR-351-27	46	Montebel		432	221	0.578	0.1969	0.0762436	0.7	0.611519	1.7

Appendix

AR-351-28	47	Montebel	high U	1355	489	0.405	0.1384	0.0707676	0.6	0.5609	1.5
AR-351-29	48	Montebel		282	141	0.56	0.1887	0.0735313	0.7	0.568648	1.9
AR-351-30	49	Montebel		59	18	0.353	0.1105	0.1624315	0.9	1.560703	2.1
AR-351-31	50	Montebel		174	42	0.275	0.0878	0.1697149	0.7	1.71904	1.6
AR-351-32	51	Montebel		548	277	0.567	0.1966	0.075703	0.6	0.593481	1.7
AR-351-33	52	Montebel		444	100	0.254	0.0809	0.233093	0.6	2.786532	1.4
AR-351-34	53	Montebel		93	31	0.38	0.1213	0.1723057	0.7	1.69652	1.9
AR-351-35	54	Montebel		856	485	0.636	0.2168	0.0749089	0.6	0.583496	1.5
AR-351-36	55	Montebel		700	172	0.276	0.0991	0.2162886	0.6	2.82708	1.4
AR-351-37	56	Montebel		112	47	0.471	0.1556	0.1645976	0.7	1.692367	1.9
AR-351-38	57	Montebel		664	298	0.503	0.1678	0.0784125	0.6	0.611423	1.6
AR-351-39	58	Montebel		303	166	0.612	0.2134	0.184941	0.6	2.230639	1.5
AR-351-40	59	Montebel		209	98	0.525	0.1757	0.0767449	0.7	0.601747	1.8
AR-351-41	63	Montebel		160	74	0.523	0.1715	0.0762775	0.7	0.596933	2.3
AR-351-42	64	Montebel		314	84	0.299	0.0965	0.1710384	0.6	1.724408	1.5
AR-351-43	65	Montebel		219	44	0.226	0.0734	0.1986195	0.6	2.147134	1.6
AR-351-44	66	Montebel	Th/U >1	135	143	1.196	0.3943	0.0765908	0.7	0.594786	2.2
AR-351-45	67	Montebel		68	19	0.315	0.1025	0.1706739	0.8	1.67712	2.1
AR-351-46	68	Montebel		286	85	0.334	0.1137	0.0755667	0.6	0.589127	1.6
AR-351-47	69	Montebel	high U	992	401	0.453	0.1486	0.0749228	0.6	0.580828	1.4
AR-351-48	70	Montebel		243	77	0.357	0.116	0.1648965	0.6	1.659011	1.5
AR-351-49	71	Montebel		748	138	0.207	0.0695	0.0769305	0.6	0.611064	1.5
AR-351-50	72	Montebel		793	263	0.372	0.1269	0.0757112	0.6	0.596833	1.6
	²⁰⁷ Pb	±1σ	rho	²⁰⁶ Pb	±2σ	²⁰⁷ Pb	±2σ	²⁰⁷ Pb	±2σ	Disc. I.	Disc. II.
Sample	²⁰⁶ Pb	[%]		²³⁸ U	[Ma]	²³⁵ U	[Ma]	²⁰⁶ Pb	[Ma]	[%]	[%]
AR-351-1	0.08747	2.3	0.41	1250.1	23.5	1295.2	37.6	1370.9	45.1	3.5	8.8
AR-351-2	0.05513	2.5	0.32	465.9	7.8	457.8	19.8	417.5	56.7	-1.8	-11.6
AR-351-3	0.07856	1.5	0.37	1174.8	12.9	1170	22.5	1161.2	30.1	-0.4	-1.2
AR-351-4	0.05634	1.4	0.38	467.4	5.3	467.1	11.6	465.8	32.1	-0.1	-0.3

Appendix

AR-351-5	0.05488	3.2	0.33	473.2	10.3	462.1	25.7	407.3	72.7	-2.4	-16.2
AR-351-6	0.05703	2.1	0.34	463.6	6.8	468.6	16.8	492.9	46.3	1.1	5.9
AR-351-7	0.05693	1.8	0.38	476.1	6.6	478.3	14.6	488.7	39.3	0.5	2.6
AR-351-8	0.05595	1.5	0.39	478.1	6.1	473.4	12.8	450.6	34.6	-1	-6.1
AR-351-9	0.07325	1.3	0.42	995.5	11.1	1003.4	18.3	1020.9	26.8	0.8	2.5
AR-351-10	0.07268	1.5	0.37	1001.4	10.9	1002.5	20.6	1005	30.8	0.1	0.4
AR-351-11	0.05611	1.4	0.38	455.6	5.2	455.8	11.5	456.9	32.4	0	0.3
AR-351-12	0.05662	1.3	0.38	478.3	5.1	478	11	476.8	29.7	-0.1	-0.3
AR-351-13	0.07321	2.2	0.4	1026.5	18.1	1024.3	30.8	1019.8	44.2	-0.2	-0.7
AR-351-14	0.09114	1.7	0.39	1444.9	18.5	1446.8	28.1	1449.5	32.2	0.1	0.3
AR-351-15	0.10496	1.3	0.44	1726.6	19.2	1720.7	23.8	1713.6	24.2	-0.3	-0.8
AR-351-16	0.08504	1.9	0.44	1384.6	22.9	1358.1	31.5	1316.6	36.7	-2	-5.2
AR-351-17	0.0744	1.4	0.41	1016.4	11.6	1027.9	19.3	1052.5	27.7	1.1	3.4
AR-351-18	0.06938	1.5	0.41	934.4	11.6	927.2	19.8	910.2	30.8	-0.8	-2.7
AR-351-19	0.07861	1.3	0.41	1129.4	12.5	1140.8	20.1	1162.5	26.8	1	2.8
AR-351-20	0.07262	1.3	0.44	990.4	11.9	994.5	18.9	1003.5	27.5	0.4	1.3
AR-351-21	0.05639	1.6	0.4	485.8	6.3	482.7	13	467.9	34.7	-0.6	-3.8
AR-351-22	0.07228	1.5	0.42	1002.4	12.8	999.8	21	994	30.7	-0.3	-0.8
AR-351-23	0.07115	1.4	0.42	952.7	11.7	955.4	19.4	961.8	29.3	0.3	1
AR-351-24	0.09028	1.4	0.44	1365.4	16.4	1391.4	23.1	1431.5	26.6	1.9	4.6
AR-351-25	0.09465	1.3	0.44	1495.9	16.6	1506.4	22.3	1521.1	24.5	0.7	1.7
AR-351-26	0.073	1.3	0.41	1033.9	11.3	1027.5	18.9	1013.9	27.4	-0.6	-2
AR-351-27	0.05817	1.6	0.38	473.7	6	484.5	13.5	536.3	35.6	2.2	11.7
AR-351-28	0.05748	1.3	0.43	440.8	5.4	452.1	10.6	510.2	29.2	2.5	13.6
AR-351-29	0.05609	1.8	0.36	457.4	6	457.1	14.1	455.9	39.7	-0.1	-0.3
AR-351-30	0.06969	1.9	0.45	970.3	17	954.7	26.3	919.2	39.1	-1.6	-5.6
AR-351-31	0.07346	1.4	0.45	1010.5	13.6	1015.7	20.6	1026.8	29.3	0.5	1.6
AR-351-32	0.05686	1.5	0.36	470.4	5.4	473.1	12.5	486.1	34.3	0.6	3.2
AR-351-33	0.0867	1.3	0.41	1350.7	13.9	1351.9	20.8	1353.9	24.9	0.1	0.2
AR-351-34	0.07141	1.8	0.37	1024.8	13.7	1007.2	24.9	969.2	37	-1.7	-5.7

Appendix

AR-351-35	0.05649	1.4	0.38	465.7	5	466.7	11.1	471.9	30.6	0.2	1.3
AR-351-36	0.0948	1.2	0.43	1262.2	13.5	1362.7	20.4	1524.1	23.7	7.4	17.2
AR-351-37	0.07457	1.8	0.38	982.3	13	1005.7	24.3	1057	35.7	2.3	7.1
AR-351-38	0.05655	1.5	0.36	486.6	5.2	484.5	12	474.2	32.5	-0.5	-2.6
AR-351-39	0.08748	1.4	0.39	1093.9	12.2	1190.7	21.7	1371.1	27.7	8.1	20.2
AR-351-40	0.05687	1.6	0.41	476.7	6.6	478.3	13.5	486.4	36	0.4	2
AR-351-41	0.05676	2.2	0.3	473.9	6.4	475.3	17.7	482.2	49	0.3	1.7
AR-351-42	0.07312	1.4	0.4	1017.8	11.3	1017.7	19.2	1017.4	28.1	0	0
AR-351-43	0.0784	1.4	0.41	1167.9	13.9	1164.1	21.9	1157.2	29	-0.3	-0.9
AR-351-44	0.05632	2.1	0.33	475.7	6.7	473.9	16.9	465.2	46.6	-0.4	-2.3
AR-351-45	0.07127	1.9	0.37	1015.8	14.6	999.9	26.7	965.2	39.9	-1.6	-5.2
AR-351-46	0.05654	1.5	0.35	469.6	5.2	470.3	12.4	473.8	34.4	0.1	0.9
AR-351-47	0.05623	1.3	0.39	465.7	5	465	10.5	461.3	29	-0.2	-1
AR-351-48	0.07297	1.4	0.4	983.9	11.1	993	19.2	1013.1	28.5	0.9	2.9
AR-351-49	0.05761	1.4	0.39	477.8	5.4	484.2	11.6	515	30.8	1.3	7.2
AR-351-50	0.05717	1.4	0.36	470.5	5.1	475.2	11.8	498.3	32.3	1	5.6

2. BOREHOLE DATA OF THE MIDDLE MAGDALENA VALLEY BASIN AND THE EASTERN CORDILLERA.

BOREHOLE	(Coord.) X	(Coord.) Y	DEPTH (m)	KB (M)	BOTTOM FM.
AL-1	926545	954369	1073		CRETACEOUS
ANH-07	1042185.27	1135921.3	738	0	SIMITÍ
ANH-14	1061193	1109229	637	0	ARCABUCO
AN-1	990360	1260730	899	4.05	BASEMENT
AT-1	971617.8	957159.4	1219	5.80	VILLETA
BR-1	984922	1233627.7	1859	102.6	GIRÓN
BV-1	1058271	1249530	2109	6.59	UMIR
CT-11	1014455	1300445	2268	73.32	LA LUNA
CS-112	1020191	1273080	1203	79.44	-
CJ-1	1055991	1238704	3474	5.30	TAMBOR
CS-1	980886	1185366	4063	8.11	CRETACEOUS
COR-1	1093522	1108545	1525	4.68	CRETACEOUS
FR-1	969138	1222030	698	4.68	BASEMENT
GL-1k	1026526	1281390	4114	9.36	PAJA
GN-1	1030337	1291910	3810	9.98	GIRÓN
GR-1	1061309	1255347	3162	7.80	UMIR
GY-1	1006620	1198850	4149	8.42	ESMERALDAS
IF-1625	1035990	1252331	687	2.49	SALADA
LN-1P	1059265	1250832	3443	7.80	LISAMA
MN-1	1067527	1091033	975	8.11	FOMEQUE
NT-43	1059979	1267798	3201	7.51	-
OP-2	1023379	1202556	4328	8.11	CRETACEOUS
PE-10	1055376	1259143	1859	6.24	MUGROSA
RE-1	1058634	1252762	2695	3.12	UMIR
SR-1	1011259	1284765	1394	4.36	MUGROSA
SAR-1	990220	1238400	2514	4.68	-
SN-1	1017701	1309622	1833	7.36	GIRÓN
YN-7	1010852	1298565	352	6.70	-
YR-126	1016174	1303994	2311	7.98	-
YR-129	1016180	1303977	2319	7.98	-

3. SEISMIC DATA OF THE MIDDLE MAGDALENA VALLEY BASIN AND THE EASTERN CORDILLERA.

LINE NAME	SURVEY NAME	BASIN	LENGTH (km)	(Start Coord.) X	(Start Coord.) Y	(End Coord.) X	(End Coord.) Y
LAT-1996-30	LAS AMELIAS-96	MMV	24.66	995648.7175	1172914.135	1015469.183	1157927.806
L-1984-212	NARE-84	MMV	12.03	955791.6588	1199397.754	966536.0782	1193905.334
SL-1995-2070	SAN LUIS-95	MMV	23.23	1057007.626	1265439.547	1078864.094	1256799.609
CF-1977-53	SAN FERNANDO-77 WAI	MMV	27.32	996190.6494	1224471.711	1010270.625	1200855.048
CF-1977-81	SAN FERNANDO-77 WAI	MMV	34.18	984448.7059	1218854.616	1001173.848	1188902.599
SQL-2003-630	QUEBRADA LARGA 2D-2003	MMV	17.02	1011736.935	1184897.091	1026538.755	1176136.806
DM-1987-1630	DE MARES-87	MMV	36.86	1022492.025	1264965.503	1053415.174	1244290.83
SL-1995-690	SAN LUIS-95	MMV	22.30	1023880.999	1204968.365	1044808.915	1196687.519
SE-1989-1880	SANTANDER-89	MMV	30.63	972882.2524	1206846.547	989714.6542	1181260.004
DW-2008-1045	DE_MARES_W_2D-2008	MMV	40.20	991664.2154	1272881.979	1020184.782	1244570.801
TUEU-1988-13	TUNJA NORTE-88	EC	22.52	1087245.799	1096355.127	1097366.085	1116444.299
MC-1977-1013	CARARE-77	MMV	16.77	971364.6891	1222511.28	985873.4503	1230926.117
PDR-1988-06	PAZ DEL RIO-88	EC	20.02	1136052.073	1142344.726	1154814.054	1135451.599
ANHSP-2005-24	SOAPAGA 2D-2005	EC	17.50	1135646	1169002.8	1153101.2	1166196
LAT-1996-10	LAS AMELIAS-96	MMV	16.97	1009338.534	1179242.118	1023335.378	1169565.723
T-1993-1100	TUNJA-93	EC	35.21	1083177.557	1110729.476	1106853.321	1136374.386
CL-1986-1393	DEMARES-86	MMV	20.00	1047376.538	1257201.03	1047333.252	1277200.279
S-1978-01	SABALO-78	MMV	96.09	1010625.952	1282430.181	1010573.535	1282165.362
L-1964-AI	ARRUGAS-64	MMV	13.44	1057941.645	1238410.09	1057970.746	1251846.071
RO-1985-25	LA ROMPIDA-85	MMV	9.58	1006068.145	1286095.616	1015645.816	1286125.555

Appendix

TMM-1991-28	MAGD MEDIO-91 PTOB	MMV	18.00	973993.2986	1258189.366	987356.8036	1246139.677
NC-1981-06	GUAYABITO-81	MMV	37.80	1003950.423	1196682.526	1028725.588	1225201.32
ANHSP-2005-02	SOAPAGA 2D-2005	EC	17.02	1119408.7	1137143.2	1133067.9	1126822.1
S-1978-18	SUESCA-78	EC	9.07	1033521.472	1065476.496	1040771.606	1060038.512
ANT-2008-02	ANTORCHA 2D-2008	MMV	26.89	959224.7	1204057.1	958174.9	1201569.5
SQL-2003-610	QUEBRADA LARGA 2D-2003	MMV	15.85	1011176.221	1182700.497	1024826.646	1174332.02
NMS-1998-1880	NUEVO MUNDO-98	MMV	11.75	1055868.42	1257752.478	1066609.688	1252997.25
NG-1982-01	GUAYABITO-82	MMV	11.21	982012.0527	1175926.959	990776.4643	1168943.077
PDM-1992-1000	PIEDEMONTA OCCIDENTAL-92	MMV	45.99	1012923.541	1191195.887	1052375.949	1167252.687
CS-1977-61	SOGAMOSO-77	MMV	30.61	1048049.261	1286083.032	1020088.494	1298157.214
LAT-1996-40	LAS AMELIAS-96	MMV	20.66	995731.6906	1164526.033	1013539.584	1153480.809
RO-1985-19	LA ROMPIDA-85	MMV	8.62	1006037.296	1284838.516	1014656.381	1284816.556
NMS-1998-2090	NUEVO MUNDO-98	MMV	11.37	1055294.624	1266227.829	1067028.663	1265646.178
DM-2004-1200	DE MARES 2D-2004	MMV	26.13	1025769.832	1271894.292	1051782.507	1271894.494
LL-1983-1260	LLANITO-83	MMV	7.18	1024345.768	1282751.525	1030445.386	1278970.616
TMM-1991-18	MAGD MEDIO-91 PTOB	MMV	11.00	958044.2464	1212645.218	967076.5089	1206391.013
NC-1981-11	GUAYABITO-81	MMV	21.68	999578.5252	1211146.539	1011513.39	1193094.481
L-1986-F	BARBACOAS-86	MMV	8.88	976881.2152	1235187.02	983166.7953	1228927.03
L-1985-112	NARE-85	MMV	17.83	964727.1191	1218228.834	980837.6678	1210612.498
SL-1995-1260	SAN LUIS-95	MMV	34.50	1025610.191	1243282.801	1055012.019	1224766
L-1985-101	NARE-85	MMV	11.94	966659.0492	1213395.699	971254.7766	1224418.743
T-1993-1000	TUNJA-93	EC	21.83	1080165.386	1117613.613	1098021.357	1105053.263
DM-1987-1230	DE MARES-87	MMV	33.10	1013931.981	1246444.858	1042198.661	1228593.535
T-1993-1280	TUNJA-93	EC	17.89	1092416.131	1130574.508	1104739.622	1118219.256
TMM-1991-16	MAGD MEDIO-91 PTOB	MMV	12.05	956993.9453	1208645.353	966301.8131	1200999.89
SQL-2001-1210	QUEBRADA LARGA 2D-2001	MMV	15.42	1024006.914	1208431.099	1038468.751	1202421.608
TUEU-1988-10	TUNJA NORTE-88	EC	14.53	1084216.965	1115022.809	1096102.592	1106673.188

Appendix

YEKT-1995-01	OPON-95	MMV	11.80	1013492.246	1198738.209	1024628.463	1194161.906
ANHSP-2005-18	SOAPAGA 2D-2005	EC	18.90	1126346.6	1151876.6	1145111.6	1148210.8
DM-1987-1470	DE MARES-87	MMV	40.56	1017177.503	1260903.501	1051804.06	1238867.641
SE-1989-1690	SANTANDER-89	MMV	14.63	975804.7103	1186090.865	984300.3451	1174179.272
L-1985-01	CARARE-85	MMV	13.16	997478.9162	1257788.037	990908.8213	1246381.615
22BRLA-1995-12	LANCEROS-95	EC	28.24	1066442.495	1102956.273	1088340.391	1084944.922
NMS-1998-0920	NUEVO MUNDO-98	MMV	18.65	1060749.339	1266864.902	1061341.361	1253229.306
OP-1981-12	OPON CARARE-81	MMV	14.50	1013777.735	1202696.151	1027182.074	1197086.614
T-1993-1650	TUNJA-93	EC	15.30	1110629.867	1138267.981	1120823.748	1126865.187
SL-1995-1230	SAN LUIS-95	MMV	27.67	1033811.614	1233635.637	1057475.225	1219221.857
T-1993-1040	TUNJA-93	EC	20.78	1082574.216	1120866.612	1100261.535	1108481.219
CG-2007-1080	CANTAGALLO 2D-2007	MMV	14.40	1009818.244	1299407.288	1022760.682	1293095.754
L-1985-108	TISQUIRAMA-85	MMV	9.05	1050951.583	1374510.268	1059806.067	1376348.337
YEKT-1995-10	OPON-95	MMV	16.56	1015853.423	1189534.39	1015854.059	1189454.213
DM-2004-1050	DE MARES 2D-2004	MMV	25.98	1043517.772	1266144.164	1043492.872	1266144.164
DM-1987-1570	DE MARES-87	MMV	18.17	1037510.354	1252561.449	1034935.939	1244429.289
A-1985-01	SAN FERNANDO-85	MMV	22.30	976742.355	1207860.688	992544.9775	1223596.911
SQL-2001-1050	QUEBRADA LARGA 2D-2001	MMV	12.60	1022611.473	1202276.517	1034004.219	1196754.647
NC-1981-01	GUAYABITO-81	MMV	20.16	1019193.674	1235676.376	1029273.538	1218230.326
S-1977-28	SALINAS-77	MMV	5.26	1058738.669	1267870.286	1063943.098	1268163.349
T-1993-1180	TUNJA-93	EC	16.80	1106861.763	1131219.719	1119474.104	1142296.175
ANHSP-2005-01	SOAPAGA 2D-2005	EC	56.26	1146913	1175319.6	1122855.7	1126747.7
DM-1987-1420	DE MARES-87	MMV	28.20	1011261.704	1257097.272	1036561.342	1244314.243
DM-1989-1435	DE MARES-89	MMV	17.95	1000466.447	1272871.51	1013447.996	1260359.614
SL-1995-1100	SAN LUIS-95	MMV	19.86	1069212.633	1257554.743	1069185.057	1257512.926
L-1985-06	CARARE-85	MMV	11.59	988633.3625	1263231.644	997895.5848	1256114.424
SL-1995-1850	SAN LUIS-95	MMV	21.95	1055059.495	1253998.12	1076411.688	1246172.945
CF-1977-121	SAN FERNANDO-77 WAI	MMV	29.31	970131.756	1202662.079	986894.0497	1177292.3
PDR-1988-12	PAZ DEL RIO-88	EC	7.82	1147318.285	1157723.835	1153017.613	1152294.52

Appendix

SAN-1993-13	SAN FERNANDO-93	MMV	17.32	983519.7332	1179566.411	1000126.869	1173543.964
GAL-2000-87	GUAYACANES 2D-2000	MMV	24.36	993128.1692	1198081.305	1004292.582	1176228.027
CY-1987-1115	CANTAGALL YARIGUI-87	MMV	12.58	1012879.537	1296509.526	1017590.6	1308167.19
PDM-1992-1600	PIEDEMORTE OCCIDENTAL-92	MMV	36.26	1032860.393	1211547.784	1065101.105	1192572.517
YEKT-1995-04	OPON-95	MMV	10.88	1013310.651	1194524.407	1023376.301	1190395.197
L-1985-112	TISQUIRAMA-85	MMV	8.01	1051174.726	1371048.978	1059161.41	1371596.514
N-1976-18	NUTRIA-76	MMV	23.85	1035754.482	1258829.955	1059597.318	1259111.366
DM-1989-1600	DE MARES-89	MMV	20.22	1002827.643	1278154.168	1018636.822	1264072.509
ANHSP-2005-22	SOAPAGA 2D-2005	EC	19.29	1136218.7	1167639.2	1154524.5	1161338.2
LAT-1996-51	LAS AMELIAS-96	MMV	66.38	1022890.402	1185746.893	993288.2432	1141786.408
CF-1977-78	SAN FERNANDO-77 WAI	MMV	47.68	1008541.6	1205217.188	974591.7034	1171520.62
DM-1987-1600	DE MARES-87	MMV	17.45	1033700.141	1253822.714	1048707.405	1244822.441
NC-1981-08	GUAYABITO-81	MMV	16.35	994923.4121	1193310.59	1009624.441	1200466.484
SL-1995-1420	SAN LUIS-95	MMV	30.15	1033013.216	1246047.927	1060501.263	1232271.943
CF-1977-69	SAN FERNANDO-77 WAI	MMV	28.15	990960.207	1218666.658	1007005.926	1195379.464
ANHSP-2005-20	SOAPAGA 2D-2005	EC	19.76	1137141.6	1167165.2	1151685.6	1153670.6
SL-1995-1630	SAN LUIS-95	MMV	17.69	1048438.221	1247416.861	1063278.914	1237693.091
CS-1977-12	SOGAMOSO-77	MMV	33.95	1034894.159	1314780.093	1014077.475	1288451.221
CY-1987-1285	CANTAGALL YARIGUI-87	MMV	9.70	1012114.223	1302459.273	1021482.372	1297395.3
A-1985-01	CHUCURI-85	MMV	28.91	989878.7765	1220913.087	1010378.842	1241285.588
L-1991-A	OPON-91	MMV	16.50	1022000.457	1189975.953	1025897.141	1205291.181
ANHSP-2005-06	SOAPAGA 2D-2005	EC	21.50	1119076.1	1141317.1	1139647.6	1134732.3
SQL-2007-1030	QUEBRADA LARGA 2D-2007	MMV	26.59	1008762.503	1194546.797	1033359.4	1184472.447
L-1985-02	CARARE-85	MMV	6.94	991796.7339	1262800.026	987925.5812	1257040.789
OP-1981-06	OPON CARARE-81	MMV	10.78	1019703.748	1204387.125	1029333.072	1199547.993
SQL-2001-1070	QUEBRADA LARGA 2D-2001	MMV	13.61	1022311.687	1204217.117	1034805.733	1198947.438

Appendix

ANHSP-2005-14	SOAPAGA 2D-2005	EC	21.61	1122014.3	1147096.3	1142707.1	1139988.1
SAN-1993-07	SAN FERNANDO-93	MMV	17.46	1000375.293	1201609.237	1016409.525	1194705.809
RO-1985-16	LA ROMPIDA-85	MMV	11.47	1011285.779	1278354.339	1011347.741	1289826.849
L-1982-20	COECNA NARE-82	MMV	18.97	967892.8347	1223274.039	981214.0346	1209763.762
L-1985-101	TISQUIRAMA-85	MMV	12.05	1052073.944	1377094.952	1055960.501	1388500.48
L-1986-D	BARBACOAS-86	MMV	6.97	980261.1981	1234836.989	987024.1307	1233246.973
L-1985-108	NARE-85	MMV	8.27	976166.6224	1218829.058	970343.5159	1224694.176
L-1982-07	COECNA NARE-82	MMV	24.23	965618.5238	1206002.767	976264.6585	1227761.68
TUEU-1988-08	TUNJA NORTE-88	EC	15.26	1079207.195	1109890.173	1091782.752	1101262.482
OP-1981-08	OPON CARARE-81	MMV	12.47	1017461.897	1203907.794	1028767.744	1198652.233
CG-2007-1255	CANTAGALLO_2D-2007	MMV	20.71	1009940.648	1307743.479	1027972.083	1298209.674
CG-2007-1048	CANTAGALLO_2D-2007	MMV	17.07	1008430.28	1296747.782	1023112.55	1289240.667
YEBD-1995-01	OPON EXPERIMENTAL-95	MMV	7.92	1014019.552	1196406.126	1021413.6	1193355.482
DM-1987-1320	DE MARES-87	MMV	54.93	1033921.922	1274604.91	1014888.425	1241513.944
22BRLA-1995-01	LANCEROS-95	EC	38.90	1066842.732	1082069.085	1066781.533	1081990.076
DE-2008-1300	DE_MARES_E_2D-2008	MMV	50.31	1039796.012	1215679.874	1040989.265	1246255.184
T-1993-1440	TUNJA-93	EC	11.82	1099946.632	1133226.275	1107387.76	1124045.599
SQL-2001-1100	QUEBRADA LARGA 2D-2001	MMV	22.37	1025357.521	1195097.209	1025311.12	1195021.309
SL-1995-1290	SAN LUIS-95	MMV	32.65	1028481.602	1243544.148	1058455.771	1230352.71
YETI-1996-09	CASCAJALES-96	MMV	31.70	975450.8496	1174632.384	975418.5272	1174537.783
DW-2008-1000	DE_MARES_W_2D-2008	MMV	41.91	989347.5952	1271291.814	1015965.912	1239129.394
LAT-1996-20	LAS AMELIAS-96	MMV	20.90	1003169.163	1176268.519	1019703.065	1163380.979
SE-1989-2010	SANTANDER-89	MMV	30.54	976006.8056	1210127.156	992261.8425	1184169.943
ALKRC-2006-05	ALHUCEMA 2D-2006	MMV	14.30	988352.9	1239357.6	976819.5	1230735.7
DE-2008-1100	DE_MARES_E_2D-2008	MMV	32.55	1025373.137	1217257.773	1035553.833	1247726.385
S-1978-30	SABALO-78	MMV	17.45	1002571.004	1286386.601	1016000.54	1282011.27
OP-1981-10	OPON CARARE-81	MMV	9.67	1018284.46	1202160.73	1027161.515	1198327.364
DM-1987-2050	DE MARES-87	MMV	24.79	1028050.289	1287131.385	1049614.6	1274922.641

Appendix

T-1993-1490	TUNJA-93	EC	16.62	1104604.059	1137193.988	1114950.037	1124192.705
DM-1987-1630W	DE MARES-87	MMV	17.11	1008473.648	1276778.794	1022492.025	1264965.503
LL-1983-1130	LLANITO-83	MMV	10.90	1022702.714	1275336.121	1028943.521	1284254.57
P-1978-07	PEROLES-78	MMV	16.38	1058902.259	1251394.966	1058836.083	1267769.63
11BR-1986-36	SOGAMOSO-86	MMV	8.25	1028222.306	1298932.208	1029820.644	1292100.185
B-1987-08	BAUL-87	MMV	15.36	965356.0132	1194541.028	975666.0529	1183275.783
TMM-1991-24	MAGD MEDIO-91 PTOB	MMV	16.69	967014.0748	1242695.583	979516.7711	1231740.106
S-1978-18	SABALO-78	MMV	19.41	971906.3536	1253484.103	985429.3737	1238903.219
CF-1977-97	SAN FERNANDO-77 GSI	MMV	18.86	976550.7739	1214720.136	986452.9476	1198673.263
CG-2007-1296	CANTAGALLO_2D-2007	MMV	21.85	1012355.563	1312520.365	1030956.963	1302042.966
CG-2007-1000	CANTAGALLO_2D-2007	MMV	14.53	1007390.137	1292503.271	1020372.486	1286202.513
DM-1989-2030	DE MARES-89	MMV	18.57	1026817.785	1285245.383	1042996.567	1275964.608
CF-1977-48	SAN FERNANDO-77 WAI	MMV	81.40	1019474.855	1225271.404	955537.1414	1177146.287
TUEU-1988-06	TUNJA NORTE-88	EC	10.03	1080264.895	1102466.22	1088648.387	1096971.393

CV MARTIN JAVIER REYES CORREA

Colombian

Date of birth: 04.11.1991

Languages: English (Professional Level) Spanish (Native)

German (Basic) Portuguese (Basic)



Education

- **PhD Geosciences (2017-2021)**
Structural and Geodynamics department
Georg-August-Universität Göttingen, Göttingen-Germany
Advisor: Prof. Dr. Jonas Kley
- **Bsc. Geology (2008-2014)**
Sciences Faculty
EAFIT University
Advisor: Juan Carlos Quintana

Professional Experience

- **Young Researcher (2017-2021)**
Structural and Geodynamics department
Georg-August-Universität Göttingen, Göttingen-Germany
- **Consultant Geologist (2017-2021)**
Amonite S.A.S Colombia
- **Research Geologist (2016-2017)**
Research group in applied geology
Universidad Industrial de Santander
- **Geologist in Training (2015)**
Geological modeling group
Colombian Petroleum Institute
- **Research Technician (2013)**
Geological modeling group
Colombian Petroleum Institute

Scientific Production

- La Cira Basement-high; Middle Magdalena Valley Basin. in *Andean Structural Styles: A Seismic Atlas*. **Reyes, M.**, Kley, J., Mora, A., Bello-Palacios, D., Vargas, A, F., Carvajal-Torres, J., Osorno (Accepted)
- Onset and style of Mesozoic extension in the Eastern Cordillera and Middle Magdalena Valley constrained by the first volcanic events. **Reyes, M.**, Kley, J., Mora, A., Dunkl, I., Carvajal-Torres, J. (In Review)
- First-order stratigraphic boundaries of the Late Cretaceous-Paleogene retroarc foreland basin in Colombia. Carvajal-Torres, J., Catuneanu, O., Mora, A., Caballero, V., **Reyes, M.**, (In Review)
- Sequence stratigraphic framework of the Campanian-Eocene foreland basin, Colombia Carvajal-Torres, J., Catuneanu, O., **Reyes, M.**, Mora, A., Quiroz, L., Caballero, V. (In Review)
- Movement vectors and deformation mechanisms in kinematic restorations: A case study from the Colombian Eastern Cordillera Carrillo, E., Mora, A., Ketcham, R., Parra, M., Constantino, D., Robles, W., Avellaneda, W., Carvajal, J., Corcione, M., Bello, W., Figueroa, J., Gomez, J., **Reyes M.**.....(2016)